Towards tunable topological insulator surfaces: An EELS study of Bi_2Se_3/organic interfaces

Mairi McCauley

School of Physics and Astronomy
College of Science and Engineering
University of Glasgow

Submitted in fulfilment of the requirements for the degree of
Doctor of Philosophy

October 2025

Abstract

Topological insulators (TIs) such as Bi_2Se_3 can host low-loss plasmons with enhanced transport properties at their surfaces that are promising for plasmonic and optoelectronic applications. However, practical use of TIs in plasmonic devices requires tunable control over these plasmonic properties. This thesis explores the use of organic molecular overlayers as surface dopants to modify the plasmonic behaviour of Bi_2Se_3.

Four different different organic overlayers; C_{60}, graphene, H_2Pc and CuPc, were selected to modify the Bi_2Se_3 surface, whilst enclosing the TI as required for potential device integration. Electron transparent lamellae were prepared using focused ion beam techniques from bulk crystals and analysed using transmission electron microscopy (TEM) and electron energy loss spectroscopy (EELS). Plasmon behaviour across insulator/Bi_2Se_3 and Bi_2Se_3/organic interfaces was probed using EELS and momentum-resolved EELS to investigate changes to plasmon energy, confinement and dispersion. Supporting simulations, calculated from bulk dielectric functions using analytical and finite element methods, were used to interpret EELS spectra and highlight localised plasmon modes.

At a Al_2O_3/Bi_2Se_3 interface, a surface plasmon mode at 5.3 eV was identified and shown to be confined to within 2 nm of the interface. Its $\sqrt{q}$ plasmon dispersion is characteristic of a two-dimensional π plasmon, similar to π plasmons in free-standing graphene, likely originating from the the first layer of Se atoms within Bi_2Se_3. At a SiO_2/Bi_2Se_3 interface, a surface plasmon at 5.6 eV was observed to coexist with the Bi_2Se_3 π plasmon, illustrating changes to Bi_2Se_3 surface behaviour even at insulating substrate interfaces. In contrast, a highly localised plasmon at 6.3 eV was observed at the Bi_2Se_3/C_{60} interface, confined to the first layer of C_{60} molecules. It exhibited very little plasmon dispersion and, with the aid of density functional theory calculations, was proposed arise from the formation of a hybridised plasmon mode. This mode also exhibited enhanced signal in the first molecular layer and a

significant charge transfer from Bi_2Se_3 to the first layer of C_{60} molecules, affirming it to be a hybrid plasmon mode.

These findings were expanded upon by performing similar studies on Bi_2Se_3/graphene, Bi_2Se_3/H_2Pc and Bi_2Se_3/CuPc interfaces. The plasmon energy at each interface was observed at 6.0, 6.4 and 6.4 eV respectively, indicating subtle changes with varied organic overlayers. Plasmon modes at these interfaces were observed to be less confined than at a Bi_2Se_3/C_{60} interface, indicating that hybrid plasmon confinement could be dependent on a well ordered molecular surface. At lower energies, <200 meV, the plasmonic behaviour at Bi_2Se_3/H_2Pc and Bi_2Se_3/CuPc interfaces was observed to differ more substantially, with variations in plasmon energy throughout the Bi_2Se_3 layer and trends towards each interface. Bulk Bi_2Se_3 plasmon modes were observed at different energies in each sample and could be a consequence of different carrier densities from different growth methods. Distinct trends in plasmon energy towards each phthalocyanine interface point towards long interaction depths between Bi_2Se_3 and organic layers at lower energies.

This research demonstrates that organic molecular overlayers can modify the interfacial plasmonic properties in TIs and suggests a route towards tunable plasmonic devices. These results are relevant for potential applications in broadband-TI photodetectors, where organic layers could be tuned electrically or optically to modify a TI interface and enable control of absorption properties.

Declaration

This thesis has been written by myself and details the research I carried out under the supervision of Prof. Donald MacLaren and Dr. Timothy Moorsom, within the Materials and Condensed Matter Physics Group in the School of Physics and Astronomy at the University of Glasgow, from 2021 to 2025. The work described herein is my own, except where otherwise stated. This thesis has not previously been submitted for a higher degree at this or any other institution.

Some of the work presented in this thesis has been incorporated into the following publications:

- **McCauley, M.**, Ansari, A., Gity, F., Rogers, M., Burton, J., Sasaki, S., Ramasse, Q., Knox, C., Hurley, P. K., MacLaren, D. A., Moorsom, T. (2025). Investigation of hybrid plasmons in a highly crystalline Bi_2Se_3/C_{60} heterostructure using low-loss electron energy loss spectroscopy. *Communications materials*, 6, 166. DOI: 10.1038/s43246-025-00886-0

- Moorsom, T., **McCauley, M.**, Nizamuddin Bin Muhammad Mustafa, A., Ramadan, S., Burton, J., Sasaki, S., MacLaren, D. A., and Petrov, P. K. (2024). Analysis of plasmon modes in Bi_2Se_3/graphene heterostructures via electron energy loss spectroscopy. *Scientific Reports*, 14(1). DOI: 10.1038/s41598-024-81488-7

Acknowledgements

I would like to express my deepest gratitude to my supervisor, Professor Donald MacLaren, who guidance, expertise and support have been truly invaluable throughout the course of my PhD. I am also grateful to my supervisor Dr. Timothy Moorsom, whose ideas, enthusiasm and encouragement have not only advanced the progress of my research but also inspired me to explore new directions.

I am sincerely appreciative of the support and teaching provided by Dr. Sam McFadzean, Colin How and William Smith, who patiently taught me the practical aspects of electron microscopy and were always available when an instrument inevitably broke. I would also like to thank Professor Quentin Ramasse and Dr. Demie Kepaptsoglou at SuperSTEM for their invaluable assistance in performing key measurements and for their technical insight. I also extend my thanks to all the collaborators who have provided samples for my work.

My heartfelt appreciation goes to my fellow PhD students in room 408, Sara, Colin and Ben, for the many insightful discussions, support and much needed distractions throughout the past few years. I am also grateful to the rest of the MCMP group for their support and for making my time in the group truly enjoyable.

Lastly, I am incredibly thankful to my friends and family for their unwavering support, understanding and encouragement throughout this journey. A special thanks to my Dad for always being interested in my work and to my mum for always being supportive despite having no idea what I've been doing and always having to clarify that I don't study eels.

Table of contents

List of figures

List of abbreviations

2DEG	Two-dimensional electron gas
ADF	Annular dark field
ARPES	Angle resolved photoemission spectroscopy
BEM	Boundary element method
BF	Bright field
CVT	Chemical vapour transport
DFT	Density functional theory
EDS	Energy dispersive x-ray spectroscopy
EELS	Electron energy loss spectroscopy
ELNES	Energy-loss near edge-structure
FCC	Face centred cubic
FEM	Finite element method
FIB	Focussed ion beam
GPA	Geometric phase analysis
HAADF	High angle annular dark field
HOMO	Highest occupied molecular orbital
KKA	Kramers Kronig Analysis
LSPR	Localised surface plasmon resonance
LUMO	Lowest unoccupied molecular orbital
MBE	Molecular beam epitaxy
qEELS	Momentum-resolved electron energy loss spectroscopy
QL	Quintuple layer
SEM	Scanning electron microscopy
SI	Spectrum image
SPP	Surface plasmon polariton
SP	Surface plasmon
STEM	Scanning transmission electron microscopy
TEM	Transmission electron microscopy
TI	Topological insulator
TSS	Topological surface state
vdW	van der Waals
ZLP	Zero-loss peak

1 Introduction and Theory

1.1 Introduction

As technology advances, the need for high speed, nanoscale devices has surpassed the possibilities of optical devices that are limited by the diffraction limit of light, preventing further size reduction. Optical fibres and waveguides have been proven to transport information at high speeds, but are much larger than nanoscale electronic devices and cannot be scaled down due to the diffraction limit of light [1]. Plasmonics offers a solution to this, enabling the creation of devices smaller than the diffraction limit. Surface plasmon polaritons (SPPs) are central to this technology providing the means to manipulate light at the nanoscale. SPPs are electromagnetic waves confined to a material's surface or interface with another material, that transport across the surface. They present a way of coupling optical light to electronics on the nanoscale and therefore have attracted significant attention for plasmonic devices in computing [1, 2].

Due to momentum mismatch, light cannot directly couple with an SPP, requiring the use of gratings or prisms to achieve SPP excitement. Nanoscale metallic structures have been investigated to guide SPPs, with the proposal of nanorods, slot waveguides and sharp wedges to guide SPPs along the structure and achieve sub-wavelength localisation [2]. One of the main challenges of using metals in plasmonic devices is plasmon damping due to electronic scattering, which limits the conduction of surface plasmon polaritons [3, 4]. Topological insulators such as Bi_2Se_3 could provide a solution for this, since they are host to edge states that are topologically protected from scattering, known as topological surface states (TSS). Electrons within these states can experience reduced scattering, resulting in enhanced conduction and undamped transport. Since surface plasmons originate from the collective oscillations of these surface electrons, the topological protection is to transferred them, leading to reduced damping and longer plasmon lifetimes. These characteristics make TI

surface plasmons particularly attractive for plasmon device applications with high efficiency due to reduced losses from damping. Tunability of TI surface plasmons is key for potential applications, the ability to modulate plasmon energy and characteristics could enhance performance at specific energies and be used for active plasmonic devices.

With the introduction of dopants or magnetic impurities, a TI surface can be altered and changes to the TSS characteristics, such as the Fermi energy, observed [5]. Organic molecules can act as surface dopants that alter the electronic behaviour and plasmons at a TI surface, with charge transfers and hybridised states observed at TI/organic interfaces [6]. As the characteristics of an organic material can be influenced by small changes to molecular structure, such as the inclusion of metallic atoms, or by the application of an electric potential or optical pulse, further opportunities to tune the behaviour are possible. This thesis investigates the effect of organic molecular overlayers on the plasmonic behaviour at a TI surface. By enclosing the TI layer between an insulating substrate and organic overlayer, the system should be stable and not deteriorate when removed from ultra-high vacuum.

The plasmonic behaviour is studied using electron energy loss spectroscopy (EELS), a technique which can achieve both high spatial and energy resolution to map plasmon modes across a thin film. By investigating changes in plasmon energy, confinement and dispersion at various Bi_2Se_3/insulator and Bi_2Se_3/organic interfaces, the effect of molecular overlayers on a TI surface is explored. At energies in the eV range, the interaction between valence plasmons and molecular electronic states is studied, highlighting Bi_2Se_3 surface changes that are not directly changing the TSS. At lower energies <200 meV, plasmon behaviour from free carriers and TSS can be explored. Both energy ranges will be investigated throughout this thesis to explore the effect of organic overlayers on different types of plasmons. The effects of four different organic materials; C_{60}, graphene, H_2Pc and CuPc, on a Bi_2Se_3 surface are studied in cross-sections of as deposited samples. By demonstrating surface modification in as deposited samples, a foundation to expand this work to device design is made.

1.2 Topological insulators

Topological insulators (TIs) are materials which are semiconducting in the bulk, ideally with a large band gap, but have gapless edge states which allow for metallic conduction at the surfaces [3, 4]. They can be understood as a generalisation of the quantum spin Hall effect, which describes the formation of edge states in a 2D material due to strong spin-orbit coupling within a material [7].

When a strong magnetic field is applied to a material, electrons move in quantised circular orbits due to the Lorentz force, as shown in figure 1.1a. The boundaries of the material, electron are unable to complete their circular orbits and instead travel along the boundaries in edge channels [8]. When electron spin is considered, the direction of the quantised circular orbitals is opposite for opposite spins, leading to the formation of two edge channels [9]. Spin-up electrons move along one channel, shown by a dark red arrow in figure 1.1, and spin-down electrons travel the opposite way in a separate edge channel.

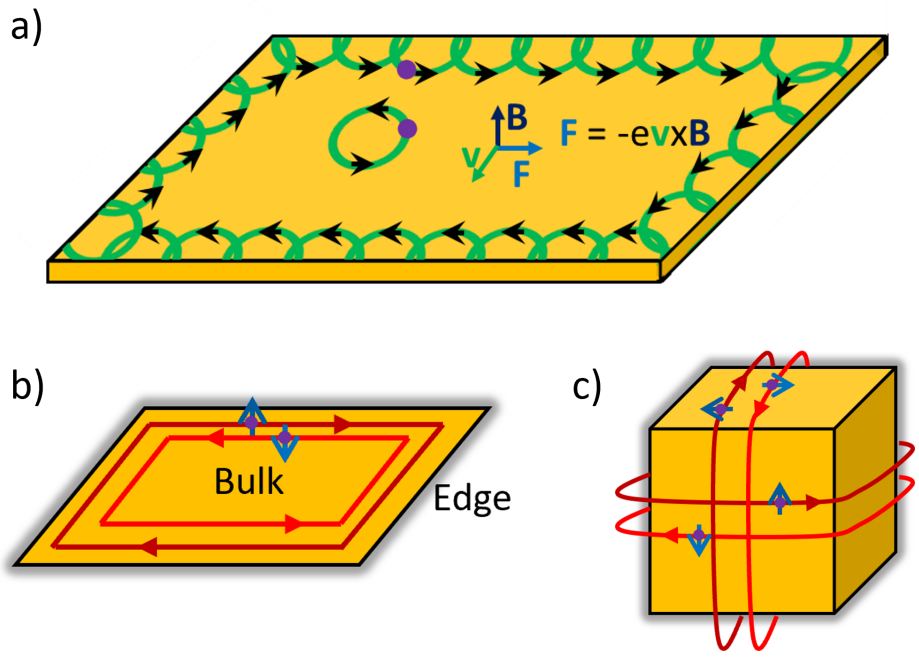

Fig. 1.1 a) Representation of the quantum Hall effect, where electrons (purple dots) follow circular trajectories (green) due to the Lorentz force, F, of an applied magnetic field, B. b) Edge states in the quantum spin Hall effect or 2D topological insulators where particles with opposite spins travel in opposite directions around the boundaries. c) In a 3D topological insulator, edge states are 2D and at all surfaces.

Upon contact with a nonmagnetic impurity, a particle with spin-up would require a spin flip to backscatter and reverse direction, introducing a negative sign into the spin [10]. Due to this, the backscattered particles interfere destructively and are not reflected. The edge state is said to be protected under time reversal symmetry. The introduction of a magnetic impurity, however, breaks time reversal symmetry and destructive interference upon backscattering no longer occurs. The quantum spin Hall effect requires strong spin-orbit coupling to occur and is only observed in systems with an odd number of particles in the edge states, which is the case for topological insulators but not for topologically trivial materials.

In 3D, the quantum spin Hall effect is observed as 2D surface states surrounding the 3D topological insulator, shown in figure 1.1c. In thin film Bi_2Se_3 lamellae studied in this thesis, the edge states should mainly be observable at the top and bottom surfaces of the TI layer at the substrate and organic interfaces. The quantum spin Hall effect can occur without the need for an external magnetic field, strong spin-orbit coupling can induce this effect. Topological insulators exhibit strong-spin orbit coupling, realising this effect. Due to time reversal symmetry, pairs of states occur with the same energy and opposite spin, $E(k,\uparrow) = E(-k,\downarrow)$. At a given energy, a pair of states with opposite momentum and spin exist, between which backscattering is forbidden. These are indicated in figure 1.2a by the blue edge spin state arrows. Although protected edge states are formed without the need for an external field in topological insulators and a distinct band structure is observed, the cyclotron orbitals of electrons indicated in figure 1.1 still require a magnetic field. Upon applying a magnetic field, measurements of the cyclotron orbitals can provide indication that a specimen is a TI, as shifts of the cyclotron frequency compared to topologically trivial specimen can be observed [11]. In general, when a magnetic field is applied to Bi_2Se_3 the cyclotron orbital radius is >15 nm which is greater than length scales relevant here, such as molecular spacing.

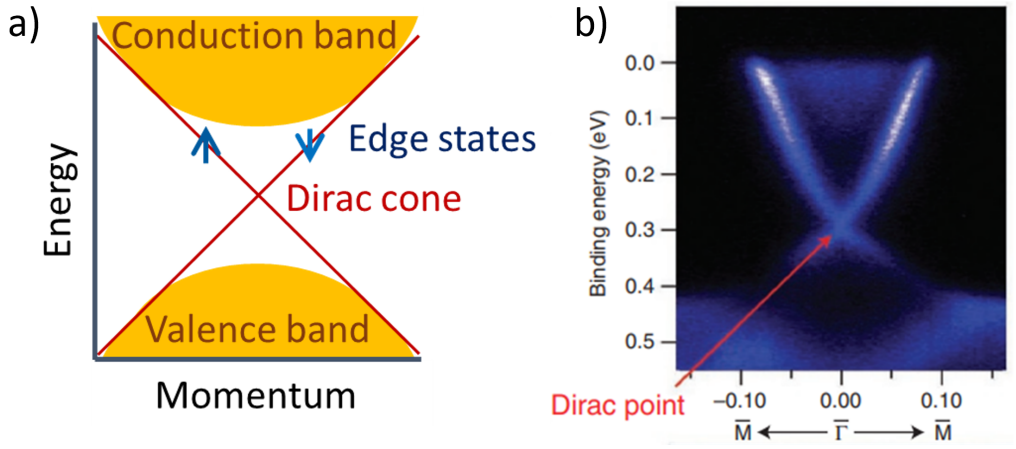

Fig. 1.2 a) Representation of the band structure at the interface between the topological insulator and the vacuum. The Dirac cone is the gapless surface state formed between the bulk bands with opposite spins at the same energy with opposite momenta. b) ARPES data of the surface states in Bi_2Se_3[12] in the ΓM momentum direction, where the Dirac cone can be seen in the centre with the crossover point indicated as the Dirac point. At the bottom of the image the intensity is from the bulk valence band and at the top from the bulk conduction band.

At the interface between a topological insulator and a topologically trivial material such as the vacuum, there is no continuous deformation possible between the band structure of the

two materials. The band gap in the system must close at or near the interface, resulting in the creation of an interfacial gapless surface state, shown in figure 1.2a. This surface state is known as a topological surface state (TSS) and forms a Dirac cone in the band structure which can be identified using angle resolved photoemission spectroscopy (ARPES), such as the data from literature presented in figure 1.2b [12]. This technique uses high energy photons to eject electrons from the crystal, revealing the electronic band structure from the momentum of the ejected electrons [10, 12]. The topological surface state of Bi_2Se_3 can be seen in figure 1.2b, where the Dirac point refers to the crossing point of the TSS. TSSs exhibit spin-momentum locking at the interface, requiring a spin flip for any change in momentum [13]. The carriers within the states experience reduced forces from the lattice, experiencing a reduced effective mass and have often been described as 'massless' Dirac fermions. These particles can experience low loss transport due to reduced backscattering [7]. The bulk and surface conduction are separate and enhanced conduction can be experienced at the surface.

The first experimental evidence of a 3D topological insulator was published in 2008 by Hsieh *et al.*, who used angle resolved photoemission spectroscopy (ARPES) to observe the topological behaviour of $Bi_{0.9}Sb_{0.1}$ [14]. Hsieh *et al.* observed five Dirac points within the surface band structure and demonstrated a single point of degeneracy at the time reversal invariant momentum, indicating that this material was indeed a topological insulator. In 2009, Bi_2Se_3 was demonstrated as a topological insulator using ARPES, hosting a single Dirac cone in its band structure [15]. The much simpler band structure has lead to a boom of research into Bi_2Se_3.

One method of confirming the existence of a TSS is by measuring the Hall resistance using transport measurements. A key indicator of a TSS are quantum oscillations in the Hall resistance with varied magnetic field, known as Shubnikov de Haas (SdH) oscillations [16]. Taskin *et al.* studied the effect of thin film thickness on the manifestation of the topological proprieties of Bi_2Se_3 by measuring SdH oscillations [17]. They observed a critical thickness of 6 nm required for massless Dirac fermions in TSS, below which SdH oscillations were not observed. At thicknesses smaller than this, hybridisation between the surface states on the top and bottom surfaces opens an energy gap at the Dirac point and TSS is no longer protected.

Collective excitations of Dirac fermions within the edge states can propagate across the surface and should have reduced damping compared to those in topologically-trivial materials [18]. These surface plasmons are known as Dirac plasmons, since they are excitations of Dirac fermions, and are confined in 2D to the surface. They will be discussed in further detail in section 1.4.2.

There are a wide array of potential applications for TIs that make use of the behaviour of the surface states. The spin properties of electrons within TSS are of interest to utilise their giant photogalvanic effects for polarisation sensing [19]. When electrons within the TSS are excited by circularly polarised light they are selectively excited into spin-polarised states, which leads to a net photocurrent that can be switched direction. Increased current has been observed when the Fermi level was positioned near the Dirac point due to reduced scattering of spin-polarised electrons into bulk states. The increased current enhances the efficiency of sensing. TIs show potential for the generation of THz radiation, with the performance of 40 nm TI films comparable to 2000 nm semiconductor films [20]. Topological insulator, $Bi_{1.9}Sb_{0.1}Te_2Se$, antenna have been demonstrated to generate THz radiation without an external bias through the photogalvanic effect. High efficiency and long lived THz oscillations were observed and attributed to the relaxation of photo-excited carriers to TSS. Enhanced optical second-harmonic generation has also been demonstrated in thin films of Bi_2Se_3, where excited plasmons contribute to a resonant enhancement of a second-harmonic signal [21]. With tuning of the TI plasmon frequency, an enhancement of signal at specific frequencies could have potential uses in frequency conversion devices, which could be used for optical communications.

Broadband photodetectors and emitters are another application where TIs show great potential. The enhanced surface conduction from a TSS results in efficient photocurrents and high sensitivity [22–24]. The narrow bulk bandgap and gapless surface states connect the conduction and valence bands in the bulk, enabling absorption over a large spectral range [25]. Heterojunctions of Bi_2Te_3/Si have been demonstrated to have an ultra-broadband photo-response ranging from ultraviolet to THz photodetection at room temperature [26]. Devices were shown to be reliable with little degradation from ambient exposure and UV illumination. The TI/Si interface has a built in electric field, improving efficiency. Bi_2Se_3 nanowire/Si heterojunctions have also been shown to have a broad spectral range, from 380 to 1310 nm, with excellent detection performance [27]. These systems have potential applications in telecommunications and as infrared sensors. The photoresponse of Bi_2Te_3 on flexible plastic substrates has been studied as a step towards wearable flexible devices and a strong photoresponse in the near infrared regime with a fast response was demonstrated [28]. By tuning the plasmon energy, the photoresponse could be enhanced at specific energies to be used for tunable devices.

1.2.1 Bi_2Se_3

Bi_2Se_3 is one of the simplest topological insulators and is part of a subset of chalogenide compounds which have been shown to be TIs, including Bi_2Se_3, Bi_2Te_3 and Sb_2Te_3 (A_2B_3).

These compounds have similar structures to each other, with layers of covalently bonded atoms, B1-A-B2-A-B1, known as quintuple layers (QLs), as shown in figure 1.3. These QLs are weakly bonded to each other via van der Waals interactions between the B1 atoms and the spacing between layers is termed the van der Waals (vdW) gap. The crystal structure

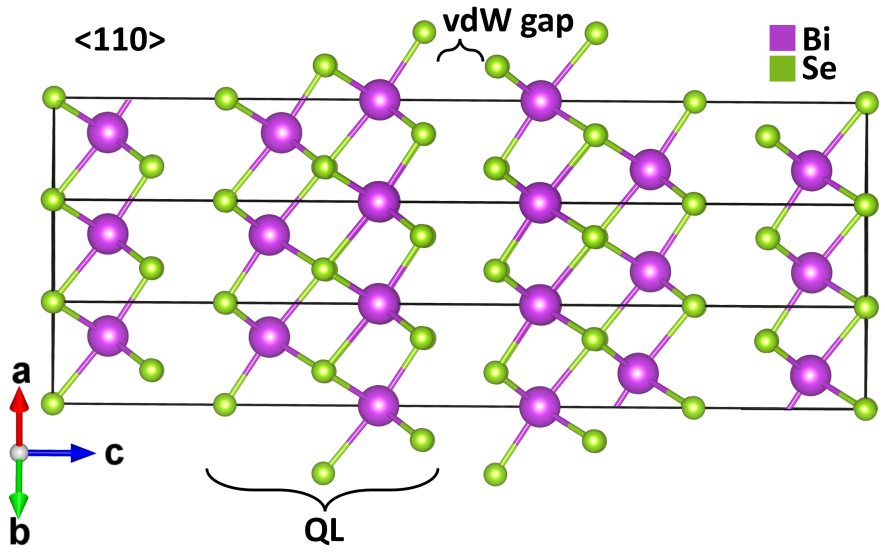

Fig. 1.3 Unit cell of Bi_2Se_3 topological insulator in the <110> direction with indicated quintuple layer (QL) Se-Bi-Se-Bi-Se and van der Waals gap (vdW) between the layers.

belongs to space group *R*-3*m* and is made up of hexagonal unit cells with dimensions of $a, b = 4.143$Å and $c = 28.636$ Å for Bi_2Se_3 [13]. The band gap of Bi_2Se_3 has been measured as 0.3 eV, which is the greater than similar TIs such as Bi_2Te_3, which has a band gap of 0.15 eV [13]. TIs, such as Bi_2Se_3, have been fabricated in several different ways such as chemical vapour deposition, exfoliation and molecular beam epitaxy, which will be discussed in chapter 2 [29–31]. The quality of Bi_2Se_3 can differ based on the growth method, with differences to defect concentration, carrier density and surface roughness affected by growth [32, 33].

Bi_2Se_3 was initially investigated for its thermoelectric properties and has been shown to be efficient at low temperature power generation and have a high Seebeck coefficient value, indicating thermoelectric efficiency [34]. The topological properties of Bi_2Se_3 were first experimentally observed by Xia *et al.* using ARPES, which demonstrated a single Dirac cone in the band structure [15]. Since this discovery, Bi_2Se_3 has been of much interest [35], with significant research into its topological properties and how these properties can be tuned for potential applications.

Bi_2Se_3 specifically has been investigated for a variety of different application including those discussed above and as field emitters [36] and humidity sensors [37]. Bi_2Se_3 shows potential for battery applications, with research into the use of doped Bi_2Se_3 as an anode material for Li ion batteries, which has shown improved discharge capacity [38].

1.2.2 Tuning the surface

To make use of the topological properties, some degree of tunability is required. The ability to tune the energy of the Dirac point and position it at the Fermi energy could minimise bulk conduction, isolating surface transport. This is useful for applications that utilise conduction within the TSS such as spintronics and plasmonic devices [39]. Protection of the TSS can be desired for integration into devices to ensure robustness of the surface behaviour. Surface dopants could produce resonant surface excitations that enhance absorption at certain energies to improve TI photodetection and emission. Modifications to the surface band structure could elicit new topological effects such as topological superconductivity [40], magnetic TIs [41, 42] or a 2DEG at the surface, which could be utilised for a host of different 2D quantum device applications.

There are several different methods of tuning the TI properties which have been explored in literature to enhance different properties for different potential applications. The composition of TIs has been explored to tune the Dirac point and enhance surface effects through minimising bulk conduction. Several studies optimise the composition of combinations of $(Bi,Sb)_2(Se,Te)_3$ in different ways to achieve this. Biasing TI layers with a gate voltage has been demonstrated to modify the energy of the Dirac point and surface carrier density. The inclusion of different dopant atoms within the TI has been shown to reduce bulk conduction, shift the Dirac point energy and elicit new topological effects. The formation of 2DEG at a TI surface has been demonstrated by the inclusion of metallic surface dopants and organic surface dopants have been shown to shift the Dirac point and form hybridised states at the surface. A brief overview of literature utilising these methods is presented here.

Composition optimisation

Selecting an ideal topological insulator material is important to obtain the optimum surface effects. Ideally the material should be insulating in the bulk, so that all of the conduction is from the topological surface states and the Fermi level is at the Dirac point. However, many of the known topological insulators display semiconducting behaviour, with narrow bandgaps and similar conductivity to metals at room temperature. This is primarily due to native defects such as Se/Te vacancies and Bi anti-site defects which are found in both

Bi_2Se_3 and Bi_2Te_3 and introduce n-type carriers [30]. In literature, different methods have been explored to optimise TIs for bulk insulation.

One such method of engineering an ideal TI, is to vary the composition of the material to quench carriers with opposite dopants to achieve the desired conduction properties. Bi_2Se_3, Bi_2Te_3 and Sb_2Te_3 have been shown to be TIs [43], so ternary alloys of these materials have been investigated to improve on the electronic properties [44]. Alloys of $Bi_2(Se,Te)_3$ are promising [45–48], as Bi_2Te_2Se naturally forms a Te-Bi-Se-Bi-Te structure, which reduces the number of Se vacancies since Se is confined to the middle of the QL, and reduces Bi/Te antisite defects since Bi is more strongly bonded to Se than Te [49]. The reduction in the number of these types of defects, reduces the bulk carrier density and n-doping of the material. $(Sb,Bi)_2Se_3$ alloys have been shown to reduce bulk carrier density compared to Bi_2Se_3 [50].

Composition optimisation of $(Bi,Sb)_2Te_3$ has been achieved to optimise the number of bulk carriers and the energy of the Dirac point [51–53]. Samples of $(Bi_{1-x}Sb_x)_2Te_3$, with varied x, were studied by Zhang *et al.* using ARPES to investigate the effect of the composition on the Dirac cone and carrier concentration [51]. They observed that, at low x, the material was heavily n-doped, with the Dirac point situated within the bulk conduction band. With increasing x, the Dirac point was up-shifted and when x>0.5, transport was dominated by surface carriers close to the Dirac point. Finally, at high concentrations of Sb, $x \approx 0.94$, a change from n-type to p-type was observed with a charge neutral state in between.

The composition of $Bi_{2-x}Sb_xTe_{3-y}Se_y$ has also been optimised to reduce the number of bulk carriers. In $Bi_{2-x}Sb_xTe_{3-y}Se_y$, there are two types of defect which contribute opposite carrier types. (Bi,Sb)/Te anti-site defects act as electron acceptors and Se vacancies act as electron donors, therefore, by optimising the composition, a case where these cancel out and the carrier density is minimised, is possible. Ren *et al.* observed an optimum composition of (x,y)=(1.25,2.5) to achieve this [54]. The composition of this alloy and Sb content, x, can be altered to tune the material from n-type to p-type and control the dominating carrier type, from non-Dirac to Dirac carriers [55]. The energy of the Dirac point can be tuned to achieve the desired TI properties.

Optimised TI compositions require specific growth conditions, which complicates sample preparation and can result in variations of composition throughout the film and regions of defects when not fully optimised. Bi_2Se_3 has been selected for the work in this thesis due to the ease of growth, with high quality thin films and simple band structure. By first demonstrating interfacial effects on Bi_2Se_3, this work could be extended to more complex composition TIs with optimised conduction properties, such as those discussed here.

Gating

As well as optimising the composition, the electronic behaviour of a TI can be modified by an applied gate voltage, which can be altered to tune the position of the Dirac point as desired. This can use useful in the design of active devices. There have been several papers which have demonstrated the effect of an applied potential on the TSS behaviour using a gating potential at either one surface or both the top and bottom surfaces [56].

Xu *et al.* investigated the quantum Hall effect in $BiSbTeSe_2$ nanoflakes by fabrication of a field effect transistor device with a gate applied to one surface [4]. They observed a temperature dependent quantum Hall state, which was observed to survive at temperatures up to 35 K. By including an additional gate at the top surface using a hexagonal boron nitride dielectric, they found that the carrier type and density could be tuned at each surface independently [57]. In thin films, dual-gating of the top and bottom surfaces has been used to tune the chemical potential of both surfaces [58]. Yang *et al.* demonstrated dual-gated devices of $(Bi_{1-x}Sb_x)_2Te_3$, with Si/SiO_2 wafers acting as the back gate and an SiN_x dielectric as the top gate. The authors demonstrated tuning of the chemical potential of both surfaces across the Dirac point. Although this was effective in adjusting the Dirac point, the requirement for constant biasing to achieve this somewhat limits the usefulness of this system.

Doping

The topological properties of TIs can also be modified using dopants to both reduce bulk carriers and modify the topological surface states. For example, Ren *et al.* doped samples of Bi_2Te_2Se with Sn [5]. Bi_2Te_2Se contains n-type bulk carriers with its Fermi level pinned to the conduction band. Doping with Sn was found to shift the Fermi level down and give rise to a larger gap between the valence and conduction bands due to acting as an acceptor when substituted for Bi [5]. The authors found that at low doping concentrations each Sn atom substituted for one hole, but at higher concentrations an impurity band was formed within the bulk band gap.

Changes to the transport properties of Bi_2Se_3 were observed upon doping with Ag. Ag atoms have been shown to substitute for Bi within the lattice and a reduction in carrier density was observed with increasing Ag concentration [59]. In some cases, Ag atoms have been observed to intercalate throughout the lattice, occupying interstitial sites. When intercalated, a reduction in carrier concentration was also observed with increasing Ag concentration [59, 60]. A downward shift in the Fermi level of Bi_2Se_3 was observed upon Ag doping and the carrier density was observed to be temperature dependent [61]. Other metallic dopants have been demonstrated to change the properties of Bi_2Se_3 including Mn [62, 41, 42] and Cu

[63, 64]. For example, in aged samples of Cu-doped Bi_2Te_3, suppression of bulk conduction was observed due to the formation of Cu clusters between QLs, resulting in disorder and reduced carrier mobility [63]. This improved the ability to observe surface conduction from TSS. Mn doping of TIs has been shown to result in varied magnetic phases depending on how the Mn has incorporated into the structure [42]. For example, ferromagnetic ordering was observed when Mn substituted on Bi or Se sites in Bi_2Se_3. After doping, the TI properties are not easily modified and the growth parameters of each doped material must be optimised to achieve evenly doped films with the desired properties.

Surface doping

Another method of tuning the TI surface states is to introduce impurities to the surface in the form of surface dopants. By doping the surface, the conduction properties of the TI can be optimised in growth before modifying the surface to tune the TSS. This could allow for the TI to be enclosed, with the top surface covered by the surface dopant and the bottom surface in contact with a substrate, protecting the surface from atmosphere. The properties of the TI can then modified in different ways, depending on what is desired, without re-optimising TI growth.

Several different metals have been interfaced with TIs to achieve some degree of modification of the surface. For example, Bianchi *et al.* introduced Rb atoms to the surface of Bi_2Se_3, which intercalated into the Bi_2Se_3 vdW gaps upon annealing. They observed the formation of a 2DEG at the surface [65]. Other metals including Au, Pd and Ir were studied on a Bi_2Se_3 surface by Walsh *et al.*, who observed very little interaction between the Bi_2Se_3 surface and Au but significant interaction with Pd and Ir resulting in the formation of new layers at the interface [66]. Absorption of hydrogen at the surface of Bi_2Se_3 has been predicted to cause surface reconstruction but maintain the TSS [67].

Organic molecules have been proposed as a surface dopant to alter the TI surface and a variety of different organics have been studied. One benefit to the use of organic surface dopants is the possibility of tuning the electronic behaviour of the molecules with an applied electric field or optical excitation, which could in turn modify the TI surface behaviour [68]. Organic dopants can also be modified optically [69], providing a route to optically controlled TI properties. The topological surface state of Bi_2Te_3 was predicted to be preserved with minimal changes to the electronic structure upon physisorption of benzene, using density functional theory calculations [70]. However, the benzene layer could be used to protect the surface from contaminants and preserve the TSS.

The effect of electron donor molecules on the surface of TIs has been studied and shown to modify the Bi_2Se_3 surface. Molecules of TTN absorbed on a Bi_2Se_3 surface were observed

to cause downward band bending at the Bi_2Se_3 surface and the formation of a 2D electron gas [71]. Charge transfer was observed, as well as a shift to the Dirac point of the surface state. Electron acceptor molecules of F_4-TCNQ have also been studied and were shown to transfer charge from Bi_2Se_3 to the molecules, reducing the carrier concentration in Bi_2Se_3 [72]. In other work, TCNQ molecules were observed to not induce charge transfer across an interface with Bi_2Se_3 and did not effect the TSS [73].

Phthalocyanine molecules have been demonstrated to induce changes to the topological surface states of various TIs. The effect of C_{60} and metal-free phthalocyanine on the surface of Bi_2Se_3 has been shown by Jakobs *et al.* using ARPES and is shown in figure 1.4A. This work indicated a change to the Fermi level by C_{60} and a shift of the Dirac point by H_2Pc [6]. H_2Pc was also shown to form a hybridised state at the surface. On Bi_2Te_3 surfaces, MnPc molecules have been shown to hybridise with the surface and transfer charge, whilst maintaining the TSS [76, 77]. This hybridisation was observed to occur from the first monolayer of MnPc atoms which were disordered on the surface and return to bulk MnPc properties in the second layer [78]. On a Bi_2Te_3 surface, CoPc molecules were observed to transfer a small amount of charge but not fully suppress the TSS [79]. On a Bi_2Se_3 surface, CoPc was observed to downshift the Dirac cone by ARPES, as shown in figure 1.4B, indicating a charge transfer [74]. The TSS was observed to remain intact below the first QL of Bi_2Se_3. In ultra-high vacuum, CuPc molecules on a Bi_2Se_3 surface were observed to transfer charge to the surface and become positively charged [75]. The Dirac point was observed to shift by -336 mV in STS measurements shown in figure 1.4C.

Results from literature, shown in figure 1.4, were carried out using highly surface sensitive techniques. ARPES spectra, for example, are dominated by the band structure of the topmost layer of atoms, so measurements of the TI band structure with dopants are difficult. This leads to questions over whether the band structure is measured in regions with molecular dopants or regions where there are gaps between molecular dopants. In practice, samples must be stable in atmosphere to prove useful in future devices. Many of the examples discussed here require ultra-high vacuum and the topological behaviour does not withstand atmosphere. Therefore, this thesis will explore thin film samples which enclose the TI interfaces between an insulating substrate and organic molecular overlayer. The effect of more than a couple of monolayers of organic molecules on the surface cannot be measured by APRES, limiting the results of these studies. For this reason we use electron energy loss spectroscopy (EELS) to investigate the interfaces and probe changes to the TI surface through plasmon behaviour.

This thesis will investigate the effect of various organic molecular thin films on the surface of Bi_2Se_3, through observations of changes to plasmon behaviour in different energy ranges. The effect of C_{60} molecules on Bi_2Se_3 surface plasmonics at an energy range of

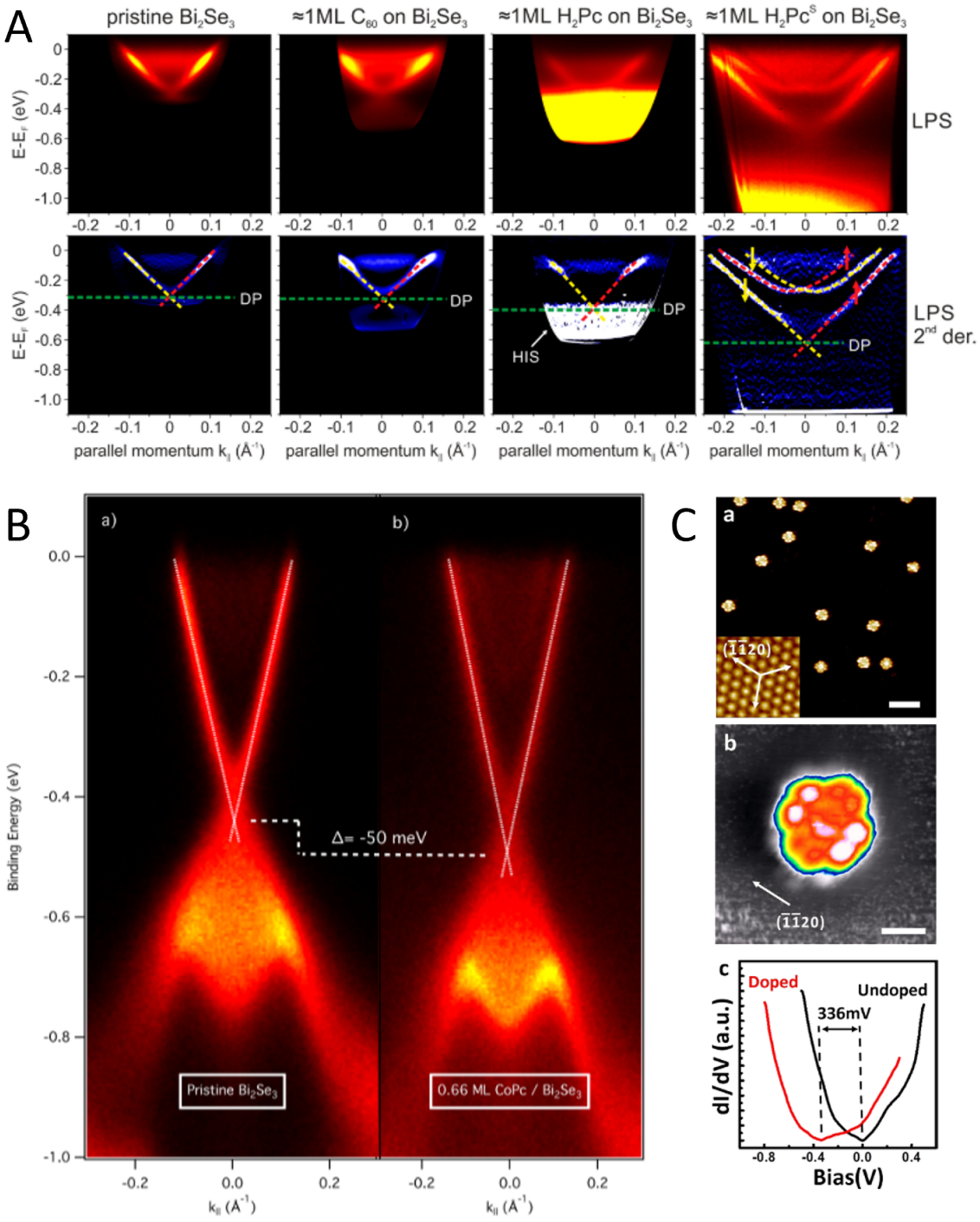

Fig. 1.4 Examples from literature of the effect of organic molecules including phthalocyanine molecules on Bi_2Se_3 surfaces. A) ARPES spectra of Bi_2Se_3 with organic molecular dopants C_{60}, H_2Pc and H_2Pc^S replicated from literature [6]. The original ARPES data and 2nd derivative show a shift of the Dirac point and formation of a hybridised state due to molecular adsorbates. B) APRES spectra of pristine Bi_2Se_3 and 0.66 mL CoPc/Bi_2Se_3, where the Dirac point has shifted by 50 meV when dopants are present, replicated from [74]. C) Scanning tunnelling microscopy images (a,b) of CuPc molecules on a Bi_2Se_3 surface and scanning tunnelling spectroscopy measurements of the undoped surface and surface doped with CuPc indicating a shift of the Dirac point of -336 mV, replicated from [75].

1-27 eV is demonstrated in chapter 4 and molecular layers of graphene, H_2Pc and CuPc are studied in chapter 5. The 1-27 eV energy range contains plasmon excitations of π electrons within both the Bi_2Se_3 film and organic molecules, as well as molecular energy levels of the organics. By probing plasmons at this energy range, we can observe coupling and bonding between the molecules and TI thin film, which should indicate changes to the surface without directly probing TSS. The energy region containing the TSS, 10-200 meV, is investigated in chapter 6 to investigate the TSS and low energy TI plasmons.

1.3 Electron Scattering

The principles of electron scattering underpin all parts of this research. Upon incidence with a specimen an electron beam can undergo a variety of different interactions, as shown in figure 1.5. The result of each type of scattering can be used in different ways to understand a sample using a variety of techniques.

Secondary electrons are electrons which have been ejected from a specimen due to an incident electron beam [80]. As shown in figure 1.5, these signals are emitted upwards from the sample and can be detected by a detector positioned above the specimen. In a scanning electron microscope (SEM) secondary electrons are one of the main signals collected and are used to image larger specimens and within this thesis are used for imaging during sample preparation. Characteristic x-rays are emitted from atoms within a sample as they undergo relaxation after excitement from incident electrons. X-rays are emitted with specific energies relating to the energies of bound states within the sample, so can be used for chemical analysis. These are detected and used in energy-dispersive x-ray spectroscopy (EDS) which will be briefly discussed in this thesis.

For thin samples, some forward-scattered electrons are transmitted and can be detected in transmission electron microscopy (TEM) and electron energy loss spectroscopy (EELS). Elastically scattered electrons form diffraction patterns and images when collected for TEM and scanning TEM. Inelastically scattered electrons are used in EELS for chemical analysis and plasmon investigations. These transmitted signals make up the majority of this thesis and are used to understand the structure, chemistry and plasmonics of various samples.

1.3.1 Elastic scattering

Elastic scattering arises from interactions between incident electrons and the electrostatic potential of atomic nuclei and electrons in the specimen. At high scattering angles, >50 mrad, the interaction with the screened Coulomb potential of individual atoms dominates and the

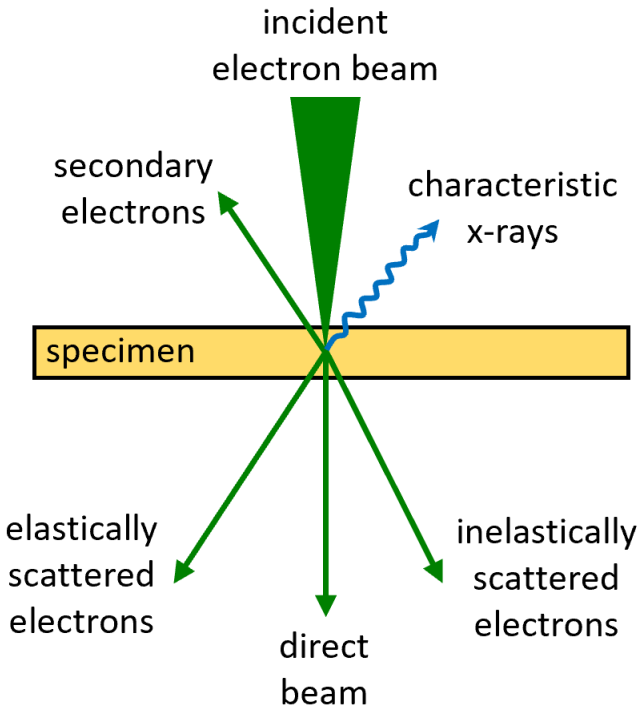

Fig. 1.5 Upon incidence with a specimen and electron beam excites various signals which can be detected to understand the specimen. Back-scattered signals include secondary electrons which are ejected from the material and characteristic x-rays emitted from specimen atoms. Detectors positioned above the specimen can be used to measure these signals. Forward-scattered signals include elastically scattered electrons, which provide information on mass and crystalline structure and inelastically scattered electrons, which can be used to understand chemical properties. Forward-scattered signals can be collected by transmission electron microscopy techniques.

scattering is mainly incoherent. This process is classically described by Rutherford scattering, where the path of an electron is changed by an angle, θ, due to its interaction with the nuclei. During the scattering process, momentum is transferred from the electron to the nucleus, but the electrons energy remains unchanged. This can be described by the differential cross section, which describes the probability of an incident electron being scattered in a sample, $d\sigma$, per unit solid angle, $d\Omega$ [81]. For elastic scattering, the elastic differential cross-section becomes

$$\frac{d\sigma}{d\Omega} = \frac{4\gamma^2 Z^2}{a_0^2 k_0^4} \frac{1}{\left(\theta^2 + \theta_0^2\right)^2}, \tag{1.1}$$

where θ is the scattering angle, θ_0 is a characteristic angle of elastic scattering, $\gamma = (1 - \frac{v^2}{c^2})^{-1/2}$ is the relativistic factor, $k_0 = \gamma m_0 v/\hbar$ is the magnitude of the incident electron wavevector, a_0 is the first Bohr radius and Z is the atomic number. For isolated atoms,

equation 1.1 describes the angular distribution of elastic Rutherford scattering and indicates the approximate Z^2 dependence of the cross-section.

In crystalline materials at finite temperature, atoms vibrate about their equilibrium positions perturbing the scattering potential. When incident electrons interact with these vibrating atoms, they exchange a small amount of momentum and energy with the lattice. This generates a diffuse 'quasi-elastic' scattering known as thermal diffuse scattering (TDS), which redistributes part of the incident beam into a broad, incoherent background. The intensity scales approximately as $Z^{1.6-1.9}$, weaker than ideal Rutherford scattering due to screening of the potential and multiple scattering [82]. The strength of TDS increases with temperature due to larger vibrational amplitudes at higher temperatures. Since electrons interact simultaneously with many independent atomic vibrations (multi-phonon processes), TDS is incoherent and spans a large angular range, acting as a localised source of high-angle intensity near atomic columns [83]. At large angles, the contribution of TDS can be greater than Rutherford and coherent elastic scattering and provides the contrast exploited by HAADF STEM imaging to be discussed in chapter 2.

The number of elastic scattering events incurred by an electron as it passes through a material is dependent on the elastic differential cross-section, σ_e, and the density of atoms within the material, n_a. Since there is a relationship between atomic number and angular dependence of elastic scattering, the amount of scattering undergone by an electron in a material differs for different materials. This can be described by the elastic mean free path,

$$\lambda_e = \frac{1}{\sigma_e n_a}, \tag{1.2}$$

which describes the mean distance between elastic collisions with no change in energy.

At smaller scattering angles, coherent elastic scattering from the crystal lattice becomes significant, and the Rutherford scattering description no longer holds. The scattered electron waves interfere constructively according to the structure factor, which defines the amplitude and phase of scattering from all atoms within a unit cell and determines the relative intensities of diffracted beams. For a crystalline specimen with an orthorhombic unit cell with dimensions a, b, c, the Bragg condition is fulfilled for Miller indices h, k, l, when

$$sin(\theta_B) = \frac{n\lambda}{2}\sqrt{\frac{h^2}{a^2} + \frac{k^2}{b^2} + \frac{l^2}{c^2}} \tag{1.3}$$

where θ_B is the Bragg angle and λ is the incident electron wavelength. A diffraction pattern is formed from this coherent scattering, where bright spots occur when the Bragg condition is met. For crystals containing multiple elements, the diffraction pattern becomes more

complex, with variations in spot intensities arising from differences in atomic scattering factors, the structure factor and thickness variations [80]. In addition to Bragg spots, TDS gives rise to a weak background intensity between spots that increases with temperature and scattering angle. The diffraction pattern can be used to obtain information on the crystal structure such as lattice spacing and defects.

1.3.2 Inelastic scattering

Some scattering between incident electrons and a specimen results in a transfer of energy, which can excite phonons, plasmons and atomic shell electrons within a sample [84]. This scattering is known as inelastic scattering and the energy transferred to the specimen during these events can be determined by recording the energy of transmitted electrons. The energy lost during transmission is used in electron energy loss spectroscopy (EELS) to study chemical and optical properties of materials.

A variety of different processes are excited by inelastic scattering events and can provide different information about a sample. Upon interaction with the inner and outer shells of atomically bound electrons, energy can be transferred from an incident electron to one in a shell resulting in ionisation. This results in energy losses which are characteristic of energy level transitions in each element and can be used to identify elements within a sample using EELS. As well as resulting in a characteristic energy loss for transmitted electrons, x-rays are also produced as secondary effects when the atom relaxes from the excited state. Characteristic x-rays can be collected and analysed using energy dispersive x-ray spectroscopy (EDS). Processes excited with small energy losses can be observed using EELS and include atomic vibrations, known as phonons, which are excited with energies that typically lie in the meV range. Collective oscillations of free or valence electrons, known as plasmons, are excited with energy losses that range from meV to 10s of eV. Plasmon excitations are the main focus of this thesis and will be discussed in more detail in section 1.4.

During an inelastic scattering event, an electron with initial wavevector, $\mathbf{k}_0$, is scattered through an angle, θ, and its wavevector is now denoted $\mathbf{k}_1$. In the scattering event momentum, $\mathbf{q} = \mathbf{k}_0 - \mathbf{k}_1$, is transferred from the lattice, as shown in figure 1.6 [84]. The probability of an inelastic scattering event per unit solid angle can be described by the differential cross section of inelastic scattering given by

$$\frac{d\sigma}{d\Omega} = \frac{4\gamma^2 Z^2}{a_0^2 k_0^4} \frac{1}{(\theta^2 + \bar{\theta}_E^2)^2} \left\{ 1 - \left[\frac{\theta_0^4}{\theta^2 + \bar{\theta}_E^2 + \theta_0^2} \right] \right\}, \tag{1.4}$$

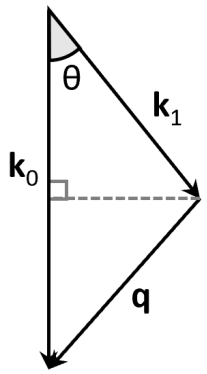

Fig. 1.6 Wavevector diagram of an inelastic scattering event where an incident electron with wavevector $\mathbf{k}_0$ is scattered by an angle θ and is transferred momentum $\mathbf{q}$ by the specimen.

where $\bar{\theta}_E = \bar{E}/(\gamma m_0 v^2)$ is the characteristic angle for an average energy loss, $\bar{E}$, and all other parameters are the same as before. Equation 1.4 is derived from Morse's theory of atomic scattering and describes the angular dependence of inelastic scattering. Most inelastic scattering occurs over the angular range $\bar{\theta}_E < \theta < \theta_0$, with scattering reducing by $(1/\theta)^4$ above θ_0. This means that, compared to elastic scattering, most inelastic scatting occurs at smaller angles.

For a continuous energy loss, the double-differential inelastic scattering cross-section can be used to understand both the angular and energy dependence of electron scattering [81]. The properties of a solid can be described by the dielectric response function $\varepsilon(q,E)$, which can be used to obtain a generalised description of electron scattering. For small scattering angles, $d\mathbf{q} \approx \mathbf{k}_0\theta$, the double-differential inelastic scattering cross-section is

$$\frac{d^2\sigma}{d\Omega dE} \approx \frac{\Im[-1/\varepsilon(q,E)]}{\pi^2 a_0 m_0 v^2 n_a}\left(\frac{1}{\theta^2+\theta_E^2}\right), \tag{1.5}$$

where $\theta_E = E/(\gamma m_0 v^2)$ is the characteristic angle, n_a is the number of atoms per unit volume and the imaginary part of $[-1/\varepsilon(q,E)]$ is the energy loss function with a dielectric response function of $\varepsilon(q,E)$.

Incident electrons continue to scatter in the above ways until they are stopped or escape the material. Therefore, electrons can undergo multiple scattering interactions before they leave the sample making their energy loss a summation of all of these processes. The region of sample within which the electron beam interacts is defined as the interaction volume. The inelastic mean free path, λ_i, describes the average distance an electron travels between scattering events and is calculated from equation 1.2 using the inelastic differential cross-section, σ_i, from equation 1.4. The thickness of sample required for electron transmission is

dependent on the mean free path of the material. From an EELS spectrum, the thickness of a sample can be determined using the known inelastic mean free path value with a t/λ_i value measured in the spectrum. For imaging and spectroscopy, samples should have a t/λ_i value of less than 1 with lower values of around 0.5 desired.

1.3.3 Phonons

At ultra-low energies, less than 500 meV, vibrational modes such as phonons are excited. In molecules, vibrational modes relate to different vibrations of the molecule. There are many different vibrational modes which can occur, including bond stretching and bending. These vibrations occur at energies specific to the material and can be used to understand the structure and bonding of molecules. These molecular vibrations are commonly imaged using infrared and Raman spectroscopies, which use infrared and visible photons to excite the vibrational modes of the molecule [85]. Each technique has its own selection rules with the requirement of a change in dipole moment accompanying a vibration for infrared active modes and a change in polarisability for Raman active modes [85].

In solids, phonons are quantised lattice vibrations from vibrations of atoms within the lattice. The scattering cross-section for a vibrational mode can be much smaller than plasmon and core excitations. For example, the scattering cross section for a CO_2 bending mode at 82 meV is 4×10^3 barn, where 1 barn $= 1 \times 10^{-24}$ cm^{-1} [86]. This is much smaller than the scattering cross-section for plasmon scattering which is on the order of 1×10^6 barn. The scattering cross-section for a vibrational excitation, as given by a dipole description, can be described by

$$\sigma_v(\beta) = \frac{8\pi a_0^2 R^2}{E_v m_0 v^2} f_v ln\left(1 + \frac{\beta^2}{\theta_E^2}\right), \tag{1.6}$$

where a_0 is the Bohr radius, $R = 13.3$ eV is the Rydberg energy, f_v is the dipole oscillator strength, β is the collection semi-angle and other variables have the same definitions as before [86]. The form of equation 1.6 is given as integrated over scattering angle up to the collection semi-angle angle, β. This small scattering cross-section means that small collection angles can be used to acquire spectra of vibrational modes. Due to the annular width of phonon scattering being small, delocalisation of some phonon modes can be large, with length scales of as much as 25 nm predicted [86]. This delocalisation is largest for modes with a large dipole contribution, for example, longitudinal optical phonons in MgO [87]. Other modes display a much smaller degree of delocalisation with atomic-level localisation observed for some modes such as bulk longitudinal acoustic phonons in MgO [87]. The interaction between incident electrons and the combination of multiple phonon processes gives rise to the TDS discussed in section 1.3.1.

There are different types of phonon modes which can be distinguished by their length scales and dispersion. When neighbouring atoms within a lattice move in unison in the same direction, their vibrations are described as acoustic phonons and act as sound waves which transport through the crystal. Optical phonons describe when neighbouring atoms move in opposite directions as they vibrate and can be excited by electromagnetic fields [88]. The dispersion of acoustic phonons is much greater than optical phonons and the energy tends to 0 as $q \to 0$.

1.4 Plasmons

Plasmons are quantised oscillations of electrons within a material that can be excited upon interaction with the electric field of photons or electrons [89]. Electrons within a solid oscillate at characteristic frequencies in response to the external electric field and can propagate throughout a material. The free election gas and positive ions in a metal can be considered as a gas of charged ions which is overall neutral i.e. a plasma. When an electric field is present, charges within the plasma move and the gas is no longer in equilibrium. A restoring force drives the charges to oscillate until an equilibrium is found. These collective oscillations are known as plasmons [89].

An electron within a metal, with mass m, experiences a Coulomb force from an applied electric field, $\mathbf{E}$, and its equation of motion can be given by

$$m\ddot{\mathbf{x}} + m\gamma\dot{\mathbf{x}} = -e\mathbf{E}, \tag{1.7}$$

where γ is damping [1]. For an electric field with a harmonic time dependence of $\mathbf{E}(t) = \mathbf{E}_0 e^{-i\omega t}$, the resulting displacement of the electron can be described by

$$\mathbf{x}(t) = \frac{e}{m(\omega^2 + i\gamma\omega)}\mathbf{E}(t), \tag{1.8}$$

and the collective displacement of N electrons contributes to the polarisation, $\mathbf{P} = -Ne\mathbf{x}$. The dielectric displacement can then be found using $\mathbf{D} = \varepsilon_0\mathbf{E} + \mathbf{P}$, to give

$$\mathbf{D} = \varepsilon_0 \left(1 - \frac{Ne^2}{m(\omega^2 + i\gamma\omega)}\right)\mathbf{E}. \tag{1.9}$$

The plasma frequency can be defined as

$$\omega_p^2 = \frac{Ne^2}{\varepsilon_0 m}, \tag{1.10}$$

and describes the frequency at which electrons can no longer completely screen an external electric field. The plasma frequency is the natural frequency at which free electrons oscillate and are quantised as plasmons. As these plasmons are from bulk electrons, they are termed as bulk or volume plasmons and their energy depends on the 3D bulk carrier density. In most metals, the plasma frequency of bulk plasmons is on the order of 3 to 25 eV. At high frequencies the dielectric function can be expressed as

$$\varepsilon(\omega) = 1 - \frac{\omega_p^2}{(\omega^2 + i\gamma\omega)} \approx 1 - \frac{\omega_p^2}{\omega^2}, \tag{1.11}$$

for small damping, γ.

Plasmons can be excited from valence electrons within a material from specific valence energy levels [90]. For example, π plasmons are excited from electrons within π states and $\pi + \sigma$ plasmons from both π and σ states. Valence plasmons can be excited from electrons in valence states in the bulk of a material as volume plasmons, or from localised states, which could occur at interfaces due to bonding. Volume plasmon energy and peak shape are dependent on the valence electron density and hence can be altered by chemical changes in a material. The energy of a valence plasmon can be calculated from equation 1.10 using the number of carriers in the valence band. In circumstances where electrons are confined in 2D such as in 2D materials or in 2D electronic states, plasmon excitations are also confined in 2D. If electrons are confined to a 2D localised state, their localisation will be observable in EELS maps. 2D plasmons can be characterised by differences in their plasmon dispersion compared to other types of plasmon [91].

At a metal/dielectric interface, coupling between metal plasmon oscillations and dielectric electric fields can occur, giving rise to surface plasmon polaritons (SPP) that can propagate along the interface, as illustrated in figure 1.7a. They are characterised by an evanescent wave decaying towards the bulk and vacuum [89]. These SPPs can be considered as electromagnetic waves confined in the material due to the coupling between the electrons and electromagnetic fields [89]. The energy of a surface plasmon, E_{sp} is related to the energy of the bulk plasmon in a metal, E_p, by

$$E_{sp} = E_p / \sqrt{1 + \varepsilon_d}, \tag{1.12}$$

at the interface between a metal and dielectric with dielectric function ε_d. SPPs at thin film interfaces cannot be directly excited by photons due to momentum mismatch, therefore, materials are often patterned into sub-wavelength structures to get around this [92].

Localised surface plasmon resonances (LSPR), shown in figure 1.7b, are non-propagating excitations which occur on the surface of sub-wavelength size metallic nanoparticles [89]. Upon interaction with an external electric field, electrons within the nanoparticle are displaced

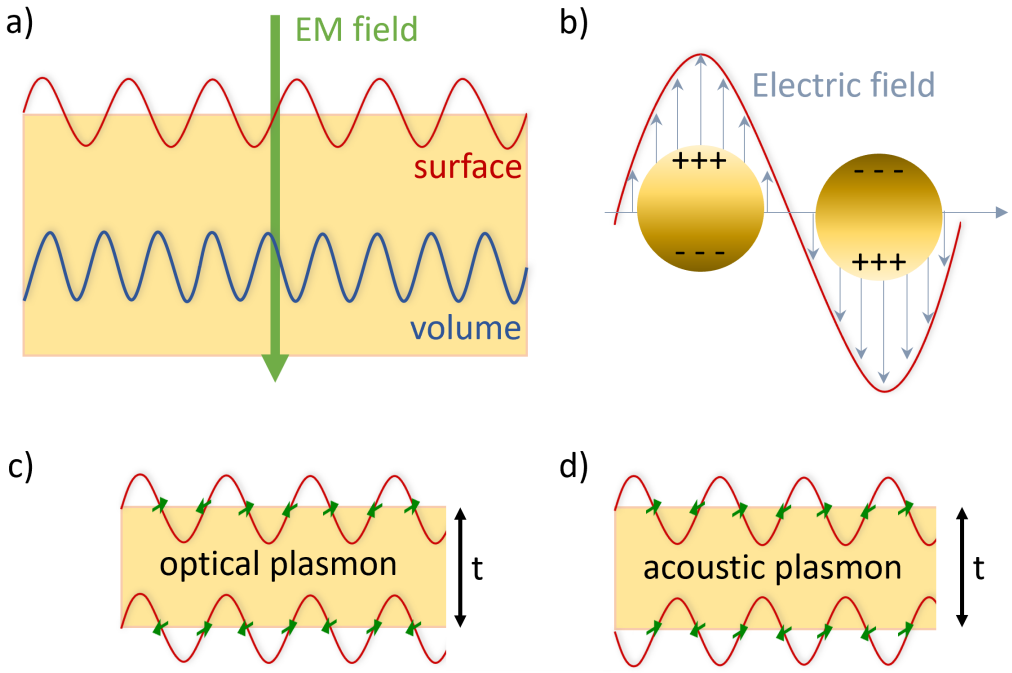

Fig. 1.7 Different types of plasmon which can be excited when an electromagnetic (EM) field interacts with a material. a) In the bulk of a sample volume plasmons are excited and at the surface, lower energy surface plasmons are excited which can propagate along a surface as surface plasmon polaritons (SPP). b) Localised surface plasmon resonances (LSPR) occur in nanoparticle specimen and are non propagating. c) In very thin films of thickness, t, surface plasmon waves on the top and bottom surfaces couple. When in-phase, optical plasmons are excited and d) when out-of-phase, acoustic plasmons are excited.

and a dipole forms between the positive ion lattice and electron cloud across the nanoparticle. The curved surface of a nanoparticle gives rise to a strong restoring force and oscillation of charges. A LSPR occurs when frequency of the external field matches the natural oscillation frequency of the nanoparticle and results in an enhancement of the local electromagnetic field surrounding the nanoparticle [89]. The energy of an LSPR can be shifted by changes in particle shape or size for the same material. LSPRs have been extensively studied due to their ability to enhance the electric field surrounding a nanoparticle, with plasmon energies influenced by nanoparticle shape and size, increasing the versatility of LSPRs [93]. Where nanoparticles are in close proximity, coupling between LSPRs can occur. They will be simulated and discussed further in section 3.6.

For thin films, the surface plasmons created on both surfaces can become coupled together giving rise to two coupled plasmon modes, the optical and acoustic plasmons, from the interference between out-of-phase and in-phase surface plasmons, as visualised in figure 1.7c,d [94]. A surface plasmon mode is made up of two components, charge and spin. When

surface plasmons on either surface are in-phase, as shown in figure 1.7c, the coupled plasmon mode is termed an optical plasmon. The spin of the surface plasmons, shown as green arrows, cancels out, whilst the charge is not, resulting in a plasmon mode with no spin-component [95]. The opposite is true for the out-of-phase case, where charge cancels out but spin does not, resulting in spin-waves known as acoustic plasmons. Acoustic plasmons give rise to the possibility of pure spin currents which are of interest for spintronic applications [23]. Whilst optical spectroscopy can be used to probe the optical plasmon mode, the acoustic mode cannot be detected. The acoustic mode requires momentum transfer to be excited, which does not occur in most optical spectroscopies. Momentum transfer can, however, be probed using EELS making observation of acoustic plasmon modes possible. In Bi_2Se_3 an acoustic plasmon mode has been observed to arise at 30 meV [94].

Information on plasmonic excitations within a material is included in the dielectric function of the material, $\varepsilon(q,E)$, which can be obtained from the energy loss function measured using EELS. The dielectric function is found from Kramer-Kronig analysis of EELS spectra and will be discussed in chapter 3 [81].

The double differential cross-section for a plasmon excitation in EELS can be found using equation 1.5 and plasmon energy, E_P, and peak width, ΔE_P, contained within the dielectric function such that

$$\frac{d^2\sigma}{d\Omega dE} \approx \frac{1}{\pi^2 a_0 m_0 v^2 n_a} \frac{\Delta E_P E_P^2 E}{(E^2 - E_P^2)^2 + (\Delta E_P E)^2} \left(\frac{1}{\theta^2 + \theta_E^2} \right), \tag{1.13}$$

where θ_E is a characteristic scattering energy of a plasmon excitation given by $E_p/2E_0$ [80]. A sharp cutoff to the angular distribution of plasmon scattering is predicted above a critical angle θ_c and will be discussed in more detail in relation to calculated EELS spectra in chapter 3.

The mean free path for plasmon excitations is on the order of 100 nm. Plasmons are typically heavily damped with lifetimes of only around 10^{-15} s and are localised to <10 nm [80]. The degree of damping is dependent on the band structure of the material [81].

There are several different types of plasmons that can be excited in the bulk or at the surface of a material, as illustrated in figure 1.7. Different types of plasmon, illustrated in figure 1.7, can be excited depending on the position of an incident electron beam. For example, with the beam positioned on a thick region of bulk material, volume plasmons are excited. When the beam is positioned at an interface between a material and vacuum, surface plasmons can be excited as well as volume plasmons. By positioning the beam in an aloof position in vacuum, close to an interface with a material, surface plasmons can be excited

without exciting volume plasmons. Therefore by collecting EELS spectra at different beam positions, it is possible to distinguish bulk and surface plasmon modes.

Plasmons have a wide variety of different applications including as waveguides and sensors. For example, SPPs are of interest for the transmission of light through sub-wavelength apertures due to the confinement of light as plasmonic excitations. Additionally, surface plasmons in nanostructures have been shown to enhance emission from nearby molecules, which could be useful for biological sensing applications [96].

1.4.1 Plasmon dispersion

Different types of plasmons can be distinguished from each other by the dispersion of their energy with increasing momentum. As shown in figure 1.6, momentum can be transferred in an inelastic scattering event. Momentum-resolved EELS, discussed in section 2.6, can be used to access this momentum information and observe the plasmon dispersion.

The plasmon dispersion relation describes variations in amplitude, phase and speed of propagation of the plasmon wave and can be found by measuring the change in plasmon peak energy with momentum transfer. The dispersion relation of volume plasmons is parabolic [81, 97] and described by

$$E_P(\mathbf{q}) = E_P(0) + \frac{3}{5}\frac{E_F}{E_P}\frac{\hbar^2}{m_0}\mathbf{q}^2, \tag{1.14}$$

where $E_P(\mathbf{q})$ is the plasmon resonance energy at momentum $\boldsymbol{q}$, $E_P(0)$ is the plasmon resonance energy at zero momentum, E_F is the Fermi energy and m_0 is the electron rest mass.

The plasmon dispersion relation for an SPP can be expressed in terms of plasmon frequency by

$$k_{SPP} = \frac{\omega}{c}\sqrt{\frac{\omega^2 - \omega_{sp}^2}{2\omega^2 - \omega_{sp}^2}}, \tag{1.15}$$

where ω_{sp} is the surface plasmon frequency. The dispersion can be rearranged to obtain a relation in terms of $\omega(k_{SPP})$,

$$\omega^2(k_{SPP}) = \frac{\omega_{sp}^2}{2} + k_{SPP}^2c^2 - \sqrt{\frac{\omega_{sp}^2}{4} + k_{SPP}^4c^4}, \tag{1.16}$$

which indicates a significantly different dependence compared to bulk plasmons [98, 99].

Changes to the plasmon dispersion can also be used to distinguish more unusual types of plasmons and excitations. For example, linear dispersion is expected for acoustic plasmons, with energy starting from 0 eV when $q = 0$ [39, 95]. 2D π plasmons in graphene have been observed to obey a linear dispersion relation due to the cone-like band structure, which differs

from the parabolic dispersion of the π plasmon in bulk graphite [100]. Plasmon dispersion trends in topological insulators can differ due to plasmons excited from Dirac fermions in their TSS [94, 101]. Coupling between phonons and plasmons has also been shown to result in changes to plasmon dispersion trends [102].

1.4.2 Plasmons in topological insulators

The SPPs in topological insulators differ from those in metals due to the presence of Dirac fermions at the TI surface. Plasmons excited from Dirac fermions in TI surface states, known as Dirac plasmons, experience reduced scattering from the lattice and reduced plasmon damping. This allows for Dirac plasmons to have lossless transport, which could be a solution to improving transport in plasmonic devices. These plasmons are confined to the 2D surfaces of a 3D TI. One of the biggest drawbacks of metallic plasmon systems to the strong plasmon damping which occurs due to scattering and reduces transport distance. As a result more complex structures must be made in order to mitigate damping effects. However due to the lower losses in TIs, they are ideally suited to plasmonic devices [103].

Dirac plasmons were first detected in graphene, which, despite not being a topological insulator, has Dirac cones in its band structure and is host to Dirac electrons [104]. The frequencies of these plasmons were found to be tuneable through gating, leading to developments in graphene-based plasmonics and the fabrication of hybrid graphene plasmonic devices. The fabrication of these graphene based devices is difficult due to the requirement for mono-layer graphene sheets, which must be cleaved from the bulk. This challenge is removed when using topological insulators as the presence of TSS and Dirac electrons are not dictated by the thickness of the bulk. Dirac plasmons were first detected in the TI, Bi_2Se_3, using infrared spectroscopy by Di Pietro *et al.* [18]. Their presence was confirmed using resistivity and Hall measurements on ribbons with varied TI thickness. The plasmon dispersion was observed to fit to the dispersion law for Dirac plasmons. Using momentum-resolved HREELS measurements, Politano *et al.* suggested the presence of a Dirac plasmon mode in Bi_2Se_3 up to 200 meV with a characteristic dispersion [105]. Although the Dirac plasmon was observed by both techniques, only EELS can probe the localisation of the plasmon mode to the surface and to distinguish the Dirac plasmon from other modes in cross-sectional specimen, localisation is essential.

EELS measurements can probe the localisation of a plasmon to a surface or interface but to distinguish a Dirac plasmon from other surface plasmons such as SPPs, 2D plasmons and acoustic modes, the dispersion relation can be used [23]. This can be obtained using momentum-resolved EELS techniques discussed in section 2.6. The dispersion relation from Dirac plasmons has been calculated by Deshko *et al.* for Bi_2Se_3 nanoribbons by considering

the dispersion for 2D plasmon modes [106]. The plasmon dispersion of 2D modes follows a $\sqrt{q}$ dispersion which can distinguish them from other plasmon modes such as 3D volume plasmons with a parabolic dispersion of equation 1.14 and localised excitations with no dispersion. When 2D carriers have an effective mass, m^*, the plasmon dispersion can be described by

$$\omega^2_{Massive} = \frac{e^2}{4\varepsilon_0\varepsilon_r}\frac{n_M}{m^*}q, \tag{1.17}$$

where e is electron charge, ε_r is the average permittivity of the surrounding material and n_M is the 2D carrier density. This equation is presented in angular frequency, ω, which is easily converted to energy in eV.Equation 1.17 indicates the dispersion of a 2D plasmon which can be easily distinguished from 3D plasmons in equation 1.14. Dirac plasmon excitations from TSS in topological insulators arise when the 2D carriers in the TSS are Dirac fermions. The effective mass of these carriers is very small and the Dirac plasmon dispersion becomes

$$\omega^2_{Dirac} = \frac{e^2}{4\varepsilon_0\varepsilon_r}\frac{v_F\sqrt{2\pi n_D}}{h}q, \tag{1.18}$$

where n_D is the 2D Dirac carrier density, v_F is the Fermi velocity and ε_0 is the permittivity of free space [103]. For Dirac plasmons excited in a TI, with dielectric function ε_{TI} and thickness d, surrounded by materials with dielectric functions ε_T and ε_B, the plasmon dispersion can be described by

$$\omega^2_{Dirac} = \frac{v_F k_F e^2}{\varepsilon_0 h}\frac{q}{\varepsilon_T + \varepsilon_B + qd\varepsilon_{TI}}, \tag{1.19}$$

where k_F is the Fermi wavevector. Mapping the plasmon dispersion is key to distinguishing Dirac plasmons from other surface modes. Coupling between Dirac plasmons and optical phonons has been suggested by Hale *et al.*, who observed the dispersion of a coupled mode in Bi_2Se_3 nanoribbon arrays [107]. The frequency of Dirac plasmons in arrays of Bi_2Se_3 nanoribbons was observed to depend on the Bi_2Se_3 thickness, indicating a means of tuning Dirac plasmon modes [108].

Acoustic plasmons are expected to occur in thin films of TIs, where surface plasmons from top and bottom surfaces can interfere [95]. In TIs, acoustic plasmons are predicted to arise from Dirac plasmon modes excited at both surfaces, leading to unique acoustic plasmon properties [109]. EELS can be used to observe acoustic plasmons and the plasmon dispersion of this mode should allow for it to be distinguished from other plasmon types. Jia *et al.* investigated the acoustic mode in Bi_2Se_3 and reportedly observed an acoustic plasmon mode with linear dispersion and weak damping [94]. The prospect of spin-plasmons with high

mobility in TIs is exciting for the generation of spin-currents and spintronic applications [39].

1.4.3 Surface plasmons and molecules

When an organic molecule is introduced to the surface of a thin film or nanoparticle that is host to surface plasmons, coupling can occur between the molecule and surface plasmon [110]. This coupling can result in a redshift of plasmon energy and can be due to a change in relative permittivity at the surface or due to coupling with a molecular resonance [111].

For organic molecules with electronic absorption energies far from the energy of plasmons in the thin film or nanoparticle, their adsorption on the surface can increase the refractive index of the environment around the surface [111]. This can result in increased screening of the Coulomb restoring force acting on excited electrons, which redshifts the energy of the plasmon resonance. The redshift is small but can increase due to greater screening if the refractive index increase is greater. This effect is the basis of refractive index sensors.

When the organic molecule has resonances close to the plasmon energy of the film or nanoparticle, much larger redshifts are observed. A molecular transition can couple with the plasmon resonance and form a hybridised state analogous with hybridisation of atomic states in molecules. The strength of this effect can be dependent on molecular dipole orientation [112] and enhancement of surface enhanced Raman spectroscopy is observed. Dye molecules with molecular resonances that can be changed with light illumination can be used to exploit this effect to optically switch the plasmon energy for active plasmonic devices [113]. Coupling between molecular resonances of ZnPc and surface plasmons on Ag thin films has been demonstrated by Yeh *et al.*, who observed a redshift and splitting of the Ag surface plasmon into two branches with a decrease in surface plasmon propagation length [69].

A hybridised state formed from the interaction between surface plasmons and molecules can be 2D confined to the surface [114]. The effect of surface plasmon-molecule coupling and the modification of TSS described the section 1.2.2, should both contribute to the plasmonic behaviour at Bi_2Se_3/organic interfaces in the energy ranges investigated in this thesis. Since coupling between the surface and molecules is dependent on molecular resonance energy, optically or chemically changing the molecular resonance could influence the TI surface plasmons and be used for active plasmonic devices [115]. Absorption at specific energies could be enhanced and benefit optoelectronic TI devices.

Plasmons can be excited and observed through optical methods or electron energy loss spectroscopy (EELS). The biggest benefit to using EELS vs. optical techniques is the possibility to observe highly localised plasmons with greater spatial resolution. As the

wavelength of electrons is much smaller than photons increased spatial resolution is possible. This is especially useful when observing surface plasmon or interface modes as these will be highly localised to a small area and the spectrum could be dominated with bulk modes if acquired over a larger region. Furthermore, how a surface plasmon decays away from the interface can provide further information on the type of interaction present. Another benefit to the use of EELS to study plasmons as opposed to optical spectroscopy techniques is the ability to observe 'dark modes' which are not excited by photons such as acoustic plasmons.

1.5 Scope of this thesis

This thesis investigates the plasmonic modes in the topological insulator $Bi_2Se_3$and how these modes are influenced by proximity to various organic materials. The aim of this research is to demonstrate how organic molecular dopants modify surface plasmon behaviour, giving insight into changes to surface states and bonding at these interfaces. Demonstrating the modification of Bi_2Se_3 surface states due to organic molecular overlayers is a step towards creating a tunable TI surface for applications in plasmonics.

Chapter 2 outlines the experimental techniques used to prepare, image and analyse samples. These include sample preparation by focused ion beam (FIB) techniques, which was optimised for organic interfaces by thinning at cryogenic temperatures. Electron microscopy techniques used for imaging and spectroscopic analysis including (scanning) transmission electron microscopy ((S)TEM), electron energy loss spectroscopy (EELS) and momentum-resolved (qEELS), are detailed. Chapter 3 discusses simulations of EELS spectra, carried out in python and 'COMSOL' for a variety of nanoparticle and thin film systems. The presence of a rough interface and localised interface states are simulated to illustrate their effect on EELS spectra and plasmon confinement at an interface. These simulations are used throughout the rest of the thesis to aid in interpretation of experimental results.

In chapter 4, the plasmonic behaviour in samples of $Al_2O_3/Bi_2Se_3/C_{60}$ is examined using transmission electron microscopy (TEM), EELS, and momentum-resolved EELS, revealing distinct interfacial plasmon modes and hybridization effects. Chapter 5 expands this investigation to include other organic overlayers including graphene, H_2Pc and CuPc to explore how different molecular dopants change the energy and localisation of Bi_2Se_3 plasmons. Finally, chapter 6 focusses on ultra-low energy behaviour between 20 and 300 meV at Bi_2Se_3/H_2Pc and Bi_2Se_3/CuPc interfaces, which was expected to encompass the Dirac plasmon. This chapter investigates changes in low-energy plasmon modes linked to carrier density and TI surface states.

This thesis will demonstrate that the inclusion of molecular dopant layers can modify the Bi_2Se_3 surface and show clear differences compared to interfaces with insulating substrates. The observed shifts plasmon energy, confinement, and dispersion reflect changes in the surface electronic structure driven by molecular interactions. These findings indicate that organic molecular overlayers could provide a route to tunable TI plasmons that can be enclosed within a device. This work lays the foundation for developing tunable, TI/organic plasmonic devices based on Bi_2Se_3, with potential applications in photodetection and sensing.

2 Methods and Instrumentation

2.1 Introduction

Electron microscopy is a powerful technique that allows us to observe materials on a nanoscale and image objects smaller than the wavelength of light. Information about the chemistry and optical properties can also be obtained by electron microscopy techniques. The combination of the structural and chemical information obtained from analytical electron microscopy techniques can provide an in-depth understanding of a sample which can explain properties observed over larger length scales.

The preparation and analysis of high quality samples underpins all of the work in this thesis and requires expertise in operating a variety of instruments. Thin film samples of Bi_2Se_3 with various organic overlayers were prepared using focused ion beam (FIB) lift-out techniques to extract lamellae and thin them until they are electron transparent, less than 100 nm thick. Structural analysis was then carried out using transmission electron microscopy (TEM) and scanning transmission electron microscopy (STEM) to assess the crystallinity and interfaces of samples. Plasmon modes were analysed using electron energy loss spectroscopy (EELS) and momentum-resolved electron energy loss spectroscopy (qEELS). This chapter will provide an overview of the equipment and techniques used to obtain experimental results presented throughout this thesis.

2.2 Sample preparation

2.2.1 Growth methods

Samples were grown at the University of Leeds by collaborators using two techniques which will be briefly described here. Molecular beam epitaxy (MBE) at the Henry Royce

deposition system was used to grow the majority of samples used throughout this research. Firstly, a sapphire substrate was loaded into the system and heated to 773 K to remove any contaminants [116, 117]. Bi_2Se_3 was grown by evaporation of bismuth and selenium sources and the flux ratio of Bi:Se was maintained throughout, as monitored by an ion-gauge flux monitor, to ensure the correct composition was grown [30]. As Se does not stick to the substrate or other Se layers, the growth is controlled solely by the Bi flux and the Bi:Se ratio is self-limited, simplifying growth. The first few layers of Bi_2Se_3 were grown at a lower temperature than the rest of the film to ensure even deposition and the correct lattice structure to be grown. The rest of the layer was then grown at a higher temperature until the desired thickness was reached. For samples discussed in this thesis, the desired thickness was around 15 nm. The growth was monitored at each step using reflection high-energy electron diffraction (RHEED) patterns to ensure the correct lattice structure [118]. RHEED works by striking the surface of a specimen at a shallow angle with high-energy electrons, which are diffracted from the surface and detected. The diffracted electrons form a diffraction pattern which can be used to determine the surface structure.

Some Bi_2Se_3 samples, discussed in chapter 5, were grown by vapour transport growth (VTG) on SiO_2 substrates [119]. This technique is particularly useful in the fast growth of thick single crystals, whereas MBE growth is preferable for flat thin film growth with consistent thickness. A polycrystalline Bi_2Se_3 source and silicon substrate were sealed inside a quartz tube in an argon atmosphere. They were maintained 873 K and 823 K respectively, with a temperature gradient between them until the 35 hr growth was completed. Resulting Bi_2Se_3 crystals varied in size from a few μm to $\approx 50\mu$m and large flat crystals were selected for investigation.

Organic molecular layers were deposited on Bi_2Se_3 films by MBE at the Henry Royce deposition system in a designated organics chamber. The molecular source was heated to a set temperature and molecules were released into the sample chamber to deposit on the Bi_2Se_3 surface [116]. The growth rate was monitored using a quartz crystal, which changes oscillation frequency after material deposition. Finally, a metallic cap was deposited on top of the organic layer by electron-beam evaporation to protect the sample from oxygen exposure.

2.2.2 Focused Ion Beam (FIB)

For all transmission electron microscopy work, samples must be thin enough for the electron beam of the microscope to easily transmit through the sample. A thickness of less than 100 nm is required, with thinner requirements when lower electron accelerating voltages are used, which is the case for many of the EELS measurements, where samples were ideally between

20 and 50 nm thick. In this thesis, lamellae were extracted from bulk samples using focused ion beam (FIB) lift-out techniques and thinned to the appropriate thickness [120–122].

FIB lift-out is a technique which uses an ion beam to mill away material from a specimen. The ion beam, in this case gallium or xenon, has a large penetration depth and can remove atoms from the sample, making it useful for the removal of both small and large amounts of material depending on beam currents chosen [121]. At large beam currents, the ion beam has a large penetration depth and can remove large areas of material with ease. Lower beam currents are used to remove smaller amounts of material and to thin specimen to an even thickness with minimal damage to the remaining material. Low voltages can then be used to polish the samples to produce smooth surfaces.

Material can also be deposited by the FIB instrument, for example protective platinum layers and to weld objects together [123]. A metalorganic precursor gas is introduced near the specimen surface and an electron or ion beam is directed towards the surface. The high energy electrons/ions interact with the gas, resulting in cracking of the metalorganic gas molecules, decomposing them into their component parts. In the case of Pt deposition, a Pt containing metalorganic gas such as $C_9H_{16}Pt$ is decomposed into volatile hydrocarbons, which leave the surface, and non-volatile C and Pt atoms which are deposited on the surface [124, 125]. The deposited material is made up of Pt nanoparticles surrounded by amorphous carbon and is typically deposited during the preparation of TEM specimen.

FIB lift-out techniques have been commonly used for TEM preparation to reliably produce samples thin enough for TEM. There are few limits to the types of materials which can be prepared using FIB and there is no requirement for solvents [121, 126]. FIB preparation can be done on small target areas and obtain uniform thicknesses over desired regions. This allows for site-specific TEM investigations of specimens such as nanoscale electrical devices and nanostructures [121]. Samples can be reliably prepared by FIB in as little as a few hours.

There are some difficulties in the use of FIB preparation which need to be considered. The bombardment of ions at a material can result in a build up of charge. If this charge cannot be dissipated it can produce charging effects which makes imaging and milling of the sample difficult. For example, drift can be observed, resulting in milling at different locations than desired. This effect is particularly problematic for samples with an insulating substrate such as sapphire. To limit charging several steps can be taken. A sputter coating of carbon or gold can be applied to provide a route for charge dissipation [121]. Additionally, silver paint can be used to attach the bulk sample to a specimen holder, providing as much contact as possible.

Two dual-beam focused ion beam (FIB) instruments were used for sample preparation. Both instruments combine both a scanning electron microscope (SEM) and FIB to allow

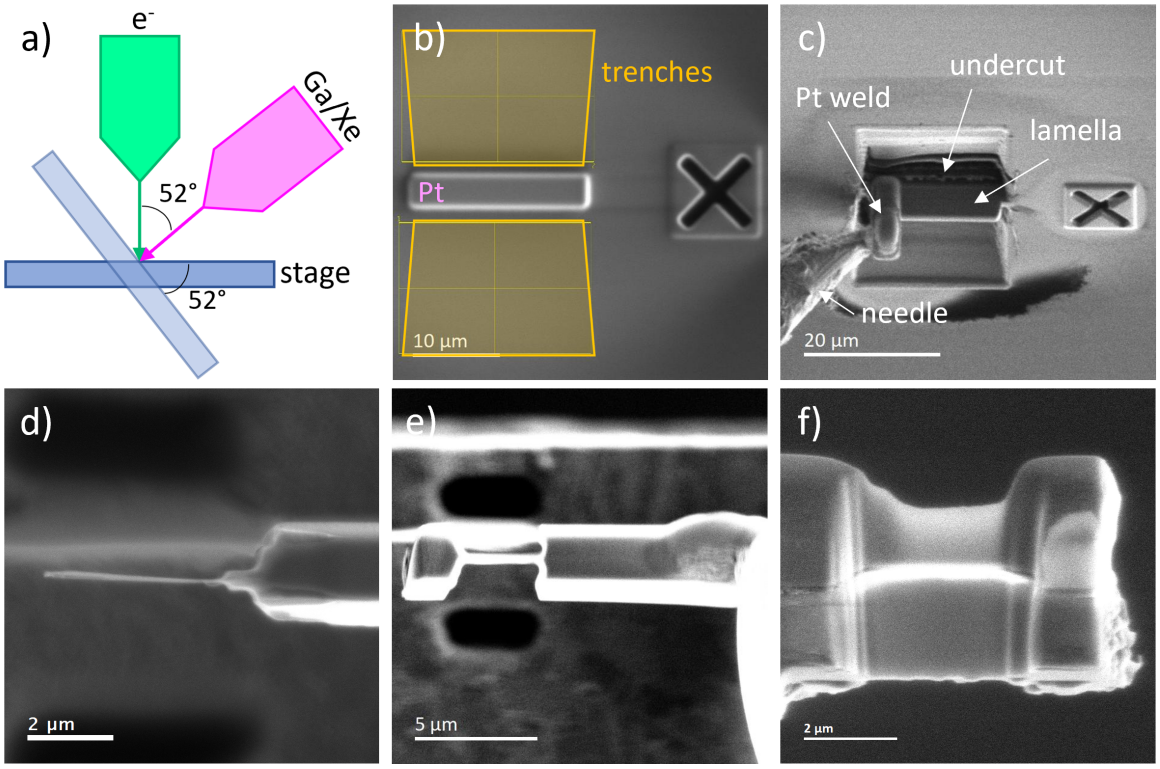

Fig. 2.1 a) Schematic of electron, e^-, and ion, Ga/Xe, sources and the specimen stage. The ion beam is 52° tilted relative to the electron beam and both beams are aligned to image the same region of the specimen. During preparation of a sample, the stage will be tilted by 52° so that either the electron beam or ion beam are directly above the specimen depending on the preparation step. b-f) Stages of the preparation of a TEM lamella. b) Deposition of a platinum protection layer and trench milling of the yellow highlighted regions. c) The sample has been undercut and remains attached to the bulk at the right side of the lamella. It has been welded to a micromanipulator needle with platinum. d) Finished lamella using the standard procedure and e) finished lamella with a thick section remaining at the end. f) Electron beam image of the front surface of a finished lamella with a thick section remaining at the end.

for simultaneous electron and ion beam imaging. The sample is mounted on a stage in the instrument and held at high vacuum. The SEM electron beam is positioned above the stage with the FIB positioned at a 52° angle from the vertical, as shown in figure 2.1a. The two beams are aligned such that both are in focus at the same position on the sample when it is at what is known as eucentric height.

The FEI Nova Nanolab 200 uses Ga^+ ions for milling and the FEI Helios Plasma FIB uses xenon ions. In the case of the gallium instrument, a Ga reservoir is heated and the molten Ga flows to a sharp tungsten tip. With the application of an electron field, the Ga tip becomes a point source of ions which are extracted with an applied voltage giving the desired emission current [121]. The Ga ions are then accelerated towards the sample. In the

PFIB, a Xe plasma source is used and Xe ions are extracted from the plasma and accelerated towards the sample using an electric field. The Ga source has the benefit of a smaller probe size, allowing for more precision, however, in many materials the Ga ions can implant into the sample [127]. Ga implantation can contaminate samples and can be a significant problem in sensitive samples. Due to the inertness of Xe, it is ideal for FIB milling as it does not react with or implant into samples. The Xe FIB is capable of faster milling rates than the Ga FIB because the heavier Xe ions transfer momentum more efficiently to specimen atoms, resulting in higher sputter yields and because higher beam currents are available [128]. The efficiency of momentum transfer is maximised when the ion mass is similar to the mass of specimen atoms so the relative milling rate of Ga or Xe depends on the material. Of the two instruments available, only the FEI Nova Nanolab 200 was capable of cooling to cryogenic temperatures, so sample preparation was carried out on this instrument when cryogenic temperatures were required.

2.2.3 Standard FIB preparation

To prepare a sample for TEM, the selected region of the sample was first protected with a 300 nm layer of platinum deposited by the electron beam. This protective layer was deposited before the region has been exposed to the ion beam, so that ions did not penetrate the sample and instead can only reach the protective layer [123]. The sample was then tilted to 52° to allow for the ion beam to be normal to the stage. A further 1 μm of platinum was deposited by the ion beam on the same region, which can be seen in figure 2.1b as a rectangle at the centre of the image. This platinum layer prevented damage to the sample by the ion beam during liftout and thinning steps and also provided an amorphous layer to aid in STEM microscope alignment [120]. Trenches were cut on either side of the protected area, as indicated in figure 2.1b, to a depth of around 5 μm using the ion beam at 30 keV and 6.7 nA, with the milling time extended for harder substrates such as sapphire. In comparison to silicon, milling the same depth in sapphire took around 3 times as long. Both sides were then cleaned using a 'cleaning cross section' pattern at a tilt of $\pm$1.5° from 52°. The 'cleaning cross section' pattern milled lines horizontally along the edge of the desired region and line by line became progressively deeper as it approached the protected region. This allowed for slower and more controlled milling.

The stage was then tilted back to 0°, normal to the electron beam, to undercut the lamella for extraction. An 'L-shape' was cut around the lamella using a 30 kV 1.8 nA ion beam, as shown in figure 2.1c, leaving only one side connected to the bulk. The undercut was monitored by imaging with the ion beam and a clear change in contrast was observed when the lamella was fully undercut. When preparing samples on sapphire substrates, the imaging

was worse due to charging effects. Therefore, to ensure that the sample was fully detached, it was rotated 180° and undercut from the other side. To speed up this process, currents of up to 6.7 nA were used on some samples.

To proceed with lamella extraction, a micromanipulator needle was brought into contact with the free side of the lamella whilst being monitored with the ion beam at 30 keV and 0.23 nA. When a sapphire substrate was present, the point of contact between the needle and lamella was observed in the image by a quick change in brightness and an improvement in imaging quality as the surface charge was dissipated, so that the imaging was not distorted. The needle was welded to the lamella, as shown in figure 2.1c, using 1 μm of Pt, deposited using the ion beam at 30 keV and 0.23 nA. The lamella was then freed from the bulk by further milling of the attached side using the ion beam at 30 kV and 1.8 nA. The extracted lamella was then brought into contact with a copper holder for TEM specimen whilst being monitored by ion beam imaging. This was welded using 1 μm of Pt as before and then was detached from the micromanipulator needle [121].

The thick lamella was thinned from both the front and back side using parameters tabulated in table 2.1. Firstly, rectangular regions were milled away to reduce the thickness to around 1 μm using 30 kV ion beam currents of 0.23 nA or 74 pA from both sides at a tilt of $\pm 1.5°$ or $\pm 2°$ from 52°, depending on the substrate. Higher angles were used for sapphire substrates to cut away more of the substrate and samples with an organic layer were thinned starting from a beam current of 74 pA to reduce damage [122]. Thinning then continued at 74 pA line by line using a cleaning cross section pattern at a reduced tilt angle of $\pm 1.2°$ or $\pm 1.5°$ until electron transparent. For Si substrates, a change in the shade of the lamella was observed in the electron image, indicating the lamella was becoming close to electron transparent. It was much more difficult to tell when a lamella with a sapphire substrate was thin enough. Therefore, the thickness of the Pt level was monitored and thinning was stopped when there was less than around 100-200 nm of Pt left or a hole was observed to form in the lamella close to the sample was observed. Finally, the thinned region was polished using a 5 kV and 47 pA ion beam at a tilt of $\pm 7°$. An example of a finished lamella is shown in figure 2.1d.

Although this method was successful in preparation of many samples, those with organic layers often delaminated during the thinning process. This may result from the large differences in hardness between layers or the formation of an interfacial charge dipole, both of which could promote preferential milling at the interface and lead to delamination [120]. To limit delamination of layers and reduce the negative effect of any delamination, samples were thinned leaving a thick region on either side of the thinned region as shown in figure 2.1e. This reduced the likelihood of any separated regions curving away from each other,

	Room Temperature		Cryogenic Temperature	
Step	**Voltage/Current**	**Tilt Angle**	**Voltage/Current**	**Tilt Angle**
Bulk removal	30 kV 74 pA	±2	30 kV 93 pA	±2
Cleaning	30 kV 74 pA	±2	30 kV 93 pA	±2
Cleaning	30 kV 74 pA	±1.5	30 kV 93 pA	±1.5
Polish	5 kV 47 pA	±7	4 kV 47 pA	±7

Table 2.1 FIB lamella thinning steps for a cross-section sample on a sapphire substrate for both room temperature preparation on the PFIB and cryogenic thinning on the Ga FIB.

allowing for samples with delamination to still be thinned to electron transparency [129]. Additionally, all thinning was carried out using an ion beam of 30 kV and 74 pA or below for samples sensitive to FIB damage.

2.2.4 Cryogenic thinning

Typically used for preparation of biological samples, cryogenic-FIB has been shown to produce high quality specimen for TEM investigation [130]. The use of cryogenic temperatures for FIB preparation has been shown to minimise structural damage caused by ion beams and reduce contamination in beam-sensitive materials [131, 132]. At low temperatures, thermal damage incurred from heating the sample is reduced. During milling, heating of the sample could result in amorphisation and changes to the crystal structure and could result in chemical changes. For layered samples with large differences in hardness between layers, milling rates differ between layers resulting in an uneven thickness of the sample and increased damage at interfaces. In specimen prepared at cryogenic temperatures, this interfacial damage was found to be reduced. Organic materials can be easily damaged by the ion beam. Upon interaction with the sample the ion beam imparts energy to the specimen, which can result in sample heating and increase damage within the organic layer.

To prevent delamination of organic layers, samples containing any organic layers were thinned at cryogenic temperatures after extraction from the bulk at room temperature [133, 131, 132]. This method improved the success rate of producing intact, hole-free samples with uniform thickness. For lower-voltage electron microscopy measurements thinner samples are needed so extended thinning times were required during sample preparation and the final steps of thinning had to be monitored very closely to prevent destruction of samples. Care was also taken to prevent redeposition of Pt across the surface, as Pt can act as an electronic dopant in the organic layers discussed in chapter 4.

The initial extraction was carried out as described in section 2.2.3 on the Xe PFIB before being transferred to the Ga FIB. The cryogenic thinning was carried out on the Ga FIB as

this instrument had a stage capable of cooling to temperatures as low as 95 K. The extracted lamella on a copper holder was positioned on the specimen stage in the Ga FIB chamber and the stage cooled to 98 K. An anti-contaminator was positioned close to the pole piece and cooled to a lower temperature of 95 K to reduce contamination during preparation. After cooling, the lamella was thinned to leave a thick region at each side. Tilts and currents used are tabulated in table 2.1, and were similar to those used in the room temperature method. Currents no higher than 93 pA were used to limit additional damage to the lamella. The differences in currents used were due to the pre-aligned currents available on each instrument.

After thinning, a final polish was carried out to the front and backside of the lamella using a 5 kV ion beam at a current of 47 pA for between 30 to 120 seconds on each side. This polish was carried out at tilt angles of $\pm 7^{\circ}$. A smaller region than the full thinned part is polished to prevent redeposition from surrounding Pt from the thicker surrounding parts. As some samples presented throughout this research were affected by Pt redeposition, further steps could be taken to fully ensure that this does not happen, such as sputtering a thick carbon layer onto the bulk sample before liftout to increase the distance between these layers.

Samples of Bi_2Se_3 with varied organic molecular overlayers including graphene, copper phthalocyanine and hydrogen phthalocyanine, which will be investigated in chapter 5, were prepared using the cryogenic thinning technique.

2.2.5 Exfoliation for plan view samples

As Bi_2Se_3 is a van der Waals bonded material, its layers are only weakly attached to each other through van der Waals bonding and can therefore be cleaved apart. There are several methods which are deployed to do this, with many requiring clean room facilities and complex equipment. However, there is a straight-forward way to separate layers using exfoliation with 'scotch tape' [134].

Starting with a bulk Bi_2Se_3 crystal, layers were separated by pressing the sample against a piece of scotch tape and removing it. This attached some layers of Bi_2Se_3 to the tape. Further layers were removed by folding the tape back on itself several times, leaving lots of thin layers on the tape. Care was taken to not overlap the thin crystals to avoid overlapping crystals at different orientations.

The tape with crystals was then pressed against a clean silicon wafer and pressure applied using a glass slide. After removal of the tape from the wafer, some thin crystals were left on the silicon wafer and visible using an optical microscope. The crystals were then attached to a lacey carbon copper grid by pressing it against the wafer in regions where crystals could be seen under the optical microscope. Crystals which were attached to the grid were of varying size and thickness. The overall yield of single crystalline Bi_2Se_3 flakes, which are

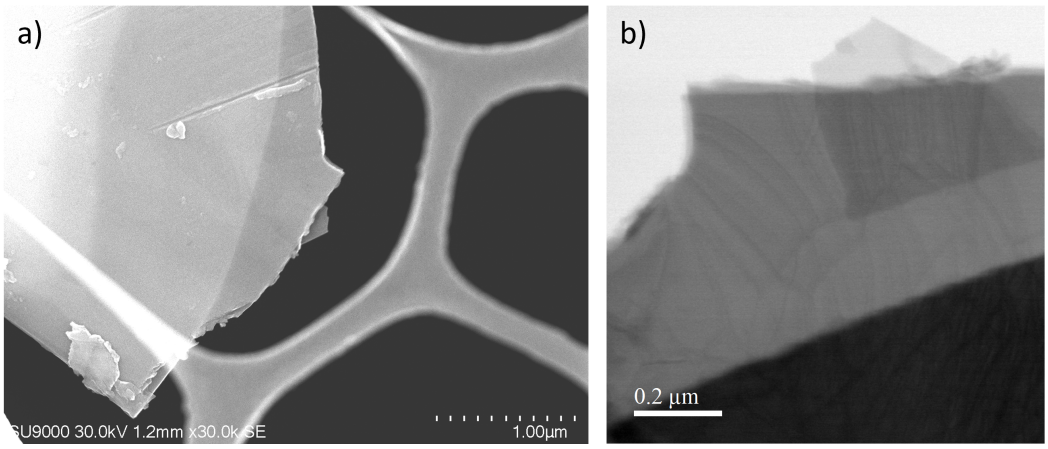

Fig. 2.2 Plan view images of an exfoliated crystal of Bi_2Se_3. a) SEM image of the flake on a lacey carbon grid, where changes in contrast indicate differing thicknesses in parts of the crystal. b) STEM image of the same crystal in a), where the small flake at the top was measured to be around 10 QL thick (10 nm) and the crystal in the centre of the image measured to be around 50 QL (50 nm).

thin enough for TEM was very low, with only a few single crystalline flakes of thickness less than 50 nm on several grids.

Images of a Bi_2Se_3 crystal prepared this way is presented in figure 2.2. Crystals of different thicknesses can be observed overlapping and the thickness of these crystals was measured using EELS, which will be described in section 2.5. The crystal at the centre of figure 2.2b was measured to have a thickness of around 50 nm which is 50 QLs, whilst the small overlapping crystal at the top of this image was around 10 nm thick or 10 QLs. By preparation of samples this way, plan view orientations can be accessed and the sample can be held in vacuum without and interface with a substrate. This crystal was not observed to deteriorate quickly from air exposure, but it is possible that oxygen can diffuse into the crystal [135], so crystals were stored in vacuum and imaged close to the time of preparation.

2.3 Transmission electron microscopy (TEM)

Transmission electron microscopy (TEM) is an imaging technique where electrons are transmitted through a sample and collected to form an image. Electrons accelerated through a potential of 200 kV have a wavelength of 2.5 pm, which is significantly smaller than the wavelength of visible light (400-700 nm), allowing for much greater spatial resolution than optical microscopy. The spatial resolution of TEM is limited by aberrations but atomic scale imaging is possible. Throughout this research three instruments were used: a Tecnai T20, a JEOL ARM 200 CFEG and the SuperSTEM3 Nion UltraSTEM 100MC ‘HERMES’.

A simplified schematic of the electron microscope column for TEM is presented in figure 2.3a. After emission from a electron source, electrons converge at the gun crossover point and the path of the electron beam is indicated in green in figure 2.3a. The electron column comprises a series of electron lenses and apertures that demagnify the source to form a probe or parallel beam at the specimen and magnify the transmitted signal for imaging. The upper part of the column, known as the condenser system, is comprised of several condenser lenses (C1, C2, C mini) and a condenser (C) aperture, shown in purple. The 'Cs corrector' denotes a spherical aberration corrector which reduces beam aberrations described later. The next part of the column is the objective system, indicated in blue, comprised of an upper and lower objective (O) lens surrounding the specimen and an objective aperture below the specimen. A selected area diffraction (SAD) aperture is positioned below the objective aperture and its purpose will be discussed more below. Finally, the projector system, indicated in red, is comprised of an intermediate and projector lens, used to magnify the image. Figure 2.3b depicts a schematic of a microscope used for scanning TEM (STEM). Key differences include the inclusion of scan coils used to scan the beam, which is focused on the sample for STEM, and the absence of some apertures. The electron column is held under ultra-high vacuum conditions to protect the source and prevent unwanted scattering of the electron beam throughout the column. In practice, the column is much more complex and some microscopes can be used for both TEM and STEM.

The electron gun is the source of electrons, which were accelerated with a high voltage of 200 kV, 80 kV or 60 kV for this work. The T20 makes use of a LaB_6 filament thermionic source to produce electrons. A direct current is applied to the filament to heat it and trigger electron emission. The electrons obtain the energy of the accelerating voltage upon emission [136]. The ARM and SuperSTEM3 use cold field emission guns (CFEG) which operate on the principle that electric field strength is enhanced at sharp points. These sources consist of sharp tips under ultra-high vacuum, where the application of a voltage causes electrons to be emitted from the tip via quantum tunnelling [80]. A CFEG has the benefit of producing an electron beam with a very small energy spread, typically of 0.4 eV, which is ideal for EELS analysis. They also benefit from a high brightness, defined as the electron current per unit area per unit solid angle emitted from the source, enabling small probe sizes.

Electrons are guided through the column by a series of electromagnetic lenses, shown in figure 2.3a. Copper coils surround each lens and generate a magnetic field from a supplied current, as illustrated in figure 2.4. The magnetic field is concentrated in the centre of the lens at the bore. Electrons follow a helical path as they travel through the column and when passing through an electromagnetic lens they experience a Lorentz force from the radius of the lens towards the optic axis. The Lorentz force, $\mathbf{F}$, experienced by a electron with velocity

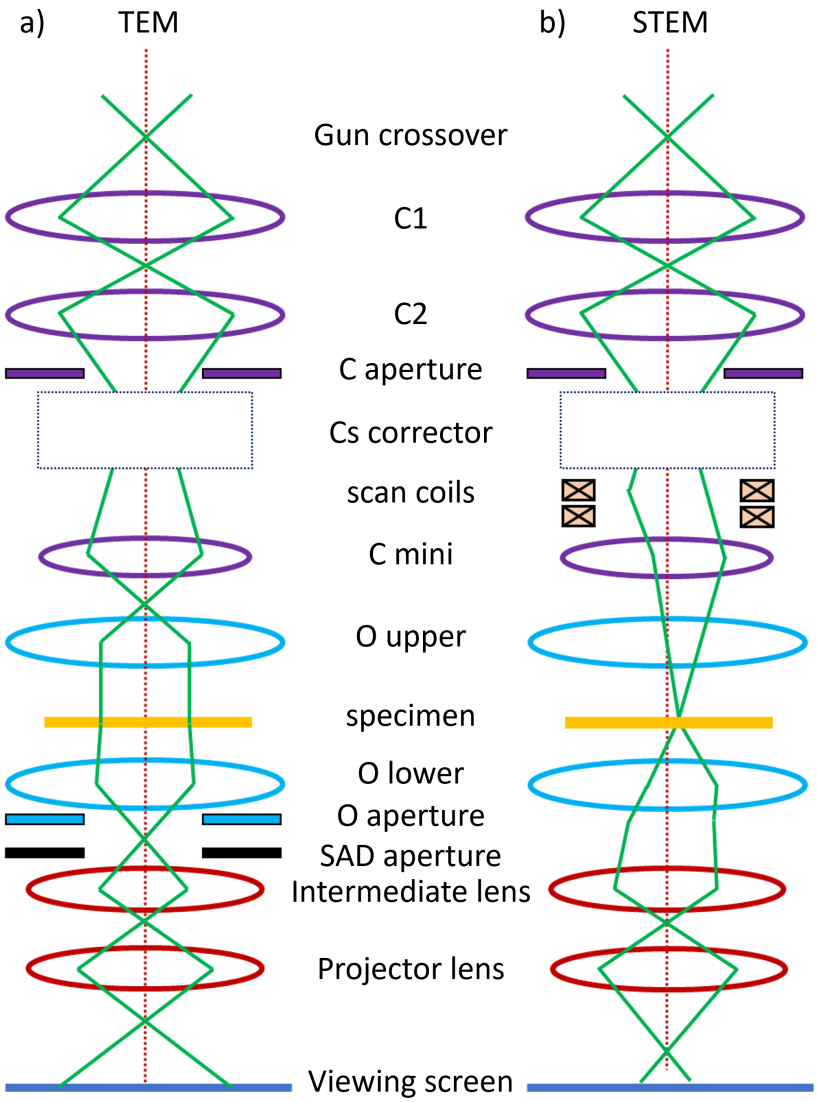

Fig. 2.3 Schematic of a a) TEM and b) STEM microscope column, where the electron beam path is represented in green. After emission from an electron gun, electrons are passed through a series of electromagnetic lenses and apertures to illuminate the specimen with a parallel beam in TEM and focused beam in STEM. Condenser lenses (C1, C2, C mini) and a condenser (C) aperture form the probe which will be incident on the specimen. The spherical aberration (Cs) corrector is used to correct beam aberrations. Objective lenses, O upper and O lower, form the image. The intermediate lens determines whether a diffraction pattern or image is observed at the viewing screen or detector. Projector lenses magnify the image. The selected area diffraction (SAD) aperture can be used to select a smaller area of the sample in TEM. Scan coils are used in STEM mode to scan the focused electron probe across the sample.

v is described by

$$\mathbf{F} = -e(\mathbf{v} \times \mathbf{B}) \tag{2.1}$$

where **B** is the magnetic flux and e is the electron charge. This force increases radially, resulting in a focusing effect [80].

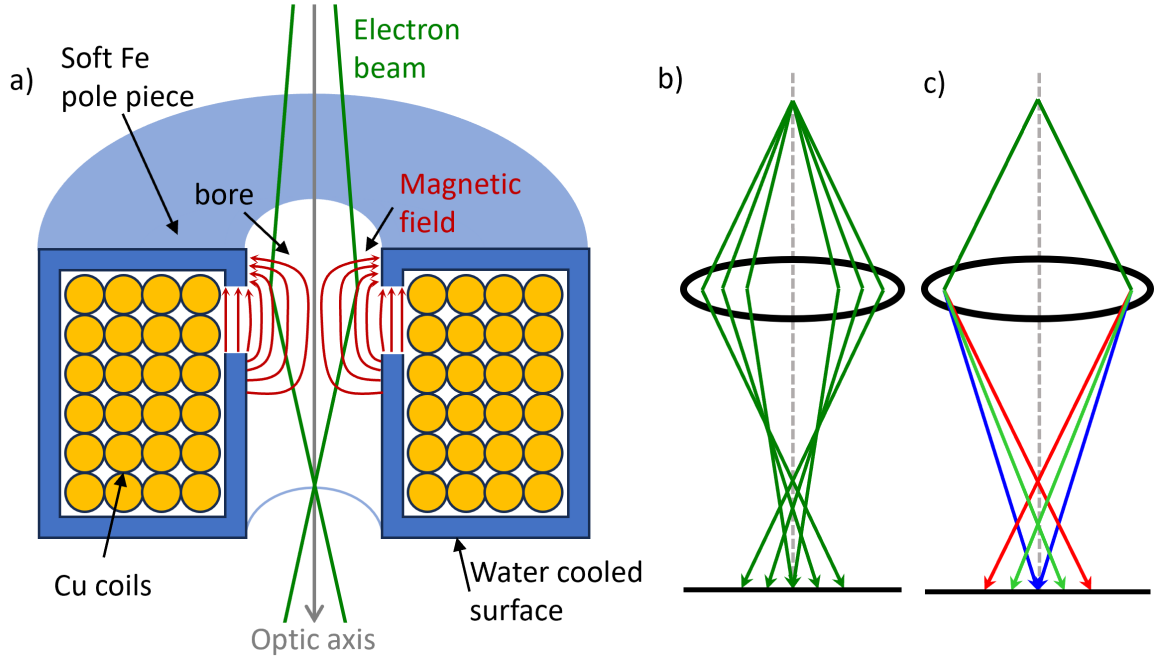

Fig. 2.4 a) Schematic of the cross-section of an electromagnetic lens. The electron beam is directed through the centre, pole piece, of the lens where it experiences a strong magnetic field that manipulates its path. The lens is surrounded by copper coils that generate a magnetic field when a current is passed through. The magnetic field is concentrated at the centre of the lens, as indicated by red field lines. b) Lens diagram depicting spherical aberration, where higher angle electrons are more strongly focused, resulting in no sharp focal point. c) Chromatic aberrations occur due to stronger deflection of higher energy electrons.

The condenser system is the first set of lenses in the column, denoted C1 and C2 in figure 2.3. These lenses are used to form the probe which is incident on the specimen. The strength of each lens can be varied to change the probe size to magnify the electron source. Corrector coils are used to correct beam aberrations in the focused beam from electromagnetic lenses, which limit the resolution of of imaging and spectroscopy [137]. Spherical aberration occurs because off-axis electrons that pass through a lens at high angles are bent more strongly back toward the optic axis, as shown in figure 2.4b. As a result, the beam does not focus to a sharp point but instead forms a disc of finite size [80]. Chromatic aberration arises because electrons with different energies within the beam experience varying degrees of

focusing by the electromagnetic lens, due to the Lorentz force in equation 2.1. Electrons of different energies have different focal points with stronger focussing for those with lower energy resulting in a disc instead of sharp point, as illustrated in figure 2.4c. This is reduced in SuperSTEM with inclusion of a monochromator which reduces the energy spread of the electron beam from a zero-loss peak full width at half maximum (FWHM) of 450 meV in the ARM to 5 meV in SuperSTEM [138]. Although the reduction in energy spread due to a monochromator improves the energy resolution, the beam current is reduced significantly resulting in a much lower signal-to-noise ratio. This can make it difficult to have adequate image contrast to observe structure and when longer exposure times are used to compensate for this, increased sensitivity to sample drift can decrease the quality of images. Stigmation coils are used to remove astigmatism, which arises from non-uniformities in the magnetic field due to electromagnetic lenses not being perfectly cylindrical [80].

The specimen is positioned in the column on a double-tilt holder which can be tilted and rotated to adjust the orientation and height of the sample. This allows for a sample to be orientated along high crystallographic zones. For conventional TEM, the beam is incident on the sample with a parallel beam illumination as shown in figure 2.3a. Images are formed in TEM by the objective lens which is separated into upper and lower parts on either side of the specimen, figure 2.3a. The upper objective lens, O upper, acts as an additional condenser lens. After transmission through a specimen, the electron beam is passed through the lower objective lens, 'O lower' in figure 2.3a, and further lenses, known as the projection system, are used to select whether an image or diffraction pattern is detected.

A simplified schematic illustrating the imaging and diffraction modes of this system is shown in figure 2.5. Either the image plane or back focal plane (BFP) can be projected onto the viewing screen or detector depending on the lens configuration. At the BFP, electrically scattered electrons converge to form a diffraction pattern, which is projected to the viewing screen in diffraction mode. A selected area diffraction (SAD) aperture is positioned at the image plane and allow selection of electrons transmitted from a specific region of the sample. The electron beam passes then through the intermediate and projector lenses, which magnify the diffraction pattern. This process is illustrated in figure 2.5b, where a red dot represents a diffraction spot that can be traced through the system.

In imaging mode, electrons transmitted from the sample are focussed by the objective lens and pass through an objective aperture, forming an image at the image plane. The image, illustrated as a pink arrow in figure 2.5a, can be followed through the system as it is further magnified by the intermediate and projector lenses and projected onto the viewing screen or detector. The objective aperture restricts the angular range of scattered electrons which form the image, to achieve 'bright field' and 'dark field' contrast. Bright field images are

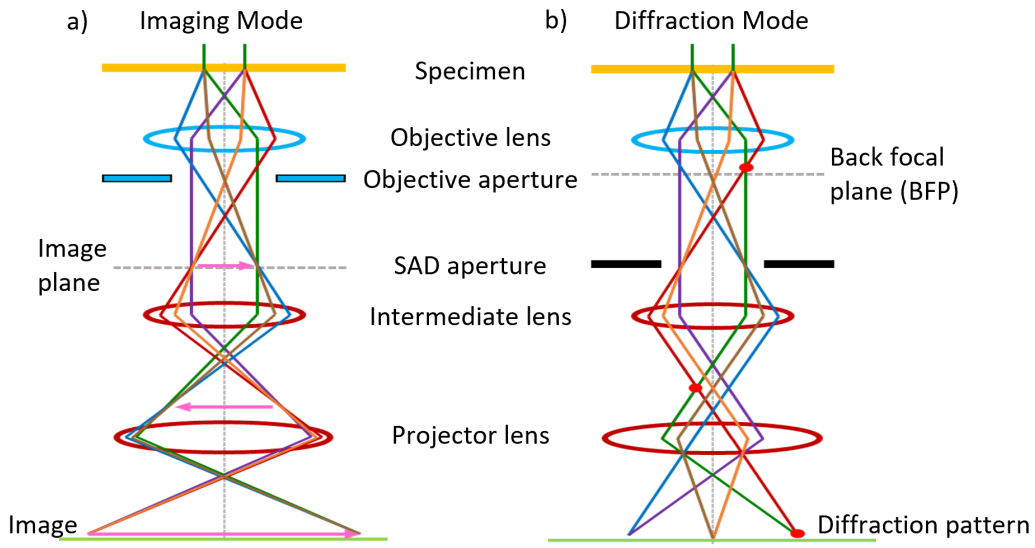

Fig. 2.5 A simplified schematic of the image forming process for a) imaging and b) diffraction mode [80]. After the specimen, the beam passes through an objective lens After passing through a specimen and objective lens, a diffraction pattern is formed at the back focal plane (BFP) and an image formed at the image plane. By changing the strength of intermediate lenses either the image, shown as a pink arrow, or diffraction pattern, shown as a red dot, is projected to the viewing screen or detector in a) imaging mode or b) diffraction mode respectively. An objective aperture at the BFP can be used in image mode to limit scattering angles to form bright field and dark field contrast. In diffraction mode, a selected area diffraction (SAD) aperture at the image plane is used to only transmit electrons from a small area of the image.

formed when the objective aperture is positioned along the optic axis to allow only electrons transmitted directly though the sample to pass, resulting in images where heavier elements generally have the least intensity. For dark field imaging, the aperture position is adjusted to select electrons scattered by larger angles, for example specific diffraction spots to view specific crystal gains.

2.4 Scanning transmission electron microscopy (STEM)

Similar to TEM, scanning transmission electron microscopy (STEM) is used to image materials with high spatial resolution [90]. In STEM mode, the electron beam is focused on the sample, as shown in 2.3b. The electron beam is converged to an atomic-sized probe by the condenser lenses in the upper part of the column. Strong excitement of the C1 lens results in a smaller probe size at the specimen. The angle at which the beam converges on the sample is denoted the convergence angle, α, and different convergence angles can be used for

different measurements. Momentum-resolved experiments, which are discussed in section 2.6, require smaller convergence angles than other imaging and spectroscopy measurements used in this work. The probe size, convergence angle and probe current are related and the choice of a small probe size increases the convergence angle for a given current [137]. Scan coils are used to scan the beam across the sample to build up images pixel by pixel. Two sets of scan coils are used defect the beam twice to ensure the beam is parallel to the optic axis upon reaching the specimen [80].

In conventional STEM transmitted electrons are collected by three types of STEM detector based on their scattering angle, resulting in different contrast between images from each detector due to the angular dependence of electron scattering discussed in section 1.3. Figure 2.6 depicts these three detectors, which each span a different annular range. The annular range of each detector is also dependent on the camera length, which refers to the effective projection distance from the sample to the detector as determined by the settings of the projector lens system. For the ARM microscope used in this work, the camera length was typically set to 6 cm and was reduced to 2 cm for EELS measurements. Values given for the annular ranges of detectors here are approximate and only give an indication of the actual angles subtended by the detectors.

The bright field (BF) detector, positioned at the bottom of the column, collects electrons scattered by small angles, up to approximately 30 mrad for a 6 cm camera length in the ARM. This BF annular range, β_{BF}, is usually chosen to match the convergence angle of the beam at the specimen so that image intensity is dominated by electrons that have undergone little scattering in the sample. In these images light elements and less dense material appear most intense as discussed in section 1.3 [80]. For the samples discussed, this results in the organic layers having the greatest intensity in BF images. An annular dark field detector (ADF) surrounds the BF detector and collects electrons with larger scattering angles, β_{ADF}. The inner radius of an ADF detector is often between 35 and 100 mrad and was calibrated as approximately 81 mrad at 8 cm and 107 mrad at 6 cm camera lengths in the ARM. The ADF outer radius is often between 100 and 200 mrad. In this range contrast arises from a combination of coherent Bragg diffraction and incoherent thermal diffuse scattering, producing a mixture of diffraction and mass-contrast. The relative contributions of these mechanisms depend on the inner detector angle, when it is greater than around 3 times the convergence angle, incoherent scattering becomes more significant [82]. The high angle annular (HAADF) detector collects electrons scattered by even larger angles, β_{HAADF}, and often spans an angular range that also collects above 200 mrad, with inner and outer radii approximately between 70-250 mrad. At these large scattering angles, the dominant contribution arises from thermal diffuse scattering, where electrons are incoherently scattered

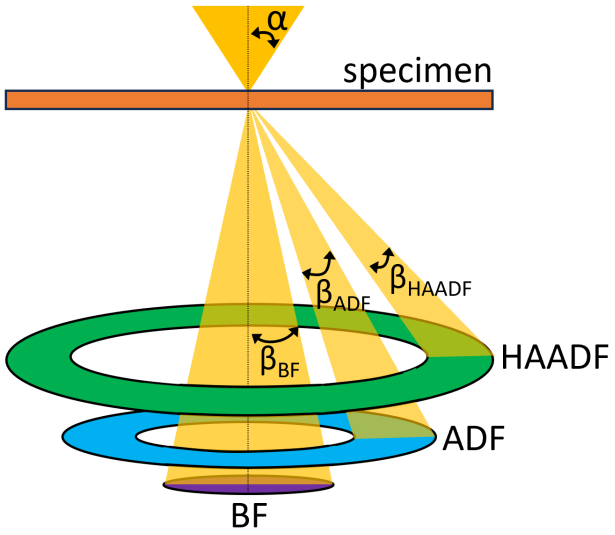

Fig. 2.6 Three STEM detectors collecting electrons scattered from the sample. The angular ranges of these detectors very between instruments and depend on convergence angle and camera length. The bright field (BF) detector typically collects electrons with scattering angles, β_{BF}, up to 35 mrad, the annular dark field (ADF) detector collects those scattered by, β_{ADF} =35/70 to 100/200 mrad and the high annular dark field (HAADF) detector collects electrons with scattering angles, β_{HAADF}, between 70 and 250 mrad. These values are approximate and intended only as a guide. For EELS measurements the BF detector is removed and electrons enter the EELS spectrometer.

by thermally vibrating atoms, as described in section 1.3.1, and not purely Rutherford scattering. The intensity is strongly localised to atomic columns and approximately scales with atomic number Z^n, where n is often close to 2. This gives contrast between light and heavy elements known as Z-contrast. Beam channelling along atomic columns in crystalline samples also contributes to contrast in HAADF images.

In addition to the schematic presented in figure 2.3b, some STEM microscopes make use of a monochromator to further reduce the energy spread of the electron beam. This is the case for SuperSTEM3, the instrument used to collect many of the momentum-resolved EELS measurements presented in chapter 4 and 6. The monochromator in SuperSTEM3 is termed an 'alpha-type' and can be understood as two back-to-back magnetic prisms with a slit in the middle [139, 138]. A simple schematic of this type of monochromator is presented in figure 2.7. The electron beam is removed from the column and passed through a magnetic prism that disperses electrons based on their energy. As they pass through a magnetic prism, electrons experience a Lorentz force from a perpendicular magnetic field and are deflected with the deflection angle dependent on the velocity of the electron given by equation 2.1.

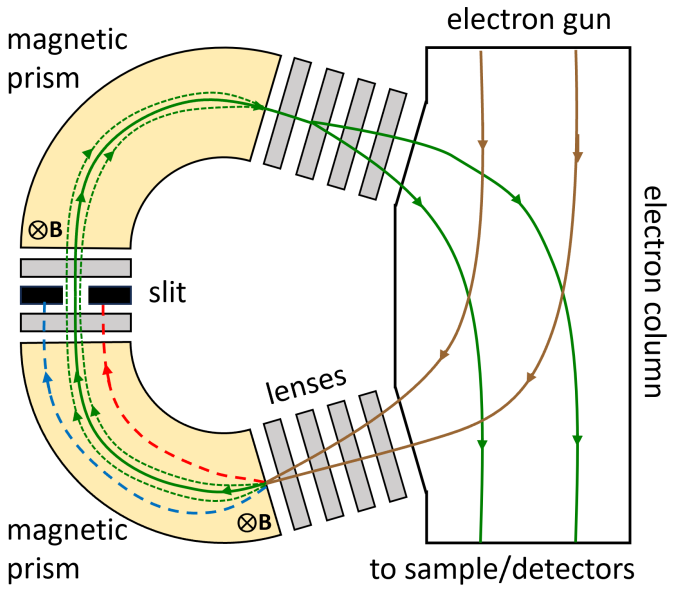

Fig. 2.7 Schematic of the 'alpha-type' monochromator in SuperSTEM3 [139]. Electrons travelling through the electron column are passed into the monochromator through a series of lenses. A magnetic prism then separates the path of electrons based on their energy by the Lorentz force. Electrons are then passed through an energy-selecting slit, which only allows a small subset of electrons with the specified energy to pass. A further magnetic prism recombines the electrons with desired energies and passes the beam back to the electron column.

Electrons with different energies travel at different velocities follow different paths through the prism based on their energy as shown in figure 2.7. The dispersed electrons are passed through a 'v-shaped' energy-selecting slit that is positioned so that only a small selection of electrons with similar energies to each other can pass. The spread of electron energies allowed to pass can be changed by moving the 'v-shaped' slit, changing the size of the slit, to balance the need for little energy spread in the beam with the amount of electron current desired. Next, the electron beam passes through the second spectrometer where it is combined and passed back into the main electron column [139].

The best energy spread obtained on SuperSTEM3 in this research was 7 meV but this type of monochromator has been demonstrated to produce beams with energy spreads of 5.7 meV at 60 kV [138]. The energy spread of the beam is primarily limited by beam diameter at the silt, which is determined by factors including source size and the diffraction limit. Future developments to monochromators to achieve even smaller energy spreads include improvements to aberration correction that could decrease the beam diameter at the slit without changing the beam current [138]. The requirement of sufficient current to image

a specimen limits further reduction of the energy spread of the beam since the number of electrons that can pass through the slit reduces with deceased energy spread. The energy resolution of an electron microscope is affected by the energy spread of the beam, beam stability and aberrations [138].

2.5 Electron energy loss spectroscopy (EELS)

Electron energy loss spectroscopy (EELS) is an analytical technique used with TEM and STEM. As electrons are transmitted through the sample some are scattered inelastically, resulting in characteristic losses in energy of the transmitted electrons [81]. The transmitted electrons are collected and the energy lost from scattering in the specimen can reveal information on chemical composition and plasmonic behaviour. In this thesis, this technique is carried out with STEM and the beam is scanned over the sample to make up a spectrum image (SI) with an EELS spectrum recorded at each beam position [140]. HAADF and ADF images are collected simultaneously for each beam position alongside the EELS spectrum.

As discussed in section 1.3, the differential cross-section describes the probability of an electron being scattered by a given atom when in the sample. In an inelastic scattering event, momentum is transferred from the incident electron to the sample resulting in both a change of energy and scattering angle [84]. The change in energy from inelastic scattering provides characteristic information about the sample.

The EELS spectrometer, sketched in figure 2.8, is positioned at the bottom of the column with its entrance aperture of an adequate size to maximise the amount of collected electrons, i.e. the collection angle is chosen to be greater than the beams' convergence angle at the sample [81]. Electrons which are collected by the BF detector in STEM are instead collected by the EELS spectrometer and those with higher scattering angles are still collected by ADF and HAADF detectors. EELS spectra presented in this thesis, collected on the ARM, make use of a 2 cm camera length, 29 mrad convergence semi-angle, 36 mrad collection semi-angle formed by a 2.5 mm aperture. After passing through the aperture into the EELS spectrometer, a magnetic prism separates the electrons based on their velocity via the Lorentz force. As the electron's velocity is determined by its energy, the amount of energy lost whilst travelling through the sample determines the electrons path. The 'alpha-type' monochromator described above can be considered as two back-to-back EELS spectrometers [139]. Several multipole optical elements are then used to magnify and focus the spectrum and minimise aberrations. The electrons are then collected by a CCD camera or direct electron detector to form an EELS spectrum.

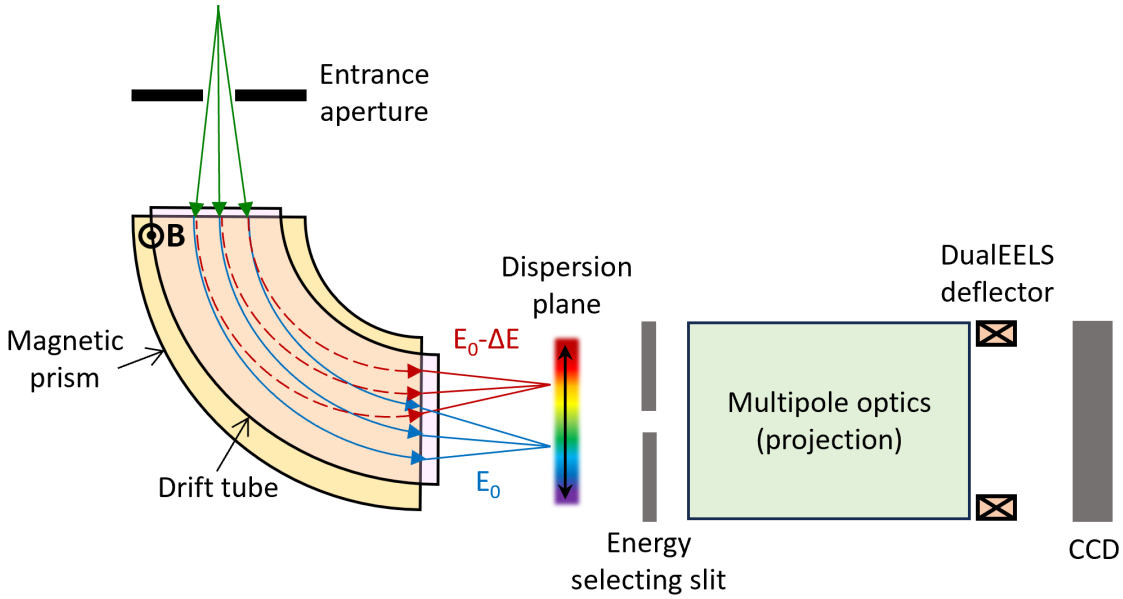

Fig. 2.8 Schematic of an EELS spectrometer. Electrons pass through an entrance aperture and are dispersed based on their energy by a magnetic prism in the drift tube. Electrons then pass through an energy selecting slit and multipole optics before being detected by a CCD detector. The dual EELS deflector positions the selected energy range onto the desired region of the detector.

The majority of transmitted electrons undergo very little or no inelastic scattering in the sample, resulting in a very intense peak at energy losses around zero, known as the zero-loss peak (ZLP), shown in figure 2.9a. The ZLP can quickly saturate the detector and, since other signals have much lower intensity, very little signal at relevant energies is obtained. This is known as dynamic range and can be a significant hindrance to EELS analysis. As the CCD detector has a limited number of channels, the range of energies of electrons that can be detected at a given time is also limited. To get around these limitations, 'Dual EELS' detection was developed to allow for collection of spectra over different energy ranges at the same time [141]. Two spectra with different exposure times and energy ranges are collected simultaneously onto separate regions of the detector. This is achieved using an electrostatic shutter called a fast beam switch, which blanks the beam between acquisition of spectra. A low energy EELS spectrum is recorded on the bottom section of the detector with a small exposure time to not saturate the detector. The beam is then blanked by the shutter and the spectrum deflected. An EELS spectrum at a higher energy range, with a longer exposure time, is then recorded after un-blanking the beam.

An EELS spectrum, shown schematically in figure 2.9, contains information on inelastic scattering processes described in section 1.3. The lower energy region from around 0-100

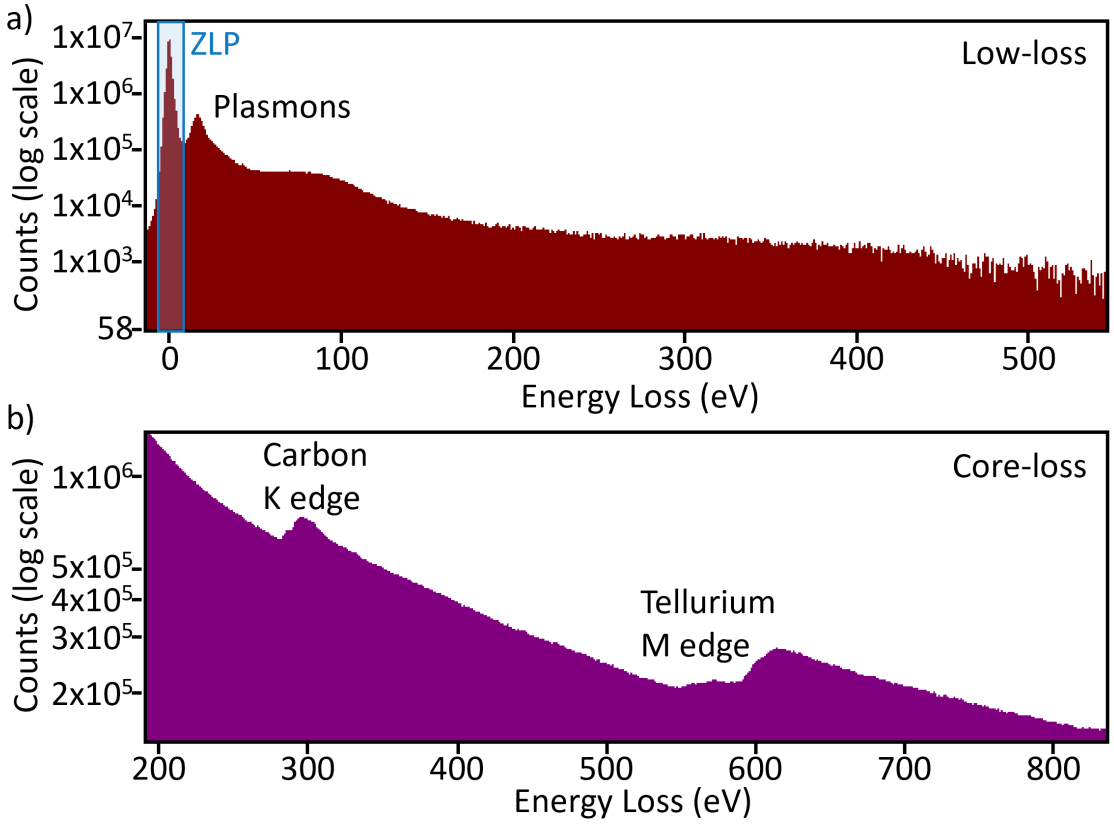

Fig. 2.9 Example of dual EELS spectra where a) low-loss data and b) core-loss data were acquired simultaneously for an sample of $BiSbTe_3$ with some carbon contamination. In a) the zero-loss peak can be observed as the most intense feature followed by a plasmon peak. In b) EELS edges can be observed for carbon and tellurium with a decaying background also present. Both EELS spectra are presented on a log scale for clarity.

eV, shown in figure 2.9a, contains scattering from inner and outer electrons, plasmons and phonons and is referred to as low-loss. This energy region is dominated by the zero loss peak (ZLP) which is due to the transmission of electrons that have only been scattered elastically, having lost no energy in the sample. When aligning the microscope, the width of the ZLP is minimised and its intensity is maximised to ensure the greatest amount of signal is collected with the greatest resolution. Plasmon excitations are the next most dominant feature in this energy region and can be used to determine the thickness of a sample using a calculation discussed further below. As the low-loss region contains the ZLP and thickness information it is always collected, requiring dual EELS to be used to collect higher energies. At higher energy losses the number of electrons counted decreases significantly, as seen in figure 2.9a, requiring longer exposure times to improve the signal to noise ratio. This makes dual EELS mode particularly useful as it allows for the low-loss region to be collected with a shorted

exposure time to prevent saturation from the higher intensity features whilst collecting a higher energy loss spectrum for longer.

At higher energies, an EELS spectrum contains scattering from inner (core) atomic electrons which can be used to provide chemical analysis of a sample. Figure 2.9b contains an EELS spectrum for an sample of $BiSbTe_3$, recorded at the same time as the low loss spectrum in panel a. This core-loss spectrum can be used to map elements throughout a sample and can provide information on composition, oxidation states and bonding. The carbon K edge can be observed starting at 285 eV and the tellurium M edge at 583 eV, along with a decaying background.

During imaging and collection of EELS data the structure or chemistry of a specimen can be damaged by the electron beam [142, 143]. This damage can occur from the breaking of chemical bonds due to inelastic scattering, displacement of atoms from the crystal lattice and specimen heating from excitement of phonons [81]. Radiolysis occurs due to inelastic scattering within a sample and can be reduced by cooling the sample during imaging [144]. Knock-on damage describes the displacement of atoms within a sample due to elastic scattering and can be reduced by reduction of the operating voltage. For samples discussed in this thesis, primarily organic layers, knock-on damage can be a significant problem. The threshold energy for knock-on damage in single layer graphene has been shown to be approximately 85 kV [145], therefore an operating voltage of 60 or 80 kV instead of 200 kV has been used for the majority of measurements presented here.

2.5.1 Low-Loss EELS

At low energies of below 100 eV, an EELS spectrum primarily contains plasmonic losses, interband transitions and bandgaps. As described in section 1.4, the interaction between the electric field of an incident electron beam and electrons in the sample results in the generation of plasmons, which are oscillations of the materials' electrons that propagate through the sample. These plasmons occur at characteristic energies and are influenced by interface and shape effects.

While plasmonic losses dominate many materials in this energy range, discrete electronic transitions can also be excited. In molecules, molecular orbitals are close in energy to each other and electrons within molecular orbitals can be excited by the incident beam. Single electron transitions between energy levels close to the highest occupied molecular orbital (HOMO) and lowest unoccupied molecular orbital (LUMO) can be seen in low-loss EELS spectra. Outer shell atomic electrons can be excited by the electron beam into empty states and can be observed by EELS. The energies of these transitions can be influenced by bonding.

Another key feature in this energy range is the presence of bandgap excitations. Bandgaps between the valence and conduction bands of a solid are observed in EELS spectra as an abrupt increase in EELS intensity at the bandgap energy for direct bandgaps. For many materials, the energies of their bandgaps are very small, such as Bi_2Se_3 at 0.3 eV, and can not be observed in the energy ranges of EELS discussed in chapters 4 and 5. In insulators such as Al_2O_3 and SiO_2, used as substrates for samples in this research, the bandgap can be clearly observed in low-loss EELS spectra between 8 and 10 eV. They appear as a step edge in the spectrum and will be discussed in more detail in chapter 4.

At even lower energy losses, typically less than 300 meV, phonon excitations can also be resolved in EELS. These phonon modes arise from lattice vibrations as well as bond vibrations in molecules. In this energy range, both phonon modes and low energy plasmons are excited.

In addition to probing electronic and vibrational excitations, sample thickness can be determined from low-loss EELS data. This is achieved by comparing the integrated intensity of the ZLP, I_{ZLP}, to the total integrated intensity of the spectrum, I_{tot}, using

$$t = \lambda_i ln\left(\frac{I_{tot}}{I_{ZLP}}\right), \tag{2.2}$$

where λ_i is the inelastic mean free path. This equation is derived from Poisson statistics by considering inelastic scattering as independent events that obey Poisson statistics [81]. The intensity at the ZLP is maximum when all signal is transmitted without scattering i.e. thickness is zero, and reduces exponentially with increasing thickness. For the specimen studied throughout this thesis, the inelastic mean free path was approximated at 200 kV and 60 kV. At 200 kV the inelastic mean free paths for Al_2O_3, SiO_2 and amorphous carbon (aC) are 140, 155 and 160 nm respectively. At lower accelerating voltages the inelastic mean free paths are reduced, with λ_i of approximately 57, 63 and 65 nm for Al_2O_3, SiO_2 and aC at 60 kV. For Bi_2Se_3, λ_i is estimated as 125 nm at 200 kV and 51 nm at 60 kV. For organic overlayers such as C_{60} and phthalocyanines, λ_i is expected to be slightly greater than aC due to the lower density.

There are several key advantages to using EELS to investigate plasmon and phonon modes as opposed to optical methods. The high spatial resolution possible when performing EELS spectrum imaging allows for the localisation of features to be observed, which can make it easy to distinguish bulk and surface plasmon modes. By mapping the localisation of peaks, the effects of structural defects and interface on the plasmon and phonon behaviour can be determined from EELS spectra.

2.5.2 Core-Loss EELS

At higher energy losses, core transitions are observed in EELS spectra and can be used for elemental quantification. Upon interaction with the core-electrons of an atom, an incident electron can transfer energy to a core-electron, exciting it to a higher energy level. For example, a core-electron within the K shell of a carbon atom can be excited to a higher level by receiving 284 eV of energy from an incident electron. In the core-loss spectrum in figure 2.9, a sharp peak can be observed at this energy followed by a collection of subsequent peaks and is known as the carbon K edge. After subtracting background signal, this edge provides quantitative information on the amount of carbon in this particular region of the sample. For each element present, a core-loss edge peak can be identified at different energies allowing for a clear identification of different elements. Some edge peaks are sharp and distinct such as carbon but others can be more difficult to observe and can overlap with those of other elements. For example, oxygen and antimony edges are close in energy, at 532 and 528 eV respectively, but can be distinguished by their peak shapes for qualitative analysis.

Quantitative analysis can be achieved by comparison of the integrated intensity of a core-loss edge, after removal of background and multiple scattering effects, to calculated inelastic scattering cross-sections [81]. The cross-sections are often derived using atomic models such as the Hartree-Slater model [146]. Elemental maps acquired from core-loss EELS data provide spatial information on the location of elements present. These will be used throughout this thesis to determine locations of dopant elements and diffusion of atoms between layers.

As well as information on the location and quantities of different elements, changes in their bonding can also be observed. The energy-loss near edge-structure (ELNES) can provide further information, which is useful in fingerprinting a material. The structure near an edge represents the local density of states above the Fermi energy and indicates the final state of an excited electron. This structure can change depending on the coordination of an atom [81]. For example, differences in the ELNES structure of the Mn L edge indicate changes in oxidation state [147] and differences in the C K edge can indicate the ratio of sp^2 and sp^3 hybridised carbon atoms [148].

The ELNES structure was considered for C_{60} and CuPc samples discussed in chapter 5, where the difference in the carbon K edge could be used to distinguish between the two materials and act as an indicator of damage. The carbon EELS edge has two main features: an initial sharp spike starting at around 284 eV and a broad feature starting at 290 eV. The initial peak (pre-edge feature) is from sp^2 hybridised carbon and differs slightly in energy and shape depending on the form of carbon present [148]. The ratio of the sp^2 peak to the broad feature (σ^*) is indicative of the ratio of double to single bonded carbon atoms

present. Therefore, changes in this ratio after electron beam imaging can indicate damage to the organic material [149]. The reduction in the pre-edge feature was observed to occur much faster in phthalocyanine samples compared to C_{60} samples and was evident by the end of EELS scans over the layer at 200 kV. Therefore subsequent data was obtained at lower accelerating voltages such as 60 or 80 kV to prevent this damage. By reducing the energy of incident electrons, knock-on damage due to elastic scattering is reduced.

Other damage processes, such as radiolysis, depend on the amount of energy deposited per unit volume of specimen, so limiting the electron-dose is also important [144]. This can be minimised by limiting measurement time and performing successive measurements in different areas of a sample. At an accelerating voltage of 80 kV, the ELNES structure was not observed to change during SI acquisition, indicating that the electron-dose was not high enough to substantially damage the chemical structure.

In cases where EELS edges are far apart in energy and cannot be collected simultaneously, energy dispersive x-ray spectroscopy (EDS) can be performed simultaneously and used to supplement the data. After a core-electron is excited to a higher energy level by an incident electron it will will relax back to its original state and release a photon with the energy of the transition. These photons are in the x-ray energy range and can be collected by an EDS detector positioned above the sample in the TEM. The x-rays have characteristic energy of the energy level transition they were emitted from, which is unique for different elements and can indicate how much of an element is present [80]. EDS can be performed in SEM and (S)TEM configurations with the detector positioned above the sample in both cases. SEM EDS was performed to supplement data in section 5.2.

2.6 Momentum resolved electron energy loss spectroscopy

2.6.1 Momentum-resolution in EELS

Upon incidence with a specimen incident electrons are inelastically scattered and a transfer of both energy and momentum occur, as described in section 1.3.2 and indicated in figure 2.10. An incident electron with momentum $\mathbf{k}_0$ passing through a specimen undergoes inelastic scattering events and is transmitted with a momentum of $\mathbf{k}_1$. The electron has been scattered by an angle, θ, and undergone a momentum change of $\mathbf{q}$. The scattering angle is related to the momentum transferred in the scattering event by

$$\mathbf{q}(\theta) = 4\pi \sin(\theta/2)/\lambda, \tag{2.3}$$

where λ is the electron wavelength [150].

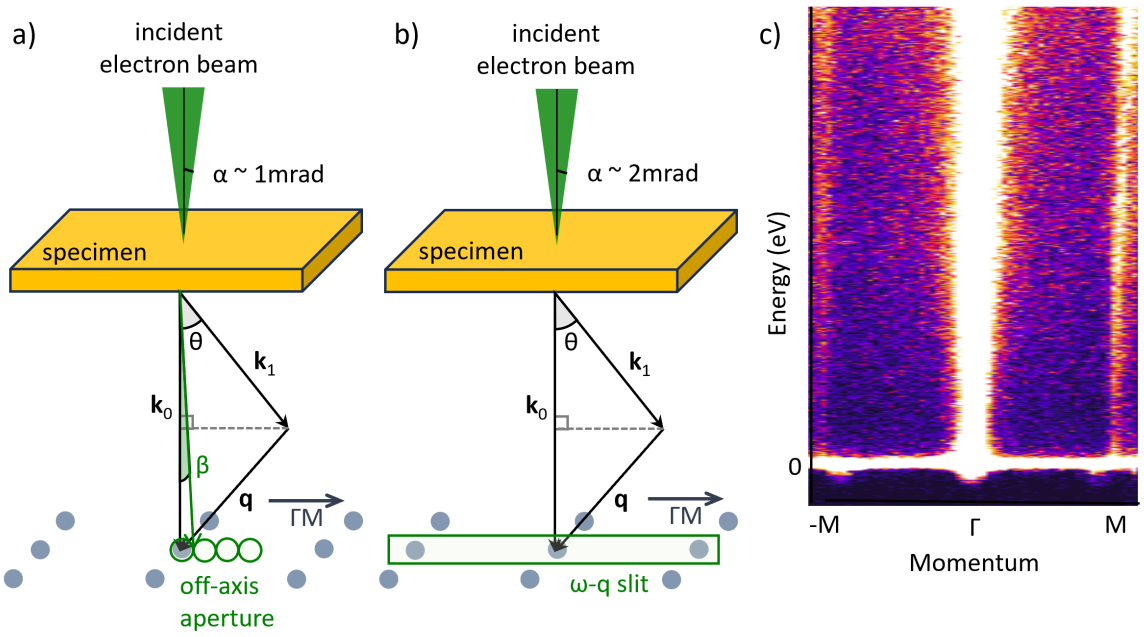

Fig. 2.10 Schematics of momentum-resolved EELS techniques where an electron beam is transmitted through a specimen and scattered by an angle, θ, which relates to the momentum transferred from the specimen lattice. EELS spectra are recorded using a circular or slit aperture. a) Off-axis acquisition using a convergence semi-angle, α, of 1 mrad and a circular aperture, which is moved off-axis to collect data. The collection semiangle, β, is dependent on the relative size of the aperture at the diffraction plane. b)'$\omega - q$' slit acquisition using a convergence semi-angle, α, of 2 mrad and a rectangular slit aperture to collect 2D EELS spectra. c) Example of an EELS dataset collected using the '$\omega - q$' slit method where a plot of momentum vs energy is obtained along a selected momentum direction.

When performing EELS experiments using the method outlined in section 2.5, we are only interested in the energy of scattered electrons and sum electrons over a large range of scattering angles. To obtain both the energy loss and momentum transferred from the specimen, two different momentum-resolved techniques are commonly applied and used throughout this thesis. These methods will be expanded upon in section 2.6.2 and 2.6.3.

The first method makes use of a standard circular EELS aperture, which is set up such that it only collects a small range of scattering angles [150–152]. In this configuration, data is acquired by offsetting the aperture in momentum with respect to the central Bragg position as shown in figure 2.10a. The relative offset from the optic axis is achieved by projection shifts, which shift the diffraction pattern relative to the aperture. Each qEELS spectrum is recorded separately after shifting the projection along the desired momentum direction of the sample.

The second method requires an '$\omega - q$' slit which refers to a rectangular EELS aperture aligned perpendicular to the dispersion plane. This allows for the collection of a 2D spectrum with energy and momentum in the x and y axes as shown in figure 2.10b [153, 101]. This method requires careful alignment of the orientation of the same to ensure the momentum direction aligns with the desired direction along the Brillouin zone of the sample. In chapter 6 this method is utilised to map the dispersion of plasmon modes.

2.6.2 Off-axis acquisition

A schematic of the off-axis acquisition method is shown in figure 2.10a, where the relative angular range subtended by the aperture, known as the collection semi-angle, β, is small compared to the separation of diffraction spots [150, 152]. This is achieved with a combination of increased camera length, smaller aperture and smaller convergence angle. Using a smaller convergence semi-angle decreases the radius of diffraction spots which increases the space between them, allowing for the aperture to only cover a small region of the Brillouin zone in reciprocal space, as shown in figure 2.10a. Additionally, the camera length is increased which decreases the collection angle compared to the diffraction pattern, resulting in higher momentum resolution.

The radius of the unscattered beam without an aperture, known as the bright field disc, in momentum space is calculated using $\theta = \alpha$ in equation 2.3, where θ is the scattering angle and α is the convergence semi-angle of the beam at the sample as indicated in figure 2.10a. From the collection semi-angle, β, the momentum range over which an EELS spectrum is collected can be found by letting $\theta = \beta$ in equation 2.3. The momentum resolution can then be found from equation 2.3 by setting $\theta = \sqrt{\alpha^2 + \beta^2}$. The resolution is determined by the relative size of the EELS aperture and diffraction pattern which results from both the collection and convergence semi-angles.

After acquisition of a spectrum at the central Bragg position, where momentum transfer is zero, the diffraction pattern was displaced along a direction in momentum space with respect to the aperture position [151]. This was achieved by adjusting projector lens values and could be carried out in any momentum direction in plane with the sample. At each position, the aperture was offset relative to the central Bragg position and an EELS spectrum was acquired. A high symmetry momentum direction was selected from the diffraction pattern and spectra were acquired at several positions along the Brillouin zone to map the dispersion of peaks within the spectra [154]. As the diffraction pattern could be displaced in any direction, a selection of different symmetry points and momentum directions could be investigated without the requirement to rotate the sample. Momentum-resolved EELS data

in chapter 4 was collected by displacing the aperture relative to the ΓM direction as indicated in figure 2.10a.

The momentum of qEELS spectra at each aperture position was calibrated using a diffraction pattern of the sample acquired during the experiments. The size and position of the EELS aperture relative to the diffraction pattern were found for each aperture position and converted into momentum using the known values from the diffraction pattern and equation 2.3. Fitted peak energies in each qEELS spectrum were then used to map the dispersion of modes with energy and determine dispersion relations.

The off-axis acquisition approach requires separate EELS datasets to be recorded at each EELS aperture position, which can be time consuming, limiting the number of datasets that can be recorded in a given time frame. Additionally, only a small number of data points can be achieved between Bragg spots along the selected momentum direction due to the size of the aperture and overlapping positions must be used to maximise the number of data points. With few data points, it can be difficult to map the dispersion of modes. For this reason, the '$\omega - q$' slit method can be used, however, this is not always available and qEELS data presented in chapter 4 makes use of the 'off-axis' method for this reason.

2.6.3 ω-q slit acquisition

At the entrance to the EELS spectrometer, a rectangular aperture can be used, instead of a circular one, to achieve momentum-resolved data [153]. This rectangular aperture, referred to as an '$\omega - q$' slit throughout this thesis, is used to collect a 2D dataset with energy and momentum axes [91, 101, 155–157]. Figure 2.10b shows a schematic of the '$\omega - q$' slit acquisition method as implemented at SuperSTEM. The slit is perpendicular to the dispersion plane of the spectrometer and the sample is aligned with a high symmetry momentum axis along the direction of the slit. This results in a spectrum being acquired at each position along the length of the slit.

Similar to the off-axis acquisition method, the beam is converged on the sample with a small convergence semi-angle, α, which, in the data presented in chapter 5, was 2 mrad. This convergence angle is selected so that the beam is slightly smaller than the slit to prevent scattering from the slit. Transmitted electrons with varied momentum pass through the slit into the spectrometer and are collected by a direct electron detector as a 2D image, as shown in figure 2.10c. The sample is positioned such that the desired high symmetry axis is in line with the slit indicated in figure 2.10b. The sample orientation determines the momentum direction which can be recorded, therefore, positioning the sample with the correct rotation is especially important. The orientation of the sample could be slightly adjusted by excitation of projector lenses but this was limited to small rotation angles since changes to these lenses

results in both rotation and magnification of the diffraction plane. To investigate plasmon dispersion across interfaces, the beam can be scanned across the sample and a 2D EELS dataset acquired at each position to build up a spectrum image.

An example 2D EELS dataset acquired using this method is presented in figure 2.10c with momentum vs. energy axes. The Γ point at the centre of the spectrum is defined as zero momentum transfer and contains the highest intensity. Other diffraction spots along the selected axis can be seen with the most intensity at 0 eV. The distance between the diffraction spots is known for the crystal and can be used to calibrate the momentum axis. Using this method it is possible to achieve more data points within the first Brillouin zone of Bi_2Se_3, which is a significant improvement on the number of off axis data points obtained using the off-axis approach in chapter 4. This technique, however, is more challenging to use due to the availability of an '$\omega - q$' slit as well as additional challenges in alignment.

2.7 EELS data analysis

2.7.1 EELS data processing

Most EELS datasets were acquired by the spectrum imaging methodology described in section 2.5. A selected region was scanned over and at each pixel several different signals were acquired to build up an image of the sample as well as collect spectroscopic information. Signals from the HAADF and ADF STEM detectors were acquired as well as low-loss EELS, core-loss EELS and EDX data as required.

For some qEELS data, larger datasets were acquired from the use of the '$\omega - q$' slit described in section 2.6.3. At each pixel, a HAADF signal was collected alongside 2D qEELS data. Due to the short exposure time required to avoid saturating the detector from the intense ZLP, datasets were collected at each pixel 50-5000 times to collect enough EELS signal. Each 2D qEELS dataset was first aligned in energy using a python script to align the energies of the ZLP in each EELS spectrum along q. Frames collected in the same position of the sample were then summed together to improve the signal to noise ratio and ensure there was enough signal in regions away from the Bragg spots.

Spectrum images were processed by first normalising the data with respect to the integrated intensity of the ZLP to remove some effects resulting from thickness variations throughout the sample. Low-loss data was then deconvolved using a Fourier-log deconvolution technique, which will be discussed in more detail in section 3.2. This deconvolution was used to remove effects due to electrons undergoing multiple scattering events whilst travelling through the specimen and recover a single-scattering EELS spectrum [81]. For core-loss

EELS data, a similar deconvolution method was used known as Fourier-ratio deconvolution. This method uses the ZLP recorded in the low-loss data collected at the same time as the core-loss data, to remove multiple-scattering effects.

At ultra-low energies, peaks can be difficult to observe close to the ZLP, which can be especially difficult at momenta far from any Bragg spots. To increase visibility of some low-energy peaks observed close to other peaks, that data was scaled by the square of energy loss (IxE^2). This allowed for small peaks observed in the data to be easier to fit.

2.7.2 Fitting of low-loss data

Analysis of low-loss EELS data was carried out using 'Digital Micrograph' and 'Hyperspy' software. Firstly, the ZLP was aligned to 0 eV across the full spectrum image to adjust any drifts throughout the image acquisition. Spectra were then deconvolved using Fourier-log decomposition techniques, which will be discussed in section 3.2, to remove multiple scattering effects. In particularly noisy datasets, spectra were de-noised using multivariate statistical analysis [158].

Most low-loss features including phonon excitation, plasmon excitation and interband transitions appear as discrete peaks on a power-law background and it is common to fit them as a series of isolated or overlapping broadened Lorentzian peaks. The energy, width and strength of each peak can indicate the type of excitation and be used to understand its characteristics. Processed EELS spectra were fitted with a series of pseudo-Voigt, Gaussian and step functions depending on expected peaks [90]. Least-squares fitting algorithms were used for this in 'Hyperspy' [159]. Spectra were compared with references and calculations to aid in interpretation of fitted peaks. Spectrum images were used to map peak energies across samples. For some low-loss spectra, especially at ultra-low energies, deconvolution was not performed. Instead, the tail of the ZLP was removed by fitting with a power-law function [160].

Throughout this thesis, several functions were used to fit features in low-loss EELS data including Gaussian, Lorentzian and pseudo-Voigt functions. An interband transition has an energy defined by the energy difference between bands but is not infinitely sharp due to relaxation processes occurring. Transitions have a finite lifetime which homogeneously broadens the peak shape and can be described by a Lorentzian function [161]. Similarly plasmons can also be described by a Lorentzian peak shape as they act as collective damped oscillators with a characteristic lifetime. The width of the Lorentzian peak can provide information on plasmon damping [84]. Inhomogeneous broadening resulting from non-uniform structure and instrumental broadening can be accounted for using a Gaussian function or pseudo-Voigt function. Each peak accounts for three fitting parameters, describing its

energy, amplitude and width. Some parameters were fixed (e.g. the relative amplitudes of C_{60} interband transitions and bandgap energy) and others were constrained such as peak energy, x_0. The equation for each function used is presented here. The Gaussian function is used to describe inhomogeneous broadening in spectroscopy that occurs due to atoms or molecules experiencing a statistical distribution of different environments [161]. This function is from statistics and is described by

$$f(x) = \frac{A}{\sigma\sqrt{2\pi}} \exp\left[-\frac{(x-x_0)^2}{2\sigma^2}\right], \tag{2.4}$$

where x_0 is the peak position, A is the amplitude of the function and $2\sigma\sqrt{2\ln 2}$ is the full-width at half-maximum (FWHM) of the peak.

The Lorentzian function describes the homogeneous broadening of a spectral feature resulting from finite lifetimes associated with relaxation processes and damping. This function has the form

$$f(x) = \frac{A}{\pi}\left[\frac{\gamma}{(x-x_0)^2+\gamma^2}\right] \tag{2.5}$$

where x_0 is the peak position, A is the amplitude of the function and 2γ is the FWHM of the peak.

Pseudo-Voigt functions can be used to fit plasmon modes and interband transitions in low-loss EELS spectra to account for intrinsic Lorentzian broadening, intrinsic and instrumental Gaussian broadening [97]. Instrumental broadening is described by a Gaussian function because it arises from the sum of many small random uncertainties in energy measurements, such as the spread of electron energy and the detector response. This function is a convolution of Gaussian and Lorentzian functions and can be described by the equation

$$f(x) = A\Re\{\omega[z(x-x_0)]\} \tag{2.6}$$

where A is the function area and $\Re$ is the the real part of ω. $\omega(z)$ and $z(x)$ are defined by

$$\omega(z) = e^{-z^2}\mathrm{erfc}(-iz) \qquad \text{and} \qquad z(x) = \frac{x+i\gamma}{\sqrt{2}\sigma}, \tag{2.7}$$

where x_0 is the centre peak position and A is the function area. The complementary error function, erfc, is defined by

$$\mathrm{erfc}(z) = \frac{2}{\sqrt{\pi}}\int_z^\infty e^{-t^2}dt. \tag{2.8}$$

The FWHM of the Gaussian function is $2\sigma\sqrt{2\ln 2}$ and the FWHM of the Lorentzian function is 2γ.

Step edges are characteristic of a bandgap which, for the insulating substrates used for this research, is in the low-loss energy range considered in this thesis. As the bandgap edge arises from the excitation of electrons to the conduction band, the shape is partially determined by the Fermi-Dirac distribution, with the form of a logistic function. These can be fitted using a logistic function with equation

$$f(x) = \frac{A}{1+\exp\left[-c\left(x-x_0\right)\right]} \tag{2.9}$$

where A is the maximum value, x_0 is the centre of the step and c is the steepness of the slope [159]. Although there are several functions which could be used to fit a step-edge, the logistic function has few parameters, which reduces uncertainty in the fit and can model both the energy and slope of the feature.

The combination of these functions was used to fit each low-loss EELS spectrum. For spectra with several overlapping peaks, fitting was first performed with fewer peaks and the residuals were assessed to determine any requirement for additional peaks to be added to the fit. Fitting was then repeated using the number of peaks indicated by the residuals to obtain a well fitted spectrum. Fitted peaks were then compared with literature to interpret fitted peaks.

2.8 Conclusion

The methods and techniques outlined in this chapter form the basis of the research presented in this thesis. All thin film samples with TI/organic interfaces were prepared for TEM using FIB techniques as described in section 2.2 and investigated in each results chapter. Samples discussed in chapter 5 were prepared using the optimised cryogenic thinning method in section 2.2.4. Sample quality and crystalline structure were assessed using TEM and STEM methods as described in section 2.3 and 2.4.

Key results presented in this thesis make use of EELS, as described in section 2.5. Simulated EELS spectra are presented in chapter 3 for a variety of thin film and nanoparticle systems and aid in the understanding of experimental EELS results in chapters 4 and 5. Plasmonic behaviour at different TI/organic interfaces is investigated using low-loss EELS in chapters 4 and 5. Plasmon dispersion of bulk and interfacial plasmons are investigated by qEELS with the off-axis method utilised in chapter 4 and the '$\omega - q$' slit used in chapter 5. Low energy plasmons and phonon modes are identified and their momentum dispersion discussed using qEELS in chapter 6.

The combination of these techniques provides a detailed understanding of the structure, chemical composition and plasmonic behaviour of specimen discussed in this thesis and allows for modification of topological insulator surface plasmons to be observed.

3 Plasmon EELS Simulations

3.1 Introduction

Electron energy loss spectroscopy (EELS) is a useful tool for the study of plasmons in nanoscale materials [81, 162]. As discussed in section 2.5, an EELS spectrum is composed of many different scattering events which can have similar energies and overlapping peaks. Therefore, to identify each feature and process, the spectrum must be decomposed. Simulations can be a useful tool in this decomposition, providing expected peak energies and shapes for different processes occurring in the sample, aiding in analysis.

As an electron beam passes through a specimen, scattering occurs within the material and free electrons within the specimen are excited. The impinging electron beam experiences repulsion from electrons acting as a retarding force causing it to lose energy and decelerate. EELS can be described by the loss probability as an electron passes through a material and can be derived from Maxwell's equations using classical dielectric theory [163]. The loss probability is dependent on the force exerted by an induced electric field acting back on the electron, therefore by simulating this induced electric field, the loss probability can be calculated.

Several different methodologies have been developed to simulate low-loss EELS spectra using classical dielectric theory [164, 165]. Analytical calculations make use of the complex dielectric function to calculate the loss probability as a summation of bulk and coupled surface effects using a non-retarded approximation. This approach has been used to investigate thin films and plasmon coupling at metal-dielectric interfaces [166, 167]. This method is effective in calculating EELS spectra across interfaces in approximately infinite thin films and has been demonstrated to replicate the plasmonic behaviour in experimental systems [166]. However, for more complex systems, such as nanoparticles that host shape-dependent localised surface plasmon resonances (LSPR), a more robust 3D simulation is required.

Complex 3D systems can be simulated by solving Maxwell's equations numerically to obtain EELS spectra [168–170]. Two common ways of doing this are boundary element methods (BEM) [171] and finite element (FE) methods, both of which discretize a 3D model and solve each discrete region numerically. Boundary element methods have been used extensively to simulate EELS spectra of various nanoparticle systems, which vary in complexity from nanospheres and nanocubes [172] to coupled nanoparticle systems [173]. 'MNPBEM' software is a common simulation software which uses BEM to calculated EELS specta [171]. Simulations of LSPR carried out in MNPBEM for a variety of systems have been shown to be reliable and efficient [174]. Substrate effects have been included in simulations using a dielectric constant [175]. With boundary element simulations, the electric field is simulated at the boundaries of nanoparticles, which is well suited to the study of excitations on the surface of nanoparticles but does not provide information on variations within a volume.

Finite element methods have been used to simulate EELS spectra, with an increasing number of groups using commercial software 'COMSOL Multiphysics' to do so. The use of COMSOL to model EELS spectra and plasmonic behaviour is advantageous due to the wide functionality of the software that would provide the ability to couple these simulations with other physics such as heat flow. Additionally, the graphical user interface allows for simulations to be carried out without programming experience. Perhaps the first groups to implement EELS simulations in COMSOL were Koh *et al.* at Imperial College London and A*STAR, Singapore, who showed coupling between gold nanoprisms and identified edge and corner plasmon modes [176, 177]. Simulated electric field intensity maps were compared with experimental data and displayed localisation of edge and corner modes in agreement with the experiment. The coupling in gold bowtie nanoprisms has been further studied with the aid of COMSOL to engineer localised surface plasmon modes [178].

Since then, EELS spectra for a variety of different nanoparticle systems have been modelled including gold nanorods [179, 180], gold nanodiscs and apertures [181] and aluminium nanodiscs [182]. Additionally, increasingly complex geometries have been modelled such as gold nanogrooves filled with SiO_2, replicating shifts in surface plasmon resonance energy towards the bottom of the grooves [183]. Gap surface plasmons have been studied for different shapes of slot in silver films [184] and layered metal/dielectric hyperbolic metamaterial films using COMSOL [185]. Modelled spectra of silicon nanoparticles of gold thin films indicate coupling between gold SPP modes and plasmon resonances in the silicon nanoparticles [186]. More recently, COMSOL simulations have been implemented for the study of plasmons in nanocube dimers [187], photonic modes in CeO_2 nanocubes [188] and coupled polaritons in gold rods on SiO_2 substrates [189]. EELS spectra of WS_2 nanodiscs

have been modelled to understand how the electron beam position effects excitation of various modes [190]. COMSOL simulations were used to identify highly localised surface plasmons due to inhomogeneous doping in La-doped $BaSnO_3$ nanocrystals [191].

In addition to nanoparticles, thin films and slabs have been simulated using COMSOL for several different systems. Konečná *et al.* simulated interfacial EELS spectra over an Si/SiO_2 interface and showed the dependence of the SiO_2 optical phonon polariton on position of the electron beam [167]. Similar systems were studied by Egerton *et al.* who investigated the dependence of the distance of an electron beam to an interface in aloof mode on the vibrational spectrum of thin SiO_2 slabs [192]. Egerton *et al.* also investigated the thickness dependency of vibrational modes in a variety of thin films including hexagonal boron nitride flakes with aid of COMSOL simulations [193]. Other studies into hexagonal boron nitride have been published using COMSOL simulations to investigate phonon polaritons [194, 195].

The aim of this chapter is to provide an overview of two methods of simulating EELS spectra and discuss the merits of both. The use of FEM in COMSOL will be explored for a variety of systems including metallic nanoparticles and thin films to demonstrate the effectiveness of this simulation method and versatility to a wide array of systems. Finally, new COMSOL simulations of a Bi_2Se_3/C_{60} thin film are carried out, applying the method and simulating the spectrum. Example structures will be simulated, including nanoparticles to illustrate the effectiveness of these simulations. Then this will be applied to the systems used within this thesis.

This chapter will discuss two methods for the calculation of low-loss EELS spectra for thin films and nanoparticles. Analytical calculations in python and numerical simulations in COMSOL. Thin film systems are calculated analytically in Python using a relativistic approach for comparison with experimental EELS data. Interfacial EELS spectra are compared with experimental results to highlight features in the interface spectrum which cannot be explained by plasmon coupling across the interface. Numerical EELS simulations in COMSOL, in the energy range 1 to 25 eV, are discussed with additions to account for thin film interfaces and complex nanoparticles. Simulated EELS spectra are compared with both experimental results and analytical calculations to confirm their accuracy. Simulated EELS for silver nanoparticles of different shapes indicate the energy and localisation of different LSPRs in good agreement with literature results. These confirm the ability to simulate EELS for a large variety of systems with the possibility to extend to a wide array of new and exciting systems. A thin film of Al/Mg_2S was used as an example interface and showed the localisation of a surface plasmon to the interface. Finally, a Bi_2Se_3/C_{60} thin film interface was simulated using COMSOL to use as a reference for experimental work in later chapters. Discrepancies between the simulated spectra and experimental results point to localised

interface states not captured by plasmon coupling across the interface. These indicate the utility of EELS simulations to rule out some interfacial effects and point to more interesting interface effects.

3.2 Bulk Dielectric functions

A material's response to electromagnetic fields can be described by its dielectric function, which contains information on excitations within the material due to the applied electromagnetic field. When an electron beam is incident on a specimen, its electromagnetic field interacts with the material and it experiences the electromagnetic field from the specimen. Excitations in the material due to the electromagnetic field, including electron energy level transitions, plasmons and phonons, contribute to the dielectric function.

At very low energies, from meV to 4 eV, the dielectric function can be readily obtained from optical measurements such as ellipsometry. However, the energies of many plasmon resonances are greater than these optical techniques can measure, therefore, to access the energy range of interest of materials in this thesis, 1 to 30 eV, other techniques are required. EELS can be used to determine the dielectric function in these higher energy regions with limitations at lower energy due to the zero-loss peak (ZLP) [81]. As the ZLP is the most intense feature of an EELS spectrum, peaks from processes that occur at low energies close to the ZLP cannot be resolved.

3.2.1 Deconvolution

To calculate the complex dielectric function, $\varepsilon(E)$, from an experimental EELS spectrum, the single scattering spectrum, $S(E)$, must first be obtained. An EELS spectrum, as recorded, contains the effects of transmitted electrons scattering more than once while in the sample, known as multiple-scattering. This multiple-scattering is not taken into account in calculating the dielectric function as it can vary substantially with thickness , so must be removed first. The experimental spectrum is a convolution of the single scattering spectrum with double scattering, $D(E)$, triple scattering, $T(E)$, etc. components which are described by

$$D(E) = S(E) \otimes S(E)/(2!I_0^2), \tag{3.1}$$

$$T(E) = S(E) \otimes S(E) \otimes S(E)/(3!I_0^3)\ etc., \tag{3.2}$$

where I_0 is the initial intensity [81]. Deconvolution is required to remove multiple scattering and obtain the single scattering spectrum required for further calculations. A common

method of this, used in processing of all low-loss data presented in this thesis, is Fourier-log deconvolution [196, 81].

In practice, the recorded EELS spectrum is a convolution of the multiple scattering spectrum and an energy-dependent function which describes instrumental broadening, $R(E)$, given by

$$J(E) = R(E) \otimes [I_0\delta(E) + S(E) + D(E) + T(E) + ...], \tag{3.3}$$

where $\delta(E)$ denotes a unit area delta function. The ZLP, $Z(E)$, contains information on instrumental broadening and the initial intensity and can be expressed as $Z(E) = I_0R(E)$ such that equation 3.3 becomes

$$J(E) = Z(E) \otimes [\delta(E) + S(E)/I_0 + D(E) + T(E) + ...]. \tag{3.4}$$

Instrumental broadening can be accounted for and reduced by deconvolution as well as the removal of multiple-scattering effects. The Fourier-log deconvolution process, as applied in 'Digital Micrograph' software, makes use of Fourier transform techniques to obtain a single scattering spectrum.

The Fourier transform of the experimental spectrum can be expressed as

$$j(v) = \int_{-\infty}^{\infty} J(E)exp(2\pi ivE)dE \tag{3.5}$$

where v is the frequency in units of eV^{-1}. By taking a Fourier transform of equation 3.4 and rearranging for $s(v)$ we obtain

$$s(v) = z(v)ln[j(v)/z(v)] \tag{3.6}$$

where $z(v)$ and $j(v)$ are Fourier transforms of the zero-loss peak and experimental spectrum respectively. The single scattering spectrum can thus be obtained by taking the inverse Fourier transform of equation 3.6.

The single scattering function obtained from equation 3.6 contains some residual noise, which is not removed during deconvolution. However, this noise has little effect on the spectrum and thus the single scattering function is sufficient for further calculations and analysis.

3.2.2 Kramers-Kronig Analysis

Kramers-Kronig analysis (KKA) can be used to calculate dielectric functions from the single scattering EELS spectrum [81]. The single scattering spectrum is related to the dielectric

function, $\varepsilon(E)$, by

$$S(E) = \frac{2I_0 t}{\pi a_0 m_0 v_e^2} \Im\left[\frac{-1}{\varepsilon(E)}\right] \ln\left[1 + \left(\frac{\beta}{\theta_E}\right)^2\right], \tag{3.7}$$

using known values of the zero-loss intensity, I_0, specimen thickness, t, collection semi-angle, β, convergence semi-angle, α, and characteristic scattering angle, $\theta_E = E/(\gamma m_0 v_e^2)$. Where a_0 is the Bohr radius, γ is the relativistic factor and m_0 is the electron rest mass. The first term in equation 3.7 is a proportionality constant. The logarithmic term in equation 3.7 indicates the angular dependence of the function, since $\theta_E \propto E$, and can act as an aperture correction which increases the intensity at high losses relative to low loss. Since most parameters in equation 3.7 are known, the single scattering spectrum obtained from EELS can be used to obtain the imaginary part of the dielectric function $\Im\left[-\frac{1}{\varepsilon(E)}\right]$.

A Kramers-Kronig transformation is used to derive

$$\Re\left[\frac{1}{\varepsilon(E)}\right] = 1 - \frac{2}{\pi} P \int_0^\infty \Im\left[-\frac{1}{\varepsilon(E)}\right] \frac{E' dE'}{E'^2 - E^2}, \tag{3.8}$$

where P is the Cauchy principal value of the integral and $\Re$ denotes the real part. The Cauchy principal value is a mathematical method which allows for an integral that otherwise does not converge due to singularities, to be solved. In this case, it avoids the pole at $E = E'$. The term $\frac{E'}{E'^2 - E^2}$ acts as a weighting function giving weight to energy losses, E', close to E. Equation 3.8 can be used to obtain the complex dielectric function and can be evaluated using Fourier techniques to increase computation speed [81]. The real, $\varepsilon_1(E)$, and imaginary, $\varepsilon_2(E)$, parts of the complex dielectric function were then calculated from

$$\varepsilon(E) = \varepsilon_1(E) + i\varepsilon_2(E) = \frac{\Re[\frac{1}{\varepsilon(E)}] + \Im[\frac{-1}{\varepsilon(E)}]}{\Re[\frac{1}{\varepsilon(E)}]^2 + \Im[\frac{-1}{\varepsilon(E)}]^2}. \tag{3.9}$$

Although COMSOL can take the complex dielectric function as an input directly, in practice it was found to be unreliable because negative values in the real part of the dielectric function resulted in rounding errors and inaccuracies in EELS spectra. Dielectric functions were converted into refractive indices by

$$\begin{aligned} n^2 &= \frac{1}{2}\sqrt{(\varepsilon_1^2 + \varepsilon_2^2) + \varepsilon_1}, \\ \kappa^2 &= \frac{1}{2}\sqrt{(\varepsilon_1^2 + \varepsilon_2^2) - \varepsilon_1}, \end{aligned} \tag{3.10}$$

and inputted into COMSOL to prevent these errors.

Figure 3.1 shows dielectric functions and refractive indices used for simulations in this thesis. Information on bulk plasmon energies and bandgaps is present in the dielectric function. The dielectric function of Al_2O_3, calculated from KKA of bulk EELS data, is presented in figure 3.1a and has some key features which relate to peaks observed in the EELS spectrum [197]. In the imaginary part, ε_2, shown in blue, the function is approximately zero below 8.5 eV, which is the bandgap energy. The real part, ε_1, in red is shown to to cross zero at 24.8 eV, which aligns with the energy of a volume plasmon.

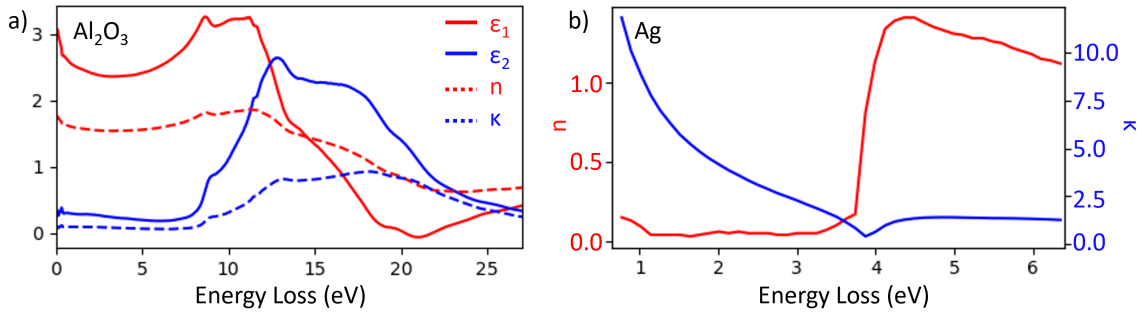

Fig. 3.1 a) Solid: The complex dielectric function of Al_2O_3, with the real part ε_1 in red and imaginary part ε_2 in blue calculated from EELS data taken from the bulk of the Al_2O_3 substrate. Dashed: The complex refractive index of Al_2O_3, converted from the dielectric function, where n is the real part, in red, and κ is the imaginary part, in blue. b) Silver refractive index from reference [198] with the real part, n, in red and imaginary part κ in blue.

The complex refractive index of Al_2O_3, converted from the dielectric function using equation 3.10, is presented in figure 3.1a.The bandgap can be observed in the imaginary part of the refractive index as a quick increase in κ. In the refractive index data for silver shown in figure 3.1b, the real part is close to zero before increasing dramatically at 3.8 eV, the energy of a volume plasmon.

Bulk dielectric functions and refractive indices for each material discussed were either calculated using the above method from bulk EELS data or obtained from reference data. By using the dielectric function from the same experimental EELS data that comparisons will be made to, the influence of structural defects, which could cause small changes in relative peak heights, is included.

The use of KK analysis to obtain dielectric functions has some limitations. At low energies, the ZLP dominates an EELS spectrum and it is not possible to recover information at energies close to the ZLP. Another limitation is that noise in the EELS data is carried through to the dielectric function, which can limit the accuracy of the dielectric function.

Radiative-losses in EELS spectra, which can obscure band-gap features, can also complicate calculated dielectric functions [199].

3.3 Analytical calculations

An EELS spectrum can be calculated analytically using complex dielectric functions [166, 167]. The EELS spectrum can be considered as the probability of an excitation, P, per unit frequency, ω, per unit path, z, as an electron travels through a medium. Equation 3.11 is derived from Maxwell's equations for a charged beam travelling through a semi-infinite material with a dielectric function of ε_1, parallel to an interface with a material characterised by ε_2 [200]. As it passes through the material, a retarding force acts upon the electron beam and the loss probability can be determined. A non-retarded limit, corresponding to a non-relativistic electron beam, $v_e/c \to 0$, is applied to simplify the solution. EELS spectra, $\Gamma^{NR}_{interface}$, between materials with dielectric functions ε_1 and ε_2 at a distance, b, from the interface in material 1 were calculated by

$$\Gamma^{NR}_{interface} = \frac{2te^2}{4\pi^2\varepsilon_0\hbar v_e^2}\Im\left[\underbrace{-\frac{\ln(2q_y^c v_e/\omega)}{\varepsilon_1}}_{\text{bulk}} + \underbrace{K_0\left(\frac{2\omega b}{v_e}\right)\left(\frac{1}{\varepsilon_1}-\frac{2}{\varepsilon_1+\varepsilon_2}\right)}_{\text{interface}}\right], \tag{3.11}$$

where K_0 is the zero-order Bessel function of the second kind and q_y^c is the cutoff momentum. The thickness of the cross-section, t, and electron velocity, v_e, were set to the same values as experimental measurements to provide a comparison.

The cutoff momentum is related to the momentum dependence of electron scattering, which was discussed in section 1.3.2. Due to the conservation of energy and momentum, when the phase velocity of excited plasmons is similar to the Fermi velocity, v_F, energy transfer can occur resulting in plasmon damping [81]. Since the momentum of a transmitted electron is related to the scattering angle, shown in figure 1.6, scattering from plasmons drops significantly above a cutoff angle, θ_c, related to the critical wavevector, q_c, by

$$q_c \simeq \frac{E_p}{\hbar v_F} \approx k_0\theta_c, \tag{3.12}$$

where E_p is the plasmon energy and k_0 is the incident wavevector. The cutoff momentum, q_y^c, was selected to be around this value. In cases where the dielectric function was obtained from experimental EELS data acquired with a smaller collection angle than convergence angle, the cutoff angle, θ_c, was not reached in the data. In cases where comparison to experimental

EELS data acquired with a smaller collection angle than convergence angle was desired, the cutoff momentum was reduced to account for the fact that some higher momentum signals were not collected. The cutoff momentum is therefore related to the spectrometer aperture.

Equation 3.11 can be broken down into two main components. The first term is a bulk contribution, which decreases on approach to the interface and the second term is an interface term, which decreases away from the interface. At large impact parameters, the function tends to bulk. The $1/\varepsilon_1$ term in the interface term is from the begrenzung effect, which arises due to screening of fields from surface excitations and reduces the bulk contribution towards an interface [90].

To consider the relativistic effects of the electron beam, the non-retarded approximation was not used and EELS spectra were calculated by

$$\Gamma = \frac{e^2}{2\pi^2\varepsilon_0\hbar v_e^2}\int_0^{q_y^c}\Im\left\{\underbrace{-\frac{1-\varepsilon_1\left(\frac{v_e}{c}\right)^2}{\alpha_1\varepsilon_1}}_{\text{bulk}} + \underbrace{\frac{e^{-2\alpha_1 b}}{\varepsilon_1\alpha_1(\alpha_1+\alpha_2)}\left[\frac{2\alpha_1^2(\varepsilon_2-\varepsilon_1)}{\varepsilon_1\alpha_2+\varepsilon_2\alpha_1}+(\alpha_2-\alpha_1)\left(1-\varepsilon_1\left(\frac{v_e}{c}\right)^2\right)\right]}_{\text{interface}}\right\}dq_y, \quad (3.13)$$

where q_y^c is the cut-off momentum defined by the spectrometer aperture, v_e is the electron velocity, fundamental constants have their usual symbols [200]. With

$$\alpha_n^2 = ((\omega/v_e)^2 + q_y^2) - \varepsilon_n\omega^2/c^2.$$

The thickness of the cross-section t is determined by known mean free path values, λ, and EELS measurements of t/λ, as discussed in chapter 2. An impact parameter, b, was used as the horizontal distance between the interface and the beam. The first term in the integral in equation 3.13 contains the contribution from the bulk of material 1, while the second term contains the interface contribution.

At the interface between two materials, plasmons can couple, resulting in changes to the interfacial EELS spectrum. This is expected in most systems and can be described by classical dielectric theory [163]. In some cases, additional processes can occur such as bonding at the interface or the emergence of a 2D electron gas (2DEG) which are not explained by plasmon coupling. Calculating how plasmon coupling changes the interfacial spectra and comparing to experimental data can indicate features present within an experimental spectrum which are not due to this coupling and could perhaps be attributed to other processes.

Analytical calculations making use of equations 3.11 and 3.13 have been used to investigate thin films and plasmon coupling at metal-dielectric interfaces [166, 167]. Calculated EELS spectra across interfaces in approximately infinite thin films have been demonstrated to replicate the plasmonic behaviour in experimental systems [166]. When compared to non-retarded calculations there was little difference in resulting EELS spectra at the energies of interest and only slight differences around the zero loss peak. Therefore the relativistic approach was taken since it included potential effects of the electron been and did not add much complexity to the calculations.

A brief description of the calculated EELS spectrum across an Al_2O_3/Bi_2Se_3 interface is discussed here to demonstrate the calculations. Throughout this thesis, equation 3.13 was used to calculate EELS spectra across each cross section to compare to experimental results.

3.3.1 Results

EELS spectra were calculated using equation 3.11 for samples of Al_2O_3/Bi_2Se_3 and compared with experimental results, presented in figure 3.2. These results will be discussed in more detail in chapter 4, where the experimental data is analysed with reference to the calculations.

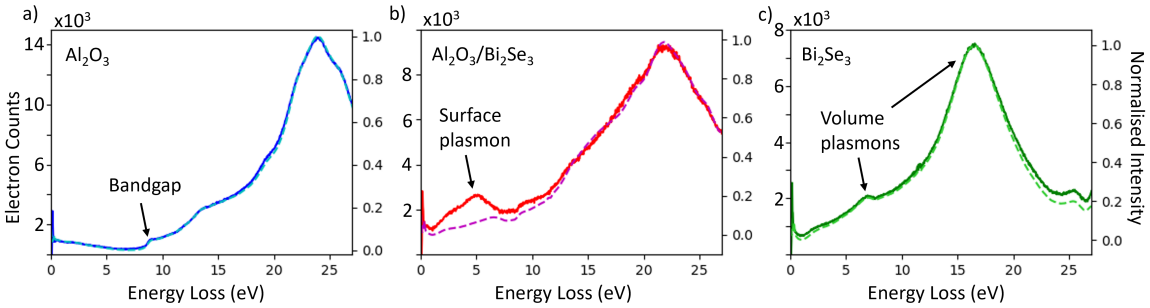

Fig. 3.2 Calculated EELS spectra and experimental data in a) bulk Al_2O_3, b) Al_2O_3/Bi_2Se_3 interface and c) bulk Bi_2Se_3. Dashed lines are calculated spectra and solid lines are experimental data. Bulk spectra are well replicated by the calculations and the interface has some differences.

For bulk Al_2O_3, the EELS spectrum, shown in figure 3.2a, is directly replicated from the dielectric function, indicating that the calculated spectrum does not have any artefacts from calculating the dielectric function present. The same is true for bulk Bi_2Se_3, where two plasmon peaks can be clearly identified and are indicated in 3.2c. The calculated bulk spectra, dashed lines, are very close to the experimental data, solid lines, in figure 3.2a,c. At the interface, calculated with a small impact parameter, there is less agreement with experimental data. Calculated EELS spectra across the Al_2O_3/Bi_2Se_3 interface, as shown in figure 3.2b,

differ from experimental results with the absence of an interfacial feature around 5 eV. This rules out plasmon coupling as the origin of the surface plasmon and points to an origin not described by the calculation.

In figure 3.2c, there is some discrepancy at higher energies between the experimental and calculated Bi_2Se_3 EELS spectra. This difference is most likely due to the selection of cut-off momentum chosen for the calculation. The experimental data was acquired using a convergence semi-angle of 30 mrad and a collection semi-angle of 22 mrad, which limits the momentum range of collected electrons, thus a smaller cut-off momentum is required to replicate EELS data.

These calculations are simple and work well for investigating thin film systems without substantial thickness variations. Throughout this thesis, analytical calculations using equation 3.13 have been used for each system to replicate EELS spectra over each interface. In cases where the plasmonic properties of a nanoparticle or a more complex sample are to be investigated, this approach falls short as shape effects must be considered for nanoparticles making the calculations increasingly complex. Therefore other methods of calculating EELS spectra were investigated which can include this added complexity in a straight forward way.

3.4 Numerical Theory and Calculations

COMSOL software was used to extend calculation of EELS spectra to 3D to allow for more complex systems to be investigated. This method has been used in literature for various nanoparticle systems [176–182, 185]. The simulation method is outlined for application in both thin film and nanoparticle systems.

As an electron with velocity v_e passes through a material it induces an electric field $\mathbf{E}_{ind}$ which exerts an electrostatic force back on the electron. This induced field can be calculated using finite element (FE) methods in COMSOL and used to calculate the loss probability and EELS spectrum. Finite elements is a numerical method of solving partial differential equations which is common in electromagnetic problems.

The 3D simulation region is segmented into smaller 3D domains using a mesh, and the calculation is then performed at each nodal point of the mesh. To build up the full 3D simulation, interpolation between the nodal points is used to approximate the solution over the full 3D simulation regime. The nodal density of the mesh can be varied for different parts of the model, such as using a higher density within a nanoparticle and along the electron beam path and a lower density in vacuum away from the specimen to decrease computation time. The distance between nodal points should be smaller than the wavelength corresponding to the largest energy loss, around 40 nm in this case. This differs from boundary element

methods used by other plasmon simulation tools such as 'MNPBEM' which performs the calculation over discretized surfaces instead of volumes [171, 164]. Although the use of FE methods can increase computation time, it allows for the electric field within a large volume to be calculated, which is useful when considering thin films and their interfaces.

The electron beam was modelled by a line current in the z-axis passing through the material with a current of $I = I_0 \exp(i\omega z/v_e)$. The position of the electron beam was varied to change the probe position, recreating STEM EELS experiments for bulk, surface and aloof beam positions. The accelerating voltage of the electron beam was encapsulated in the electron velocity, v_e, where 200 kV is equivalent to $0.7 \times c$ ms^{-1} to replicate experimental conditions. At each energy loss, ω, for a given electron velocity, v_e, the z-component of the induced electric field, $\mathbf{E}_{ind,z}$, was integrated along a line segment in the z-axis by

$$\Gamma_{loss} = \frac{e}{\pi\hbar\omega}\int_{-\infty}^{\infty} dz \Re\left[\mathbf{E}_{ind,z}\exp\left(-\frac{i\omega z}{v_e}\right)\right], \tag{3.14}$$

to obtain the loss function. Following the approach of Govyadinov *et al.*[194], the electric field was obtained twice, with ($\mathbf{E}_d$) and without ($\mathbf{E}_0$) the material present, to subtract the background field and isolate the induced field, $\mathbf{E}_{ind}$, using

$$\mathbf{E}_{ind} = \mathbf{E}_d - \mathbf{E}_0. \tag{3.15}$$

The integration in equation 3.14 was performed in COMSOL on E_d and E_0 independently before the subtraction of equation 3.15. The induced electric field was then multiplied by the prefactor term in equation 3.14. Plots of the distribution of the induced electric field along with EELS spectra taken at different probe positions allows for observation of localised surface modes and interfacial plasmons.

3.4.1 Simulation setup

The FE model was simulated within COMSOL using a rectangular box of vacuum, $\varepsilon = 1$, with an additional rectangle on each face to act as a boundary preventing nonphysical reflections of the electric field. These additional regions are termed as perfectly matched layer (PML) boundaries within COMSOL. The nanoparticle was placed at the centre of the box as depicted in figure 3.3. Where a thin film was modelled, the material region was extended to the edges of the PML boundaries to act as an infinite plane. To reduce the computational cost of some thin film simulations, a symmetry boundary was included in the y-axis, in plane with the beam path, to reduce the size of the model.

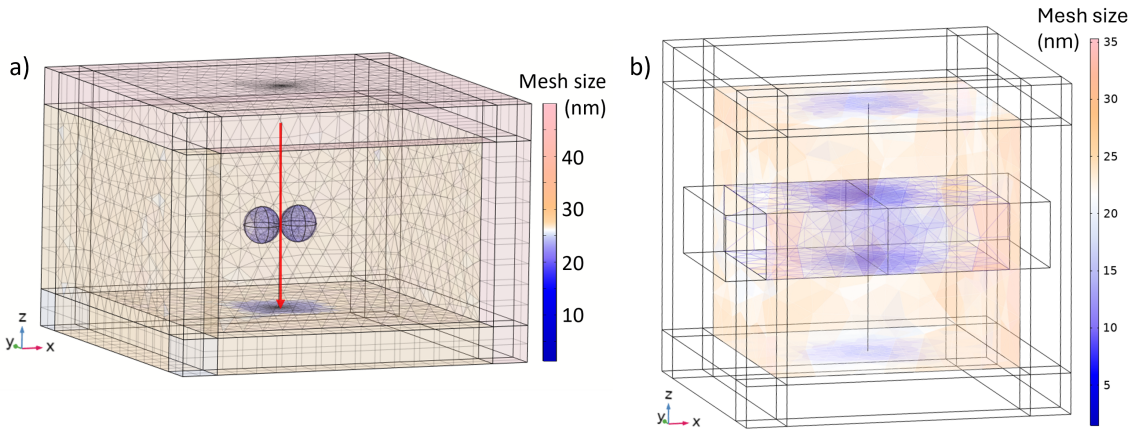

Fig. 3.3 a) Schematic of the COMSOL finite element model setup used for dimer spheres with the mesh applied where the beam path is indicated by a red arrow. The distance between mesh nodes is highlighted by the colour map where the highest density of nodes is within the dimer spheres and along the beam path. b) Thin film schematic with applied mesh. The nanoparticle/film is surrounded by vacuum with perfectly matched layer boundaries at the edges of the model.

The simulation region was discretized by a tetrahedral mesh with the highest node density within the nanoparticle or film and along the beam path as shown in figure 3.3. The PML boundary regions were meshed by rectangles with the distance between nodes smaller than the electron wavelength. The simulation was computed in the frequency domain for electromagnetic waves for a range of energy values, ω. Simulations were solved using a iterative linear solver which iterated until a convergence of 0.01 was obtained. Further details of the simulation setup are provided in appendix A. To replicate the experimental conditions, the data could then be convolved with a Gaussian function with a FWHM the same as the zero loss peak in the experimental dataset [201, 189]. This allows for some instrumental broadening to be included in the simulated dataset, providing a better comparison with experimental data. This also provides an indication of how well peaks will be resolved with a given spectral resolution.

Simulations of EELS spectra of various nanoparticles and thin films were carried out using the above method in COMSOL to highlight the usefulness and versatility of the method. Common dielectric functions and refractive indices from literature were used to represent each material and have been commonly used in other plasmon simulations.

3.5 Nanoparticle Plasmonics

3.5.1 Silver nanospheres and dimers

There has been substantial interest, both experimentally and in simulations, in the excitation of localised surface plasmon resonances (LSPR) in nanostructures, often for sensing applications [202, 203]. The electromagnetic field around a nanoparticle is strongly enhanced by a LSPR and the wavelength of the resonance is dependent on the environment surrounding the particle, meaning that they can be use as a sensor for the local environment [202].

In real systems, shape effects play a significant role in surface plasmon energies and localisation. Reducing the size of a nanoparticle can result in a redshift of surface plasmon energies and proximity to other particles gives rise to coupling effects [170]. These effects have been studied substantially in silver nanospheres [204, 205] providing a useful test to confirm the accuracy of the simulations before moving to more complex systems.

The surface charge distribution in nanoparticles can be described by shape-dependent plasmon eigenmodes which contribute to the spectrum [206]. These eigenmodes are dependent on the nanoparticle geometry such as breathing modes in a sphere and corner modes in nanocubes [170, 207, 208]. Although the electric field distribution at each eigenmode is independent of material, the energies at which these occur are influenced by the dielectric function. By varying the electron probe position, different eigenmodes can be excited. When excitation occurs at a node of an eigenmode it contributes to the EELS spectrum. Multiple eigenmodes are often excited simultaneously, all contributing to the EELS spectrum as a linear combination [201].

Plasmon modes in silver nanospheres were simulated for a sphere of diameter 100 nm surrounded by vacuum. With the electron beam positioned centrally down the middle of the sphere, a bulk plasmon was excited at 3.8 eV and is clearly observable in the simulated EELS spectrum shown in figure 3.4b. As the beam position was moved towards the edge of the sphere, a surface plasmon at 3.6 eV was observed with increasing intensity. In an aloof position, 5 nm from the edge of the sphere, the bulk plasmon was no longer present but the surface mode remained at 3.6 eV. Additionally, a broader peak at 3.1 eV emerges in proximity to the edge of the sphere. The feature at 3.6 eV can be described as a standing wave surface plasmon polariton [204] and quasiplanar mode (QP) excited around the circumference of the sphere. The electric field distribution at different energies and beam positions are presented in figure 3.4c with the background containing the unscattered electron beam subtracted.

From the electric field plots in figure 3.4, the localisation of surface modes can be observed at 3.6 eV with the electric field intensity increased at the surfaces of the sphere. The surface plasmon feature also has contributions from the lowest energy dipolar plasmon

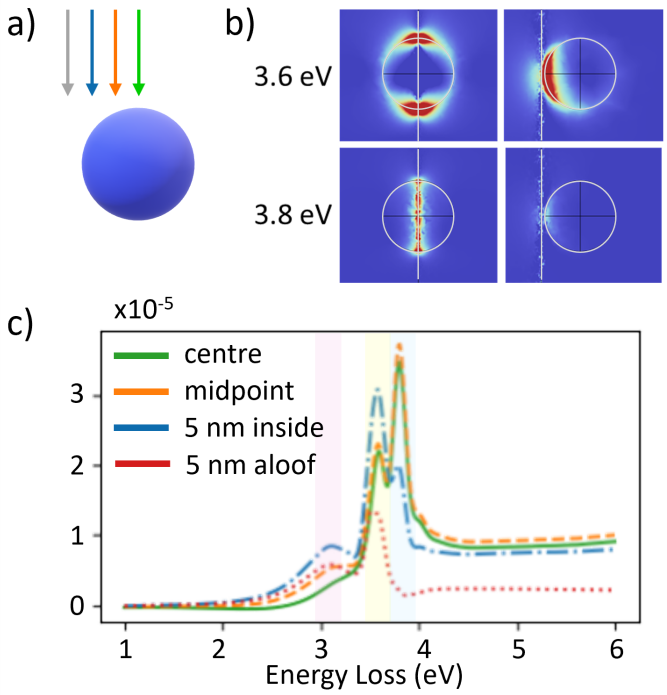

Fig. 3.4 Simulated EELS spectra from a silver sphere of diameter 100 nm at different probe positions indicated in part a). b) Electric field (E_{ind}) distribution at surface plasmon (3.6 eV) and volume plasmon (3.8 eV) energies for central and aloof beam positions. c) Simulated EELS spectra at each probe position.

resonance predicted to occur at 3.5 eV [143]. Other types of simulations such as BEM are in agreement with these results [205]. Experimental EELS spectra from literature of smaller nanospheres shows a similar trend with the surface plasmon lower in energy than the bulk [143, 204].

In proximity to each other, the LSPRs in adjacent nanoparticles interact electromagnetically and hybridised plasmonic states are formed [209]. When the dipoles of LSPRs of adjacent particles are aligned, a bonding mode is observed, as shown in figure 3.5a, and when opposed, an anti-bonding mode forms. As anti-bonding modes do not have a dipole, they cannot be excited by optical means. EELS is a useful technique for investigating these types of systems as it allows for observation of both 'bright' bonding modes and 'dark' anti-bonding modes, which are not observed by optical methods. The energy of coupled modes depend on both the size of spheres and their separation. For example, a smaller separation results in greater coupling between nanoparticles and hence lower coupling mode energy [210]. Two 50 nm Ag spheres with a separation of 3 nm were excited at different electron probe positions to investigate coupling between them. The resulting EELS spectra and electric field distributions are shown in figure 3.5.

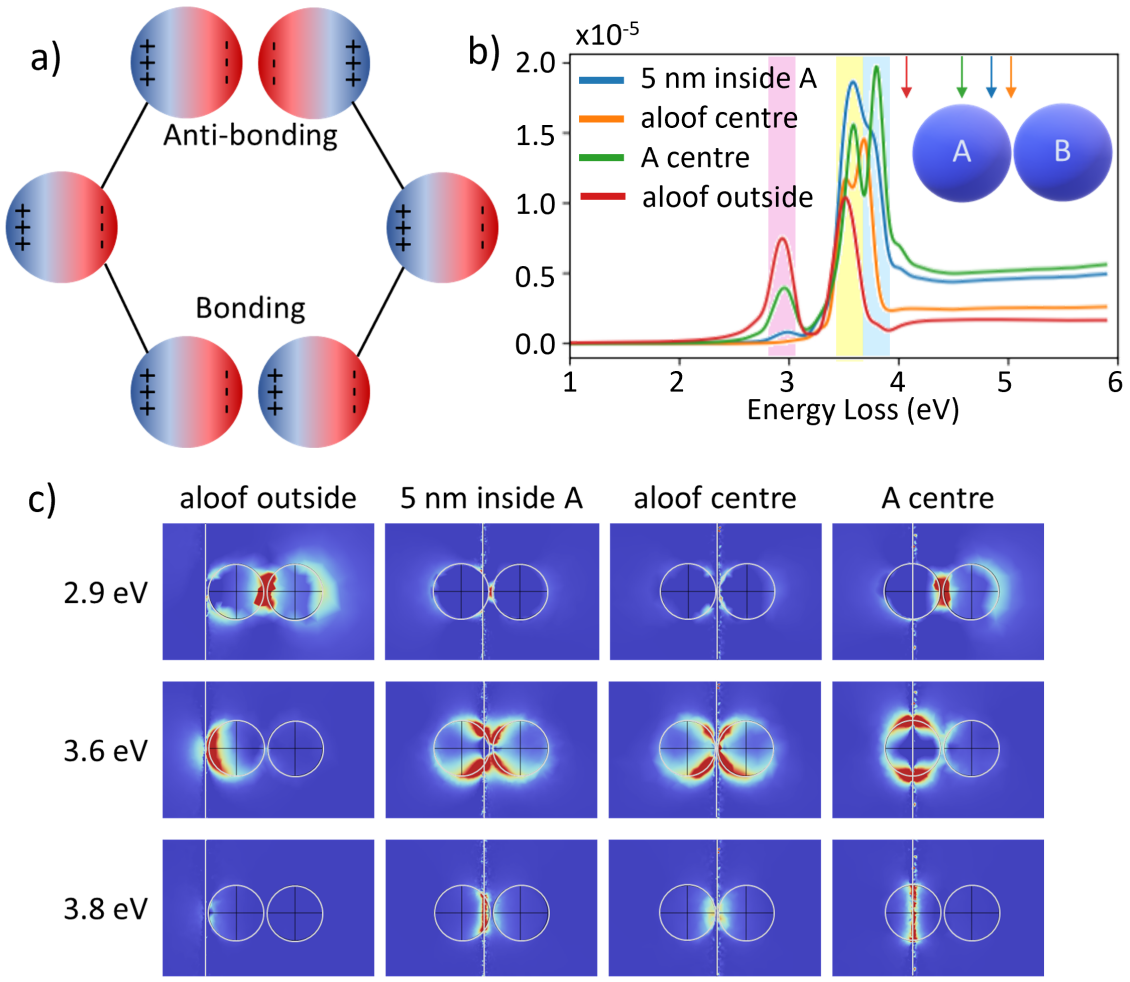

Fig. 3.5 Simulated silver nanosphere dimers with a diameter of 50 nm and a separation of 3 nm excited at different probe positions. a) Hybridised states of nanosphere dimers with the dipole of LSPR indicated. b) Simulated EELS spectra at different electron beam positions, as indicated, with a bulk plasmon energy of 3.8 eV, surface plasmon at 3.6 eV and coupling mode at 2.9 eV. c) Electric field induced by the electron beam at peak energies for different probe positions.

As with a single nanoparticle, the position of the electron probe determines which plasmon modes are excited. With the probe positioned through the centre of sphere A, the 3.8 eV bulk plasmon was excited as well as a 3.6 eV surface plasmon around the circumference of the sphere [210]. At 2.9 eV an additional peak was present and upon inspection of the electric field distribution, figure 3.5c, this excitation was localised to the gap between dimers. This excitation was most excited with the beam in aloof position at the opposite side from the gap. It can be attributed to longitudinal bonding between the spheres [205] and is a 'bright' bonding mode, which has also been observed in optical experiments. The 'dark' SPR anti-bonding mode is situated higher in energy and excited when the beam is positioned

between nanoparticles [143]. With the probe positioned in the gap between particles, the 'bright' mode was not excited as it was symmetry-forbidden. Instead excitation is strongest at 3.7 and 3.5 eV, where surface plasmons of each sphere are excited.

As the gap size between the nanoparticles is decreased, the bonding SPR mode has been shown to decrease in energy [210]. In the absence of a gap, Koh *et al.* observed similar EELS spectra which contained bright, 2.2 eV, and dark, 3.3 eV, coupling modes when the beam was aloof and a bulk plasmon at 3.8 eV [143]. The COMSOL simulations presented in this section are in agreement with literature and are able to accurately replicate the effects of nanosphere coupling. These simulations were straight forward to set up and required a computation time of only a few hours to complete on a standard desktop PC.

3.5.2 Nanodiscs and shape effects

The shape of a nanoparticle has a large impact on its surface plasmon resonance modes. To investigate these shape effects, thin silver nanoshapes were simulated to compare to literature data. Nanodiscs of diameter 300 nm and thickness 30 nm were selected to illustrate the plasmonic behaviour at different probe locations. Simulated EELS spectra with the probe positioned in the centre and towards the edge of the disc are presented in figure 3.6a with the associated induced electric field distribution in figure 3.6b. The spectrum was broadened by convolution with a Gaussian of with 0.15 eV to account for experimental resolution [201].

In both spectra, a large peak was present at 3.8 eV which can be attributed to the bulk plasmon mode from the silver, which was most excited in the region of the beam path. Excitation from the centre results in excitation of a 'breathing' mode, where the charge oscillates radially from the centre. In figure 3.6a the breathing mode was identified at 2.9 eV and both the energy and field distribution are in agreement with experimental and MNPBEM simulations [211]. Additional peak energies, excited when the beam was positioned at the nanoparticle edge, and their localisation were in agreement with Schmidt *et al.* who studied plasmon modes in silver nanodiscs and nanotriangles [201]. Modes identified in the discs upon edge excitation were assigned to the dipole, quadrupole and hexapole modes. Each of these modes presented as an excitation around the circumference of the disc in EELS maps and electric field distribution maps. When the simulation was performed without substrate, as in figure 3.6, the peaks were higher in energy than with a substrate present. With the probe positioned close to the edge of the disc an excitation was observed at 2.1 eV, at which the electric field is increased around the circumference. This mode can be assigned to the quadrupole mode as identified by Schmidt *et al.* at the same energy [201]. To slightly higher energy is the hexapole mode at 2.6 eV.

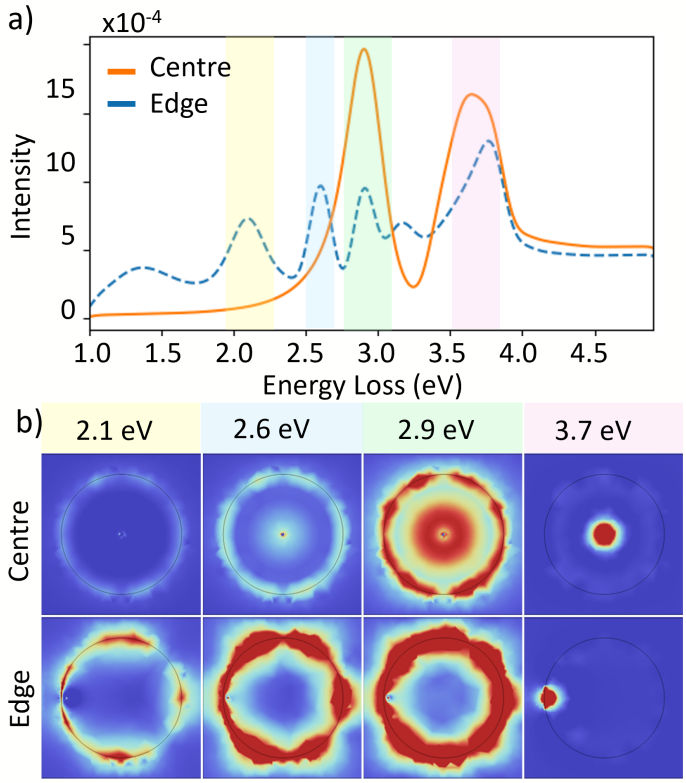

Fig. 3.6 Simulated EELS spectra and electric field distribution for silver nanodiscs with diameter 300 nm and thickness 30 nm. a) Simulated spectra with the beam positioned in the centre and near the edge of the silver disc. b) Electric field distribution from a top down view, shows the localisation of plasmon mode at different energies where peaks are identified in the spectra.

Another common shape studied is the triangular nanoprism, which is often used as nanoantenna in applications. EELS spectra were simulated for a silver triangular prism of side length 555 nm and thickness 30 nm for comparison to experimental data from Kawasaki *et al.* [212]. The resulting spectra and induced electric field distribution are presented in figure 3.7 from excitation with a 100 kV electron beam at corner, edge and centre positions. Excitation from an electron beam positioned at the centre was dominated by the bulk Ag plasmon at 3.8 eV but modes at corner and edge positions are also excited.

When excited from the corner, additional peaks are excited at various energies 0.9, 1.4 and 2.1 eV, which can be assigned to dipole, hexapole and higher order modes. These are observed in the electric field distribution in figure 3.7b and occur at corner positions. Additional excitations are also observed at higher energies, 3.3 eV, which can be attributed to plasmons at the top and bottom surfaces and along edges. Upon edge excitation, the dipole mode at 0.9 eV is not excited, instead a sub-peak at 1.6 eV is excited alongside the 1.4

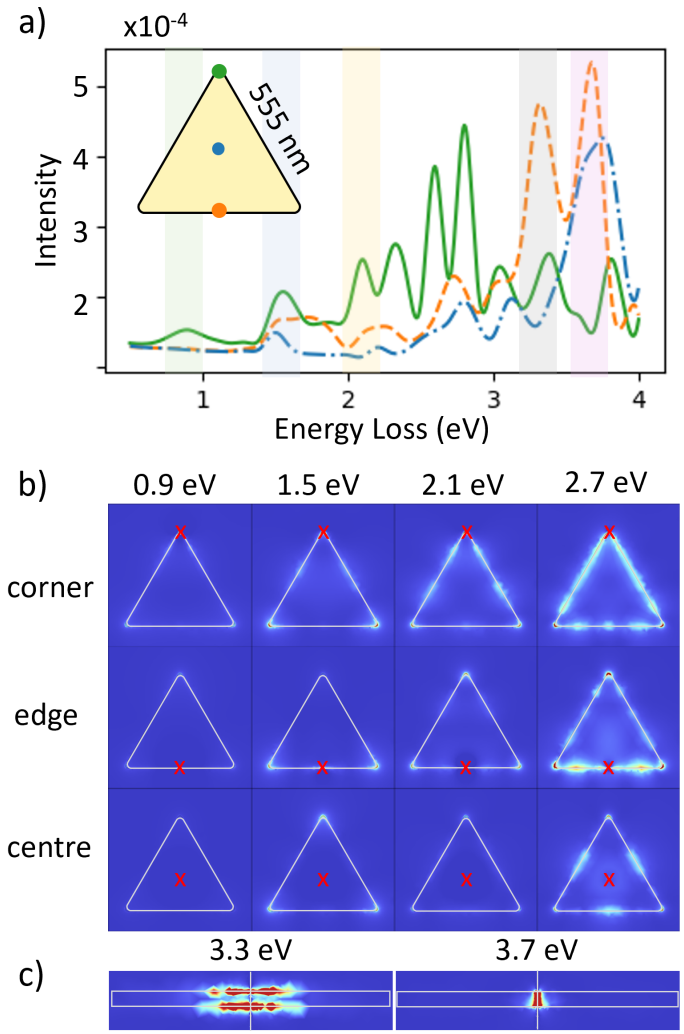

Fig. 3.7 a) Simulated EELS spectra of a silver nanoprism (side length 555 nm and thickness 30 nm) excited at corner, centre and edge positions with a 100 kV electron beam. b) Induced electric field distribution at selected energies for each electron beam position.

eV hexapole mode. This peak has been attributed to hybridisation between the edge mode and breathing modes [212]. The induced electric field distribution, figure 3.7b, at 2.7 eV indicates an edge mode present at this energy. At 3.3 eV, a large peak is observed primarily with edge excitation, at which the induced electric field is most intense at the edge on the top and bottom surfaces.

Schmidt *et al.* studied how the plasmon modes changed as a nanodisk morphed into a nanotriangle [201]. They observed a shift of the breathing mode to higher energy for the triangle and the disappearance of the quadrupole mode. The simulations presented above are in agreement with this.

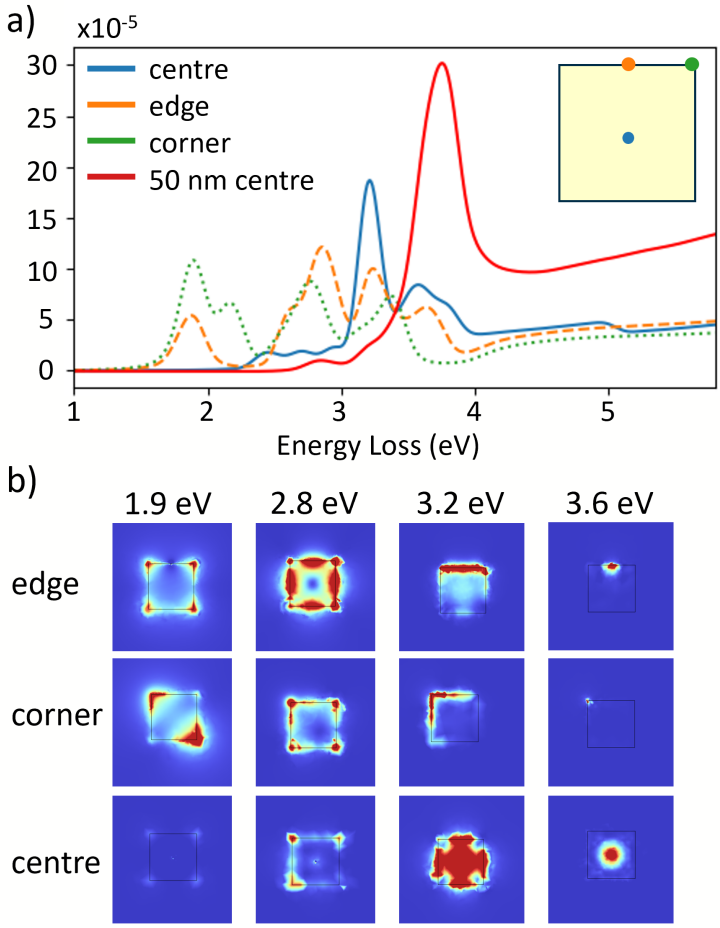

Fig. 3.8 a) Simulated EELS spectra with different electron probe positions for a 10 nm thick square and 50 nm thick square. b) Induced electric field on the surface of the square at different energies and the indicated probe position. Peaks in the EELS spectra show an increased electric field at different locations on the square with the corners most excited at 1.9 eV and edges at 2.8 eV.

Simulations of a squared shaped Ag nanoparticle show similar results to other nanoparticles, with an excitation of the bulk plasmon (3.8 eV) even with a central beam, as shown in figure 3.8a. For a nanoparticle with a thickness of 50 nm, the bulk plasmon mode dominates the spectrum upon centre excitation, but for a thinner nanoparticle of 10 nm, there is only a small excitement of this mode. Since there is less bulk material to excite, the peak is less intense and surface modes dominate the spectrum. For the 10 nm thick square, figure 3.8, a central probe position excites the particle most a 3.2 eV, where there is also significant edge excitation. Excitation of the edges is observed in the electric field for both probe positions. At 2.9 eV, the corner positions are excited as well as edges. This is consistent with a summation of eigenmodes excited at this energy and This is known as the dipole mode [205]. From the

electric field distribution in figure 3.8b, the localisation of each mode is clearly observed. At 1.9 eV corner modes are excited, whilst at 2.8 eV both corner and edge modes are present. These results accurately replicate experimental data.

The simulation method is successful in replicating the effects that nanoparticle shape has on the plasmon resonances and EELS spectrum. The ability to handle both large thin films and nanoparticles makes this a versatile tool for simulating different complex systems. For example, EELS from nanoparticles deposited at an interface on a thin film could be simulated. Additionally, the ability to observed localisation of plasmon modes in the induced electric field is useful for identification of different types of surface modes.

Compared to other plasmon simulation tools such as MNPBEM [171], there is one key limitation, plasmon eigenmodes cannot be easily simulated alongside the spectra. This limits the identification of specific plasmon modes from nanoparticle excitations. Similar Ag nanoparticle systems have been studied using BEM methods implemented in MNPBEM software [171]. These systems include Ag prisms [213] and nanoparticle dimers [173] similar to those discussed here. Since BEM only models the surface of nanoparticles, volume effects are not considered, but the use of FEM can account for these and be used to simulate complex systems.

3.5.3 Substrate considerations

In practice, nanoparticles are not suspended in a vacuum but tend to be deposited on a substrate. Generally, the substrate is either not included in simulations for simplicity or included as an average value of relative permittivity. Commonly, silicon nitrate (Si_3N_4) is used as a substrate for nanoparticles, since it is readily available and can be very thin and electron transparent. The substrate has been included in nanoparticle simulations to best compare to experimental results using an average value for the permittivity which varied between literature [201, 210, 212].

The effect of an Si_3N_4 substrate was simulated for a truncated spherical silver nanoparticle with a diameter of 100 nm on a 30 nm thick substrate. This system was selected to compare with simulated and experimental EELS data from Li *et al.* [204]. Figure 3.9b contains the spectrum of the nanoparticle suspended in vacuum and on the substrate with the beam positioned at the centre of the particle.

When excited from the middle of the nanoparticle, the most intense feature in the EELS spectrum is the bulk plasmon peak peak at 3.8 eV followed by a smaller peak at 3.6 eV for the quasiplanar mode (QP), as described for a single sphere previously. The electric field distribution, shown in figure 3.9f, shows excitement at the top and bottom surface of the nanoparticle at 3.6 eV for the QP mode and excitement in the middle of the particle at 3.8 eV

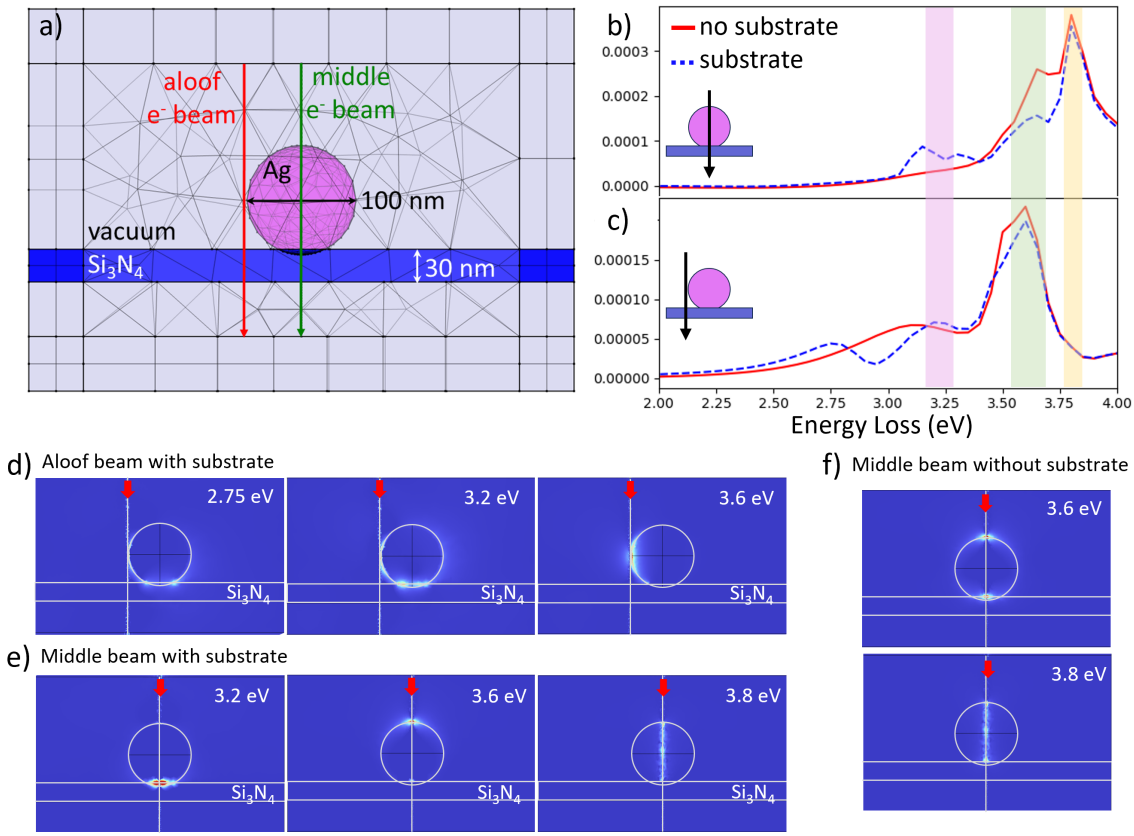

Fig. 3.9 Simulated EELS spectra for a truncated silver sphere with diameter 100 nm on a 30 nm Si_3N_4 substrate. a) Mesh used for the simulation. b) Simulated spectra with the electron beam positioned in the middle of the nanoparticle with and without a substrate present. The bulk plasmon (yellow), quasiplanar (QP) mode (green) and substrate localised dipole mode (pink) are highlighted. c) Simulated spectra of the nanosphere excited from an aloof position with and without substrate. d) Electric field distribution at 2.75, 3.2 and 3.6 eV for an aloof beam with the substrate present. e) Electric field distribution at 3.2, 3.6 and 3.8 eV for a middle position beam with the substrate present and f) electric field distribution at 3.6 and 3.8 eV for a middle position beam with no substrate present.

for a bulk plasmon. With a substrate present, there are additional peaks at 3.15 and 3.3 eV and the QP mode is less intense but no noticeable shift in peak energies for the bulk plasmon or QP mode. The additional peaks can be compared with a broad peak at 3.2 eV in Li *et al.*, which is associated with a substrate localised dipole mode [204]. At 3.2 eV the electric field, shown in figure 3.9e, is greatest along the interface between the nanoparticle and substrate.

Excitement by an aloof beam, 2 nm from the edge of the nanoparticle, is shown in figure 3.9c for the same nanoparticle with and without a substrate present. The bulk plasmon peak at 3.8 eV is no longer present and the spectrum is dominated by the QP mode which excites the circumference of the nanoparticle. A broad feature around 3.1 eV is present in

the absence of a substrate, which can be attributed to a dipole mode. With a substrate present peaks are observed at 2.75 and 3.2 eV, which show increased excitement at the interface with Si_3N_4 in figure 3.9d. At 2.75 eV, the points at which the nanoparticle meets the substrate are most excited and at 3.2 eV the substrate/nanoparticle interface is excited as with a middle positioned beam.

Although the effect of Si_3N_4 substrate on the plasmonic behaviour of the nanoparticle is small, the inclusion of the substrate makes for a more accurate model and can be used to rule out any shifts due to substrate when investigating complex nanoparticle shapes or arrays. Other substrates may have a larger impact on the plasmonic behaviour and using this setup it is simple to include any substrate in the simulations to give more accurate results. Furthermore, this opens the possibility of simulating nanoparticles on thin film multi-layers or at positions on the interfaces between two thin films. These could be useful inclusions for simulation of complex structures in the future work of others. For example, in our thin films, at the interface between TI/C_{60} there was an enhancement of EELS signal at the interface, which will be shown in chapter 4. If there was desire to couple this with a nanoparticle to investigate if this would enhance the plasmonic signal when in proximity to this interface then simulations would aid in the investigation. This method allows for that to be modelled with a thin film interface acting as a substrate with nanoparticles on top. The simulation of plasmon EELS spectra using the above method in COMSOL therefore opens the door for the study of many different interesting systems by providing simulation spectra and electric field distributions of equivalent systems to experimental samples. The simulations were straightforward to perform due to the interactive GUI, with no requirement for complex coding ability. It is a useful tool to aid in investigation of both thin films and nanoparticles in many complex systems.

3.6 Interfacial Plasmons in Thin Films

So far, the effects of nanoparticle shape and substrate on LSPR have been demonstrated using COMSOL simulations. The main focus of this thesis is thin film interfaces, which will be simulated in COMSOL in this section. Firstly, metallic thin films will be simulated to confirm the accuracy of calculated EELS spectra, before moving to thin film interfaces. The plasmonic behaviour at dielectric/metal interface will be simulated and indicate the successful simulation of interfacial plasmons. Simulations are then carried out for the Bi_2Se_3/C_{60} interface to provide a reference for the experimental work in the chapters to follow.

3.6.1 Metallic thin films

EELS spectra of metal thin films were simulated to test the model. Refractive indices from silver and gold are readily available [198, 214] and were applied to a 50 nm thick material slab with vacuum on the top and bottom faces. The resulting spectra are plotted alongside equivalent experimental data from literature [215, 216] in figure 3.10. The spectra contain plasmon peaks with energies and lineshapes in agreement with experimental data from thin films, shown in figure 3.10. For a silver thin film, the primary feature in the EELS spectrum is a sharp volume plasmon at 3.8 eV. By approximating the thin film as an infinite plane, any shape effects or surface features are minimised and the surface contributions from the top and bottom surfaces are not significant compared to the large amount of bulk material. The same can be said for gold, which contains a broad peak at 2.3 eV from a volume plasmon.

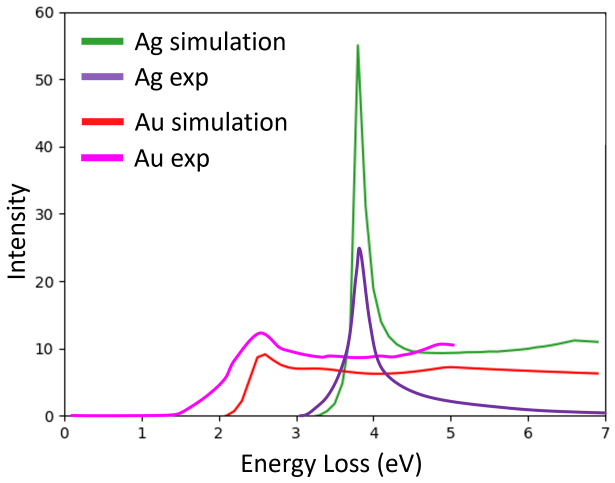

Fig. 3.10 Simulated and experimental EELS spectra from metal thin films of thickness 50 nm. The simulated spectra make us of refractive indices for silver [198] and gold [214] from literature. Both peak energy and lineshape are in agreement with experimental spectra for silver [215] and gold [216] thin films. Experimental spectra have been scaled in arbitrary intensity to be similar to the simulations for display.

There has been substantial research into these metals with simulations carried out for gold and silver thin films using COMSOL and other methods [184, 189]. The plasmonic behaviour is of interest in systems of these materials due to their high conductivity and plasmon energies in the visible spectrum.

3.6.2 Al/Mg_2Si

The plasmonic behaviour at an interface between a metal and dielectric can give insight into hybridisation occurring between materials. At the interface between a metal and dielectric, a surface plasmon polariton (SPP) can be excited, as discussed in section 1.4. The SPP energy is determined by the dielectric properties of materials on either side of the interface. EELS spectra were simulated for thin films of Al/Mg_2Si to illustrate the behaviour of plasmons across the interface and assess the viability of simulating SPPs in COMSOL. This system's electrical properties are well studied for use in metal-semiconductor diodes [217] and has been studied with EELS previously. A slab of thickness 50 nm was split in half, with one side filled with Al and the other Mg_2Si using refractive indices calculated from dielectric functions from literature [166, 218]. The resulting simulated spectra are presented in figure 3.11 and show the excitation of bulk and surface plasmons as an electron beam was scanned across the metal/dielectric interface.

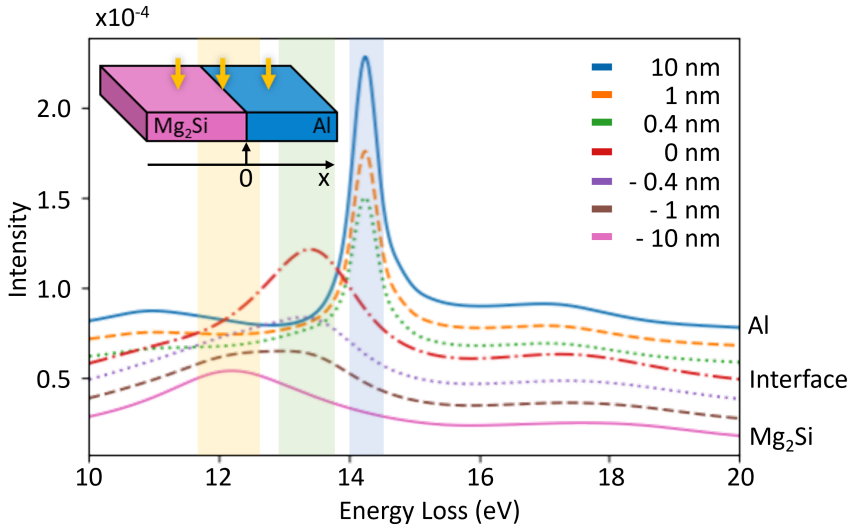

Fig. 3.11 Simulated EELS spectra across the interface between thin films of Al ($x > 0$) and Mg_2Si ($x < 0$). An offset in energy is added to each spectrum and spectra from 0 nm to -10 nm have been multiplied by 2 for clarity. The volume plasmon of Mg_2Si at 12.2 eV is highlighted in yellow, Al volume plasmon at 14.25 eV in blue and the interfacial plasmon energy at 13.4 eV in green.

In aluminium, a sharp plasmon peak was identified at 14.25 eV and reduces in intensity and energy as the beam moves towards the interface. At the other side of the interface, a volume plasmon is excited in Mg_2Si at 12.2 eV, which is much broader and smaller in intensity. For clarity, the spectra on the Mg_2Si side of the interface in figure 3.11 have been multiplied by 2 to allow for the weak Mg_2Si volume plasmon to be observed on the same plot

as the Al volume plasmon. At a metal/dielectric interface, the surface plasmon energy can be estimated using equation 1.12. For $\varepsilon_m \approx -0.18$ for Al in this energy range, the calculated energy of a surface plasmon at the Al/Mg_2Si was approximately 13.5 eV. In figure 3.11, a broad peak is observed at 13.4 eV when the beam is positioned at the interface, which is similar to the calculated value. This interfacial plasmon mode is an SPP that is confined to the interface due to the change in dielectric [126].

An SPP is known to decay evanescently on either side of the interface as $e^{-|k_z||z|}$ and the penetration depth into the dielectric can be defined as $\hat{z} = 1/|k_z|$, where

$$k_z = \frac{\omega}{c}\sqrt{\left|\frac{\varepsilon_d^2}{\varepsilon_d + \varepsilon_m}\right|}, \tag{3.16}$$

with variables the same as in section 1.4 [1]. The decay length of an SPP therefore differs on either side of the interface due to differences in dielectric function and the penetration depth is dependent on the energy of the plasmon mode. Using values of $\varepsilon_m = -0.18$, $\varepsilon_d = 0.52$ and an energy of 13.4 eV, the penetration depth is 18 nm into Al and 20 nm into Mg_2Si. In the simulated spectra in figure 3.11, the intensity of the SPP appears to decay away from the interface over a shorter length scale than predicted from the above calculation. Moving away from the interface into Al, this peak quickly disappears due to the much greater intensity of the Al peak, whereas towards Mg_2Si, this peak is still observed at 1 nm away from the interface. The short decay length of this interfacial peak is in agreement with experimental results from Maclean *et al.*, which show the same interface peak at 13.4 eV decaying away from the interface [166]. In the data presented in figure 3.11, the interface mode has completely decayed by 10 nm into either side of the interface. The variations in apparent decay length of the surface mode from the above calculation can be understood when considering the strong excitation of volume plasmons in the bulk of either material. Since the bulk plasmon excitation has a much greater spectral intensity in Al, contributions of aloof excitement of the SPP mode are obscured by the bulk plasmon peak. Since the SPP intensity has an exponential decay, it becomes obscured by the Mg_2Si bulk plasmon further away from the interface but before the SPP penetration depth. Additionally, limited spatial resolution in experimental work, thickness variations and a non atomically sharp interface can alter the apparent decay length of interfacial features in experimental EELS spectra compared to both analytical calculations presented by Maclean *et al.* and in COMSOL simulations here [166]. In experimental results presented by Maclean *et al.* samples were shown to have a 1 nm region of different contrast at the interface indicating a potential intermixing or strained region which influenced spectra near the interface. They also observed periodic variations of the interface position in samples, which will be explored more in section 3.6.3.

Another observable feature in the simulated data is a broad peak around 11 eV in Al, observed in the blue trace in figure 3.11, which was not present in the experimental work from Maclean et al [166]. From electric field distribution plots, this peak can be seen localised at the top and bottom interfaces of the slab at the Al region. To determine if this peak was an Al surface plasmon, an Al/vacuum interface was modelled and an EELS spectrum simulated with the beam positioned in an aloof position 1 nm from the interface. In an aloof position, volume plasmon modes are not excited, but, due to the decay of a surface plasmon away from both sides of an interface, surface plasmon modes are excited. In the simulated spectrum, the 11 eV peak dominated the spectrum, indicating that this is a surface plasmon peak from the aluminium/vacuum interface. The calculated energy of a surface plasmon at the Al/vacuum interface using equation 1.12 was 10.1 eV, which is similar to the observed result here. This surface plasmon has been observed by Li *et al.* at a slightly lower energy, 10.5 eV, due to the presence of oxygen on the surface, which has been shown to redshift the surface plasmon energy [48]. The presence of a surface plasmon from the top and bottom surfaces in simulations of 50 nm thick films indicates the need to consider the possibility of surface plasmons contributing to bulk EELS spectra in cross-section specimen studied throughout this work. Many of the samples investigated in this thesis were of thicknesses less than 50 nm so could have some small surface contributions at energies lower than bulk plasmons and is considered in chapter 6.

3.6.3 Bi_2Se_3/C_{60}

In materials with broader plasmon peaks and electronic transitions close in energy to plasmon modes, it can be difficult to distinguish features from each other in EELS spectra. In some systems, interactions occurring at an interface can result in localised states not described by bulk dielectric functions. Excitations of plasmons from these states can be more localised than SPPs with different decay lengths. By modelling EELS spectra across the interface from bulk dielectric functions, some of these effects can be accounted for to help distinguish more complex interfacial behaviour.

In the materials discussed throughout this thesis, complex interactions could occur at interfaces including hybridisation effects across TI/organic interfaces and the presence of surface localised states. The methodology adopted here is to compare experimental interfacial peak energies with modelled spectra containing expected SPP energies to highlight behaviour that could point to localised interface effects. Simulations of EELS spectra across a Bi_2Se_3/C_{60} interface were carried out to illustrate the expected behaviour of SPPs at this interface to provide a reference for experiments in further chapters. Refractive indices for Bi_2Se_3 and C_{60}, calculated from bulk EELS data using the methodology described in section

3.2, were applied to the mesh presented in figure 3.3b, with a sample thickness of 50 nm. The simulated spectra, with varied beam positions, are presented in figure 3.12 and indicate a subtle shift in plasmon energy across the interface

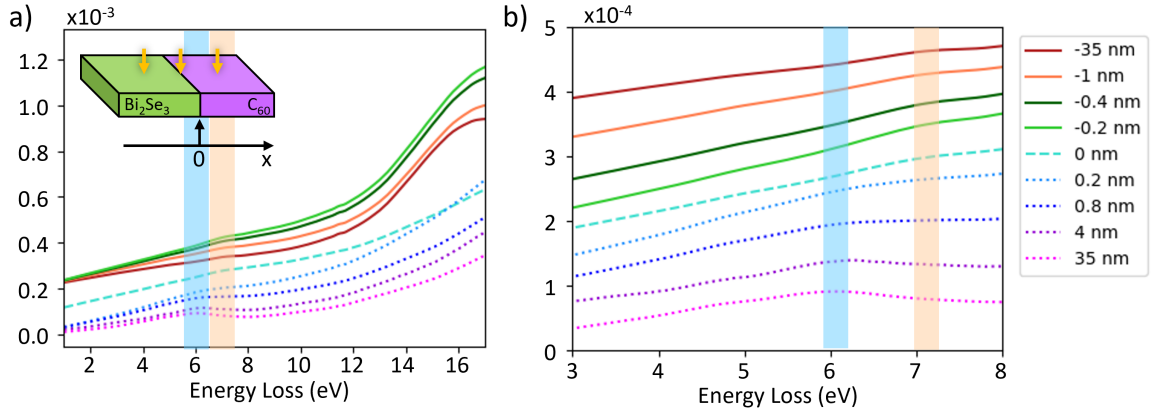

Fig. 3.12 Simulated EELS spectra across a Bi_2Se_3/C_{60} thin film interface. a) Simulated EELS spectra over an energy range of 1 to 17 eV where a volume plasmon is present at 17 eV in agreement with experimental data. b) The same simulated spectra where an interband transition in C_{60} at 6 eV is highlighted in blue and a π plasmon in Bi_2Se_3 at 7.1 eV in orange. Spectra have been shifted vertically for presentation.

At 35 nm away from the interface in Bi_2Se_3 a large volume plasmon is observed at 17 eV in the far right of figure 3.12a. The peak fitting methodology, presented in section 2.7.2 for experimental data, was also utilised to analyse simulated spectra. Across the interface this feature is observed to vanish, with a peak at higher energy, beyond the edge of the simulated energy range, observed in the C_{60} layer. At lower energies, subtle shifts in peak energy are observed across the interface. Figure 3.12b magnifies the lower energy features for clearer identification. At 7.1 eV, highlighted orange in figure 3.12b, a peak is observed in all spectra on the Bi_2Se_3 side of the interface. This is the Bi_2Se_3 π plasmon which will be discussed in detail in chapter 4. At the C_{60} side of the interface a peak at 6 eV, indicated in blue, is observed and is attributed to the combination of a bulk plasmon and interband transition. The plasmon peaks in these materials are much broader than in the metals discussed before due to dielectric losses, indicated by a large imaginary part of the dielectric function [81]. Due to the significant overlap of features in this area and the lack of sharp plasmon peaks, shifts in energy and the excitement of SPPs appear more subtle in EELS spectra.

At the Bi_2Se_3/C_{60} interface, shown in cyan in figure 3.12b, the 7.1 eV excitation remains and no sharp peak for an SPP mode can be observed. Around this energy $\varepsilon_d \approx 2$ in the C_{60} layer and the expected SPP energy is 4.1 eV from equation 1.12 [126]. The electric field distribution at this energy (without subtraction of the incident beam) is shown in figure 3.13.

Even with the incident electron beam positioned 35 nm into the Bi_2Se_3 layer, the interface plasmon appears to be excited. This is due to the long penetration depth expected for this SPP mode of 44 nm in the TI. At higher energies, such as 17.0 eV shown in figure 3.13b, greater intensity can be observed around the incident beam due to excitement of bulk plasmon modes. From this simulation, it is clear that despite the long penetration depth of an SPP and the aloof excitement of SPPs, they become obscured by greater intensity bulk plasmon excitations away from the interface. Whilst the penetration depth of an SPP at this interface is around 40 nm, plasmon excitations from localised states are expected to be more confined.

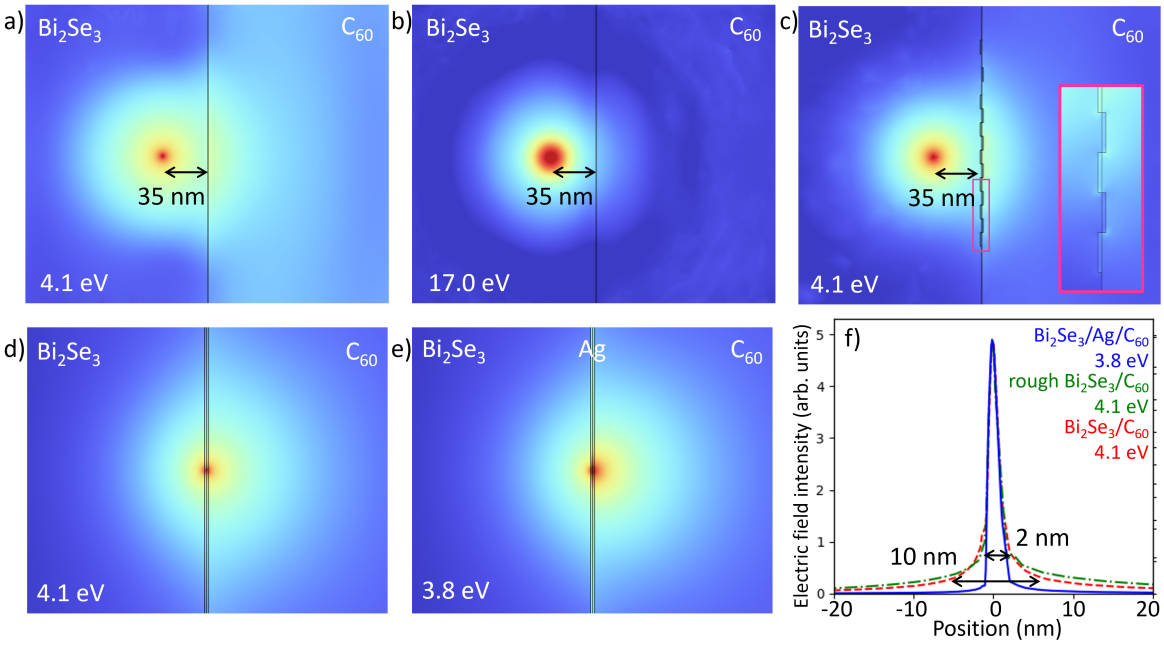

Fig. 3.13 Electric field distribution in the x-y plane in a Bi_2Se_3/C_{60} thin film with excitement by an electron beam positions in the Bi_2Se_3 layer 35 nm from the interface. a) At 4.1 eV, the electric field map shows an SPP excitation at the interface, excited even with the beam posited 35 nm from the interface. b) At 17.0 eV, a strong excitation around the beam is observed due to the bulk plasmon in Bi_2Se_3. c) The electric field distribution at 4.1 eV with the inclusion of 1 nm step edges on either side of the interface. Insert: magnified region of the interface where increased intensity is seen at step edges. d) Electric field distribution at 4.1 eV when excited at the interface. e) Electric field distribution at 3.8 eV, excited at the interface, with the inclusion of a 2 nm Ag layer at the interface. f) Profile of the electric field distribution in c,d,e across the interface for a $Bi_2Se_3/Ag/C_{60}$ interface in blue, a rough Bi_2Se_3/C_{60} interface in green (dash-dot) and a sharp Bi_2Se_3/C_{60} interface in red (dash).

In some samples, an interface may not be atomically flat, such as in the sample discussed in section 5.4 and step edges may exist at the interface. In samples of Bi_2Se_3 step edges of 1-2 QL (nm) can occur at the top surface resulting in a rough surface. For example, the

sample studied in chapter 4 contains occasional step edges at the Bi_2Se_3 top surface that are well separated from each other. In chapter 5, a Bi_2Se_3/CuPc sample is investigated and shown to contain regions with several small step edges close to each other. The effect of step edges was simulated using the above model and including a rough interface composed of 1x10 nm rectangles on either side of the interface to simulate Bi_2Se_3 step edges. The electric field distribution at 4.1 eV, with the beam positioned 35 nm away from the interface, is presented in figure 3.13c. The interface can be seen to be excited at this energy similar to a sharp interface. A profile of the electric field was taken across the interface with the sample excited at the interface and is presented in figure 3.13f for both a sharp interface (red) and rough interface (green). The decay of the electric field away from the interface was similar in both cases, with a slightly increased intensity in the region surrounding the interface for a rough surface. This effect was very small so would be difficult to distinguish in EELS maps and, therefore, no appreciable change in the EELS data is expected for a small surface roughness in the case of an SPP excitation. Although very little difference is observed to the intensity and decay length of an interface plasmon when summed over a rough surface, the intensity the electric field intensity does appear to be greater at the corner of step edges, as seen in the insert in figure 3.13c. Since step edge corners are much less sharp in real samples, any effects would be much smaller but would still warrant further investigation into the effect of step edges at this interface and could be an interesting extension of the work presented in chapter 4.

To investigate the confinement of a plasmon excitation from a localised state and highlight differences from an SPP mode, simulations were carried out using the above model with the inclusion of a 2 nm Ag layer at the interface. The Ag layer is intended to model a two dimensional localised interface state with metallic conduction and excitations of its bulk plasmon represent excitations of a localised interface plasmon. Figure 3.13d,e shows the electric field distribution at a Bi_2Se_3/C_{60} interface and a Bi_2Se_3/Ag/C_{60} interface at 4.1 and 3.8 eV respectively, when excited by an electron beam at the interface. These energies were selected as the Bi_2Se_3/C_{60} SPP mode is expected at 4.1 eV and, as shown in previous sections, the Ag bulk plasmon has an energy of 3.8 eV. To achieve an equivalent comparison, with the same mesh, the central 2 nm of the model are meshed as separate regions which appear in the plot. When no Ag layer was present, the excitation at the interface decayed away from the central beam position with an exponential trend, with no evidence of localisation to the central meshed region. In figure 3.13e, a strong excitation is observed in the central Ag layer at 3.8 eV from the bulk plasmon mode. The intensity of the electric field across the Bi_2Se_3/Ag/C_{60} interface is shown in figure 3.13f and can be seen to have a sharp drop in intensity at the Ag interfaces and not the steady exponential decay observed when the

Ag layer is absent. This suggests that plasmon excitations from a localised state, behaving like bulk plasmons, are confined to the location of the state and do not show the same decay behaviour as regular SPP modes. Although this model is simplified containing a 2 nm layer instead of a 2D state and the plasmon dispersion will differ from that of a localised orbital excitation, limiting exact comparisons, it can still provide some useful insight. This result indicates that localised plasmons and SPP modes will not have the same confinement and could be distinguished from each other in EELS maps.

In the case of a plasmon excitation from electrons within π states in a single layer of atoms, the mode will be confined to an atomic layer and quickly decay in intensity perpendicular to the layer, similar to bulk plasmons [91]. An evanescent field will not extend to the penetration depth as was the case for an SPP. At a molecular interface, bonding and hybridisation can occur between molecular electronic states and plasmons at the interface of a dielectric. This results in localised states arising at the interface and plasmon excitations of electrons within these states. These hybridised plasmon modes would be more confined than SPP modes and observable in EELS maps. For example, when thin films of MnPc were deposited on a Bi_2Te_3 surface, the electronic behaviour of only the first two layers of MnPc molecules was changed, indicating states confined to the interface [78]. Differences in the confinement of a plasmon excitation, as well as differences in dispersion, can aid in assignment of these modes.

In cross-sectional specimen investigated by EELS and in simulations presented here, the metallic layer is just a line within the sample, but in a device it is an infinite sheet of metal. This changes the shielding experienced in other regions of the sample, limiting the comparison of cross-sectional specimen to actual devices. When in a cross-section, the electron beam can interact with material on the far side of the metallic layer before and after it enters the sample, resulting in excitations in that material. However, when in a device, the infinite metal sheet screens the material on the other side limiting excitations of the material on the far side of the interface. This is a limitation in studying these systems using EELS and the simulations presented in this chapter.

The intention of these simulations is to compare with experimental EELS spectra to highlight interfacial excitations from localised states. It turns out that experimental EELS spectra acquired across this interface do show differences from the simulated results in figure 3.12. Variations in both interfacial peak energy and confinement are observed, hinting towards interesting localised interactions at the Bi_2Se_3/C_{60} interface. This will be discussed in chapter 4, using simulated spectra as a reference to aid in interpretation of experimental results.

The absence of excitations from localised states and hybridised modes in simulated EELS spectra can be considered as both a limitation and benefit. This can be a limitation as spectra cannot be completely replicated by these simulations to validate experimental results. However, the absence of localised excitations from simulations allows for comparisons to be made with experimental data to highlight peaks arising from localised states. This can be used to aid in interpretation of EELS spectra with overlapping features and explore interesting interfacial interactions.

3.7 Conclusion

The purpose of this chapter was to discuss different methods of calculating EELS spectra and highlight their effectiveness in aiding with understanding of experimental EELS data for a variety of systems. Simulated spectra have been shown to replicate energies, lineshapes and localisation of plasmons in various nanoparticles and thin films. The influence of a rough thin film interface was investigated and shown to be small. The presence of a localised interface state was modelled and indicated differences in interfacial plasmon confinement compared to a regular surface plasmon. and localised surface state on EELS spectra

Numerical simulations of low-loss EELS spectra in COMSOL replicate experimental data for a wide variety of systems. Silver nanospheres and nanosphere dimers were simulated, resulting in spectra containing plasmon eigenmodes and coupling modes which agree with literature. The ability to simulate nanoparticle shape effects was highlighted with circular, square and triangular discs which show localisation of plasmon modes in the electric field and EELS spectra in agreement with experimental results. The effect of a substrate on the plasmon EELS spectrum of a silver nanoparticle has been shown to introduce additional excitation at the interface with the substrate.

EELS spectra of metallic thin films indicate bulk and surface plasmon behaviour, with localisation visualised in electric field distribution plots. Coupled interfacial plasmons were simulated for metal-dielectric interfaces with agreement to both experimental work and other simulation methods. Simulated EELS of topological insulator/organic interfaces reveal differences from experimental data, pointing towards hybridisation at the interface that is not captured in the model. A rough Bi_2Se_3 surface was shown to only slightly lengthen the decay length of an SPP excitation, to an extent not likely resolvable by EELS, and did not influence plasmon energy. Step edges observed in samples in chapters 4 and 5 will therefore have little effect on EELS spectra. The presence of a localised interface state, modelled as an Ag layer, resulted in a highly confined plasmon excitation at the interface, which was more localised than an SPP excitation. Although not an exact comparison to possible hybridised

states at a Bi_2Se_3/organic interface, this model provides some insight into potential plasmon confinement that could aid in understanding EELS maps presented throughout this thesis.

With the graphical interface provided in COMSOL, this simulation method can be easily expanded to more complicated systems with ease. For example, combinations of the systems presented throughout this chapter can be easily implemented to combine both nanoparticles and thin film interfaces. Furthermore, other types of simulations such as thermal heating and electric transport can be combined to obtain a complete characterisation of a system for applications. Compared to other EELS simulation software, longer computation times are often required to obtain solutions across the full 3D domain but these can be minimised by the use of symmetry conditions. The use of this method is limited due to the need for commercial software which can be expensive. However, due to the ease of use, increased complexity of systems that can be studied and the ability to couple other types of simulations, EELS simulations in COMSOL are an excellent companion to experimental work.

This chapter has replicated previous COMSOL studies of various nanoparticle systems in vacuum and on substrates. Thin film interfaces, which have previously been simulated in COMSOL, were explored for different materials and new approaches added to expand upon this work and investigate the effect of a rough interface or localised interface states on EELS spectra. Analytically calculated EELS spectra replicate bulk EELS data well and provide information on plasmon coupling over interfaces in thin film systems. These simulations have been shown to rule out plasmon coupling to explain interface localised peaks in experimental data and point to more interesting effects. They provide a useful tool to understand EELS spectra at interfaces. Throughout this thesis, calculated EELS spectra will be compared to experimental low-loss EELS data at a variety of different interfaces to understand features present. Additionally, calculated spectra will be used to fit experimental spectra across interfaces, highlighting features which are not present in calculations. By mapping the residuals of these fits, the localisation of such peaks can be observed.

4 Modulation of interfacial plasmons in Bi_2Se_3 with C_{60} molecular layers

4.1 Introduction

The ability to tune and switch the surface plasmonic behaviour of topological insulators (TIs) is vital to the practical use of these materials in future devices. Surface dopants have been shown to alter the Fermi energy of TI surface states and can protect or suppress topological behaviour, as discussed in section 1.2.2 [219, 66, 62]. The use of overlayers to achieve surface modification could prove useful since the TI remains intact without the requirement of optimising doping throughout the crystal. A wide array of different overlayers can be used providing varied effects, for example, metallic atoms such as Rb have been shown to create a two-dimensional electron gas (2DEG) at the surface [12, 65]. However, due to the reactivity of the dopants, these tend to be unstable unless maintained in high vacuum, which is not ideal for practical use. Organic thin films and dyes have also been shown to alter the TI surface behaviour and are more stable at standard pressures [71, 72, 74, 220–222]. Organic molecular layers could also provide a means of tuning the TI surface by the application of an external voltage, which can change the chemical potential of the organic [68, 223]. A first step in this process would be to determine the degree of modification to the TI surface by molecular overlayers.

Organic molecules have been proven to alter the surface band structure by Jakobs *et al.*, as observed using angle-resolved photoemission spectroscopy (ARPES) [6, 71]. Increased Rashba splitting was observed at TI-molecular interfaces, but as ARPES is a surface technique, the penetration depth is small, limiting the research to very thin layers of organic molecules [224]. For practical use, structures must be stable and functional at room temperature and so thicker layers of organic molecules could provide a more robust method of

altering the TI surface behaviour. Different organic materials are expected to have different effects on the Bi_2Se_3 and to test the effect of an organic thin film on the surface using EELS, a stable molecule that can withstand an electron beam is required. Organic materials tend to be sensitive to the atmosphere and the electron beam, with oxygen diffusion through organic layers possible, with extended exposure to air and amorphisation occurring quickly in the electron microscope [225]. C_{60} molecules have been shown to be stable and withstand time under an electron beam with minimal damage [149, 142], making C_{60} an ideal starting material. Additionally, high quality crystalline growth of C_{60} will be demonstrated on Bi_2Se_3 thin films in this chapter.

Fullerenes such as C_{60} have been studied extensively since their discovery in the 1980s and have been utilised for their wide bandgap and highly visible absorption, with applications in field effect transistors [226]. C_{60} is not very reactive and in solid form, molecules are bound together by vdW interactions. C_{60} molecules are easily modified with ligands or adatoms, which can alter the properties and expand the functionality. C_{60} was observed to change the Fermi energy but maintain the Dirac cone and topological surface state (TSS) when isolated C_{60} molecules were deposited on a Bi_2Se_3 thin film [6]. This was for a single C_{60} molecule, and the effect of thin film layers of C_{60} on the surface states is not known. C_{60} has a high electron affinity, which should result in charge transfer from the Bi_2Se_3 across the interface [227].

Each molecule has a cavity at its centre that can be doped with metallic elements to alter the chemical and electronic properties [228, 229]. The ability to change the dopant atom to alter C_{60} properties provides an additional advantage and makes C_{60} a good candidate as an organic dopant layer to modify the Bi_2Se_3 surface.

With the application of an electric voltage, the chemical potential of the C_{60} layers could be tuned, opening the prospect for tunable TI surface states [68]. The carrier density has been shown to increase with applied voltage [230] and electronic excitations have been shown to shift in energy [68]. The development of electrically tunable plasmonic devices has focused on semiconductors with a narrow bandgap such as graphene and requires a gate electrode on at least one surface [231]. The samples discussed here have been grown on substrates compatible with gating and research is ongoing to develop a top gating method on C_{60}. The ability to alter the behaviour of C_{60} with an applied gate voltage or metallic dopant provides many possibilities for tuning the system to fits the needs of future devices and extend the possible applications.

As discussed in section 1.4, the surface plasmon polariton (SPP) modes of Bi_2Se_3 have been observed at energies less than 200 meV, in the THz regime [94, 105]. To study these SSP modes directly, ultra-low energy EELS can be performed, however, it is also possible to

probe 2D π-plasmons at higher energies to understand changes to the TI surface modes [97]. 2D π-plasmons have been observed at TI surfaces and in 2D materials such as graphene [232, 233] and can indicate the presence of a 2D surface state [97]. By observing changes to the π-plasmon mode due to the presence of molecular overlayers, we can investigate changes to the TI surface state.

This chapter will investigate the Bi_2Se_3 surface plasmonic behaviour at interfaces with C_{60} molecular overlayers and compare it with the plasmonic behaviour at interfaces with Al_2O_3 substrate. Cross-sections are extracted from MBE grown thin films of Bi_2Se_3/C_{60} on sapphire substrates grown by collaborators at the University of Leeds. The structure of samples is first investigated to determine the crystallinity, quantity of defects and quality of interfaces. Plasmon modes are investigated by EELS in bulk and interface regions of the samples and compared to calculated spectra to determine modes localised to interfaces. Interfacial features are then investigated using momentum-resolved EELS to map their dispersion and understand the origins of these features. Density functional theory calculations performed by collaborators Ansari and Gity at Tyndall National Institute, University College Cork, are used to aid in interpretation of these results.

4.2 Structural analysis

Thin films of Bi_2Se_3 with a thickness of 15 nm were grown on c-plane orientated sapphire substrates by MBE at the University of Leeds. C_{60} was then deposited by MBE whilst the sample remained in ultra high vacuum. Two lamellae, termed A and B, were extracted from the samples using standard FIB procedures discussed in chapter 2. Sample A was prepared using the standard procedure and sample B was thinned with a thick region left on either side. During thinning of sample B, some platinum redeposited over the sample and can be seen in figure 4.1b. The redeposited platinum did not appear to alter the underlying structure of the $Al_2O_3/Bi_2Se_3/C_{60}$ sample as the atomic ordering was unchanged in TEM and STEM images and diffraction patterns were the same for both samples. Additionally, no changes to the low-loss EELS spectrum collected from Al_2O_3 and Bi_2Se_3 were observed. Both samples had similar TI layer thickness of 15 QL ($\approx$15 nm) and were orientated along the same zone axis, perpendicular to the c-axis of Bi_2Se_3 as shown in figure 1.3 in chapter 1. The lamellae were each around 26-35 nm thick in the regions imaged as measured by an EELS t/λ_i measurement of 0.72 in Bi_2Se_3 with a 60 kV electron beam [81].

Figure 4.2a presents a STEM image of a cross-section of the sample, with atom-resolved features clearly visible. The image shows the interface of the TI layer with the substrate and C_{60} overlayer to be atomically sharp. Some damage can be observed at the Al_2O_3/Bi_2Se_3

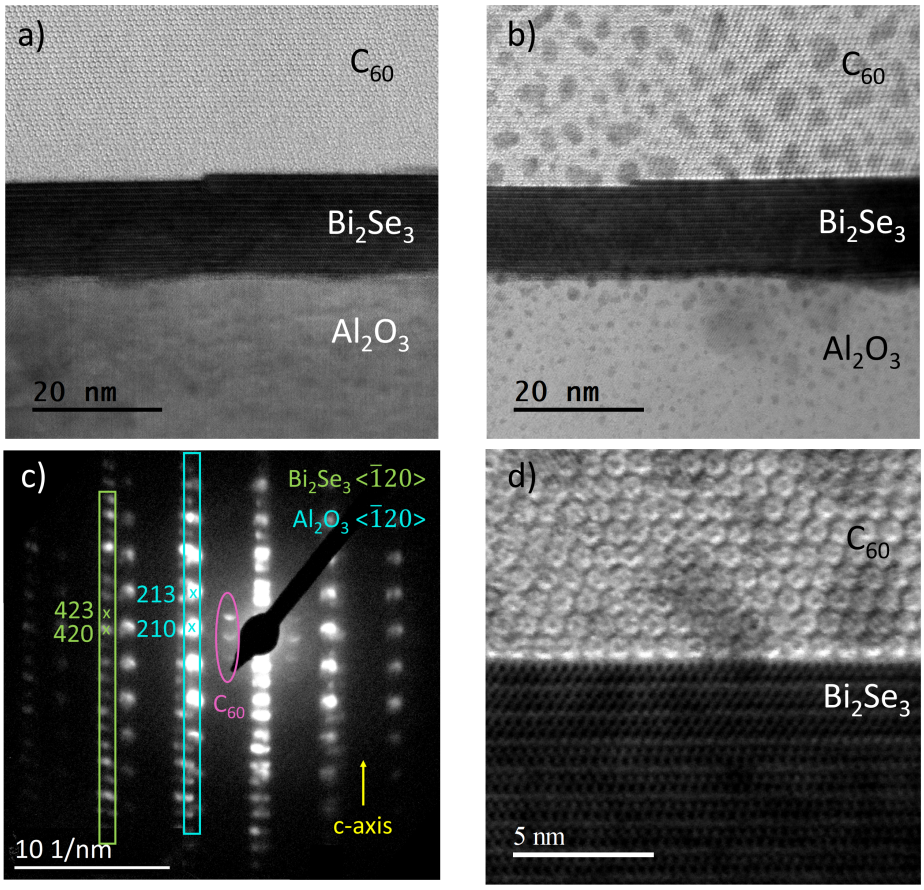

Fig. 4.1 BF STEM images of the sample a) overview of sample A, b) overview of sample B. A step edge in the Bi_2Se_3 layer is observed in both samples and provided a reference point to locate these region of the samples. c) CBED diffraction pattern of sample B where the Al_2O_3, Bi_2Se_3 and C_{60} lattice spots can be observed. d) BF STEM image of sample B at a higher magnification showing the sharp interface between Bi_2Se_3 and C_{60}.

interface, which likely occurred during FIB preparation due to the hardness of sapphire. Both Al_2O_3 and Bi_2Se_3 have a hexagonal structure and their c-axes are aligned in the diffraction pattern in figure 4.2b, where the most intense diffraction spots are from Al_2O_3 and the weaker ones from Bi_2Se_3. The measured lattice parameters for Bi_2Se_3 are $a,b = 4.3 \pm 0.1$Å and $c = 28.7 \pm 0.1$Å which agree with the expected reference structure of $a,b = 4.41$Å and $c = 28.64$Å for unstrained Bi_2Se_3 [234, 29]. For Al_2O_3 these parameters are $a,b = 4.7 \pm 0.1$Å and $c = 12.9 \pm 0.1$Å in agreement with literature values of $a,b = 4.76$Å and $c = 12.99$Å [235]. The growth direction of these samples is along the c-axis which is indicated in figure 4.2c. The layered structure of Bi_2Se_3 can be observed clearly in this image with the brightest spots being Bi atoms and the dark lines where van der Waals (vdW) gaps occur between quintuple layers as described in section 1.2.

The Bi_2Se_3 films were highly uniform with no grain boundaries observed in the 700 nm thinned region of the lamella of sample A and large grain sizes ranging from 100-400 nm in sample B. Common defects often found in samples of Bi_2Se_3 include native defects which include Se vacancies, interstitial atoms and Bi_{Se} antisite defects which lead to the n-type behaviour of the material [236, 237]. These defects were not observed in images of the samples discussed here, however, individual point defects can be difficult to resolve in STEM images therefore the presence of these defects cannot be fully ruled out. The plasmonic behaviour of interest in this thesis should be unaffected by this type of defect, with the main result of their presence being an increase in bulk carrier density. Another frequently observed defect involves changes to the QL structure with Bi layers interstitial within vdW gaps [237] or changes to the number of covalently bonded layers between 3 to 7 layers. Due to the high quality MBE growth of these films, this type of defect has not been observed. Step edges were observed at the Bi_2Se_3/C_{60} interface in both images in figure 4.1 which appear to be one QL high. EELS data was not acquired at these step edges but further investigation into the electronic behaviour at these defects could be interesting as step edges could alter the surface propagation behaviour.

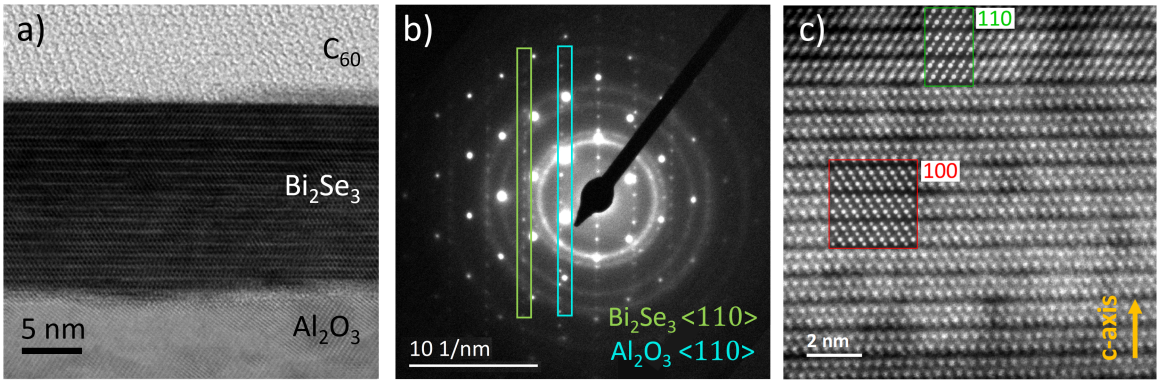

Fig. 4.2 a) BF STEM image showing the layered structure where a twin plane occurs three QL from the top of Bi_2Se_3. b) SAD diffraction pattern over the sample with diffraction spots for the Al_2O_3 and Bi_2Se_3 lattices and diffraction rings from the amorphous Pt layer deposited during FIB preparation. c) HAADF STEM images of the Bi_2Se_3 layer where the twin plane occurs three QL from the top. Simulated STEM images for sample orientations <100> and <110> are overlaid on either side of the defect.

In some samples a twin plane formed within the TI layer, which in sample A was 3 QLs from the top surface as indicated in figure 4.2a. This twin plane represents a change in growth direction with the unit cell rotated by 58-61° around the c-axis. Figure 4.2c contains a HAADF image of the Bi_2Se_3 layer where the twin plane is seen on the right overlaid with simulated HAADF images at different crystal orientations. 'Dr Probe' multislice software

was used to simulate two HAADF images of Bi_2Se_3 with the sample orientation rotated 60° around the c-axis recreating the image on either side of the twin plane. Simulated images were produced for an accelerating voltage of 200 kV and the HAADF detector was set to cover an angular range of 70 to 250 mrad. The simulated HAADF images appear sharper than the experimental data because the simulations assume an idealised electron probe, detector response and limited thermal vibrations. Experimental images are blurred by lens aberrations, thermal diffuse scattering, sample drift and noise, which reduce the contrast and sharpness of atomic columns. This type of defect is very common in TI films with very little change in energy favourably from the two growth directions [238–240]. As the growth orientation changes after a van der Waals gap there is very little strain within the layers on either side of the gap, however a slight increase in the size of the Van der Waals gap can be observed. In this case the gap increase was found to be less than one pixel of the image but has been shown in literature to increase up to 0.12 Åin Bi_2Te_3 samples [240].

Figure 4.3 shows the high crystallinity of the C_{60} layer with a face centred cubic lattice structure with measured unit cell size of 14.1 Å in agreement with literature for an unstrained lattice [241, 242]. Columns of C_{60} molecules are observed in BF images in figure 4.3a where darker contrast is present in the centre of each molecular column due to the cavity at the centre of each molecule. The diffraction pattern in figure 4.3b shows the <110> zone axis of C_{60} which is in line with the beam, with the c-axis of the FCC structure aligned along the grown direction which runs vertically along the image in figure 4.3a. Several intrinsic stacking faults, as highlighted in figure 4.3c, were observed to originate from the interface with Bi_2Se_3 and often coincided with step edges in the Bi_2Se_3 seen in figure 4.1. The stacking faults could be clearly identified by the use of geometric phase analysis (GPA) on TEM images [243].

GPA was used to measure lattice strain and distortions within TEM images by comparing phases in different regions of the lattice. A fast Fourier transform (FFT) was first obtained from the TEM/STEM image and two g-vectors are selected in the FFT. The phase of each g-vector was then calculated and compared to determine relative distortions and strain in the lattice. Large strain values indicate changes to the structure such as stacking faults which are shown in figure 4.3c. The strain calculated along these faults appears to be 8-12% horizontally in the image. This large strain value was due to a discontinuity in the phase at the stacking fault and is not quantitatively accurate, therefore, only used to highlight the fault [244, 245]. The relationship between Bi_2Se_3 and C_{60} in this structure is through van der Waals epitaxy, which is a weak interaction that does not significantly strain the lattice towards the interface. It has been observed that at steps edges, additional strain can be introduced due to the presence of Bi dangling bonds which bond with C_{60} molecules [116]. This was shown

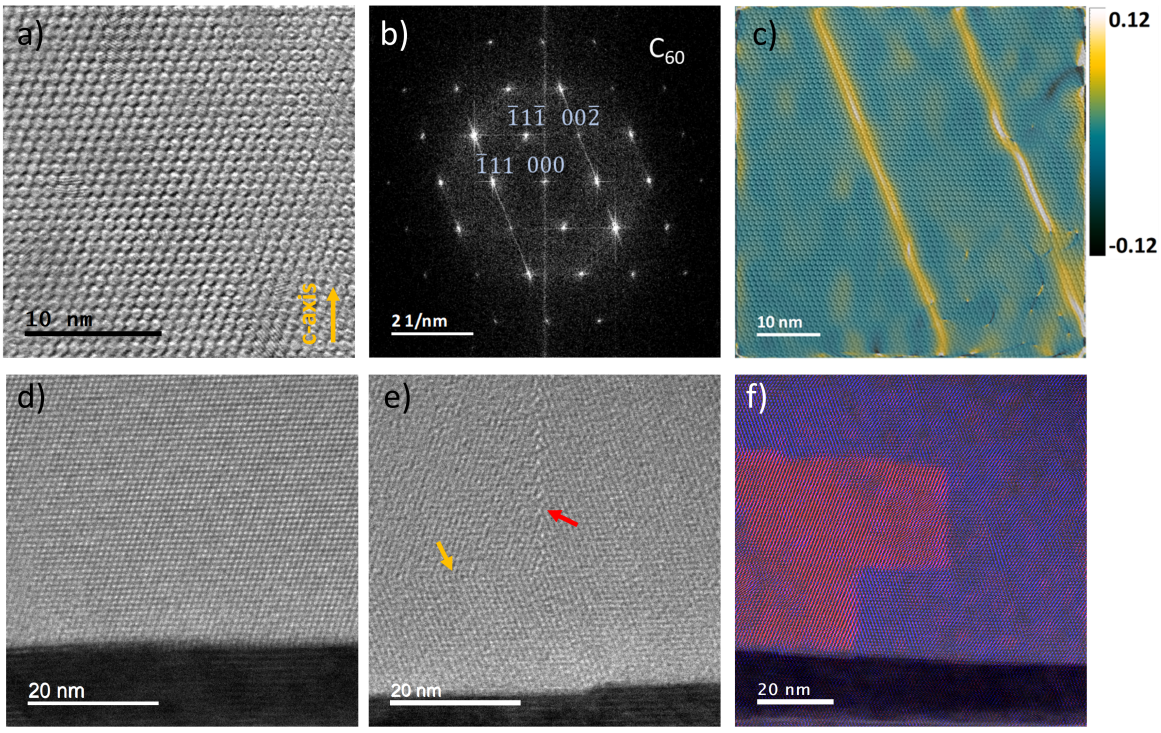

Fig. 4.3 a) BF STEM image where columns of C_{60} molecules were observed with a face centred cubic structure. Fourier filtering was used to decrease the appearance of Pt surface contamination. b) FFT of the C_{60} lattice with diffraction spots indexed. c) Geometric phase analysis of an image of the C_{60} lattice which highlights stacking faults [243]. d) BF TEM image of a region of the Bi_2Se_3/C_{60} interface with no defects. e) BF TEM image of a region of the Bi_2Se_3/C_{60} interface where two grains can be observed with their grain boundaries indicated with the yellow (twin) and red arrows. f) Overlaid phase images of two C_{60} grains shown in red and blue.

to occur over much larger step edges resulting in amorphisation of C_{60} at the interface which was not observed here.

As well as intrinsic stacking faults seen in figure 4.3c, some twin plane defects were observed within the C_{60} layer which have been commonly observed in literature [246, 242, 247]. Figure 4.3e contains a TEM image where two C_{60} grains can be observed with their boundaries highlighted. The yellow arrow indicates a coherent twin plane boundary, where a change in growth direction of C_{60} was observed. At the centre of the image, the grain boundary between a region which has changed growth direction due to a twin plane and a region with the original growth direction, is indicated by the red arrow. This grain boundary is orientated perpendicular to the growth direction, with symmetric grains on either side. This type of grain boundary is often referred to as a tilt boundary [248]. The grains observed did not extend throughout the full layer due to the presence of further twin planes realigning the

two grains. This can be seen in figure 4.3f where two grains are shown in different colours, red and blue, from phases images obtained from the FFT of the TEM image. The vertical boundaries of these two grains are tilt boundaries similar to the one indicated in figure 4.3e and the horizontal boundaries are twin plane defects similar to the one identified in figure 4.3e. In some regions different crystal grains were observed on either side of the stacking faults with a slightly different orientation. Diffraction spots from two crystal orientations on either side of a stacking fault are highlighted in the diffraction pattern in figure 4.3c. On average, the spacing between defects horizontally along the C_{60} layer was on the order of 20-30 nm.

Overall these samples were of a high enough quality to use to investigate their plasmonic properties using EELS. The t/λ_i value at 60 kV was around 0.7 for both samples which is suitable for measurements. This indicates a thickness of 36 nm in the Bi_2Se_3 from the inelastic mean free path value of 51 nm in section 2.5.

4.3 EELS

Surface plasmons give information about properties at the surface or interface of a material. Using EELS we can observe changes in the plasmon spectrum at interfaces to reveal information about changes in chemical potential and bonding at an interface. Differences in the plasmon spectrum from a TI/insulator and a TI/organic interface can highlight changes to the surface due to the presence organic molecules.

Firstly, plasmons and electron transitions in EELS spectra from bulk regions are identified and their origins understood with the aid of literature. Secondly, changes to EELS spectra approaching interfaces will provide information on interactions occurring at the interface and the localisation of these features will give insight into the length-scales of interfacial interactions. By comparing experimental data to calculations of interfacial EELS spectra from bulk dielectric functions, plasmons originating from surface states and interfacial hybridisation can be highlighted and distinguished from the effect of interfacial plasmon coupling.

EELS spectra were acquired from several samples of $Al_2O_3/Bi_2Se_3/C_{60}$ at 60 kV at SuperSTEM, using methods described in chapter 2. The data presented was acquired using a convergence angle of 30 mrad and a collection angle of 22 mrad. In momentum space this equates to collecting over the first two Brillouin zones of Bi_2Se_3. Spectra from each main region of the sample are presented in figure 4.4b for bulk and interface regions.

EELS spectra were calculated analytically using equation 3.13 in section 3.3 to replicate experimental EELS spectra [166, 167]. A relativistic calculation was performed as this did

not significantly increase computation time. Dielectric functions were derived from Kramers-Kronig analysis of bulk spectra collected from the Al_2O_3, Bi_2Se_3 and C_{60} regions of the experimental dataset and used in equation 3.13 to calculate EELS spectra on approach to each interface. Calculated EELS spectra are depicted as dashed lines in figure 4.4b for each region of the sample. Features in bulk spectra will first be discussed as they should be replicated by the calculations. Next, experimental spectra at both interfaces will be investigated and compared with calculated spectra. Differences between the experimental and calculated interface spectra can highlight features which originate from interface localised interactions such as surface plasmons.

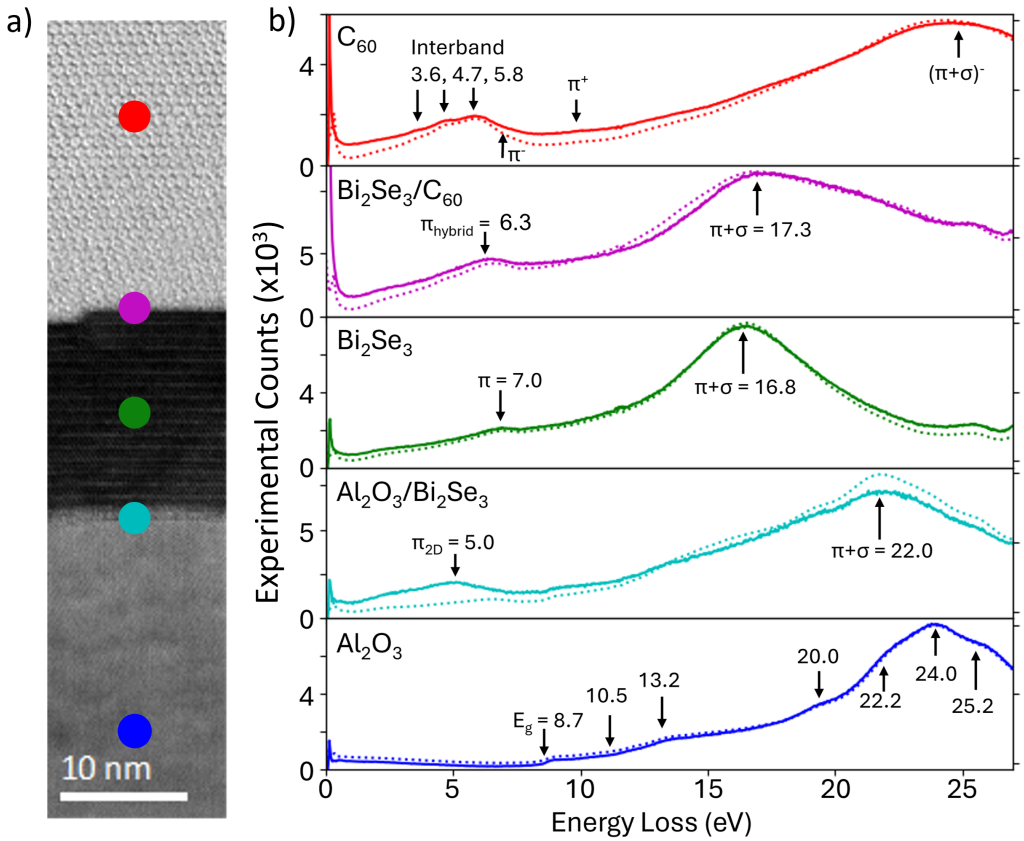

Fig. 4.4 a) BF STEM image showing the cross section of the $Al_2O_3/Bi_2Se_3/C_{60}$ sample from bottom to top. b) EELS spectra from each region as indicated on the STEM image, solid lines, and analytically calculated spectra from each region, dashed lines. Interband transitions, plasmons and bandgaps are indicated on each spectrum.

Peak fitting was carried out in 'Hyperspy' for each spectrum using the procedure outlined in section 2.7.2, where plasmon peaks were fitted as pseudo-Voigt functions with equation 2.6. To account for background noise, an additional constant offset function was included in

the fit, with its minimum value set to 0. Fitting was carried out with as few peaks as possible initially, which was 2 peaks for TI and C_{60} bulk and their interface representing the π and $\pi+\sigma$ plasmons which are indicated in figure 4.4b. The residuals of this fit in C_{60} revealed several peaks which could be explained by additional features observed in literature. These peaks were fitted using additional pseudo-Voigt functions and are shown in figure 4.5a. At higher energies, greater than 25 eV, Bi core edges are present in the bulk Bi_2Se_3 spectrum and additional peaks were included in the fit to account for these edges, as shown in figure 4.5b.

In bulk Al_2O_3, the bandgap is observed at 8.7 eV as a rapid increase in spectral intensity, indicative of a direct bandgap [249].This bandgap was fitted with a logistic function described by equation 2.9. Upon comparison with spectra from literature, other features in the spectrum were identified. Peaks at energies 10.5, 13.2, 20.0 and 25.0 eV were attributed to interband transitions observed in literature [250, 251] and the peak at 24.0 eV identified as a volume plasmon [252]. The peak at 22.2 eV was observed to slightly change in regions of the sapphire (in this and other samples) where the most FIB damage was seen, indicating defects such as oxygen deficiency due to damage, which is consistent with peaks emerging due to surface reduction [250]. The calculated spectrum, shown as a dashed line in figure 4.4b, in bulk Al_2O_3 is in agreement with the experimental dataset, validating the calculations.

The EELS spectrum from bulk Bi_2Se_3 contained two plasmon peaks and two Bi edges shown in figure 4.5b. Peaks at 26.4 and 28.3 eV are due to core-level Bi transitions from 5*d* orbitals to the conduction band and are shown at the far right of figure 4.5b with the latter edge slightly out of frame [253]. The plasmon peaks were identified at 7.2 eV for a π-plasmon and 17.3 eV for a $\sigma+\pi$ plasmon [97]. The π-plasmon originates from excitations of electrons in π-bonds within the bulk of the material.

Seven peaks were identified in the bulk C_{60} spectrum shown in figure 4.5a, most of which appear only weakly in comparison to the dominant volume plasmon (peak 7) at 25 eV. Initially, the spectrum was fitted with two peaks with energy constrained between 3 and 7 eV and 20 and 27 eV, revealing additional peaks in the residuals of this fit. The energies of peaks in the residuals of the fit coincided with expected interband transitions observed in literature, so, additional peaks were included in the fit [254, 228, 255, 256]. Peaks were then fitted with their energy constrained between values close to the expected peak energy. Peaks labelled 1-3 indicate allowed transitions HOMO to LUMO+1, HOMO to LUMO+2 and HOMO-1 to LUMO, present at energies 3.6, 4.7 and 5.8 eV respectively [254, 257]. The relative intensities of these three peaks are also in agreement, where the intensity of peak 3 is the greatest and peaks 1 and 2 appear as shoulders to peak 3. Peaks 4-6 were identified as $\pi \rightarrow \sigma^*$, $\sigma \rightarrow \pi^*$ and $\sigma \rightarrow \sigma^*$ interband transitions and peak 7 as a

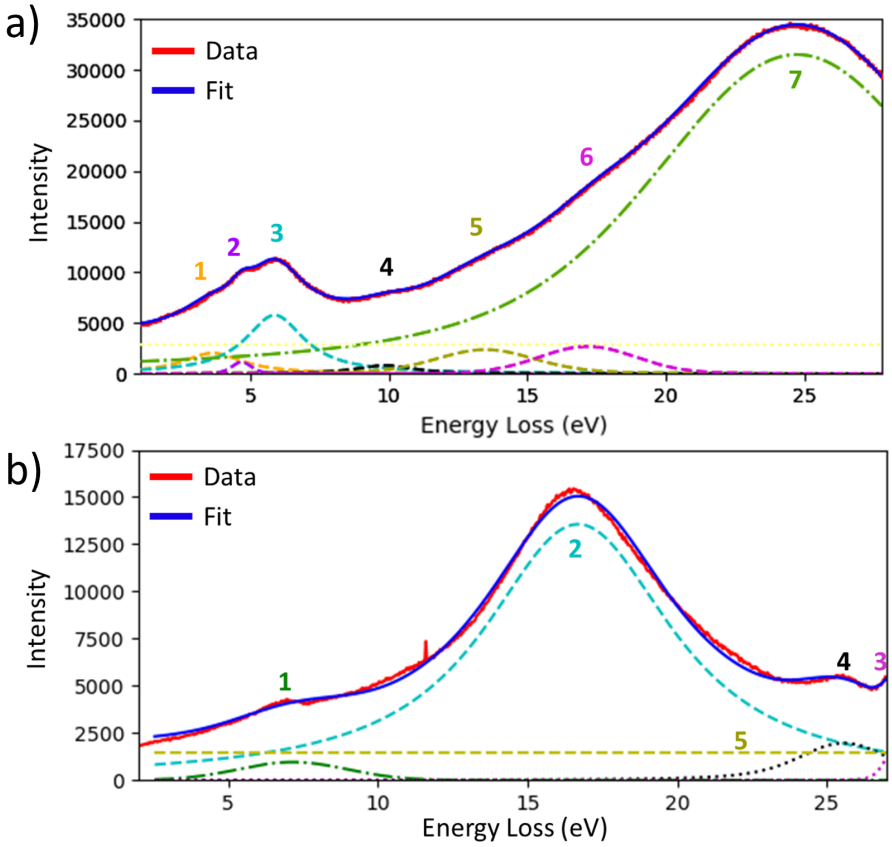

Fig. 4.5 a) EELS spectrum in bulk C_{60} with interband transitions and plasmons fitted. Where peaks labelled 1-6 are interband transitions and 7 is a bulk plasmon. b) Fitted bulk Bi_2Se_3 spectrum where 1 and 2 are π and $\pi+\sigma$ plasmons respectively, 3 and 4 are Bi edges and 5 is a uniform background modelled by a constant offset.

$\pi+\sigma$ volume plasmon. Additionally, a weak π^- plasmon was identified at 6.1 eV which is described in some reference data but not consistently across all literature [258, 259].

At the interface between Al_2O_3 and Bi_2Se_3 a surface plasmon (SP) was identified at 5.3 eV. The spatial extent of the feature is indicated in figure 4.6a and found to be active only within 2 nm of the interface, showing clear localisation at the interface rather than in the bulk material. The EELS map over the energy range 4.5 to 5.5 eV shows the greatest intensity, yellow, at the interface which decays slowly into Bi_2Se_3 to lower intensity, from yellow to red. The decay of this interface mode is not symmetrical about the interface and a much faster decay in intensity is observed towards Al_2O_3 from the interface, where the EELS map intensity quickly decreases, seen as a change from yellow to blue then black in the colour map. In the calculated EELS spectrum in figure 4.6c, shown in red, this peak is notably absent. At the higher energy part of this spectrum there is also some disagreement.

The calculated spectrum has greater intensity around 22 eV than in experimental data seen in figure 4.4b. This could derive from FIB damage from amorphisation of the sapphire in this region as the peak in Al_2O_3 at this energy is attributed to oxygen edges that are absent in pristine sapphire. Sample damage could not, however, explain the experimental peak at 5.3 eV, which is present in all datasets from several different lamellae containing a Al_2O_3/Bi_2Se_3 interface. Therefore, as it is not present in the calculated EELS spectrum, the surface plasmon cannot be described by coupling of the bulk dielectrics on either side of the interface. It is concluded that it has some other origin and is specific to the interface.

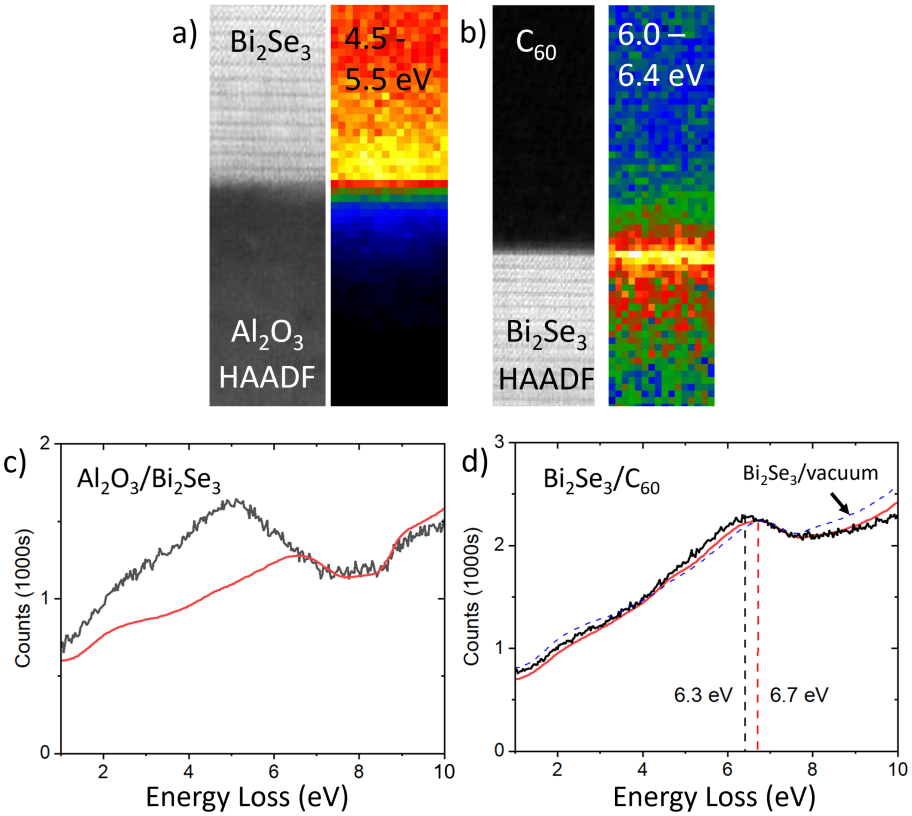

Fig. 4.6 a) HAADF STEM image of the Al_2O_3/Bi_2Se_3 interface alongside an EELS map showing the spectral intensity at 4.5-5.5 eV over the same region. b) HAADF STEM image of the Bi_2Se_3/C_{60} interface alongside an EELS map at 6.0-6.4 eV over the same region indicating an interface localised feature which decays quickly away from the interface. c) Experimental (black) and calculated (red) EELS spectrum at the Al_2O_3/Bi_2Se_3 interface where the peak at 5 eV in the experimental data is absent from the calculated spectrum. d) Experimental (black) and calculated (red) EELS spectrum at the Bi_2Se_3/C_{60} interface where the peak energies of the indicated peak are different for the calculated and experimental data. A calculated EELS spectrum of a Bi_2Se_3/vacuum interface is provided as a blue dashed line for comparison.

The Bi_2Se_3/C_{60} interface spectrum does not contain a peak at 5.3 eV localised to the interface. Instead, the interface spectrum contains a low energy peak at 6.3 eV. This peak appears to be more localised to the interface than the SP at the Al_2O_3/Bi_2Se_3 interface, with a quick decay away from either side of the interface. When compared to the calculated spectrum, shown in red in figure 4.6d, the low energy peak is red-shifted by 0.4 eV, suggesting that it is not fully captured by the analytical calculation. This indicates that this peak cannot be described by plasmon coupling across the interface and must instead be attributed to an interface localised interaction. The energy of this peak in the experimental data also differs from the calculated energy at a Bi_2Se_3/vacuum interface, shown as a dashed blue trace in figure 4.6d, suggesting that it is not due to aloof excitation of the Bi_2Se_3 π plasmon. As the energy of this surface peak differs from the surface peak at the Al_2O_3/Bi_2Se_3 interface, some modification of the Bi_2Se_3 surface has occurred due to the C_{60} layer. The analytical calculations do not include any effects of hybridisation between the Bi_2Se_3 surface and C_{60} molecules, and we therefore propose that this feature could be a hybrid plasmon resulting from hybridisation at the interface. Density functional theory (DFT) simulations will give further insight into this hybridisation in section 4.5.

To further visualise the localisation of surface modes and highlight intensity variations, spectrum images acquired across the full cross-section were fitted using calculated EELS spectra. EELS spectra were calculated analytically using the method described in section 3.3, for a series of positions at different distances, x, from each interface. This produced an array of simulated spectra, $S(E,x)$, representing the expected EELS spectrum at each impact parameter.

The experimental spectrum image (SI) was first normalised with respect to the zero-loss peak (ZLP) intensity. At each pixel in the SI, the experimental EELS spectrum, $S_{exp}(E,x)$, was then fitted using each calculated spectrum in the array as a fixed pattern function as

$$S_{\text{fit}}(x) = Af(S(E),x). \tag{4.1}$$

where A is a free scaling parameter representing the amplitude of the calculated pattern. The fitting was performed in 'HyperSpy' with A as the only free parameter. For each pixel, the quality of fit was evaluated by finding the residuals between the experimental data and the fit and expressed as

$$R^2 = 1 - \frac{SS_{\text{residuals}}}{SS_{\text{total}}}, \tag{4.2}$$

where $SS_{\text{residuals}}$ is the sum of squares of residuals between the experimental and fitted spectra and SS_{total} is the total sum of squares. The R-squared value, R^2, ranges from 0 to 1, where a greater value indicates a better fit. This procedure was repeated for all simulated positions, x,

and the calculated spectrum that yielded the highest R^2 value was identified as the best-fitting model spectrum for that pixel. The corresponding amplitude and R-squared value for the best fitting spectrum were recorded for each pixel and shown in figure 4.7b,c. The fitted spectra were used to reconstruct a fitted spectrum image and compute the residuals between experimental and fitted data.

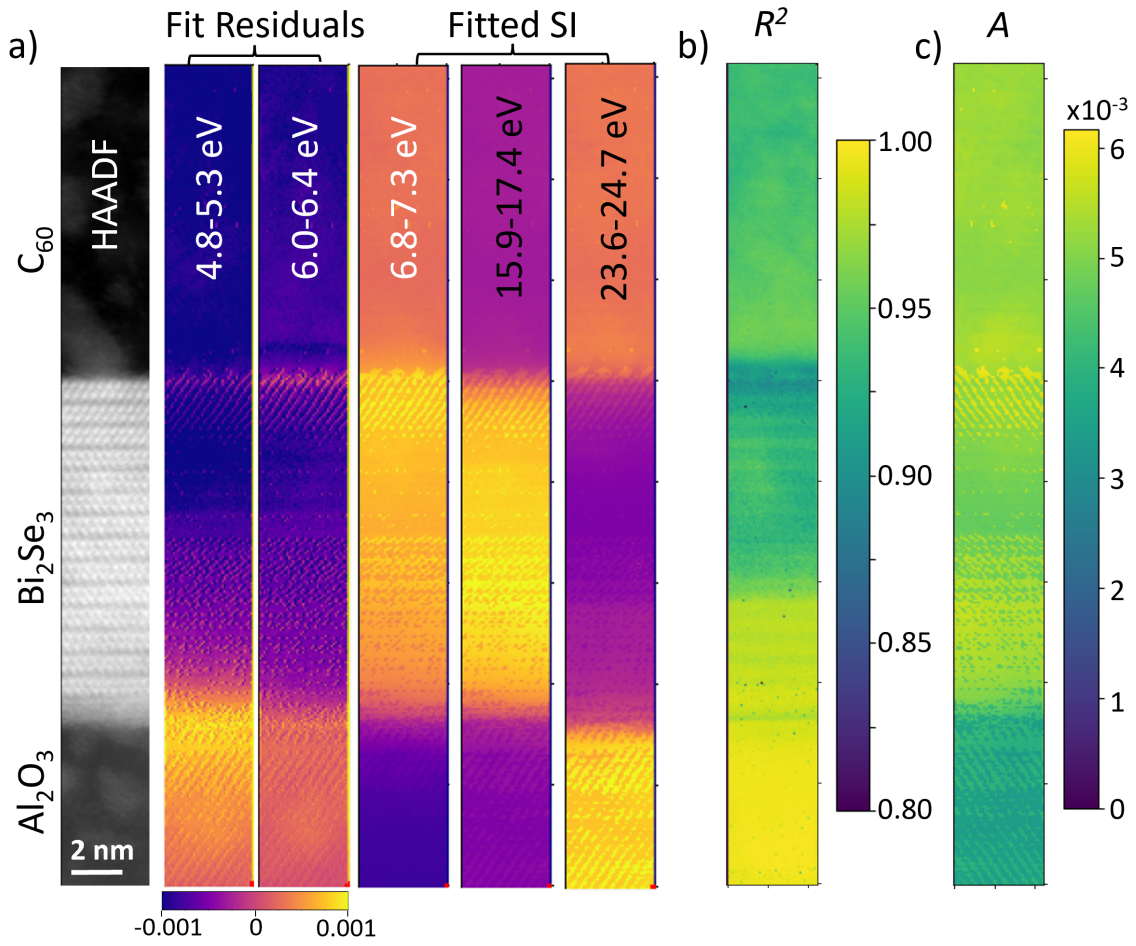

Fig. 4.7 a) Fitted EELS spectrum images and residuals over selected energy ranges. From left to right: HAADF STEM image of the data acquisition region. Residuals of the fitted SI at energies 4.9-5.1 eV and 6.0-6.4 eV which correspond to the energies of interfacial plasmons which were not replicated in calculations. The fitted SI over energy ranges 6.8-7.2, 15.9-17.4 and 23.6-24.7 eV corresponding to bulk plasmon energies which were replicated in calculations. b) Best fit R-squared values for the fitted SI image where higher R-squared values were calculated for the Al_2O_3/Bi_2Se_3 region and indicate a better fit and decreased values were obtained at interfaces. c) The amplitude of best fitting calculated spectra for each position in the SI image where lattice contrast can be observed.

Figure 4.7b depicts the highest R-squared value recorded for each pixel in the SI. The R-squared value can be seen to reduce at both interfaces, with a more significant reduction observed at the Bi_2Se_3/C_{60} interface as indicated by the blue colour at this interface. This reduction in how well the experimental data can be fitted with the calculated spectra indicates the difference between the experimental and calculated spectra differ substantially at this interface. The fit improves within 2 nm of the interface which is a similar length scale to the decay of the hybrid plasmon identified in experimental data at the Bi_2Se_3/C_{60} interface in figure 4.6b. Within the TI layer, the R-squared value is observed to drop slightly within van der Waals gaps which could be due to a difference in the relative intensities of plasmon peaks in Bi_2Se_3 in QLs and van der Waals gaps. Within van der Waals gaps, channelling of the electron beam can occur, resulting in increased intensity of the $\pi + \sigma$ plasmon mode. As the dielectric function of Bi_2Se_3 is calculated from an average region of Bi_2Se_3 across QLs and gaps, it will be most similar to the spectra acquired in QLs which could explain the small reduction in R-squared value of the fits obtained.

The amplitude of the fitted spectrum at each pixel is shown in figure 4.7c and contains some details of lattice fringes within the image. At the Bi_2Se_3/C_{60} interface four circles of increased intensity can be seen. Interestingly, these are the first layer of C_{60} molecules. This increased intensity is present in the amplitudes of fitted data, shown in figure 4.7c, indicating an enhancement of all signal at the first molecular layer. This is consistent with density functional theory (DFT) simulations, which will be discussed later in this chapter, that suggest a transfer of charge to the first layers of C_{60} molecules. The signal enhancement at the surface could be due to coupling between the surface and molecular resonances which can amplify the excitation signal. This effect has been termed as 'surface-enhanced EELS' and occurs when plasmonic resonances in an material occur at similar energies to electronic excitations and vibrations of nearby molecules [96]. The enhancement of plasmonic signal at the interface could be utilised to enhance signal in TI plasmonic devices.

Figure 4.7a contains the fitted spectrum images and residuals at different energy ranges. The residuals are useful because they allow us to identify any features which are absent in the calculated spectra. The first two plots contain residual signal from subtraction of the fitted SI from experimental data. At 4.9-5.1 eV the greatest intensity of the residuals was observed at the Al_2O_3/Bi_2Se_3 interface, where the surface plasmon was not present in the calculated spectrum. The next panel at 6.0-6.4 eV shows increased intensity at the Bi_2Se_3/C_{60} interface, which is confined to a smaller region perpendicular to the interface. From the residuals we can observe that, alongside changes in energy, the localisation of the surface features differs between both interfaces indicating that the Bi_2Se_3 surface plasmon observed at the substrate interface is substantially different to the plasmon localise to the C_{60} interface. Residual

signals in bulk Al_2O_3 appear greater than those in bulk Bi_2Se_3 and C_{60}, here and in chapter 5. This is due to the calculated spectra consistently having a slightly greater intensity than experimental results at low energy. This only occurred for the Al_2O_3 spectrum and was likely a consequence of the choice of cut-off momentum in equation 3.13. The final three panels contain the fitted SI at selected energies where bulk plasmons were observed. The first of these spans the range 6.8-7.3 eV, capturing the Bi_2Se_3 π plasmon energy, where the greatest intensity was observed in the TI layer. At 15.9-17.4 eV, the Bi_2Se_3 $\pi+\sigma$ plasmon dominates the SI, with most intensity in the Bi_2Se_3 layer. Finally, at 23.6-24.7 eV intensity is present in Al_2O_3 and C_{60} layers where their bulk plasmons dominate.

4.4 Momentum-resolved EELS

The Bi_2Se_3 surface plasmon has been shown to be at a different energy at the interface with C_{60} compared to the interface with Al_2O_3, which indicates that there has been some change at the surface. However, to better understand why we observe a change in energy and what kind of interface localised mode this could be, more information is required. By comparing the plasmon dispersion of these modes, we can obtain some further insight into their origins. The plasmon dispersion can be measured using momentum-resolved EELS as discussed in section 2.6. As different features in the low loss spectrum disperse differently, we can better determine the interactions occurring the the TI/C_{60} interface by mapping the dispersion. For example, bulk plasmons disperse parabolically and interband transitions show no dispersion.

Momentum-resolved EELS spectra at each region of the sample were recorded over a momentum range of 0 to 2.1 $Å^{-1}$ with a momentum resolution of $\pm 0.33 Å^{-1}$. Measurements were carried out at 60 kV on SuperSTEM3 using the procedure outlined in chapter 2 with a 1 mm EELS aperture and 1 mrad convergence semi-angle. The collection angle was 2.3 mrad.

The momentum of each spectrum was calibrated using the diffraction pattern from Bi_2Se_3 and positioning the EELS aperture along the ΓM direction as indicated in figure 4.8b. The size of the aperture in momentum space was calculated as 0.33 $Å^{-1}$ and was positioned 0.71, 1.00, 1.43 and 2.14 $Å^{-1}$ from the centre Bi_2Se_3 diffraction spot for sample A. The first three positions were within the first BZ of the diffraction pattern and as the final position was in the second BZ it was equivalent to 0.77 $Å^{-1}$ in the first BZ, with a much lower signal to noise ratio. For sample B, similar positions were used: 0.00, 0.77, 1.43 and 2.14 $Å^{-1}$. The probability of scattering decreases radially with increasing q away from the central Bragg position at 0 $Å^{-1}$, as described by the angular dependence of electron scattering described in section 1.3. This can be seen in the decaying intensity of a diffraction pattern away from the centre, shown in figure 4.8c. Within a circular aperture, the mean value of momentum can

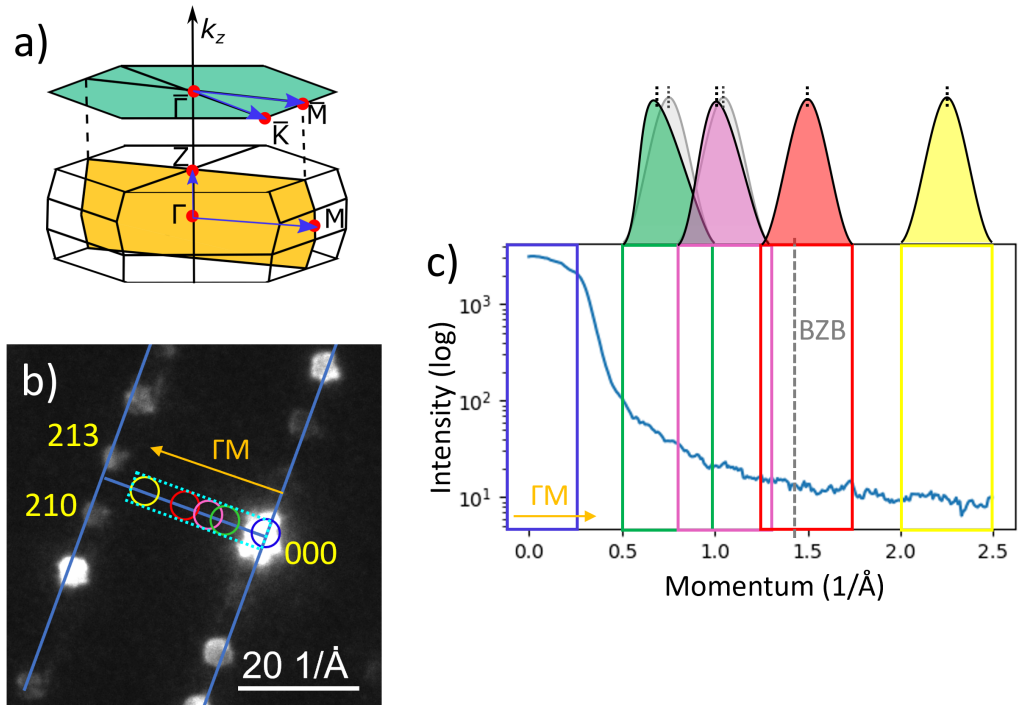

Fig. 4.8 a) Schematic of the Brillouin zone of Bi_2Se_3, where the main symmetry directions are indicated. The yellow shaded area represents a cross-section specimen and the green shaded section represents a plan view specimen. b) The Bi_2Se_3 diffraction pattern that was used to align the EELS aperture for measurements. c) The intensity of signal collected as it decays with increasing momentum. Positions of the EELS aperture in panel b are overlaid in the some colour and the Brillouin zone boundary (BZB) is indicated. A representation of the momentum of EELS signal collected from each circular aperture is presented and the average value indicated with a dashed line. At lower values of q, the average momentum is skewed slightly lower than the momentum at the centre of the aperture due to more signal at lower q being collected.

vary from the momentum at the centre of the aperture due to the contribution of more signal from lower momentum [152]. This is illustrated in figure 4.8c, where a representation of the amount of signal collected by the aperture at a given momentum is shown at each aperture position. Due to the larger amount of signal collected at lower momentum in the first two aperture positions, the average momentum of signal collected differs from the momentum at the centre of the aperture. The first off-axis qEELS dataset, highlighted in green in figure 4.8b, had an average momentum of 0.64 $Å^{-1}$ instead of its central position of 0.71 $Å^{-1}$. This change in average momentum value was calculated for each aperture position by finding the position in momentum which collected the average number of electrons within the aperture. The momentum value for this qEELS dataset was therefore adjusted to account for this in peak energy vs momentum plots. The change in momentum value at high momentum upon

applying this correction was not significant and the average momentum was very similar to the momentum at the centre of the aperture.

Momentum-resolved EELS spectra are shown in figure 4.9 for each bulk region of the sample. A linear least-squares fit of several peaks was used to fit each qEELS spectrum in Hyperspy. The low energy region between 1 and 12 eV was fitted separately to limit free parameters and prevent overfitting. Further details of the fitting method are included in chapter 2. The ZLP was modelled by a power law function included in the fit as the momentum-resolved spectra were not deconvolved for the analysis.

In bulk Bi_2Se_3, two plasmons are observed to disperse to higher energy with increasing momentum. For the $\pi + \sigma$ plasmon, shown in figure 4.9a, the initial peak energy at 0 $Å^{-1}$ was centred at 16.8 eV which is slightly lower in energy than the non-momentum-resolved EELS measurements discussed in section 4.3. All bulk plasmon peaks were observed to have slightly lower peak energy at 0 $Å^{-1}$ than their standard EELS counterparts due to the summation of peak energies to a higher momentum encapsulating some plasmon dispersion at these higher momenta. The energy of core-level transitions has no dependence on momentum transfer, therefore the two Bi edges remained at energies of 25.5 and 27 eV throughout all q-dependent measurements until they began to blend into the background noise. Due to being dispersion-less, they provide a good reference point to confirm that changes in plasmon energy are not resultant of spectrum energy misalignment. The lower energy Bi_2Se_3 π plasmon in figure 4.9c also displayed a dispersion to higher energy which is shown in figure 4.11 and discussed later. Peaks fitted in this low energy range at each momentum are shown in figure 4.10b.

Figure 4.9d shows the bulk Al_2O_3 bandgap as it changes with increasing momentum. At 0 $Å^{-1}$, the slope and energy of the bandgap was fitted with a logistic function using equation 2.9, indicating a bandgap energy of 8.5 eV with a steep onset. At subsequent momenta, the bandgap energy was fixed to the value at 0 $Å^{-1}$ and the slope fitted. This revealed that the slope of the bandgap decreased with increasing momentum. Al_2O_3 has a direct bandgap that can be observed as a steep slope in the EELS spectrum at 0 $Å^{-1}$ momentum [260, 261]. The band structure of Al_2O_3 can be described with a relatively flat valence band and a parabolic conduction band [260]. At 0 $Å^{-1}$ momentum, direct transitions between bands, which involve no momentum transfer, are recorded resulting in a steep slope, whilst, higher momenta qEELS spectra are sensitive to transitions where momentum transfer has occurred. The shape of the bandgap slope at higher momenta is less steep, as the measurements are sensitive to indirect transitions across the bandgap which require transfer of momentum [249]. The indirect transitions involve a larger energy transfer to reach the conduction band due to its parabolic shape, which results in transitions over a range of energies instead of

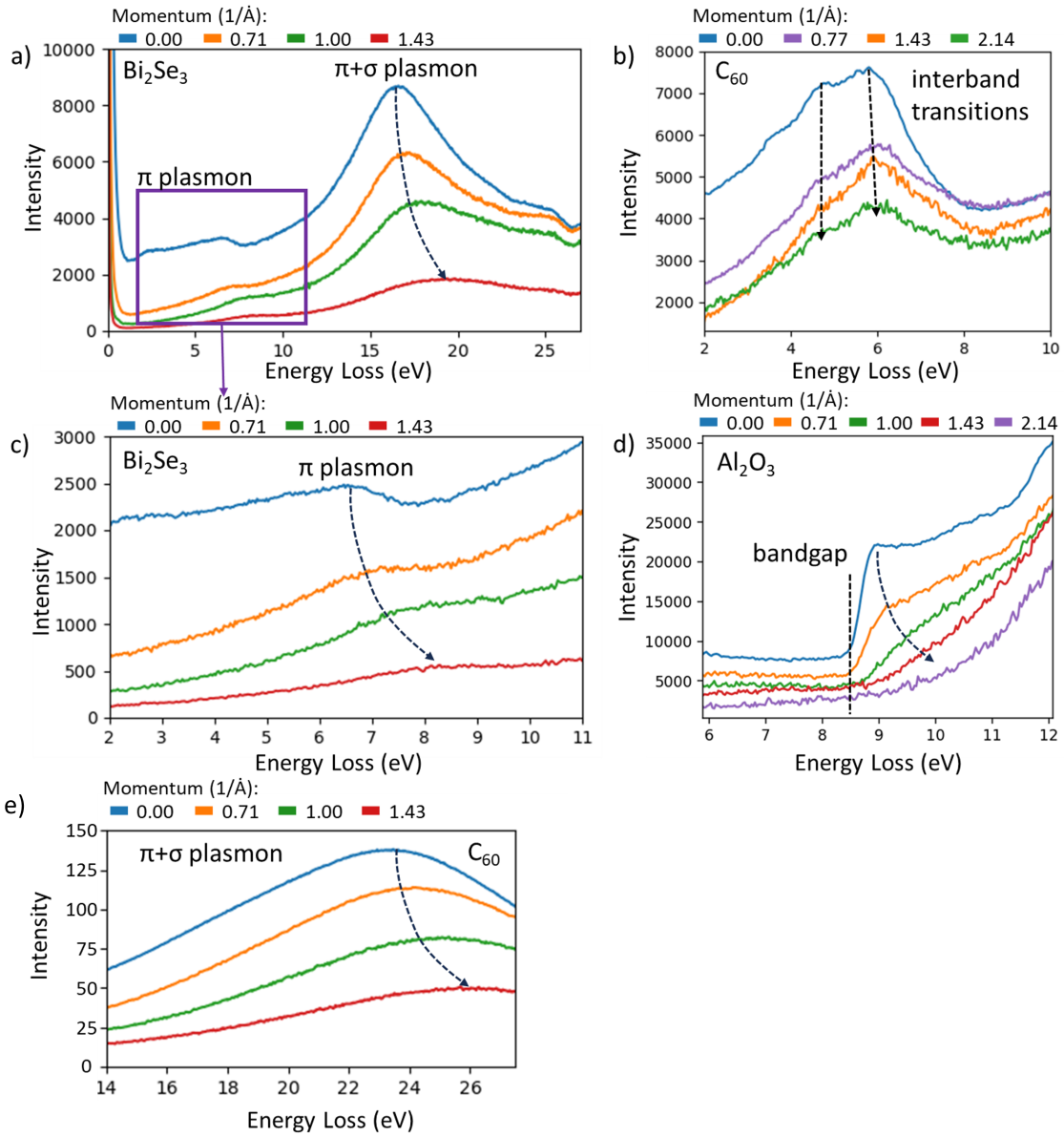

Fig. 4.9 a) Momentum-resolved EELS data for bulk Bi_2Se_3 region where the $\pi + \sigma$ plasmon energy is observed to disperse to higher energy. b) C_{60} interband transitions with increasing momentum. c) qEELS spectra for the bulk Bi_2Se_3 π plasmon from the highlighted energy region in a. d) Al_2O_3 bulk bandgap with increasing momentum where the slope is observed to change. e) C_{60} $\pi + \sigma$ plasmon dispersion displays a similar trend to the Bi_2Se_3 $\pi + \sigma$ plasmon.

at a single energy, giving rise to a shallower slope in the EELS spectrum. Alongside this change in bandgap slope, the intensity also reduces, resulting in the bandgap edge becoming indistinguishable from the tail of subsequent peaks at high momenta.

In bulk C_{60}, three interband transitions remained identifiable with increasing momentum and were not observed to disperse to higher energies, as shown in figure 4.9b. This is as expected for single electron excitations and confirms that these are indeed interband transitions [81]. The $(\pi+\sigma)$ plasmon, presented in figure 4.9e, was observed to follow a parabolic dispersion similar to Bi_2Se_3, as expected from bulk plasmons in literature.

At each interface, the qEELS data was more complicated to fit due to the presence of several overlapping peaks. Interfacial qEELS spectra at the Al_2O_3/Bi_2Se_3 and Bi_2Se_3/C_{60} interfaces are plotted in figure 4.10 alongside bulk Bi_2Se_3 with details of fitted peaks. The Al_2O_3/Bi_2Se_3 interface was fitted with a logistic function, with equation 2.9, to represent the bandgap, a pseudo-Voigt peak, with equation 2.6, for the high energy bulk plasmon and a pseudo-Voigt peak for the surface plasmon. At each momentum and interface least-squares fitting was used to fit the components included in each plot in figure 4.10. The plasmon energies and peak widths were free parameters when fitting interfaces to account for surface plasmon modes and plasmon coupling across interfaces. In the first two spectra, 0.0 and 0.66 $Å^{-1}$, the bulk Al_2O_3 bandgap was included and fixed to values fitted in bulk Al_2O_3 with only the intensity as a free parameter. An additional low-energy peak was also present in these low momentum spectra but is absent at higher momentum.The resulting peak energies of the surface plasmon are plotted in figure 4.11a.

At the interface between Bi_2Se_3 and C_{60}, detailed in figure 4.10c, peaks were fitted by a single pseudo-Voigt function at low energy and by a large Gaussian to approximate the large volume plasmon. The higher energy plasmon was observed to disperse to higher energy whilst the low energy peak, presented in green in figure 4.10c, remains at a similar energy. The additional peak around 2 eV was also included for the 0.0 $Å^{-1}$ spectrum. The peak energies of the low energy peak are plotted in figure 4.11b.

By fitting the spectrum at each interface at different momentum values, we obtain the plasmon dispersion of these localised peaks. As the surface plasmon around 5 eV at the Al_2O_3/Bi_2Se_3 interface has been shown to be localised to the interface and not described by plasmon coupling, its dispersion can allow us to understand its origins.

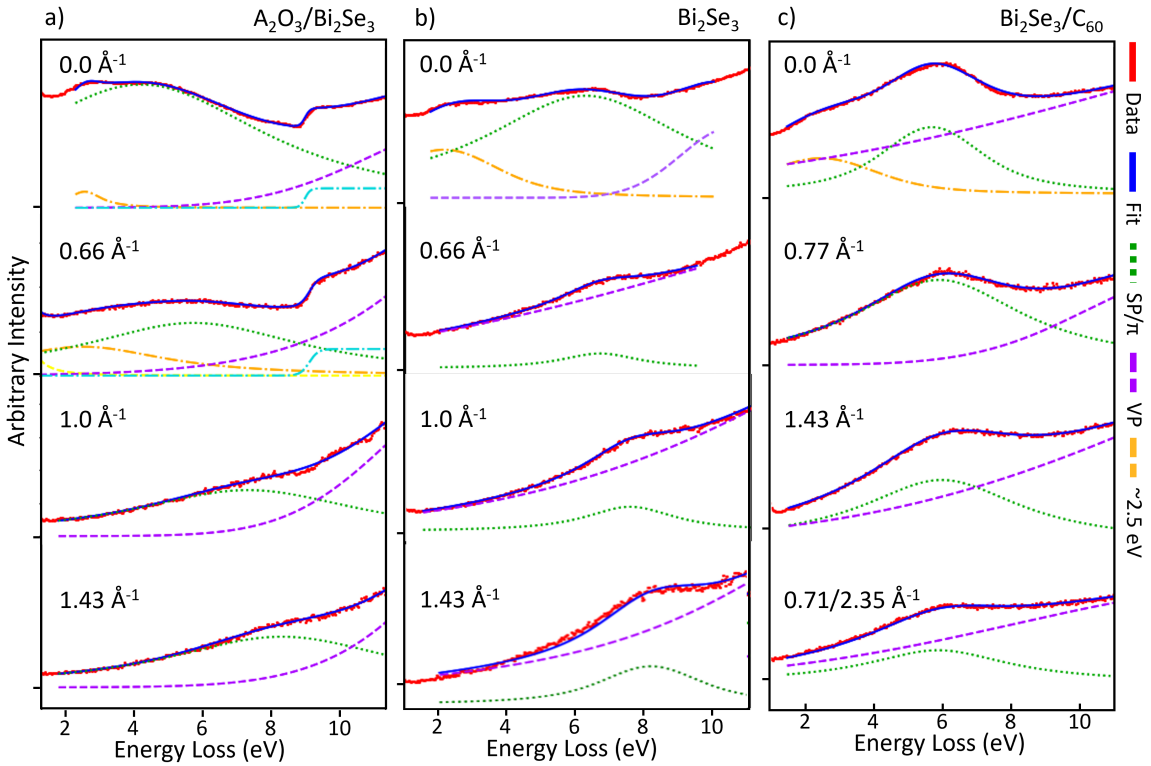

Fig. 4.10 Momentum-resolved EELS spectra at a) the Al_2O_3/Bi_2Se_3 interface, b) the bulk Bi_2Se_3 and c) the Bi_2Se_3/C_{60} interface with fitted components in the low energy region. At initial momenta an additional peak at 2.5 eV, dashed yellow, was included in the fit as an artefact which decreased, becoming insignificant, at higher momenta. A logistic function, shown in blue, was included in the fit for the first two Al_2O_3/Bi_2Se_3 interface qEELS spectra to account for the Al_2O_3 bandgap.

Plasmon dispersion

The energies of fitted plasmon peaks are plotted against momentum in figure 4.11, with error bars representing the momentum resolution and the uncertainty in peak energy from the standard deviation of the fitted value and energy resolution. Peak energies of the Bi_2Se_3 π-plasmon and Al_2O_3/Bi_2Se_3 surface plasmon are shown in figure 4.11a. The dispersion of the bulk Bi_2Se_3 π-plasmon, shown in red, can be fitted with a parabolic function, which is the expected dispersion from a bulk plasmon as described in section 1.4 [81]. The plasmon at the Al_2O_3/Bi_2Se_3 interface, shown in blue, did not disperse with the same trend. Several different functions were used to fit the SP dispersion including a parabolic, linear and root function. The surface plasmon at the Al_2O_3/Bi_2Se_3 interface was best described by a $\sqrt{q}$ dispersion as shown in figure 4.11a.

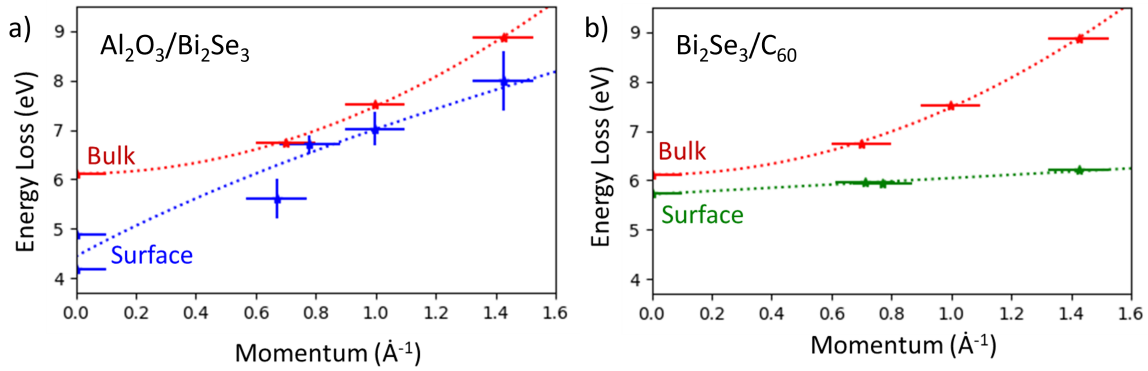

Fig. 4.11 Plasmon dispersion of plasmon peaks in bulk Bi_2Se_3 and interfaces obtained from fitting momentum-resolved EELS data. a) Dispersion of the bulk Bi_2Se_3 π-plasmon, in red, with increasing momentum fitted with a parabolic trendline and dispersion of the SP at the Al_2O_3/Bi_2Se_3 interface,in blue, fitted with a $\sqrt{q}$ trendline. b) Dispersion of the feature at the Bi_2Se_3/C_{60} interface, in green, fitted with a linear trendline and a copy of the bulk Bi_2Se_3 π-plasmon dispersion from panel a.

Unlike the SP at the Al_2O_3/Bi_2Se_3 interface, the feature at the Bi_2Se_3/C_{60} interface was observed to have very little dispersion. The clear difference between interfaces suggests some modification of the Bi_2Se_3 surface in proximity to C_{60} and the formation of a distinct surface state.

4.5 Discussion

At the interface between two materials, a surface plasmon polariton (SPP) can exist due to the change in permittivity, as discussed in section 1.3.3. The SPP is not confined in 2D to the interface and is instead characterised by an evanescent decay into the layers on either side of the interface. When there are carriers confined in 2D to an interface or surface, plasmon excitations of these carriers are 2D confined and can be termed as a 2D plasmon. In graphene, carriers are confined in 2D and excited as 2D surface plasmons. A change in permittivity is not required for the existence of these 2D plasmons and they have a different plasmon dispersion.

The $\sqrt{q}$ dispersion behaviour of the SP at the Al_2O_3/Bi_2Se_3 interface is best described as a 2D plasmon dispersion of the π plasmon [91]. Studies of plasmon dispersion in graphene suggest a $\sqrt{q}$ dispersion for π-electrons in the 2D sheet [262, 263, 157]. Liou *et al.* proposed the dispersion in graphene to follow

$$\omega_p(q) = \beta + \gamma\sqrt{q}, \tag{4.3}$$

where β is the single particle oscillator strength and

$$\gamma = 2\pi n_{2D} e^2 / m\varepsilon. \tag{4.4}$$

The electron charge, e, effective mass, m, and relative permittivity, ε, can be used to estimate the 2D electron density n_{2D} from γ. Upon fitting the dispersion data for the plasmon confined to the Al_2O_3/Bi_2Se_3 interface with equation 4.3, β was obtained as 4.14±0.02 eV and the 2D carrier density was obtained from equation 4.4. The effective mass of π electrons was approximated from DFT calculations as $1.05m_0$ and relative permittivity $\varepsilon = 2.35$ was estimated from Kramers-Kronig analysis of bulk EELS data. The 2D electron density of the π plasmon was thus calculated as $1.9 \pm 0.1 \times 10^{14}\text{cm}^{-2}$.

This value is slightly lower, although the same order of magnitude as a previous estimate of the number of π bonded electrons at the surface of Bi_2Se_3 in the terminating Se layer contributing to the surface plasmon of $\approx 7 \times 10^{14}\text{cm}^{-2}$ [264]. This value was given by Shu *et al.*, who concluded that electrons contributing to the surface π plasmon originate from unpaired electrons within the p_z orbital of Se atoms at the VdW interface whilst those from the sp^2 hybrid orbitals contribute to the $\pi + \sigma$ plasmon. In this scheme, each surface Se atom should contribute at most one electron to the 2D carrier density in the surface π plasmon. The total number of electrons within the Se surface layer was found to be $2 \times 10^{15}\text{cm}^{-2}$ from DFT, with roughly one third of π bonded electrons contributing to the surface π plasmon. As the value for the 2D electron density of the π plasmon calculated here was slightly lower than Shu *et al.*, it could suggest that a lower proportion of the π bonded electrons contribute to the surface plasmon here.

At the Bi_2Se_3/C_{60} interface, the π plasmon showed very little dispersion and fitting with equation 4.3 resulted in a value for β of $5.71 \pm 0.01eV$. Following the same calculation as above, with the relative permittivity of C_{60} estimated as $\varepsilon = 1$, the 2D electron density was found to be $2.1 \times 10^{13}\text{cm}^{-2}$, an order of magnitude smaller than at the other interface. This small value is unlikely and due to the lack of dispersion, we suggest that this behaviour could be better explained by a hybrid π plasmon at the interface.

Density functional theory (DFT) calculations of the Bi_2Se_3/C_{60} interface were carried out by collaborators to better understand the effect of C_{60} on the surface electron density of Bi_2Se_3. The charge distribution across the interface between Bi_2Se_3 and C_{60}, shown in figure 4.12, gives insight into the behaviour at the interface. Electron density was observed to accumulate at individual C_{60} molecules with the formation of an interfacial dipole due to the high electron affinity of C_{60} as shown in figure 4.12b. Bonding between the terminating Se layer in the TI thin film and the first layer of C_{60} molecules and reconstruction of the surface could explain the lack of 2D π plasmon at this interface, as electrons within surface π states

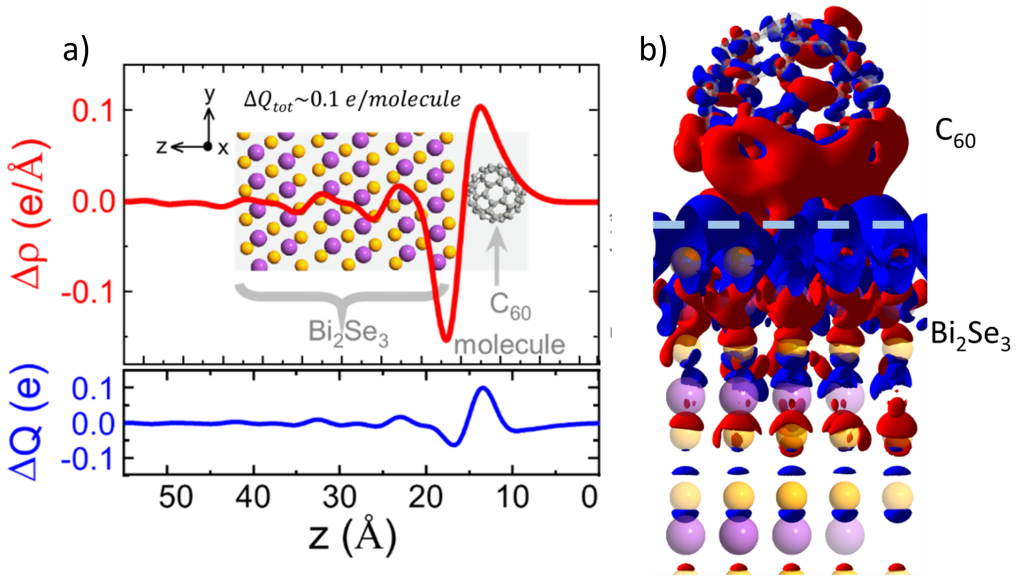

Fig. 4.12 a) Top: Change in charge density across the interface and bottom: charge transferred. b) Charge density distribution at the interface between Bi_2Se_3 and a C_{60} molecule showing charge accumulation in red and charge depletion in blue. Atoms are shown as Bi in purple and Se in yellow with the interface indicated by a dashed line. Figure produced by collaborators Ansari and Gity at Tyndall National Institute, University College Cork.

are no longer excited as 2D plasmons. This could explain the lack of plasmon dispersion observed for the interface peak and could indicate the emergence of a hybrid plasmon. The hybrid π plasmon present at the Bi_2Se_3/C_{60} is distinct from the 2D π plasmon observed at the other interface.

Hybridisation between the orbitals of C_{60} molecules and the Bi_2Se_3 surface and the charge transfer across this interface accounts for the observed discrepancies between the experimental and calculated EELS spectra. Since EELS spectra were calculated using only the bulk dielectric functions, the observed interfacial behaviour was not modelled. Additionally, localised states arising from specific bonding within localised regions of the material such as the 2D π plasmon at the Al_2O_3/Bi_2Se_3 interface were not included in the calculations. In order to model the observed interfacial behaviour, EELS spectra should be simulated considering the atomic and molecular bonding in the real system.

The electronic behaviour of C_{60} can be tuned using an applied voltage or electric field with an increase in current density observed when a larger voltage was applied [230]. Energies of C_{60} excitations have been shown to redshift due to the presence of an increasing electric field and a decease in bandgap energy observed [68]. Additional vibrational modes become active when an electric field is applied [68]. Tuning of C_{60} excitations by an applied electric field

could in turn further modify the Bi_2Se_3 surface leading to an electrically tunable interface that could be enclosed within a device.

The effect of C_{60} doping on the surface π plasmon of Bi_2Se_3 indicates that the surface states of Bi_2Se_3 can be modified by molecular layers. This change in the chemical potential of the interface gives rise to the possibility of electrically tunable TI interfaces, which could prove useful for further development of TI devices. As the electronic behaviour of C_{60} has been demonstrated to change with the application of an electric field [230], the Bi_2Se_3/C_{60} film could be enclosed between electrodes to change the interface behaviour with an applied voltage.

4.6 Conclusion

In summary, surface modification of Bi_2Se_3 by C_{60} molecular overlayers was successfully achieved and shown through EELS and momentum-resolved EELS measurements. High quality thin films of $Al_2O_3/Bi_2Se_3/C_{60}$ were confirmed by STEM imaging, which revealed large crystalline regions with minimal defects, aside from isolated twin planes and grain boundaries Low-loss EELS analysis over the cross section revealed bulk plasmons in each material, along with the Al_2O_3 bandgap and C_{60} interband transitions. Notably, plasmons localised to the Al_2O_3/Bi_2Se_3 and Bi_2Se_3/C_{60} interfaces were observed, with energies at 5 eV and 6 eV respectively. The Bi_2Se_3/C_{60} interface plasmon was strongly confined to the interface, with the bulk C_{60} EELS spectrum recovered after only around 2 nm. These findings indicate Bi_2Se_3 surface modification due to the C_{60} overlayers.

Momentum-resolved EELS revealed the dispersion of bulk and interface plasmons. A parabolic dispersion was observed of the bulk Bi_2Se_3 π plasmon, consistent with volume plasmon behaviour [81]. A $\sqrt{q}$ dispersion was observed for the Al_2O_3/Bi_2Se_3 interface plasmon, which could be classified as a 2D π plasmon with a fitted carrier density of $1.9 \pm 0.1 \times 10^{14}\text{cm}^{-2}$ [157, 91]. This is comparable to the estimated carrier density for π electrons within the surface Se layer that contribute to the surface plasmon of $\approx 7 \times 10^{14}\text{cm}^{-2}$. In contrast, the plasmon at the Bi_2Se_3/C_{60} interface showed negligible dispersion and an unphysically low carrier density from a $\sqrt{q}$ fit. DFT revealed an accumulation of electrons on C_{60} molecules, suggesting the formation of a hybrid plasmon due to interfacial charge transfer, explaining the lack of dispersion. Enhancement of EELS signals in the first layer of C_{60} molecules, indicated by spectrum imaging, is consistent with the formation of a hybrid plasmon.

These results reveal a distinct change from a 2D π plasmon at the Al_2O_3/Bi_2Se_3 interface to a hybrid plasmon at the Bi_2Se_3/C_{60} interface. This shift highlights the strong influence of

organic molecular overlayers like C_{60} on the plasmonic behaviour of TI surfaces and opens the door to engineering tunable TI/organic interfaces.

Although C_{60} was expected to have only minimal effects compared to other organic molecules, the modifications observed here are encouraging. Stronger effects could arise from other organics such as phthalocyanines, which will be explored in chapter 5. Finally, whilst this chapter focused on π plasmons in the 1-27 eV energy range, plasmonic behaviour at lower energies, in the 100 meV range, has yet to be explored. EELS analysis at lower energies should allow for observation of bulk and surface plasmons from free carriers and give insight into the Dirac plasmon mode. This will be discussed in chapter 6.

5 Surface modification of Bi_2Se_3 with organic layers of H_2Pc, CuPc and graphene

5.1 Introduction

In chapter 4, it was shown that in proximity to C_{60}, the Bi_2Se_3 surface was modified, with the formation of a hybridised state and hybrid π plasmon. The high electron affinity of C_{60} led to a charge transfer across the interface. Other organic materials could have a similar or stronger effect and molecules which are electron donors could produce interesting and different effects. To explore further how the Bi_2Se_3 surface is altered by organic molecular overlayers, several different organic dopants will be investigated in the present chapter, with a focus on graphene and phthalocyanine layers.

The effect of various different organic materials on the surface of topological insulators has been studied using surface sensitive techniques. Wang *et al.* showed a strong charge transfer was observed upon doping a Bi_2Se_3 surface with molecules of tetrafluorotetracyanoquinodimethane (F_4-TCNQ) [72, 73]. This molecule is a strong electron acceptor with a high electron affinity and was shown to accept charge from the Bi_2Se_3 surface, similar to what we observed at Bi_2Se_3/C_{60} interfaces. The transferred charge was observed to localise on nitrogen atoms within the first layer of molecules. The charge transfer observed for both systems resulted in charge accumulation on molecules at the surface.

Molecules such as phthalocyanines, with a planar structure, shown in figure 5.1c,d, are expected to produce different behaviour to C_{60}, with versatile properties depending on metal atom. The electron affinity of phthalocyanine molecules varies with metal atom and can be significantly lower than C_{60} [267]. Several different types of phthalocyanine molecules have been studied in p-n junctions with C_{60} [268, 269]. The lower electron affinity could result in a smaller interfacial dipole than was observed at a Bi_2Se_3/C_{60} interface in chapter 4 or

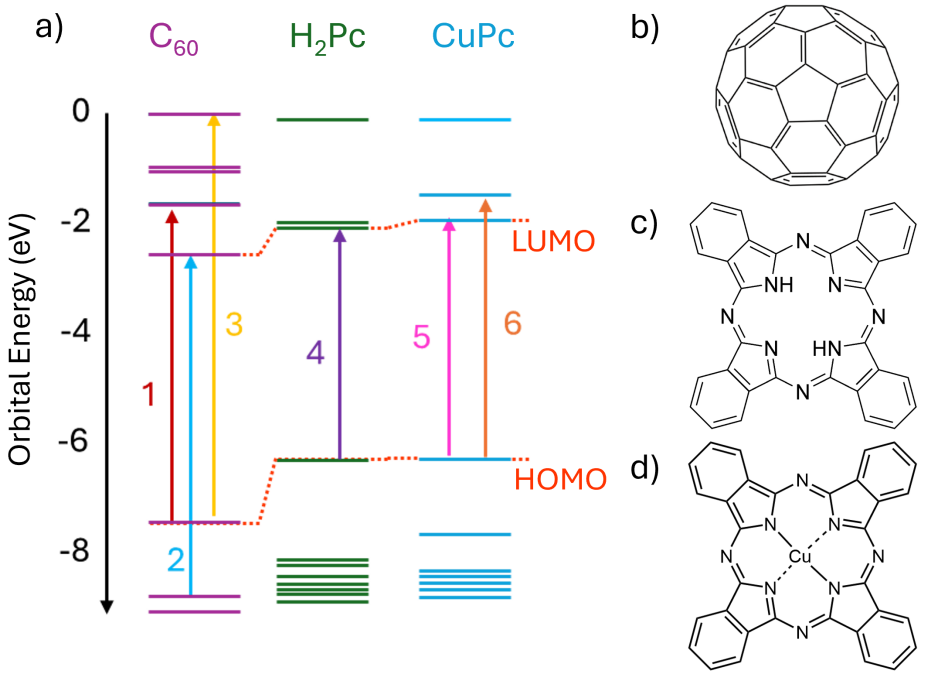

Fig. 5.1 Molecular orbitals and structures of C_{60}, H_2Pc and CuPc molecules. a) Approximate orbital energy diagram for each molecule with the HOMO and LUMO orbitals indicated [257, 265, 266]. Three interband transitions indicated in C_{60} are 1: 3.3 eV, 2: 4.8 eV and 3: 6.0 eV. In H_2Pc the HOMO-LUMO transition is indicated as 4: 2.0 eV. Two transitions close in energy are indicated in CuPc at 5: 2.1 eV and 6: 2.3 eV. b) A C_{60} molecule, also known as a 'Bucky ball', is a round molecule with a cavity at the centre. c) A H_2Pc molecule is a planar molecule with a central macrocycle and four benzene rings. d) The structure of a CuPc molecule is similar to a H_2Pc molecule with a Cu atom at the centre.

the formation of a opposite dipole, both of which could significantly alter the plasmonic behaviour at the Bi_2Se_3/organic interface. Jakobs *et al.* observed that H_2Pc had a strong effect on the band structure and topological surface state of Bi_2Se_3, which was investigated through angle-resolved photo-electron spectroscopy (ARPES) [6]. This effect was much greater than for C_{60} molecules, with a shift of 100 meV to the Bi_2Se_3 Dirac point observed for H_2Pc but no shift for C_{60}. This was attributed to the reduced separation between flat chemisorbed H_2Pc molecules and the Bi_2Se_3 surface. If the increased effect on the TSS is dependent on the separation between a molecule and the interface, then it will likely be affected by molecular ordering on the surface and orientation of molecules. Similar to C_{60}, phthalocyanines can be modified with the inclusion of different metal centres, providing the possibility of introducing further change to the surface with different metal centres [270]. The electronic properties can be varied based on the choice of metal centre included which can be almost any transition metal. The versatility in properties is especially useful as it provides an option to engineer

phthalocyanine with different metal atoms. Phthalocyanine molecules are also stable and have been studied for use in optoelectronic devices [271]. Changes in the band structure of Bi_2Te_3 have been observed due to doping the surface with CoPc molecules [79]. This surface doping resulted in changes to the topological surface state observed through ARPES. In the molecular orbital diagram presented in figure5.1a, the indicated HOMO-LUMO transitions in both Pc molecules dominate absorption spectra, with smaller contributions of higher energy transitions [265, 266]. As these interband transitions are lower in energy than the Bi_2Se_3 π/surface plasmons, coupling between the Bi_2Se_3 plasmon and molecular excitations might not occur, resulting in reduced red shifts and less signal enhancement at the interface compared to C_{60} [96]. The combination of a reduced effect on the π plasmons and greater effect of the TSS could be interesting.

As a 2D material itself, graphene is an interesting candidate to investigate interfacial behaviour with Bi_2Se_3. Where we observed localisation of electrons to individual C_{60} molecules at the Bi_2Se_3/C_{60} interface, the Bi_2Se_3/graphene interface would be expected to have different behaviour, with delocalisation of electrons across the 2D graphene sheet. Additionally, the electron affinity of a graphene monolayer is strongly influenced by defects and surface doping, which could produce further differences in results compared to the previously studied molecules.

This chapter will investigate the effect of three different organic materials on the plasmonic behaviour at an interface with Bi_2Se_3. Graphene was selected to investigate the effect of a 2D organic layer, where charge would not be expected to localise at molecular positions at the interface. Phthalocyanines, H_2Pc and CuPc, were selected as they are expected to have a stronger effect on the topological surface states than C_{60}. A comparison of H_2Pc and CuPc molecules will give insight into the effect of the metal centre. For each organic material, EELS spectra across the interface will be compared with spectra from the substrate interface to illustrate changes which can be attributed to the presence of the organic and unrelated to the growth method. This will show how the energy, lineshape and localisation changes in proximity to different organic materials. By comparison to calculated EELS spectra, these changes can be distinguished from interfacial plasmon coupling and reveal that changes can be attributed to the presence of the organic molecular overlayers, which could suggest hybridisation or formation of a 2D electron gas. This chapter will provide insights into how different organic dopant overlayers modify the plasmonic behaviour of a Bi_2Se_3 surface. The results will highlight subtle differences in TI/organic interface plasmon behaviour, hinting towards organic-induced modifications of the plasmonic response and laying foundations for the future development of tunable plasmonic devices based on TI/organic interfaces.

5.2 Bi_2Se_3/graphene

As a 2D material, graphene poses an interesting material to modify the Bi_2Se_3 surface. Similarly to topological insulators, graphene has Dirac cones at K points in its Fermi surface, leading to interesting properties. The plasmonic properties of graphene have been studied extensively in recent years for their potential uses in plasmonic devices [104, 272]. Monolayer graphene can host 2D plasmon modes, which are delocalised across the surface.

Free-standing graphene has been observed to have $\sqrt{q}$ dispersion and at interfaces with some metals, this dispersion changes to a linear one [273, 232]. This linear dispersion has been described as a consequence of the coexistence of the metal electron gas and the π electrons of graphene in the same space. The resulting surface plasmon resembles an acoustic plasmon in metals. Some contrasting results suggest that in monolayer graphene, a linear dispersion is observed and on epitaxial SiC substrates, the dispersion follows a $\sqrt{q}$ behaviour [101]. Surface roughness has also been shown to have an effect on the behaviour of plasmon mode in graphene, which can be strongly damped by increased surface roughness [232]. Plasmon modes in graphene have been shown to couple with optical phonon modes resulting in mixed plasmon/phonon characteristics [232, 274]. This literature highlights that graphene's plasmon dispersion is highly sensitive to its environment, such as interfacing materials and surface roughness, suggesting that when used as a dopant layer on Bi_2Se_3, it could significantly alter the Bi_2Se_3 surface plasmon behaviour.

The electronic properties of graphene have been demonstrated to be gate-tunable, which offers potential to actively tune a TI surface via a graphene overlayer for tunable plasmonic devices [275, 276]. The Fermi energy has been shown to change by changing charge concentration, which can be influenced by supplying an electric potential or by chemical doping [232]. It is also possible to tune the plasmonic properties of graphene by doping with external atoms. Shin *et al.* observed an increase in the energy of the π plasmon of 1.1 eV from doping with potassium atoms [277]. Although a change in plasmon energy was observed, other characteristics of the π plasmon, unique to single layer graphene, were preserved. Other metal dopants have been used to modify graphenes' plasmonic behaviour. Dzujah *et al.* predicted opening of the bandgap and emergence of mid-gap states due to substitution of transition metal atoms [278]. They predicted that this will have a small influence on π and $\pi+\sigma$ plasmons and result in metal-like characteristics for the plasmons. There is also potential to alter the plasmonic behaviour by increasing the number of graphene layers present. The energy of the $\pi+\sigma$ plasmon peak has been shown to increase with increasing number of graphene layers [279]. Graphene's plasmonic properties can be tuned through gating, chemical doping and layer thickness, making it a promising material to tune

the Bi_2Se_3 surface plasmonic behaviour. This tunability could be utilised in engineering of active plasmonic devices.

Bi_2Se_3/graphene heterostructures have been investigated by Chen *et al.*, who observed an increased photo-response due to band-bending from the heterostructure [280]. Graphene was observed to transfer charge to Bi_2Se_3 and become p-type, resulting in band-bending in Bi_2Se_3, which reduced scattering to increase photo-current. This study highlights the potential of graphene as a dopant to modify the TI surface.

This section will discuss the plasmonic behaviour observed at interfaces between Bi_2Se_3 and graphene. Cross-sections of SiO_2/Bi_2Se_3/graphene/aC, prepared by FIB, are characterised by STEM imaging and their plasmonic behaviour observed by low-loss EELS. Changes in plasmon peaks are analysed across both the substrate/TI interface and TI/organic interface to identify modifications to the Bi_2Se_3 surface in proximity to graphene. The changes to π plasmons provide a measure of changes to the surface potential and can indicate hybridisation and 2D confinement of surface states. The behaviour at the Bi_2Se_3/graphene interface will then be compared to that of other Bi_2Se_3/organic interfaces.

5.2.1 Sample preparation and structure

Single crystals of Bi_2Se_3 were grown on SiO_2 by vapour transport growth using the method discussed in section 2.2 at the University of Leeds. Graphene was then deposited on the single crystals by a wet transfer method outlined in ref [119] and its presence confirmed by Raman spectroscopy. The bulk sample containing single crystal Bi_2Se_3 flakes topped with monolayer graphene was then transported to Glasgow for electron microscopy analysis. Before FIB preparation, the sample was sputter coated with amorphous carbon (aC) to protect the surface and prevent interaction between the graphene layer and FIB deposited platinum. A TEM lamella was extracted from a Bi_2Se_3 crystal with a graphene overlayer at room temperature by PFIB before thinning to electron transparency at 98 K by Ga FIB using the procedure outlined in section 2.2.

STEM and EELS characterisation was performed on the ARM at 200 kV and additional characterisation was carried out by SEM EDS and atomic force microscopy. The graphene layer is not clear in presented STEM images due to its small width and similar contrast to aC. In the HAADF image presented in figure 5.2a, a sharp interface between SiO_2 and Bi_2Se_3 can be observed, with resolvable Bi_2Se_3 layers across the full interface. The sample is orientated along the <210> zone axis of Bi_2Se_3, as shown in the FFT in figure 5.2a, on an amorphous SiO_2 substrate. The Bi_2Se_3 crystal has a width of around 520 nm and does not show any structural defects such as point defects or interstitial defects. Bi_2Se_3 quintuple layers (QLs) can be observed in the HAADF image in figure 5.2c, where Bi atomic columns and van der

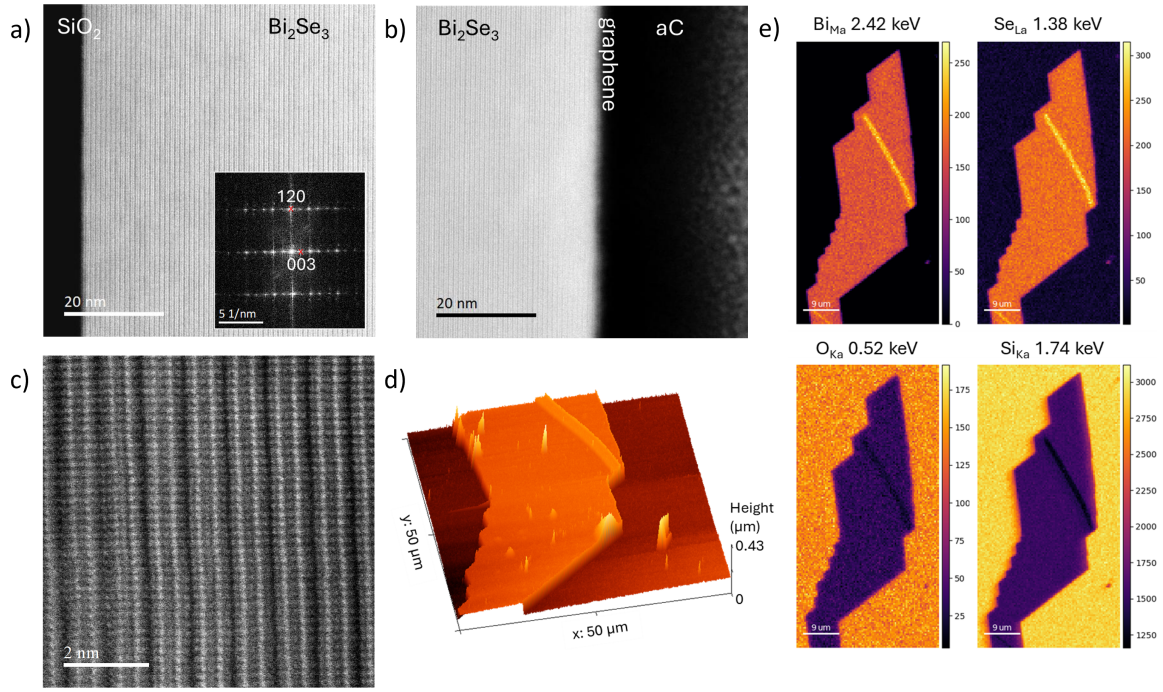

Fig. 5.2 a) HAADF STEM image of the SiO_2/Bi_2Se_3 interface region of the sample with insert: indexed FFT of Bi_2Se_3 in the sample. b) HAADF STEM image of the Bi_2Se_3/graphene/aC interface at the opposite end of the TI layer. c) Higher magnification HAADF STEM image of the Bi_2Se_3 layer. d) Atomic force microscopy (AFM) image of a Bi_2Se_3 flake with graphene on top, a long straight Bi_2Se_3 crystal has formed on top of a larger flat crystal. e) EDS images of the same flake where the flake is shown to be composed of Bi_2Se_3 with a smaller crystal of Bi_2Se_3 forming on top.

Waals gaps can be observed. Figure 5.2b shows a HAADF image of the Bi_2Se_3/graphene/aC interface. The interface does not contain any Bi_2Se_3 step edges.

Energy dispersive spectroscopy (EDS) was performed on a crystal of Bi_2Se_3/graphene to confirm the contents of the crystal. EDS was performed with scanning electron microscopy (SEM) with an electron beam voltage and current of 15 kV and 11 nA. Maps of Bi and Se content at energies of 2.42 keV and 1.38 keV respectively, shown in figure 5.2e, show that the crystal contains these elements and they are evenly distributed throughout the crystal, indicating no pockets of Bi or Se rich material. Diagonally along the top region of the crystal, a line of greater intensity is observed in both the Bi and Se maps. This is where a long thin Bi_2Se_3 crystal has formed on top of the larger flat crystal. Crystals of this long straight shape were observed across the bulk sample and were avoided when extracting cross sections. The O and Si maps at 0.52 keV and 1.74 keV show reduced intensity where the Bi_2Se_3 crystal is present.

Atomic force microscopy (AFM) was performed on the same crystal to determine roughness of the surface and is shown in figure 5.2d. This technique scans a tip across a surface to map the topology. A sharp tip, cantilever, is oscillated above the sample at a resonant frequency and experiences the surface potential of the sample. The interaction between the tip and sample results in a change to the tips oscillating frequency and the cantilever amplitude. Changes to the cantilever amplitude are detected and used to map the surface of a sample [281]. In the AFM image presented in figure 5.2c, changes in height can be observed showing the edges of the crystal. The long crystal that has grown on top of the flat crystal can be observed in this image and has a thickness of around 38 nm, whilst the flat crystal has a thickness of 106 nm. Across flat regions of the crystal, the surface roughness was determined to be less than 1 nm and Bi_2Se_3 step edges, which would be at least 1 nm (1 QL) thick were not observed. Since step edges of 2 nm did not show appreciable changes to simulated EELS spectra in section 3.6.3, the roughness here should not significantly alter results. In these measurements, the graphene layer was not directly observed.

Overall, the sample was of high quality and adequate thickness for study of interfacial plasmonics. Sample thickness was determined from EELS characterisation to be around 104 nm by calculation from measured t/λ_i values of 0.8 at 200 kV.

5.2.2 EELS characterisation

EELS spectra were recorded across both interfaces of the sample and are presented in figure 5.3. Data across the SiO_2/Bi_2Se_3 and the Bi_2Se_3/graphene/aC interfaces were collected separately due to the large width of the TI layer. Low-loss EELS fitting was carried out in 'Hyperspy', with plasmon modes fitted as pseudo-Voigt functions and the substrate bandgap fitted using a logistic function as described in section 2.5.

The EELS spectrum from bulk SiO_2 is presented in figure 5.3c and show the bandgap at an energy of 9.4 eV. In bulk Bi_2Se_3, shown in figure 5.3c, plasmons at 7 and 17.3 eV were identified as the π and $\pi+\sigma$ plasmons, as observed in previous Bi_2Se_3 samples discussed within this thesis. Bismuth $O_{4,5}$ edges are present at 26.7 and 28.5 eV therefore, the VTG Bi_2Se_3 has no substantial differences in its plasmon spectrum compared with MBE grown Bi_2Se_3 films. The Bi_2Se_3 spectrum is identical in both datasets close to the top and bottom of the Bi_2Se_3 crystal.

In amorphous carbon the bulk plasmon peak, $\pi+\sigma$, is present at 24 eV and a broad peak, shown in orange in figure 5.3c, at 5 eV is a $\pi \rightarrow \pi^*$ transition [282]. A π plasmon excitation in aC is encapsulated by this broad peak. In free-standing monolayer graphene, a π plasmon is expected at 4.7 eV but has been shown to shift in energy in the presence of a substrate or dopant [232, 278, 283, 284]. The π plasmon has been shown to shift to between 5.9 and 9.2

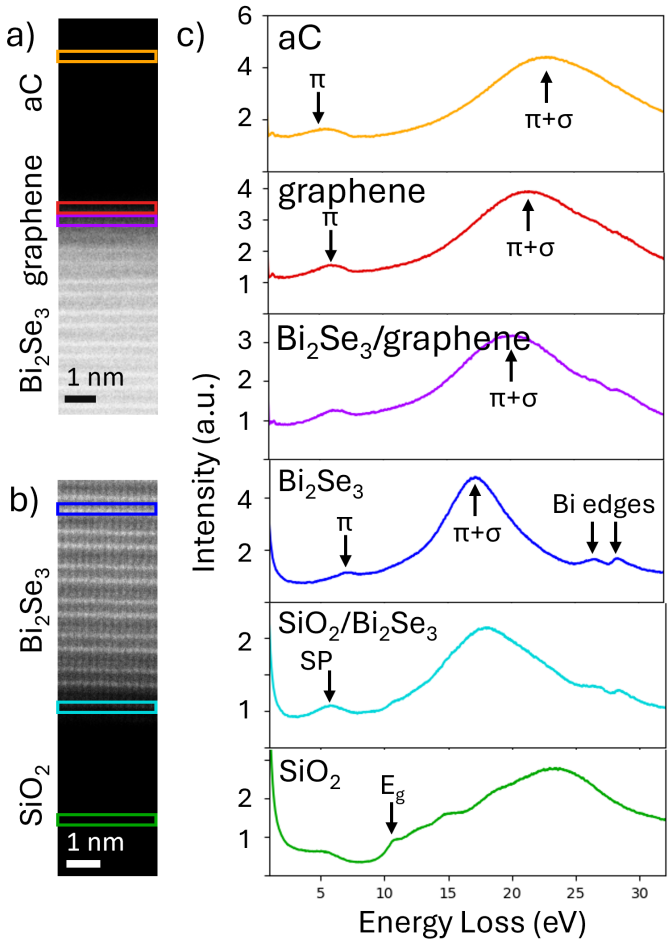

Fig. 5.3 EELS spectra in each region of a Bi_2Se_3/graphene/aC cross-section, which show the energy of plasmons and electronic transitions in the bulk of each layer and at interfaces. a) ADF image of the Bi_2Se_3/graphene/aC interface with indications of spectrum locations for c. b) ADF image of the SiO_2/Bi_2Se_3 interface. c) EELS spectra in each region of the sample with colours indicating their position on ADF images in a and b. π and $\pi+\sigma$ plasmons are indicated in aC, graphene and Bi_2Se_3. The SiO_2 bandgap is labelled E_g and a surface plasmon (SP) is identified at the SiO_2/Bi_2Se_3 interface.

eV for graphene monolayers on substrates [283] and in bulk graphite the π plasmon has an energy of between 6.5 and 7 eV [232]. Here, the π plasmon at the interface between Bi_2Se_3 and graphene has an energy of 6.0 eV, as shown in figure 5.4, which is between the energies of π plasmons in materials on either side of the interface. The $\pi \rightarrow \pi^*$ interband transitions are expected to occur at 4.3 eV in graphene but are not resolved here [278]. The higher energy $\pi+\sigma$ plasmon in free-standing graphene is expected at 14.7 eV as a weak excitation [157], but has also been demonstrated to shift to higher energies. For example, blue shifts of the $\pi+\sigma$ plasmon to 19 eV can occur when on a SiC substrate [232] and metal doping can

result in further energy shifts to 20 eV [278]. In this work, at the Bi_2Se_3/graphene interface, the $\pi + \sigma$ plasmon has an energy of around 20 eV, indicating that the graphene layer has been doped.

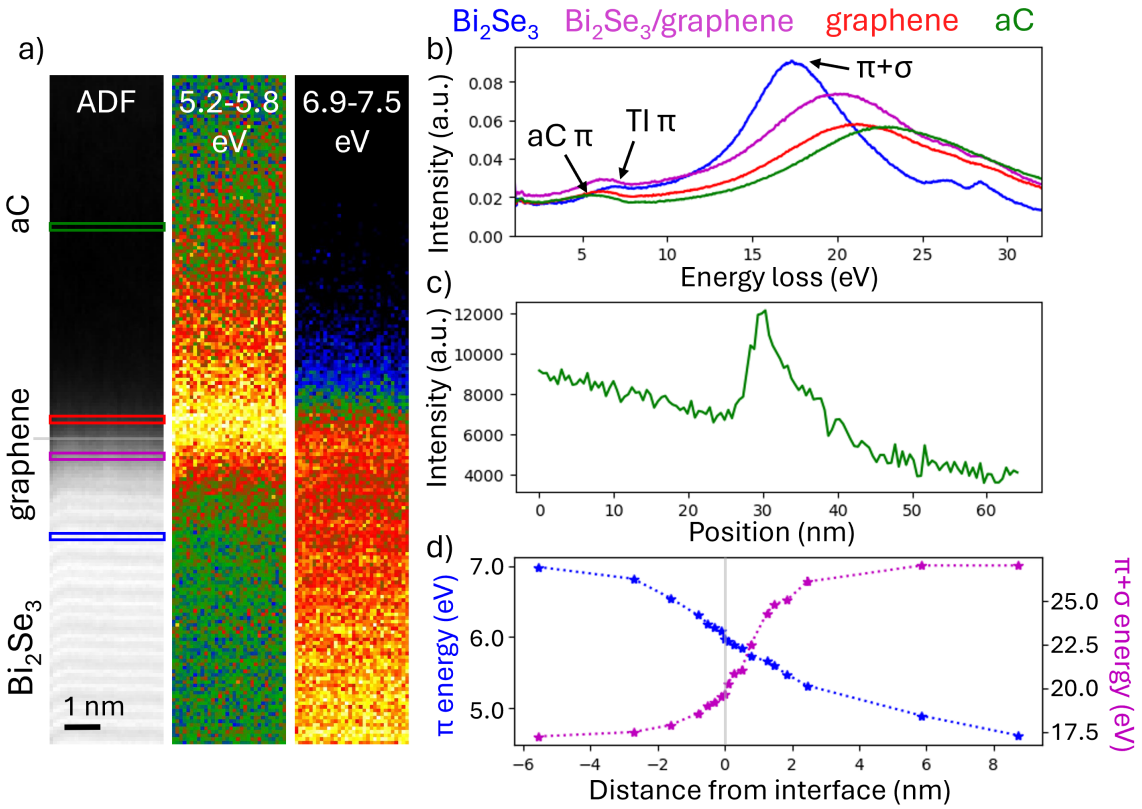

Fig. 5.4 EELS across the SiO_2/Bi_2Se_3/graphene/aC interface. a) An ADF image and EELS maps over energy regions 5.2-5.8 eV and 6.9-7.5 eV across the Bi_2Se_3/graphene/aC interface. EELS maps indicate an interface localised feature and a Bi_2Se_3 π-plasmon respectively. b) EELS spectra at regions of the sample indicated on the ADF image in a. c) Intensity profile of the EELS map over energy range 5.2-5.8 eV from Bi_2Se_3 into the organic layers. d) Plot of fitted plasmon energy for the π plasmon and $\pi + \sigma$ plasmon over the interface. The interface is taken to be the position marked by a grey line in the ADF image in a, where a change in ADF contrast was observed.

Across the interface, the peak energies of the π and $\pi + \sigma$ plasmons shift, as presented in figure 5.4d. The π plasmon energy, shown in blue, starts at 7 eV in bulk Bi_2Se_3 and redshifts linearly over a region of around 5 nm from the interface. In the EELS map over the energy 5.2-5.8 eV in figure 5.4a, the greatest intensity of observed at the interface, with a slow decay into the carbon overlayer. The π plasmon in graphene can be excited in an aloof position in aC and the aC π plasmon exists at a slightly different energy. The $\pi + \sigma$ plasmon mode starts at 17.3 eV in Bi_2Se_3 and blueshifts across the interface within 2 nm until reaching the

amorphous carbon region. The final energy of the peak in this plot appears much greater than this, but this is due to less accurate fitting in this region due to peak broadening.

The plasmonic behaviour of graphene is highly influenced by doping, which can change both the energy and dispersion of plasmons [232]. The presence of the aC layer will likely dope the graphene monolayer and it is possible for doping to occur from exposure to air. Therefore, the plasmonic behaviour at the Bi_2Se_3/graphene interface can be further modified by the selection of additional overlayers. The effect of overlayer doping would also be observed in the plasmon dispersion, therefore, this system would be interesting to investigate further using qEELS techniques.

EELS spectra over the SiO_2/Bi_2Se_3 interface, shown in figure 5.5, differ from the behaviour at the organic interface. In bulk SiO_2, the electronic bandgap was observed at an energy of 9.4 eV, identifiable as a step edge labelled E_g in figure 5.3c. Various other peaks can be identified in the bulk spectrum which are in agreement with literature, where interband transitions are expected to occur at 10.6, 12.0, 14.3 and 18.2 eV and a bulk volume plasmon is expected at 23 eV [285]. The bulk plasmon has been identified in figure 5.3c as well as several of the expected interband transitions. Between 5 and 6 eV an additional feature is present in the SiO_2 spectrum below the bandgap which we assign as an aloof excitation of a surface plasmon (SP) mode. In some literature, an impurity band edge has been observed at 5.5 eV [285], however, as the feature here does not have the step edge characteristics of a bandgap and has a distinct trend in intensity towards the interface, it is assigned as an aloof SP. Towards the interface the SP mode is observed to increase in intensity and shift slightly to 5.6 eV continuing into the first QL of Bi_2Se_3. An EELS map over the interface, over the energy region 5.1 to 5.6 eV, shown in figure 5.5a, illustrates the localisation of this SP mode to the interface. Figure 5.5c contains EELS spectra over an energy region containing the Bi_2Se_3 π plasmon and SP mode at different locations across the interface. The EELS spectrum at the interface, shown in orange, contains the SP mode at 5.6 eV. One QL into Bi_2Se_3, shown in green in figure 5.5c, a clear broadening of the feature occurs which extends over the energies of the SP mode and bulk Bi_2Se_3 π plasmon. This suggests the presence of both the SP mode and π plasmon.

Across the interface, relative amplitudes of the SP mode and bulk π plasmon change and at 1 QL into Bi_2Se_3 two peaks are required to adequately fit the spectrum in this energy range. This indicates the coexistence of these two modes. As SiO_2 is a trivial insulator, the behaviour the Bi_2Se_3 surface states at the interface should be similar to a Bi_2Se_3/vacuum interface. At an interface with vacuum, the surface plasmon mode has been observed at 5.5 eV, which is similar to this SiO_2/Bi_2Se_3 interface. The small difference between these two values could be explained by the presence of small defects in the amorphous SiO_2 [285].

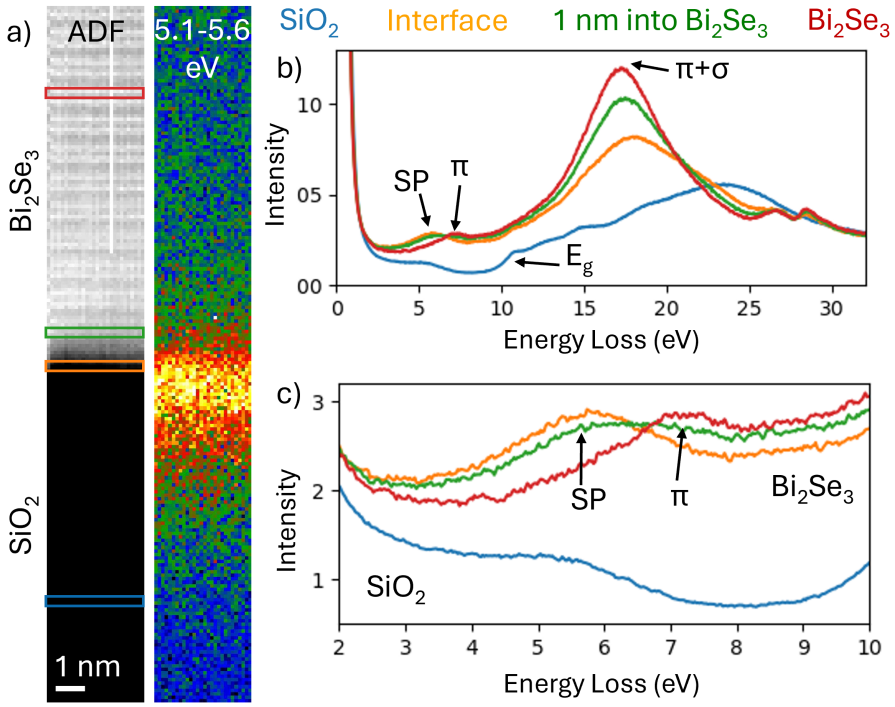

Fig. 5.5 Low-loss EELS data of the SiO_2/Bi_2Se_3 interface. a) ADF image of the interface alongside EELS map over the energy region 5.1-5.6 eV containing a surface plasmon. b) Normalised low-loss EELS spectra at regions within the sample as indicated on the ADF image in a where the colours identify each spectrum. c) EELS spectra between 2 and 10 eV for each indicated region of the sample. Two peaks are identified in the spectra with the TI π-plasmon at 5.6 eV present in both the red and green spectra and a surface plasmon (SP) at 7.0 eV, present in the green and orange spectra.

Calculated EELS of this interface are discussed in section 5.3 and shown in figure 5.7c. The calculations do not replicate the surface plasmon, but indicate a peak at the Bi_2Se_3 π plasmon energy remains at the interface.

Changes between the plasmon modes at a Bi_2Se_3/graphene interface in comparison to an SiO_2/Bi_2Se_3 interface indicate a change to the Bi_2Se_3 surface due to the presence of a graphene layer. At the SiO_2/Bi_2Se_3 interface, the coexistence of a bulk π plasmon and surface plasmon was observed up to 1 nm into the Bi_2Se_3 layer. Coexisting modes were not observed at the Bi_2Se_3/graphene interface indicating a modified surface. A redshift of the plasmon mode at the Bi_2Se_3/graphene interface to 6.0 eV was observed, which is lower in energy than the feature at the Bi_2Se_3/C_{60} interface. This difference in energy could be a consequence of difference in resonance/absorption energy between graphene (4.3 eV) and C_{60} (4.7, 5.8 eV), leading to the formation of a lower energy hybridised plasmon.

The Bi_2Se_3/graphene system could be further altered by deposition of different materials including other organics on top of the graphene layer. This doping could further alter the chemical potential and hence the Bi_2Se_3 surface. The plasmon dispersion of this mode would be interesting to study due to the variety of different trends observed in both free-standing and monolayer graphene, which could contrast greatly with the dispersion observed at a Bi_2Se_3/C_{60} interface.

5.3 Bi_2Se_3/H_2Pc

Hydrogen phthalocyanine, H_2Pc, is a planar molecule that has been used in solar cells and organic transistors, with tunable electrical and optical properties [270]. This tunability makes it a good choice of material to dope the TI surface to achieve tunable properties after deposition. The effect of a thin film of H_2Pc on the surface of Bi_2Se_3 must first be determined to demonstrate the degree of modification to the TI surface. There are several possible crystalline structures which H_2Pc can adopt including planar stacking and stacking at an angle [286]. The molecular orbital diagram of H_2Pc is presented in figure 5.1a and the HOMO-LUMO interband transition occurs at an energy of 2.0 eV [266].

It has been shown, by Jakobs *et al.*, that H_2Pc molecules, at a coverage of 1 monolayer, can shift the energy of the Dirac point and can give rise to a hybrid interface state between the topological surface state and H_2Pc HOMO due to coupling [6]. A large dipole was also observed at the interface, much greater than was observed for C_{60}. Therefore, we can expect a H_2Pc thin film layer to have a significant effect on the Bi_2Se_3 surface, which should be observable through changes around the π plasmon energy. Since measurements performed by Jakobs *et al.* used ARPES, which is surface sensitive, the effect of thick H_2Pc layers was not known. Low-loss EELS of interfacial plasmons will provide a measure of surface modification induced by the thick H_2Pc overlayer. As H_2Pc is part of a family of molecules that can include different central atoms, it provides a starting point to investigating the effect of different central atoms on the interaction with the Bi_2Se_3 surface [270]. Metal ions at the centre of a Pc molecule alter the electronic and optical properties of the molecule. The electron contribution of different central atoms to the molecule changes with the number of *d*-electrons of the ion and results in shifts to molecular energy levels and changes to the symmetry of molecular orbitals [266]. The option to alter the central atom to change the chemical properties of phthalocyanines could be useful in expanding this work.

This section will first assess the structure and quality of a cross-section specimen of $SiO_2/Bi_2Se_3/H_2Pc$ using STEM and core-loss EELS before discussing plasmon spectra. As H_2Pc molecules are less stable under an electron beam than previously discussed organic ma-

terials, beam exposure could result in the breakdown of molecules. This could be monitored by observing core-EELS spectra around the carbon K-edge, where relative peak energies are observed to change due to double bond breaking, as discussed in section 2.5. Low-loss EELS data, accompanied by calculated spectra, will indicate bulk and interfacial modes and highlight changes induced by the H_2Pc overlayer. The degree of localisation of plasmon modes to interfaces will be assessed using EELS maps to investigate the depth of interaction.

5.3.1 Structure

Bi_2Se_3 single crystals were prepared by chemical vapour transport at the University of Leeds on SiO_2 substrates. 43 nm of H_2Pc was then deposited on the surface using MBE and capped with a layer of niobium by MBE. A niobium capping layer was used to prevent oxygen diffusion into the organic layer and was selected due to its ability to expand upon oxygen adsorption to prevent diffusion through the layer. After transport to Glasgow, cross-sections were extracted from the single crystals using FIB techniques discussed in chapter 2. Lamellae were extracted at room temperature using the PFIB, before thinning at a temperature of 103 K on the Ga FIB. The cross-section discussed in this section was extracted from a flat Bi_2Se_3 crystal shown in figure 5.6a. The layer of Pt, shown in figure 5.6a, was deposited during preparation and the thinned region of this specimen was around halfway along this Pt rectangle, at the centre of the crystal.

A TEM image of the cross-section of the lamella is present in figure 5.6d and shows the 142 nm Bi_2Se_3 crystal. The crystal was orientated along the <120> zone axis, as indicated on the diffraction pattern in figure 5.6b. Large regions of the Bi_2Se_3 layer were observed to be single crystalline and of the same grain, however, this did not cover the full sample and some evidence of different grains was observed. Variation in contrast along the Bi_2Se_3 layer in figure 5.6d can be seen and in some diffraction patterns, additional diffraction spots could be observed. These additional spots were observed along the c-axis, in between the main spots and could indicate twin plane grain boundaries.

The SiO_2 substrate is amorphous and does not have a strong epitaxial relationship with the Bi_2Se_3 crystal. This produces a sharp interface with no lattice strain. The weak interactions between the TI crystal and SiO_2 substrate can result in delamination at this interface during FIB preparation, so the cross-sections investigated throughout this thesis are ones which did not delaminate.

The lamella displayed a smooth interface between Bi_2Se_3 and H_2Pc with no step edges present in Bi_2Se_3, as shown in figure 5.6e,f. No crystallinity was observed in the H_2Pc layer. This lack in crystallinity is not unexpected and could be a result of a lack of ordering within the layer or the presence of several different stacking orientations throughout the layer. As

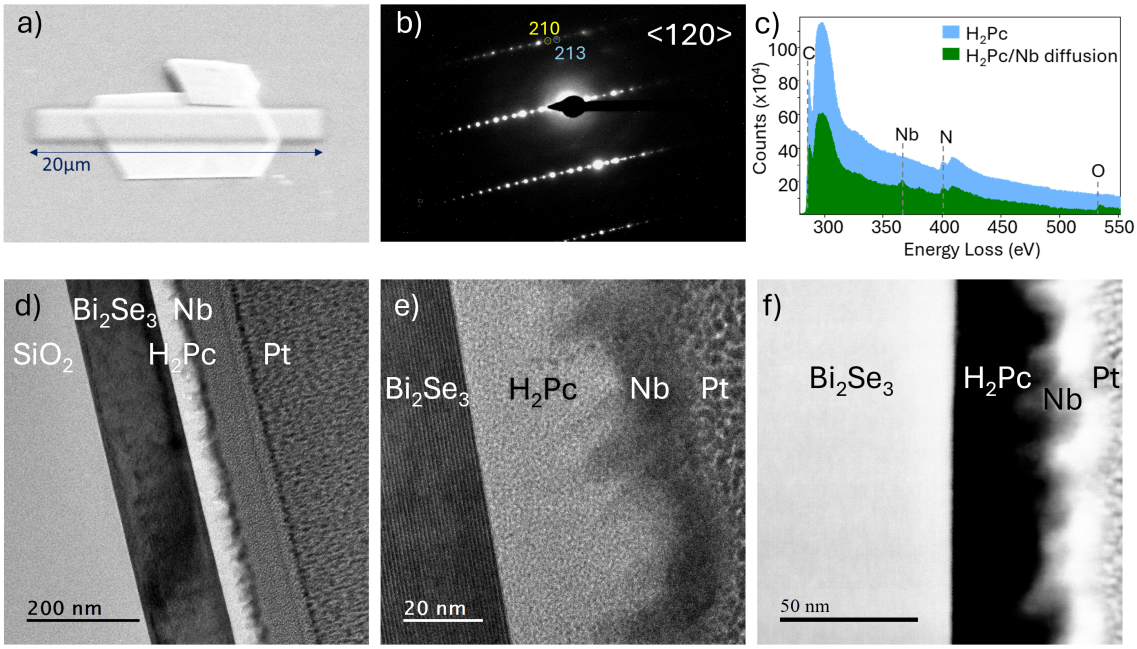

Fig. 5.6 a) SEM image of a Bi_2Se_3 crystal with H_2Pc and Nb overlayers on an SiO_2 substrate, which a cross-section was prepared from. A layer of platinum was deposited along the centre of this crystal and the cross-section extracted from this region. b) SAD diffraction pattern of the Bi_2Se_3 layer in a cross-section along zone-axis <120>. c) Core-loss EELS spectra from different regions of the H_2Pc layer where the green spectrum contains some Nb diffusion and the blue spectrum does not. Carbon, niobium, nitrogen and oxygen edges are indicated. d,e) TEM images of the cross-section with the substrate on the left. f) HAADF STEM image of the cross-section where Nb diffusion can be observed as bright regions into the H_2Pc layer.

measurements were carried out at room temperature and the electron beam can increase the sample temperature, the mobility of molecules could limit our ability to observe atomic columns.

The TEM and STEM images in figure 5.6e,f, show diffusion of the Nb cap into the H_2Pc layer. This diffusion can be observed across the full sample and reached a depth of 19 nm into the H_2Pc layer, leaving 24 nm of H_2Pc with no diffusion present. To confirm that no small quantifies of Nb had diffused further into the layer, core-loss EELS was carried out. Spectra in figure 5.6c show regions of the H_2Pc layer with and without Nb diffusion. The Nb M_3 edge is observed at 368 eV and is a clear sharp feature followed by the Nb M_2 edge at 380 eV. The energies of these edges vary slightly with changes in oxidation state and an oxygen edge is present in the region of Nb diffusion [287]. The Nb edge is not present in the bottom half of the H_2Pc layer, suggesting that no Nb has diffused all the way through and that the 24 nm region closest to the Bi_2Se_3 interface can be considered as fully H_2Pc. The

oxygen peak is also not present within the first 24 nm region of H_2Pc, indicating that the Nb cap has been successful in limiting oxygen diffusion into the organic layer.

With sharp interface, crystalline Bi_2Se_3 and oxygen-free H_2Pc, the specimen was deemed of high enough quality to investigate the plasmonic behaviour. All further STEM and EELS characterisation was carried out at accelerating voltages of 80 or 60 kV to limit damage to the H_2Pc layer, which has been shown to occur at 200 kV in other phthalocyanine samples.

5.3.2 EELS Characterisation

Low-loss EELS was carried out to investigate the plasmonic behaviour at interfaces in the SiO_2/Bi_2Se_3/H_2Pc sample. Figure 5.7 contains EELS spectra from each bulk region and interface of the sample, alongside calculated EELS spectra for each region. The calculations were performed using the relativistic analytical method of equation 3.13, described in chapter 3.3. Bulk dielectric functions for SiO_2, Bi_2Se_3 and H_2Pc, were extracted from EELS data using Kramers-Kronig analysis.

The low-loss EELS spectrum obtained for bulk SiO_2, shown in figure 5.7c, is very similar to the EELS spectrum recorded in bulk SiO_2 of the cross-section discussed in section 5.2. the bandgap, E_g, was identified at 9.8 eV, with no peaks present below this energy. Interband transition peaks observed previously at 10.6, 12.0, 14.3 and 18.2 eV are present, as well as a volume plasmon at 23 eV [285]. In bulk Bi_2Se_3, the spectrum is the same as other samples of Bi_2Se_3 shown throughout this thesis, with a π plasmon at 7.2 eV and $\pi + \sigma$ plasmon at 17.2 eV. This indicated that, although a different growth method was used for this sample and the Bi_2Se_3/C_{60} sample presented in chapter 4, there are no significant defects or changes to the material properties which influence the bulk plasmonic behaviour. The calculated spectra, shown as dotted lines in shown in figure 5.7c, replicate the experimental data, indicating that no artefacts were introduced or information lost in the KK analysis to obtain the dielectric function.

At the SiO_2/Bi_2Se_3 interface, a localised peak at 6.2 eV is present, denoted SP in figure 5.7c. This feature can be attributed to a surface plasmon mode at the interface, arising from coupling between the two materials. This mode is not predicted by the analytical calculation, which only considers bulk dielectric functions and does not consider other interface interactions that can shift the plasmon energy such as charge redistribution. The peak at the interface is very broad indicating the potential of overlapping peaks being present in this energy region. Slightly further into the TI layer, this peak is observed alongside the Bi_2Se_3 π plasmon. This is in agreement with the results observed for the SiO_2/Bi_2Se_3 interface in the Bi_2Se_3/graphene sample discussed in section 5.2 where both a surface plasmon and Bi_2Se_3 π plasmon were observed at the same time. The calculation from

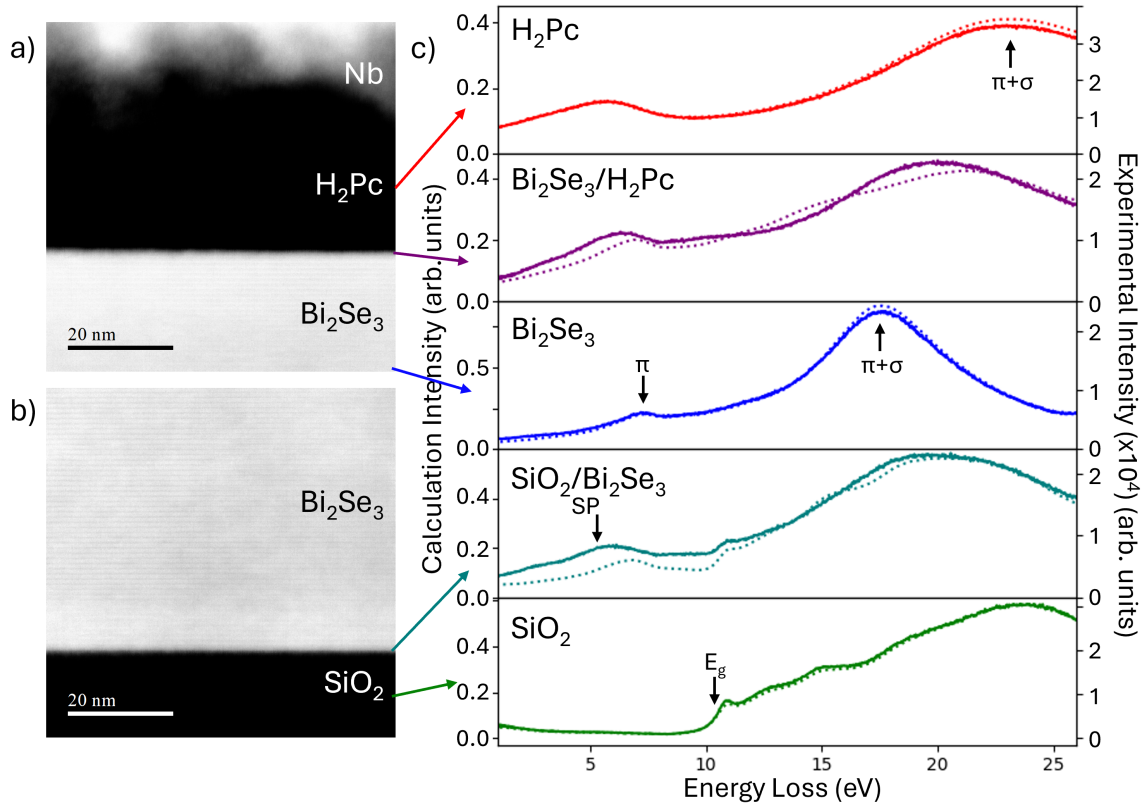

Fig. 5.7 Low-loss EELS data from each region of an $SiO_2/Bi_2Se_3/H_2Pc/Nb$ cross-section. a) HAADF STEM image of the top interface of the sample with $Bi_2Se_3/H_2Pc/Nb$ from bottom to top. b) HAADF STEM image of the bottom interface with SiO_2/Bi_2Se_3. c) Low-loss EELS data from bulk H_2Pc, Bi_2Se_3 and SiO_2 and Bi_2Se_3/H_2Pc and SiO_2/Bi_2Se_3 interfaces. Experimental data is shown with solid lines and calculated EELS spectra are shown as dotted lines. Features indicated include $\pi + \sigma$ plasmons in H_2Pc and Bi_2Se_3, π plasmon in bulk Bi_2Se_3, the SiO_2 bandgap, E_g, and surface plasmon, *SP*, at the SiO_2/Bi_2Se_3 interface.

dielectric functions does not include the surface plasmon mode but the Bi_2Se_3 π plasmon remains at the interface. However, the presence of this mode deeper into the Bi_2Se_3 layer than the Al_2O_3/Bi_2Se_3 surface mode and its decay in intensity into the layer, is more characteristic of a surface plasmon polariton mode arising from dielectric coupling than a localised 2D state.

The EELS spectrum for H_2Pc is similar to that of graphene and C_{60}, where there is a feature around 6 eV and a $\pi + \sigma$ plasmon around 23 eV. In H_2Pc the $\pi + \sigma$ plasmon is observed at 23.25 eV, which is in agreement between this experimental data and literature. The low energy feature at 5.7 eV, in this work, is a broad feature, which can be fitted with a single peak. A feature at 5.9 eV has been observed in photoemission spectra and has been attributed to ionisation of π electrons in the outer H_2Pc rings [288]. For a single

H_2Pc molecule, interband transitions have been assigned at 2.2 eV for the first valence to conduction band transition and at 37 eV for a $\pi \rightarrow \pi^*$ transition by Scrocco *et al.* [265]. They also noted a strong peak at 6.6 eV in their EELS, which was attributed to an $n \rightarrow \pi^*$ transition from nitrogen orbitals. Additional interband transitions were identified by Scrocco *et al.*, at energies at 10.4, 12.7, 18.0, 19.8 and 27.6 eV, which are not evident in EELS data presented in figure 5.7c. It is possible that these peaks are not present in our data due to the samples not being single molecules, but thick layers. The plasmon modes are delocalised and, in the absence of crystalline structure, dominate the spectrum. A plasmon mode at 21.6 eV was identified in literature, which is slightly lower in energy than the plasmon observed at 23.25 eV in our data. Dahms *et al.* observed a strong peak at 22.4 eV and attributed this to a superposition of a plasmon mode and $\sigma \rightarrow \sigma^*$ transitions [289].

At the interface between Bi_2Se_3 and H_2Pc, a low energy peak can be fitted at 6.4 eV, which differs from the energy of the low-energy peak observed in the calculated spectra at this position. The calculated spectrum indicated a peak at 7.1 eV, which is closer to that of the bulk Bi_2Se_3 π plasmon at 7.2 eV than the peak energy of 6.4 observed in the experimental interface spectrum. This indicates a slight change to the surface behaviour not captured by the calculation and could indicate its origins to be from a localised surface state or the formation of a hybrid interface state as observed by ARPES for monolayer H_2Pc [6]. The EELS spectrum calculated from bulk dielectric functions should capture the effect of a difference in refractive index across the interface to the plasmon energy, therefore, the large difference in plasmon energy in the experimental data could be due to the influence of molecular resonances or charge transfer [69]. In order to calculate EELS spectra to test this hypothesis, the materials would need to be modelled with the inclusion molecular orbitals and the atomic and molecular structure at the interface considered. This would allow for charge transfer and hybridisation to be modelled and their effect on the EELS spectrum investigated. The 2D π plasmon observed at the Al_2O_3/Bi_2Se_3 interface in chapter 4, is not present at the Bi_2Se_3/H_2Pc interface due to bonding, band-bending and charge transfer from the H_2Pc. The bulk Bi_2Se_3 π plasmon mode is instead redshifted towards the interface due to the charge dipole.

Across the Bi_2Se_3/H_2Pc interface, EELS maps, shown in figure 5.8, indicate the localisation of a plasmon mode to the interface. Unlike the Bi_2Se_3/C_{60} interface, this localisation does not appear to be limited to the first layer of molecules and instead penetrates deeper into both sides of the interface. The lack of clear molecular ordering could mean that the first layer of H_2Pc molecules are not flat along the surface and could vary in stacking angle. Variations in stacking angle could result in extended interaction with the surface. Additionally, the

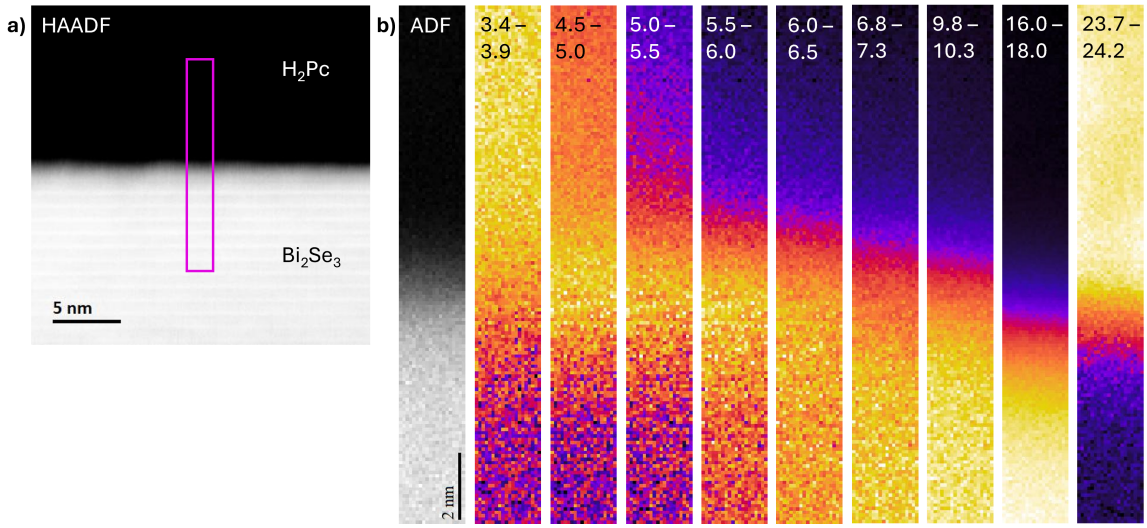

Fig. 5.8 EELS maps across the interface between Bi_2Se_3 and H_2Pc at different energies. a) HAADF STEM image of the Bi_2Se_3/H_2Pc interface where the rectangular annotation represents the region from which EELS maps were recorded. b) ADF image and EELS maps across the interface over energy ranges 3.4-3.9, 4.5-5.0, 5.0-5.5, 5.5-6.0, 6.8-7.7, 9.8-10.3, 16.0-18.0 and 23.7-24.2 eV respectively. These energy ranges were selected to highlight energies of bulk plasmons and features observed in interface spectra. Increased intensity is observed at the interface in the energy region 5.0 to 5.5 eV.

disordered H_2Pc molecules could extend the region of screening and hence, a less confined surface interaction is observed.

A localised surface mode was observed at the Bi_2Se_3/H_2Pc interface at 6.4 eV which differs from the energy of the mode at the C_{60} interface which was observed at 6.3 eV. As well as the change in energy, the localised mode was observed to persist deeper into the layers on both sides of the interface. Furthermore, the observed peak energy does not agree with the energy predicted from EELS calculations, which predict the peak energy at the surface to be at 7.1 eV from interfacial plasmon coupling effects. It is proposed that a hybrid state forms at this interface, as was shown for the Bi_2Se_3/C_{60} interface in chapter 4.

H_2Pc is an electron donor, so the charge distribution across the interface should differ from that of the Bi_2Se_3/C_{60} interface. This is consistent with the observed redshift of the interface plasmon to 6.4 eV and its extended depth into both layers, which differ from the observations in chapter 4. The results suggest charge transfer or the formation of a hybrid interface state which modifies the dielectric response at the interface. Other phthalocyanine molecules have been shown to have varied behaviour on a TI surface, such as MnPc n-doping a Bi_2Te_3 surface without influencing topological surface states [76] and CoPc showing no significant charge transfer across a TI interface [77]. These observations support the

interpretation that the interfacial plasmon energy and confinement are strongly influenced by the molecular donor properties, the degree of molecular ordering at the interface and the resulting charge distribution.

5.4 Bi_2Se_3/CuPc

To investigate the effect of a metallic centre in the phthalocyanine molecules, samples with CuPc were analysed. The properties of phthalocyanine molecules are greatly influenced by the metallic or non-metallic centre [290]. Metallic centres with different number of *d*-electrons can influence the energy of molecular orbitals, which can alter the electronic properties [290]. In the molecular orbital diagram in figure 5.1a, the energy levels of H_2Pc and CuPc are similar, with only 0.1 eV difference in HOMO-LUMO energy. Compared to other metallic centres, difference in electronic properties of H_2Pc and CuPc are small [266].

Charge transfer across the interface can influence the surface states and plasmonic behaviour, which has been shown to differ for different metallic centre phthalocyanines. Individual MnPc molecules were observed to transfer a minor amount of charge to Bi_2Te_3 surfaces resulting in n-doped Bi_2Te_3 and the formation of a hybrid state at the interface [76]. CuPc molecules, on the other hand, were observed to show no significant charge transfer to a Bi_2Te_3 surface [77]. CoPc molecules were not observed to transfer a significant amount of charge to a Bi_2Te_3 surface, but did result in hybridisation between the Bi_2Te_3 surface states and CoPc molecular orbitals [79]. Studies of MnPc on Bi_2Te_3 surfaces indicated significant charge transfer from first layer of molecules to the Bi_2Te_3 surface [78]. This study found that the topological states were not predictably changed by the MnPc molecules. These studies show great variation in the amount of charge transfer observed across a TI/phthalocyanine interface depending on the form of Pc. These observations are for small quantities of ordered molecules on the surface, but in thin films studied under an electron beam the surface could be more disordered, potentially altering the degree of charge transfer.

Ordering of molecules is also influenced by the metal centre, which can determine how molecules assemble on a substrate [77]. Molecules with a copper centre were observed to assemble with square ordering on a Bi_2Te_3 surface up to a coverage of 0.46 molecules/nm^2, whereas, molecules with a cobalt centre assemble with a quasi-hexagonal ordering at a coverage of 0.36 molecules/nm^2.

The topological surface states of Bi_2Se_3 are expected to be modified by the presence of CuPc molecules and it has been shown, by scanning tunnelling spectroscopy (STS), that the Dirac point is maintained and down shifted by 336 meV when CuPc is deposited [75]. This protection of the topological surface state (TSS), alongside a change in its energy is

desirable. Furthermore, CuPc has interband transition energies close to the energy of the Bi_2Se_3 surface π plasmon, which could result in coupling between the molecules and the surface. This coupling could result in a red-shift of the plasmon energy at the interface and the formation of a hybridised plasmon state.

This section will show that the low-loss EELS spectrum at an interface between Bi_2Se_3 and CuPc differs from a Bi_2Se_3/H_2Pc interface. Momentum-resolved EELS is used to map the plasmon dispersion across the first Brillouin zone of Bi_2Se_3 and investigate how this differs from the observed plasmon dispersion at the Bi_2Se_3/C_{60} interface discussed in chapter 4.

5.4.1 Structure

Cross-sections of Al_2O_3/Bi_2Se_3/CuPc were extracted from bulk samples, grown by MBE at the University of Leeds. lamellae were prepared for microscopy using cryogenic FIB preparation, with extraction from bulk at room temperature on the PFIB and thinning at 103 K using the Ga-FIB, as outlined in section 2.2. TEM images and a diffraction pattern of the cross-section are presented in figure 5.9.

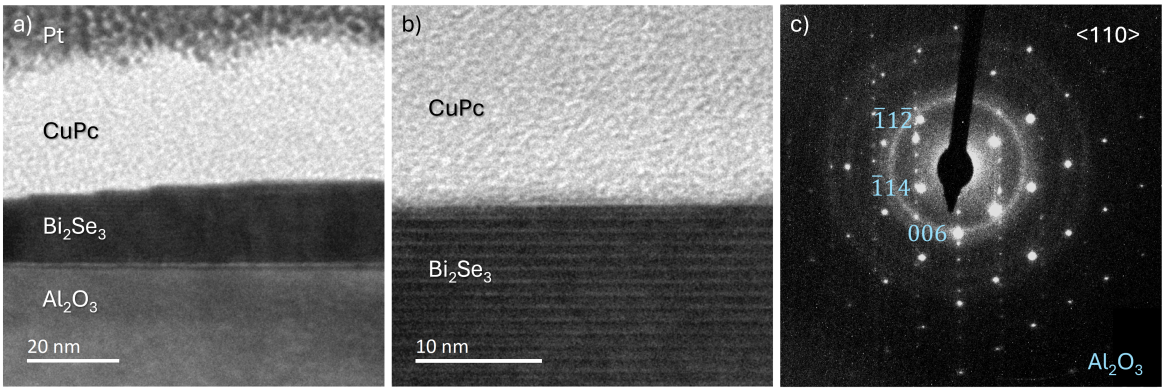

Fig. 5.9 a) TEM image of Al_2O_3/Bi_2Se_3/CuPc cross section where small step edges are observed at the Bi_2Se_3/CuPc interface. b) Higher magnified TEM image of the Bi_2Se_3/CuPc interface. Bi_2Se_3 QLs are observed with a sharp interface with CuPc. c) SAD diffraction pattern of the sample along zone axis <110>. Diffraction spots from Al_2O_3 and Bi_2Se_3 are observed.

TEM images of the Al_2O_3/Bi_2Se_3/CuPc cross-section show a Bi_2Se_3 thin film of thickness between 14 and 16 nm, with a 30 nm CuPc layer. The sample is capped with Pt which was deposited during FIB preparation. The Bi_2Se_3 layer was observed to terminate with several step edges, which can be seen in figure 5.9a, each 1 QL tall. This varied the width of the TI layer across the lamella, with some regions containing several step edges close to each other

and some regions with flat surfaces. The step edges should not have a significant effect on EELS spectra and plasmon confinement as shown in section 3.6.3. Several grains of Bi_2Se_3 were observed throughout the layer, with the TI thin film being less uniform than the other MBE grown samples presented in chapter 4. The grain size was deemed to range from 40 nm to 60 nm. EELS data was acquired within single grains of Bi_2Se_3 without step edges at the surface.

The interface between Bi_2Se_3 and CuPc has some large flat regions free of step edges and is sharp to less than 1 nm. The CuPc layer, seen in figure 5.9b, shows no crystallinity with no fringes or diffraction spots observed. This is similar to the H_2Pc sample where we also saw no evidence of crystallinity. The amorphous layer of CuPc is not unexpected due to the variety of different stacking behaviours that have been observed for CuPc. Stacking has been observed to vary depending on film thickness, with the coexistence of two different stacking orientations at thicknesses greater than 10 nm [286]. CuPc molecules on Bi_2Se_3 surfaces at coverages greater than one monolayer were observed to stack standing on edge at step edges of Bi_2Se_3 [75]. In the thin films shown in figure 5.9, there are several step edges observed along the Bi_2Se_3/CuPc interface which could result in this stacking behaviour. If any ordering is present in the CuPc layer it could be possible that it does not extend through the thickness of the film.

The cross-section was orientated such that the beam was aligned with the <110> zone axis of Al_2O_3, as indicated in figure 5.9c. The largest diffraction spots are from the Al_2O_3 substrate and the smaller ones from the Bi_2Se_3 thin film. The c-axes of the Al_2O_3 substrate and Bi_2Se_3 film are aligned along the growth direction, which is vertically upwards in TEM images in figure 5.9. Diffuse rings can also be observed in the diffraction pattern, which indicate the amorphous CuPc layer and Pt cap layer deposited during sample preparation.

The thickness of the lamella was measured as t/λ_i value of 0.6 at 80 kV. The quality of the sample was adequate for low-loss EELS analysis, despite being around the maximum thickness desired for measurements at 60 kV.

5.4.2 EELS Characterisation

Low-loss EELS spectra were acquired across the sample and an EELS spectrum from each region is presented in figure 5.10. This characterisation was performed on the ARM at 80 kV to reduce damage incurred by the beam. Successive EELS scans were performed in different regions of the lamella, so that data was not collected on damaged regions. Some beam damage could be observed after SI acquisition, indicated by a change in contrast in regions imaged, however, no change was observed in imaging or EELS between the beginning and end of the spectrum image. Analytically calculated EELS spectra are presented as dotted

lines for comparison and were calculated from bulk dielectric functions from KKA of EELS data using the method outlined in section 3.3.

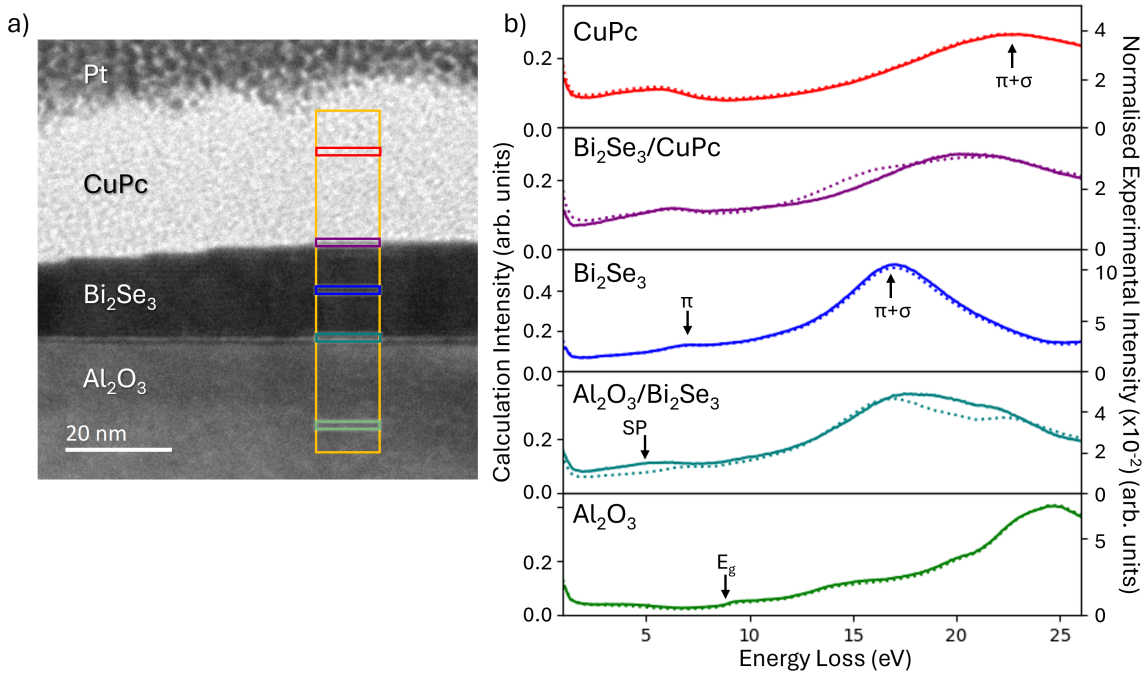

Fig. 5.10 Low-loss EELS spectra from each region of a cross-section of Al_2O_3/Bi_2Se_3/CuPc. a) TEM image of the sample. b) EELS spectra for bulk and interfaces of the sample as indicated in the TEM image in a. Plot colours are the same as indicated in each region of the image. Experimental data is presented as solid lines and calculated spectra are presented as dotted lines. π and $\pi+\sigma$ plasmons are indicated on spectra and the Al_2O_3 bandgap, E_g, is indicated in bulk Al_2O_3.

The presented EELS spectrum in the Al_2O_3 substrate, shown in green in figure 5.9b, shows the bandgap, E_g, at 8.7 eV, which is the same as observed in samples discussed in chapter 4. Additional peaks identified at 13.2, 20.0 and 25 eV agree with previous samples and are identified as interband transitions from literature [250, 251]. At 24.0 eV, the peak is attributed to a volume plasmon [252]. In bulk Bi_2Se_3, the π and $\pi+\sigma$ plasmons are identified at 7.2 and 17.3 eV respectively as indicated in figure 5.9b. Bi edges at higher energies were identified at the same energies as previous MBE grown samples but are not indicated in this figure.

Bulk CuPc shows a similar EELS spectrum to H_2Pc, with a large $\pi+\sigma$ plasmon and a less intense peak at lower energy. The high energy peak, identified as the $\pi+\sigma$ plasmon, has an energy of 22.9 eV, which is in agreement with literature values for unstrained CuPc specimen with no evidence of crystallinity [291]. The broad peak observed between 3 and 6 eV can be fitted best with two smaller peaks at energies 3.5 and 5.8 eV, where the intensity

of the second peak is greater. Fitting with both peaks in this energy range resulted in an R-squared value of greater than 0.999, indicating a good fit. In literature, several peaks have been identified in this energy range, with peaks observed at 3.8, 6 and 8 eV in thin films by Alexander *et al.* [291]. Two peaks are expected to occur around 2 eV, which have been attributed to interband transitions and inter-molecular coupling between molecules [291, 271]. These peaks are not observed here, which could be due to the large tail of the ZLP in this data and the absence of molecular ordering.

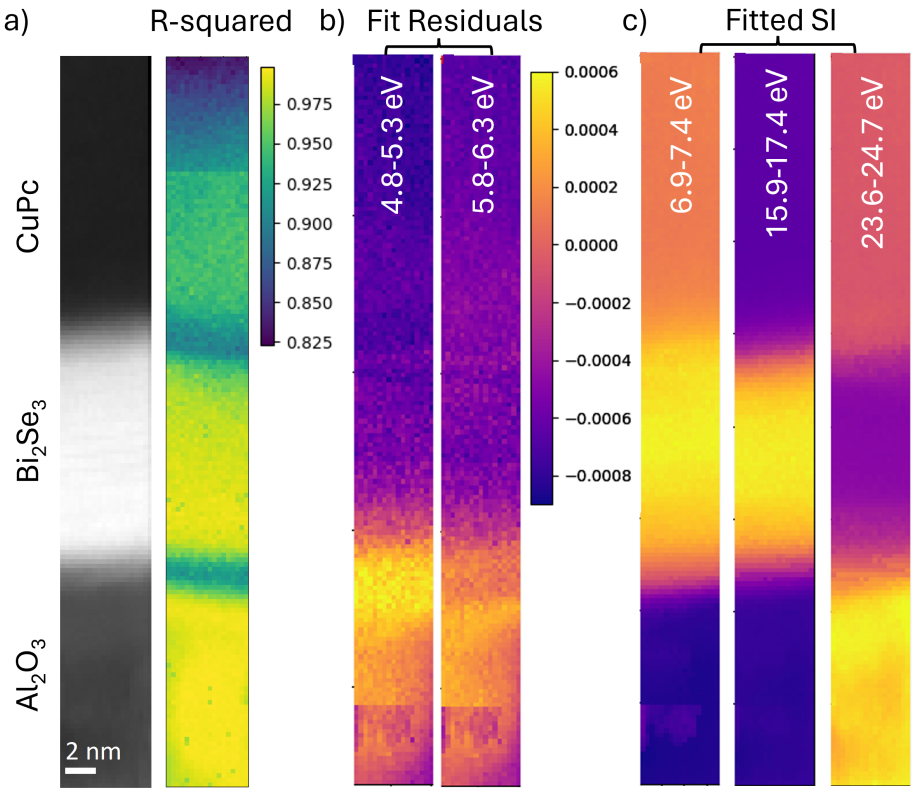

Fig. 5.11 Spectrum images across Al_2O_3/Bi_2Se_3/CuPc layers. a) ADF image of the cross section where Bi_2Se_3 is the most intense. R-squared values of the fitted spectrum, where the R-squared value at both interfaces is lower than in bulk regions of the SI. b) Residuals of experimental vs fitted spectrum over energy ranges 4.8-5.5 and 5.8-6.3 eV, where peaks were observed in EELS spectra at the interfaces. c) Fitted spectrum images over energy ranges: 6.8-7.3 eV, 15.9-17.4 eV and 23.6-24.7 eV, which contain bulk plasmon features.

Comparisons between spectra fitted with calculated spectra and experimental data are presented in figure 5.11. The experimental EELS spectrum at each pixel in the SI was fitted with a calculated EELS spectrum using the procedure outlined in section 4.3. The resulting best R-squared value for each pixel is presented alongside an ADF image in figure 5.11a, this value is greater for better fits. The spectrum image was normalised with respect to integrated

ZLP intensity to remove effects associated with thickness or variations in the mean free path between different materials. The R-squared value was lowest at interfaces, indicating the disparity between experimental and calculated spectra in these locations.

Residuals of this comparison are shown in figure 5.11b, over an energy range of 4.8-5.3 eV and show increased intensity at the SiO_2/Bi_2Se_3 interface. This increased intensity in the residuals is accompanied with a drop in R-squared value associated with the fit at the interface. The energy and localisation of this surface feature is similar to that observed in the sample discussed in chapter 4 and validates those results. As in chapter 4, this surface mode is proposed to originate from π electrons within the first layer of Se atoms in the Bi_2Se_3 layer. Although a reduction in R-squared value is observed at the Bi_2Se_3/CuPc interface, no increased intensity is observed at the location of the interface mode across the presented energy ranges.

The localisation of bulk plasmon modes can be observed in the fitted spectra in figure 5.11c, where increased intensity can be observed in Bi_2Se_3 over energy ranges containing the bulk π and $\pi+\sigma$ plasmon modes of 6.9 to 7.4 eV and 15.9 to 17.4 eV. The final panel show the EELS intensity over an energy range of 23.6 to 24.7 eV, which has the greatest intensity in the SiO_2 layer and least intensity in the Bi_2Se_3 layer. This maps the volume plasmon modes in SiO_2 and CuPc.

The behaviour at the Bi_2Se_3/CuPc interface appears to be very similar to the Bi_2Se_3/H_2Pc interface, with a peak energy of 6.4 eV at the interface. This suggests that, if a hybridised surface state has formed, the energy of this state is similar between samples. Molecular orbital energy levels for H_2Pc and CuPc vapours indicate only a small difference in the energy of HOMO and LUMO states [266]. Calculations by Zhou *et al.* indicate the HOMO of H_2Pc as 6.286 eV and CuPc as 6.259 eV and the LUMO of H_2Pc to be 2.068 eV and of CuPc to be 1.959 eV, which gives a difference in HOMO-LUMO gap of less than 0.1 eV. In comparison to other metallic centres, CuPc was indicated to have less differences in the character and symmetry of molecular orbits with H_2Pc. The inclusion of a metal centre with a high number of d-electrons such as Cu (d^9) has less effect on the electronic states near the chemical potential [290]. Coupling between molecules and thin film plasmons can depend on the energy of molecular resonances and the plasmon excitations [111]. When the energies are close, strong coupling occurs and hybridised plasmon modes can form, similar to hybridised bonds, at energies determined by energies of the molecular energy levels and film plasmon. Since the molecular transitions of H_2Pc and CuPc are close in energy, the energy of a hybridised mode would be similar in each case. Under the electron beam, the CuPc molecules will be disordered at the interface and their charge dipoles orientated in

random directions. This means that the TI surface will be interacting with the superposition of all of these dipoles and will not be confined to specific molecules on the surface.

5.5 Comparison and discussion

Four different organic molecular layers have had their effect on a Bi_2Se_3 surface investigated and showed slight differences in peak energy and localisation. These four samples will be compared to show how the Bi_2Se_3 surface spectrum changes at each interface and discuss the significance of this. For clarity, the observed feature at the Bi_2Se_3/organic interface is referred to as the interfacial plasmon mode throughout this section. Although all four samples have Bi_2Se_3 as the topological insulator, two different growth methods were used to produce these samples, with different Bi_2Se_3 thicknesses and on different substrates.

Two samples of Bi_2Se_3 were growth fully by MBE on Al_2O_3 substrates as thin films of thicknesses of around 14 nm. The first sample is Al_2O_3/Bi_2Se_3/C_{60}, which was discussed in chapter 4 and the second is Al_2O_3/Bi_2Se_3/CuPc, discussed in section 5.4. EELS spectra acquired from bulk Al_2O_3, Bi_2Se_3 and the substrate interface are presented in figure 5.12a,b and show few differences. The bulk Al_2O_3 spectrum contains a bandgap edge with onset at 8.7 eV for both samples and further peaks have the same energy and relative heights, indicating no differences between the substrate including no additional FIB damage. The bulk Bi_2Se_3 spectrum shows no clear differences between samples with the π and $\pi+\sigma$ plasmons at the same energy. This indicates that there are likely no differences between the plasmonic behaviour of Bi_2Se_3 of each sample. At the substrate interface, shown in figure 5.12b, the spectra are very similar, with the Al_2O_3 bandgap being more resolved in the Bi_2Se_3/C_{60} sample and the surface plasmon at a slightly greater intensity.

The other two samples were grown by CVT on SiO_2 substrates, with the organic layer deposited via MBE. These samples have much thicker layers of Bi_2Se_3 >100 nm and have more defects and grains within the Bi_2Se_3 layers. An increase in defect concentration could result in a greater number of bulk carriers in Bi_2Se_3 and alter the plasmonic behaviour slightly. EELS spectra for bulk substrate, bulk Bi_2Se_3 and the substrate interface are presented in figure 5.12c,d for samples SiO_2/Bi_2Se_3/graphene/aC and SiO_2/Bi_2Se_3/H_2Pc. In bulk Bi_2Se_3, a slight change in energy of the $\pi+\sigma$ plasmon is observed whilst very little difference was seen to the π plasmon energy. This could be a consequence of increased carrier density due to an increased number of defects within this crystal. Although many defects were not observed in STEM images of the Bi_2Se_3/H_2Pc sample, the presence of point defects, which are difficult to see, could increase the carrier density and thus alter the bulk plasmon energy. In bulk SiO_2, peaks after the bandgap are the same but there is a slight difference in the

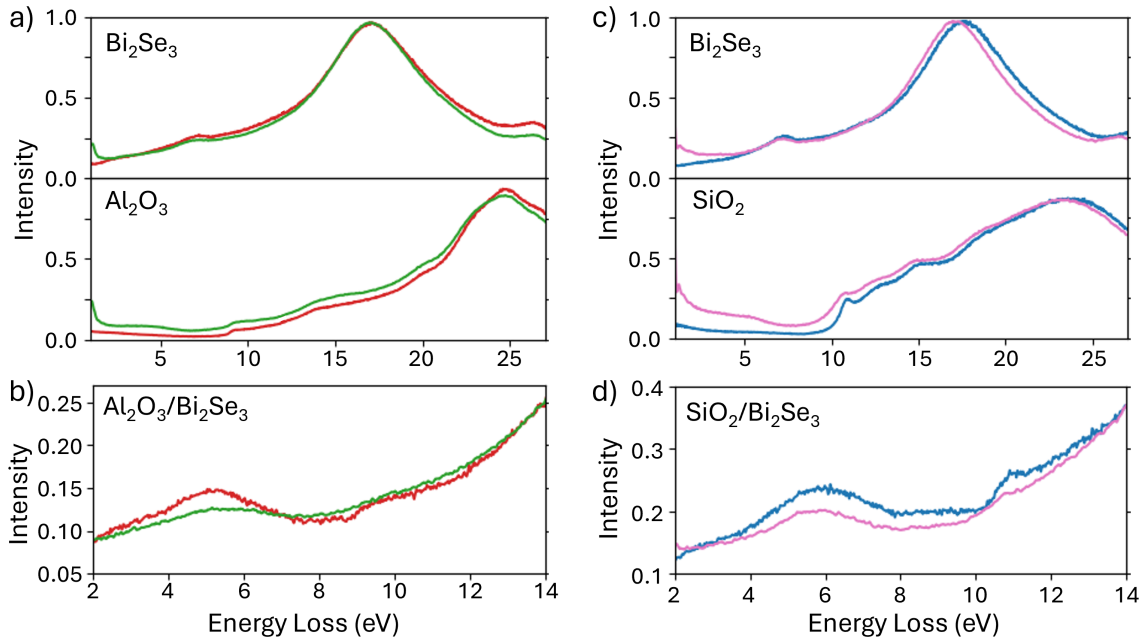

Fig. 5.12 EELS spectra in bulk substrate, Bi_2Se_3 and at the interface for four different samples. a) EELS spectra in bulk Bi_2Se_3 and Al_2O_3 for samples of $Al_2O_3/Bi_2Se_3/C_{60}$ (red) and Al_2O_3/Bi_2Se_3/CuPc (green). b) Spectra at the Al_2O_3/Bi_2Se_3 interface for both samples. c) EELS spectra in bulk Bi_2Se_3 and SiO_2 for samples SiO_2/Bi_2Se_3/graphene/aC (pink) and $SiO_2/Bi_2Se_3/H_2Pc$ (blue). d) Spectra at the SiO_2/Bi_2Se_3 interface for both samples.

bandgap edge. In the Bi_2Se_3/graphene sample, shown in pink, the slope of the bandgap is shallower than the Bi_2Se_3/H_2Pc sample shown in blue. This could be the result of differences in experimental methods. The Bi_2Se_3/graphene data was acquired at 200 kV on the ARM, with convergence and collection semi-angles of 29 and 36 mrad, whereas, the Bi_2Se_3/H_2Pc dataset was acquired at 60 kV on SuperSTEM3, with a 30 mrad convergence semi-angle and 22 mrad collection angle. Some of the observed variations in EELS spectra may arise from differences in the experimental setup. Spatial and energy resolution is inferior in data acquired on the ARM, which could account for the lack of well defined features in some spectra. Although slight differences are observed in the bulk spectra, the SiO_2/Bi_2Se_3 interface looks similar on both samples with a surface plasmon observed at 5.6 eV and the coexistence of this surface plasmon with the bulk Bi_2Se_3 π plasmon close to the interface.

Comparison between bulk Bi_2Se_3 EELS spectra of samples grown by different methods, indicates that three out of four samples have the same energy of both π and $\pi+\sigma$ plasmons. The $SiO_2/Bi_2Se_3/H_2Pc$ sample is the only one which has a slightly different energy of $\pi+\sigma$ plasmon. This could be attributed to defects within the TI layer, which could alter the number of electrons within the valence state, slightly changing the plasmon energy.

Bulk EELS spectra from C_{60}, graphene, H_2Pc and CuPc are presented in figure 5.13a and show some similarities. In each material, a $\pi + \sigma$ plasmon can be observed between 22 and 25 eV, dominating the spectrum. At lower energies, between 4 and 7 eV, further peaks are observed in each spectrum, as shown in figure 5.13b. Several interband transition peaks can be clearly observed in C_{60}, but in other materials fewer peaks can be identified. In amorphous carbon, the low energy feature is attributed to a π plasmon, which has been observed in other organics with slight variations in energy. In H_2Pc, only one peak could be fitted in the low energy range, some interband transitions could be expected around this energy but have not been observed. Other molecules such as CuPc are expected to have additional interband transitions in this region but we are unable to resolve them in this data. This could be due to a lack of ordering of the molecules, coupling between molecules or larger contributions from collective plasmon modes at this energy for example. Additionally, EELS data acquired on the ARM have reduced energy resolution compared to SuperSTEM, which could limit the ability to distinguish individual peaks. The lack of distinct interband transition peaks in the phthalocyanine EELS spectra could be due to a superposition of various excitations from disorder. Without interband transitions at uniform energies across the Pc layer, coupling between molecular excitations and TI plasmons could be reduced, explaining the smaller redshift in the Bi_2Se_3 π plasmon energy at the interface.

It was shown in chapter 4, that a 2D surface π plasmon can arise from the first layer of Se atoms at an interface of Al_2O_3 and Bi_2Se_3. This 2D plasmon could be characterised by its dispersion and localisation [91]. With C_{60} present at the interface, this mode was no longer present due to resonant interactions between C_{60} and the surface and instead a hybrid plasmon mode was observed at the interface. This plasmon was characterised as a hybrid plasmon due to its energy being redshifted from the bulk TI π plasmon, its strong localisation, signal enhancement and lack of dispersion. This varied from the expected effect from only the change in relative permittivity at the interface.

Spectra acquired at the Bi_2Se_3/organic interface are presented in figure 5.13c for each sample. There are differences in the peak energy of the low energy peak with energy differences of up to 0.4 eV between different organics. The low energy peak is observed at 6.3 eV at the Bi_2Se_3/C_{60} interface, 6.0 at Bi_2Se_3/graphene interface, 6.4 eV at the Bi_2Se_3/H_2Pc interface and 6.4 at the Bi_2Se_3/CuPc interface. The small difference in peak energy indicates slight changes in the chemical potential at each interface. Variations in the degree of redshift of the Bi_2Se_3 π plasmon energy at the organic interface between samples could be a consequence of different relative permittivity at the surface from the different organic overlayers. However, compared to the interfacial plasmon energy calculated from bulk dielectric functions, the plasmon energies observed have been redshifted to lower energies

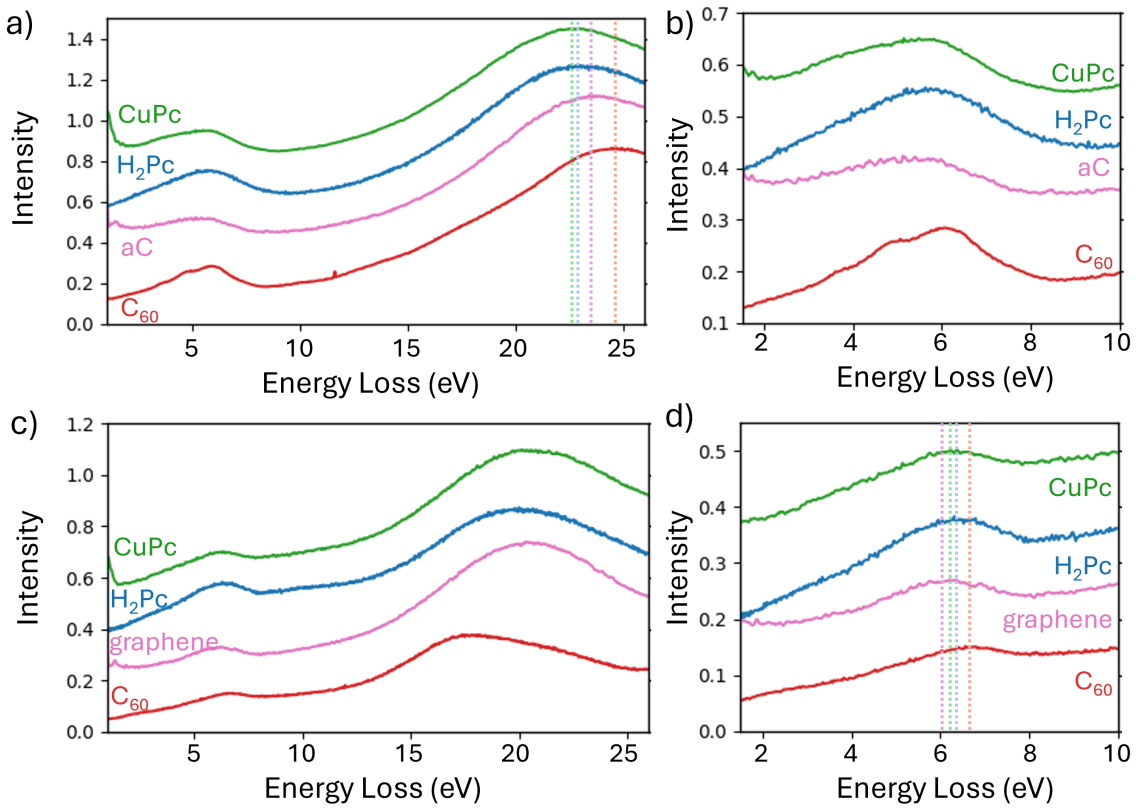

Fig. 5.13 EELS spectra in four samples with different organic molecular layers. a) EELS spectra in bulk C_{60} (red), amorphous carbon (aC) (pink), H_2Pc (blue) and CuPc (green) with the position of their $\pi + \sigma$ plasmon indicated in the same colour. b) EELS spectra of each organic over the energy range 1.5-10 eV where interband transitions and π plasmons are contained. Slight differences in peak shape and energy can be observed. c) Interfacial EELS spectra at interfaces between Bi_2Se_3 and each organic, C_{60}, graphene, H_2Pc and CuPc. d) Energy range 1.5-10 eV of the interfacial EELS spectra for each organic where the peak position is indicated with a line of the same colour. Slight differences in peak energy can be observed between samples.

by different amounts, indicating that additional interactions could be present. These include coupling mechanisms from the overlap between Bi_2Se_3 plasmon energies and molecular interband transitions, as well as changes in the local permittivity and dipoles the interfaces. Due to the energies of molecular transitions and molecular plasmons being close to that of plasmon energies in Bi_2Se_3, coupling at the interface could result in hybridised plasmon modes. The energy of these hybridised plasmons is dependent on the energy levels and resonances in the molecule, explaining why the observed energies differ between samples. In each of the discussed organic materials, molecular orbitals are shifted in energy due to

molecular bonding within each material. The relative energies of the molecular orbitals compared to the Bi_2Se_3 energy levels could result in a hybrid state with a different energy.

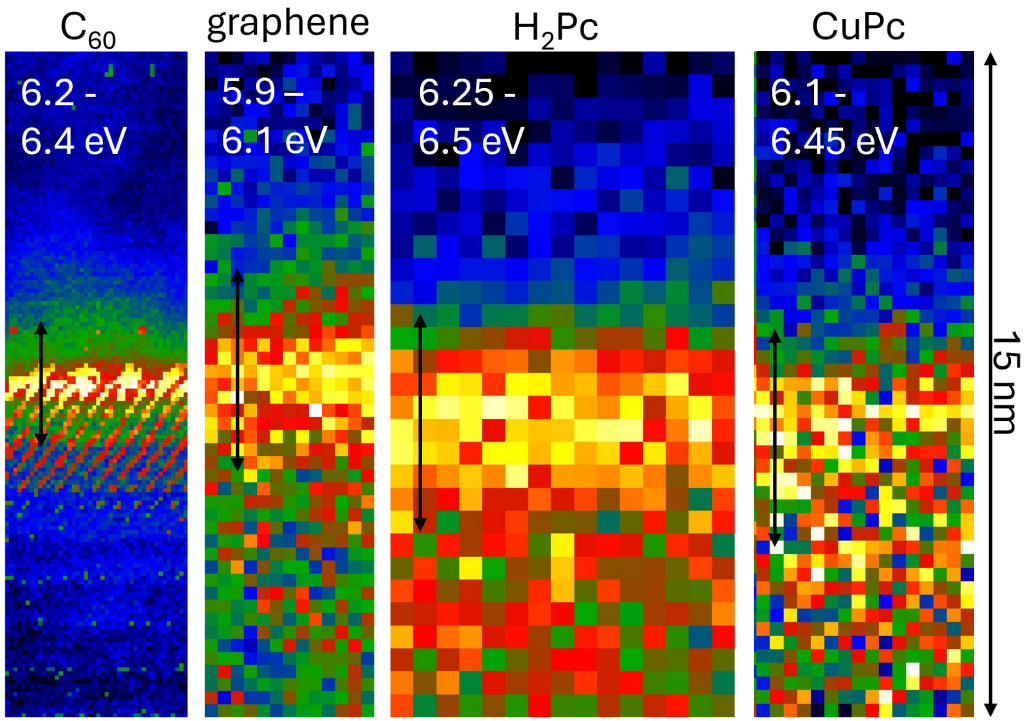

Fig. 5.14 EELS maps over Bi_2Se_3/organic interfaces spanning a 15 nm region. From left to right: EELS map over Bi_2Se_3/C_{60} interface over energy range 6.2-6.4 eV, Bi_2Se_3/graphene interface over energy range 5.9-6.1 eV, Bi_2Se_3/H_2Pc interface at 6.25-6.5 eV and Bi_2Se_3/CuPc interface over energy 6.1-6.45 eV.

The localisation of the identified interface mode can be seen in figure 5.14 for each organic interface. This localisation differs between materials, with the greatest confinement observed at the Bi_2Se_3/C_{60} interface, where the increased intensity is confined to a region of 1 nm either side of the interface. The interfacial mode is less confined in the other three samples, with H_2Pc and CuPc samples showing the least confinement. Coupling between molecular resonances and surface plasmons has been shown to have a dependence on the orientation of molecular dipoles [112]. In the Bi_2Se_3/C_{60} sample discussed in chapter 4, the C_{60} layer is highly ordered and Bi_2Se_3 surface is fully reconstructed. Dipoles within the C_{60} molecules are aligned with each other which could result in strong enhancement of the electric field at the interface, stronger coupling and a greater redshift in plasmon energy. This would also explain the strong confinement of the plasmon to the interface.

Surface doping with phthalocyanine molecules appears to have the longest length-span compared to C_{60} and graphene layers. In both phthalocyanine samples, there is no evidence

of molecular ordering so dipoles are not aligned. Compared to C_{60}, the coupling would therefore not be as strong and be less confined. If the Pc molecules are stacked in a planar or tilted arrangement as described in section 5.3, there should be coupling between molecules along a stack [271]. This could extend the surface interaction deeper into the Pc layer, contributing to why the interaction depth appears greater than other organic materials. The plasmon dispersion of these modes should also be altered due to the presence of different organic dopants. In C_{60}, very little dispersion was observed for the interface plasmon which was attributed to hybridisation between Bi_2Se_3 and C_{60} and due to a charge transfer from the Bi_2Se_3 surface onto individual C_{60} molecules. To determine if the interfacial plasmon mode at the Bi_2Se_3/phthalocyanine interface is truly hybridised, future work should include q-EELS mapping to confirm its dispersion.

Although only a monolayer of graphene is present in the cross-section discussed here, the localised mode appears over a region of the interface greater than the thickness of one graphene monolayer. This indicates that the localised mode extends into the amorphous carbon overlayer and it not purely confined to the TI/graphene interface, suggesting that some of the surface change is due to the amorphous carbon as well as the graphene layer. It will likely be the case that the graphene monolayer has been doped by either the amorphous carbon layer or the TI layer itself [232]. The effect of the graphene layer cannot be disentangled from the aC overlayer and coupling behaviour is influenced by both the graphene layer and additional overlayers. In aC, the $\pi - \pi^*$ interband transition is expected at a higher energy than in graphene, but disorder should not support strong coupling with the aC resonance and the effect of an aC overlayer should be due to changes in relative permittivity. However, the graphene/aC overlayer here shows the greatest shift in energy of the interface plasmon of the studied organics, indicating that the presence of the graphene layer could be enhancing the redshift effect. The dispersion of the interface plasmon mode should be influenced by the graphene layer, therefore, further work to study the influence of a graphene monolayer must make use of qEELS to map the dispersion of this mode. Future experiments could include investigating the effect of crystalline C_{60} over monolayer graphene on this interface to see if the EELS enhancement at the first C_{60} molecular layer still occurs and if a greater redshift to the plasmon energy is observed.

These results demonstrate that changes to the π plasmon behaviour at a Bi_2Se_3/organic interface are not purely due to a change in relative permittivity as is the case for other dielectric overlayers. The redshift to the plasmon energy was observed to be greater than expectations from bulk dielectric properties indicated in calculated EELS spectra. Molecular interband transitions occur at energies similar to the Bi_2Se_3 π plasmon, resulting in coupling effects which modify the plasmon energy, confinement and dispersion. The strength of this

interaction was observed to vary between organic layers, with strong confinement observed due to ordered crystalline C_{60} and less confinement in disordered phthalocyanine films. Smaller red shifts in energy were observed for phthalocyanine molecules, perhaps due to a lack of dipole alignment and resonance energies further from the Bi_2Se_3 π plasmon energy. C_{60} molecules were observed to redshift the plasmon energy slightly more than both phthalocyanine molecules, have greater confinement and enhance the signal at the interface. In the data presented in this chapter, no enhancement of EELS signal was observed for other organics, hinting that strong resonance coupling between the surface and molecules did not occur. The strong overlap in energy of the observed Bi_2Se_3 π plasmon and C_{60} interband transitions, as well as the highly ordered C_{60} surface, result in these differences in interface interaction.

The observed organic induced Bi_2Se_3 surface modification, with enhancement of signal at specific energies and shifts to plasmon energies, could be useful for applications of TIs as broad spectrum photodetectors which span energies from infrared to ultraviolet [23]. By coupling the Bi_2Se_3 π plasmon at the surface with organic overlayers, changes to the plasmon energy, confinement and dispersion can all be induced. This could be utilised for enhancement of photodetection in the high energy range, without compromising the low energy range. The work presented in this chapter could be expanded for use in active plasmonic devices, providing a means of switching the plasmon energy with an applied gate voltage that changes the chemical potential of the organic or with an optical pulse that changes the molecular resonance energy [69].

5.6 Conclusion

It has been shown that doping the surface of Bi_2Se_3 with an organic molecular overlayer can result in changes to the surface plasmon energy and confinement, with differences in energy of up to 0.4 eV observed for different choice of organic. Surface doping with graphene has been shown to change the energy of the interface plasmon to 6.0 eV in comparison to 6.3 eV observed for C_{60} in chapter 4. Phthalocyanine molecules showed a smaller difference in interfacial peak energy with a peak energy of 6.4 eV identified at the interface for both H_2Pc and CuPc. The variations in Bi_2Se_3/organic interfacial plasmon energy between samples highlight differences in chemical potential due to different organics. If a hybrid interface state has been formed, the energy of this state varies between dopant layer, suggesting the possibility of tuning the interfacial plasmonic properties by choice of molecular dopant.

Differences in the Bi_2Se_3, possibly due to growth method or defect concentration, were identified, although only one sample showed differences to the Bi_2Se_3 plasmon energies.

The surface plasmon mode at Al_2O_3 and SiO_2 interfaces also differed, with the coexistence of a surface mode and the Bi_2Se_3 π plasmon observed at the SiO_2/Bi_2Se_3 interface but not the Al_2O_3/Bi_2Se_3 interface. A difference in surface plasmon energy was also identified between these two interfaces, indicating that the insulating substrate does have some effect on the plasmonic behaviour of Bi_2Se_3. A comparison with a Bi_2Se_3/vacuum interface would provide a complete comparison for this effect, but due to difficulty of preparing such a specimen, has not been explored here.

This chapter has therefore shown that changes to the Bi_2Se_3 surface π plasmon energy, confinement and dispersion can arise for interactions with organic molecular overlayers. The presence of interband transitions and molecular dipoles near the Bi_2Se_3 surface, not only modifies the local dielectric environment but can lead to hybridised plasmon modes with varying degrees of localisation and redshifts in energy depending on the type of organic dopant. However, some limitations remain. Variations in sample growth, Bi_2Se_3 thickness and EELS acquisition conditions complicate the attribution of changes in EELS spectra to the presence of different organic overlayers. Differences in spatial and energy resolution between measurements taken on the ARM and on SuperSTEM3 might affect the observed results, such as degree of localisation and subtle shifts in peak energies.

Further work on these specimens would provide greater insight into the nature of the interface interactions. Calculations of charge transfer by DFT, similar to those described in chapter 4, could clarify the degree of charge transfer and hybridisation at each interface. Momentum-resolved EELS spectra could also be obtained for all three specimen to map the interfacial plasmon dispersion, helping determine its characteristics and if it is indeed a hybridised plasmon mode in each case. Comparing interfacial plasmons with those of a clean Bi_2Se_3/vacuum interface would isolate effects from both substrates and organic dopants. These findings provide a foundation for future studies exploring hybridised interface plasmons in topological insulators and for development of TI/organic systems for optoelectronic applications.

6

Modification of Bi_2Se_3 low energy plasmons with organic layers of H_2Pc and CuPc

6.1 Introduction

In the meV energy range, there are several plasmon modes in Bi_2Se_3 that should be excited and observable in EELS spectra. Several studies on the plasmon behaviour of Bi_2Se_3 in the meV range have been carried out by others using EELS with contrasting results [94, 105, 292, 293]. These studies were all carried out using high resolution EELS (HREELS), which is a surface sensitive technique that reflects low energy electrons from a crystalline surface, revealing information on low energy plasmon and phonon modes with high energy resolution [294].

Politano *et al.* observed two plasmon modes at a Bi_2Se_3 surface at 115 and 165 meV, shown in figure 6.1a,b using HREELS, which they attributed to a surface plasmon and a 2D surface plasmon mode. The dispersion of the 2nd plasmon was observed to follow the trend expected of a 2D Dirac plasmon [105]. They later observed two modes at similar energies, 104 and 174 meV, which were dispersionless in mechanically cleaved samples and indicated that their lack of dispersion was due to confinement to small grains and step edges [295]. The Dirac plasmon mode observed by Di Pietro *et al.* in microribbon arrays of Bi_2Se_3, using THz spectroscopy, was lower in energy and ranged from 6 to 16 meV across momentum-space with a Dirac dispersion [18].

Kogar *et al.* used a reflection momentum-resolved EELS technique to investigate plasmons in Bi_2Se_3 crystals of differing carrier density, n_{3D} [292]. They observed a shift in surface plasmon energy from 23 meV at low carrier densities of $1.2 \pm 0.1 \times 10^{18}$ cm^{-3} to 90 meV at a higher carrier density of $20 \pm 1 \times 10^{18}$ cm^{-3}, as shown in figure 6.1c, and indicated that the plasmon energy had a $\sqrt{n_{3D}}$ dependence on carrier density. These measurements

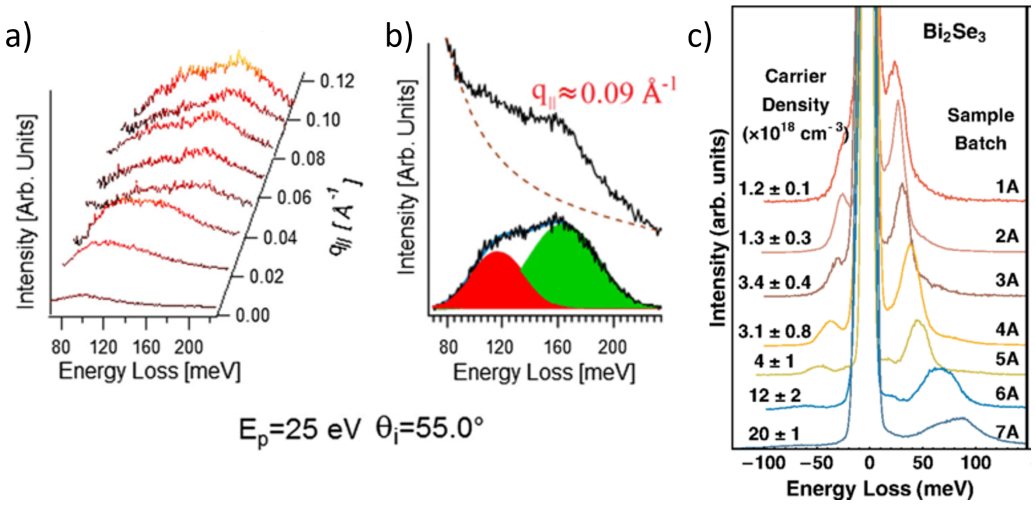

Fig. 6.1 HREELS measurements on a Bi_2Se_3 surface from literature [105, 292] a) Momentum-resolved HREELS spectra of the Bi_2Se_3 surface, where two peaks are resolved to change in relative intensity with increasing momentum [105]. b) Momentum-resolved HREELS spectrum at momentum 0.09 Å^{-1}, where two Gaussian peaks are fitted at energies 115 and 165 meV [105]. c) Momentum-resolved HREELS spectra at 0.0 Å^{-1} momentum at different carrier densities, showing an increase in surface plasmon energy with increasing carrier density [292].

were carried out using a surface sensitive technique and the plasmon mode was attributed to a surface plasmon arising from bulk carriers. This surface plasmon mode was observed to show a lack of dispersion with momentum, which was in agreement with expectations for a surface plasmon, since dispersion is expected at low momenta but becomes non-dispersive within the momentum resolution of the experiments performed. The authors observed an additional mode at 20 meV when the carrier density was high and indicated that its origin could be an A_{1g} phonon mode [296].

Jia *et al.* observed two modes at 55 and 72 meV, which did not disperse significantly with increased momentum and they attributed these features to surface and bulk plasmon modes respectively [94]. Additionally, they observed a dispersionless mode at a lower energy of 20 meV, which was assigned to an optical phonon mode. Upon doping Bi_2Se_3 with 10% Mn, the surface and bulk plasmon modes were blue shifted to 94 and 139 meV respectively, due to an increase in carrier density.

A recent study using surface sensitive high resolution EELS on Bi_2Se_3 crystals indicated a change to the plasmon behaviour upon deposition of Pt [293]. As cleaved, EELS spectra of the Bi_2Se_3 crystals revealed two peaks, which were attributed to an optical phonon at 21.7 meV and a bulk plasmon at 74 meV. After deposition of Pt, these modes were observed to shift in energy, with the optical plasmon mode at 21.2 meV and the plasmon mode at

92 meV. The shift in bulk plasmon energy was attributed to electron doping of Bi_2Se_3 near the surface by the Pt atoms. As the authors used a surface sensitive technique and obtained similar results to Kogar *et al.* [292], it is likely that they have observed a surface plasmon originating from bulk carriers.

The studies described here have all made use of surface sensitive HREELS techniques on plan view samples. This differs significantly from our system, where we observe cross-section samples by transmission EELS. Bulk plasmon modes will be excited in this setup and should dominate the spectrum in the centre of the TI layer. This should mean that observation of the surface modes identified in the literature should be confined to the interfaces and will most likely result in differing results. The benefit to using STEM EELS to study these plasmons as opposed to THz spectroscopy is the ability to observe their localisation to interfaces and they can allow us to rule out contributions from defects or contaminants through visual inspection with STEM. We can investigate buried interfaces between thick layers by cross-section analysis with high spatial resolution. The HREELS studies on Bi_2Se_3 plasmons in this low energy range vary substantially in plasmon energies and interpretation of results. By investigating cross-sections, it should be possible to distinguish bulk and surface plasmon modes by their localisation as well as energy.

With current advances in aberration correction and monochromation, it is possible to obtain transmission EELS with high spatial resolution at ultra low energies in the 10s of meV range [138, 297, 298]. This opens the door for studying both low energy plasmons and phonon modes. Unlike surface sensitive techniques, this allows us to investigate bulk modes and, with the spatial resolution of STEM, we can observe localisation of these low energy modes. Vibrational EELS is now possible and the number of groups using the technique is expanding, however, the need for highly specialised equipment makes these experiments more difficult.

It was shown in chapter 5, that phthalocyanine layers can alter the π plasmons and the surface of Bi_2Se_3 thin films. Changes to the surface state which influence the π and surface plasmon, should also have an effect on the lower energy plasmons in Bi_2Se_3. To investigate the effect at lower energies, EELS was performed on SuperSTEM3 at 60 kV, making use of the 7 meV ZLP width, possible due to monochromation. In the energy range between 30 and 300 meV, a variety of different modes were observed including plasmons, phonons and molecular vibrations.

This chapter will investigate plasmon modes in the energy range of 30 to 300 meV, which should capture the low energy plasmon modes observed in published studies [105, 292, 94, 293]. A comparison of the effect of H_2Pc and CuPc on the Bi_2Se_3 surface is carried out using samples investigated in chapter 5. The two samples investigated were grown

by different methods, which could influence the results. To provide some information on dispersion of modes, EELS was performed in an on/off axis configuration using a small 2 mrad convergence semiangle, as described in section 2.6.2. On-axis data was collected by positioning the central Bragg peak at the centre of the EELS aperture to collect electrons with small scattering angles. An off-axis dataset was acquired by displacing the diffraction pattern relative to the EELS aperture to acquire data at the middle of the Bi_2Se_3 Brillouin zone. Plasmon and phonon modes, identified by peak fitting on-axis data, will be discussed and changes in their behaviour towards interfaces investigated. Although noisy, off-axis data will show non-dispersing phonon modes present in insulating substrate and organic layers.

6.2 On/Off axis method

EELS spectra were acquired using an on/off-axis acquisition method, which uses a small convergence semiangle and collection angle to only collect electrons with a small distribution of momenta, as discussed in section 2.6. This work was performed at 60 kV on SuperSTEM3 with an energy dispersion of 1 meV per channel and ZLP width of between 7 and 12 meV. The electron beam was focused on the sample with a convergence semiangle of 2 mrad and the collection angle was measured as 4 mrad. This allowed for collection over a momentum range of ± 0.37 Å^{-1}. On-axis data was acquired with the EELS aperture centred around the central Bragg spot of Bi_2Se_3, with an average momentum transfer of 0 Å^{-1}. A second EELS spectrum was acquired around halfway along the Bi_2Se_3 Brillouin zone, as indicated in figure 6.2, to provide some indication of dispersive modes. Further measurements to map the dispersion were not carried out due to a shortness of time.

The off-axis aperture position for each sample is shown in figure 6.2, where the position indicated in yellow is for the Bi_2Se_3/H_2Pc sample and in green is for the Bi_2Se_3/CuPc sample. The aperture position does not fall directly along the ΓM direction, therefore, off-axis spectra include a change in momentum transfer along both the ΓM and ΓZ directions. The off-axis position used for the Bi_2Se_3/CuPc sample is just greater than half way along the 1st BZ of Bi_2Se_3 and for the Bi_2Se_3/H_2Pc sample, covers the momentum range from halfway along the BZ up to the 1st BZB.

6.3 H_2Pc sample

It was observed in section 5.3, that the peak energy of the mode at the Bi_2Se_3/H_2Pc interface was shifted in comparison to the substrate, calculations, and other organics. This change to the Bi_2Se_3 surface should be observable at lower energies as well. As there is a strong

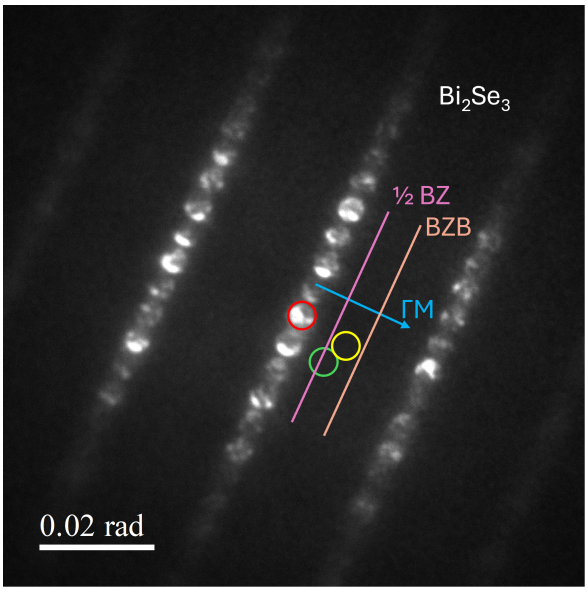

Fig. 6.2 On/off axis EELS calibration. Diffraction pattern of Bi_2Se_3 with the location of the EELS aperture and positions in momentum space indicated. The 1st Brillouin zone boundary (BZB) is show in peach, halfway between diffraction spots along the ΓM direction which is parallel to the thin film interfaces. The halfway position of the Brillouin zone is indicated in pink. Both on-axis datasets were acquired with the EELS aperture positioned around the central Bragg spot as shown by the red circle. Off-axis datasets were acquired with the aperture positioned as indicated in yellow for Bi_2Se_3/H_2Pc and in green from Bi_2Se_3/CuPc.

likelihood of charge transfer at this interface, the surface plasmon energy should differ from a free Bi_2Se_3 surface. Ultra-low-loss EELS spectra of the SiO_2/Bi_2Se_3/H_2Pc cross-section, analysed in section 5.3, were acquired for both on and off-axis aperture positions. Spectra acquired on-axis over both interfaces of the SiO_2/Bi_2Se_3/H_2Pc cross-section are presented in figure 6.3. Spectrum images over the SiO_2/Bi_2Se_3 and Bi_2Se_3/H_2Pc interfaces were acquired separately due to the large width of the Bi_2Se_3 crystal and spectra are shown with their scaled as $I \times E^2$ to allow for clearer visualisation of small peaks.

In the SiO_2 substrate, three peaks were observed at 56, 97 and 145 meV, with the final peak being the most pronounced. These features were attributed to phonon modes and have been observed in literature at similar energies of 100 and 144 meV [299]. The sharp peak at 145 meV can be seen in figure 6.3b, where it dominates the SiO_2 spectrum. Towards the SiO_2/Bi_2Se_3 interface, the energy of the sharp phonon mode reduces gradually from 145 meV at 9.2 nm from the interface to 141 meV at 1 nm from the interface. This redshift was accompanied with a gradual drop in intensity starting 13.3 nm away from the interface as shown in figure 6.3d. The EELS map in figure 6.3f also highlights the change in intensity across the interface in the 138-147 meV energy range. After reaching the interface, the peak

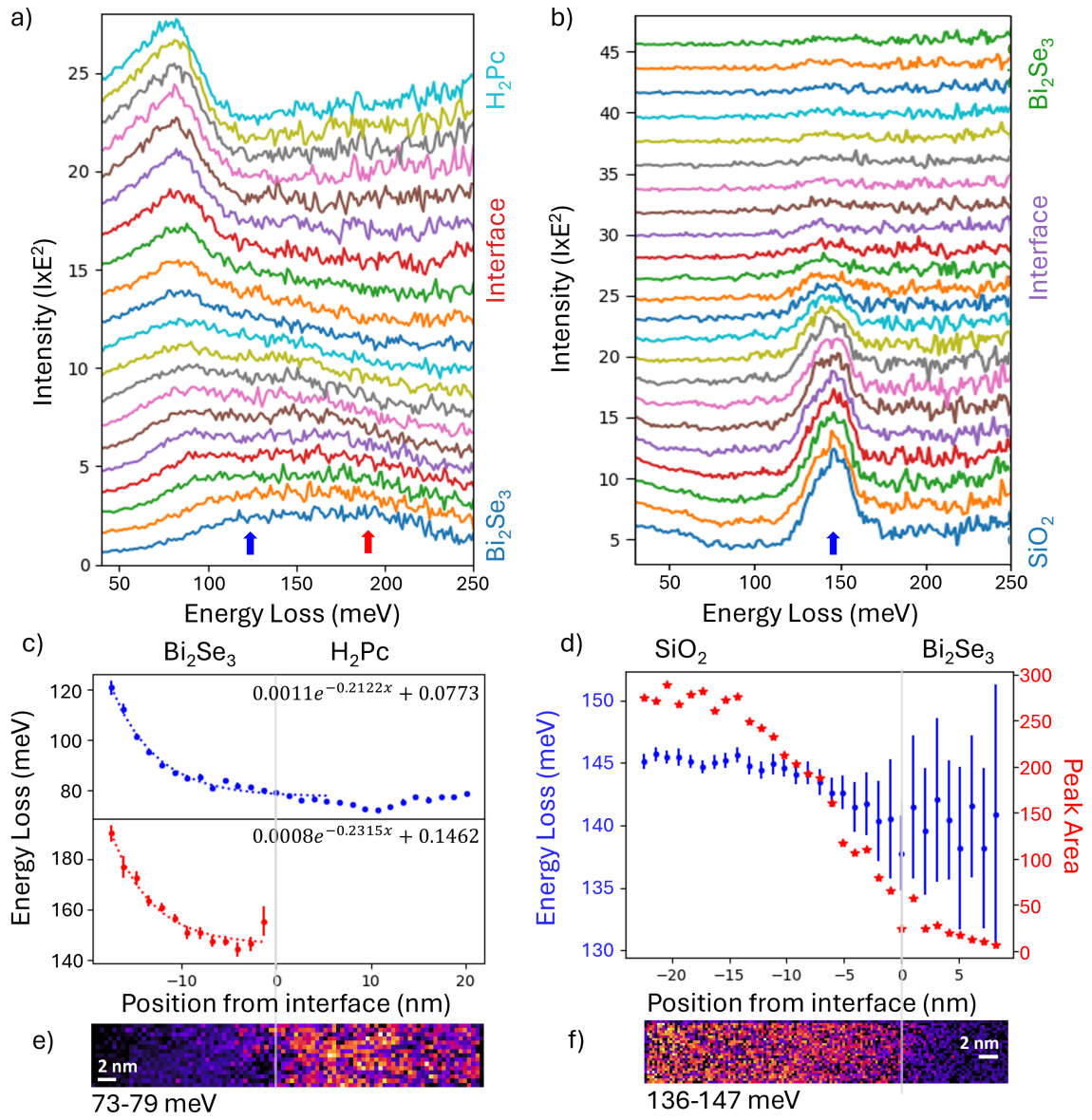

Fig. 6.3 Ultra-low-loss EELS over interfaces of a) Bi_2Se_3/H_2Pc, with spectra progressing from Bi_2Se_3 (bottom) to H_2Pc (top) and b) SiO_2/Bi_2Se_3, with spectra from SiO_2 (bottom) to Bi_2Se_3 (top). a) EELS spectra in 1.34 nm steps from 17.42 nm away from the interface in Bi_2Se_3 to 21.44 nm away from the interface in H_2Pc where the spectrum at the interface is in red as indicated. b) EELS spectra in 1.02 nm steps across the SiO_2/Bi_2Se_3 interface where an SiO_2 phonon mode is observed at 145 meV. c) Fitted peak energy of Bi_2Se_3 plasmon modes towards the Bi_2Se_3/H_2Pc interface, where the top plot shows the lower energy peak energy reducing from 120-76 meV and the bottom plot shows the higher energy peak reducing from 190-146 meV. d) Fitted peak energy and area of the SiO_2 phonon mode across the interface. The peak area decreases and uncertainty in energy increases. e) EELS map at the H_2Pc phonon energy, 73-79 meV, across the Bi_2Se_3/H_2Pc interface. f) EELS map at the SiO_2 phonon energy, 136-147 meV, across the SiO_2/Bi_2Se_3 interface.

was best fit between 138 and 142 meV, with greater uncertainty as the intensity of the peak drops until it can no longer be observed at 8.2 nm into the Bi_2Se_3 layer.

The EELS spectrum at the Bi_2Se_3 side of the interface appears to be absent of any clear features in figure 6.3b. This is unexpected and differs from the Bi_2Se_3 closer to the top H_2Pc interface shown in 6.3a, which shows clear features. The thickness of the cross-section at both interfaces was measured to be the same, with a t/λ_i value of 0.98, indicating that the lack of features was not due to the thickness variations throughout the sample. Other possibilities to explain the lack of features include quenching of the Bi_2Se_3 plasmons due to interaction with the SiO_2 substrate. Since the SiO_2 optical phonon mode has decayed to negligible intensity into the Bi_2Se_3 within 10 nm from the interface, it is not likely that coupling between this phonon and the Bi_2Se_3 plasmons can fully explain the lack of features 30 nm into the Bi_2Se_3 layer. To clarify these measurements, further EELS SI would be required, including an image across the full Bi_2Se_3 layer. This would confirm if bulk Bi_2Se_3 has been reached and if the plasmon energies continue to change throughout the layer.

In the Bi_2Se_3 layer, shown at the bottom of figure 6.3a, two peaks were observed at 120 and 190 meV, which reduce in energy upon approach to the H_2Pc interface. The redshift in energy of both modes was fitted with an exponential decay, as presented in figure 6.3c, with the first peak reducing to 76 meV, the energy of a H_2Pc vibrational mode. The second peak reduces from 190 to 146 meV towards the interface and is not observed into the H_2Pc layer. The shift in energy of these modes towards the interface confirms that they are plasmons and not phonon modes. In bulk H_2Pc, one broad peak is observed over the energy range 60 to 100 meV. This feature can be fitted with a single peak centred at 76 eV and remains at this energy over the H_2Pc layer. This feature could be from vibrations associated with the central ring of the H_2Pc molecules, macrocycle deformation modes, which have been observed by Raman spectroscopy [300]. The peaks in literature occur at 89 and 99 meV but we do not resolve several peaks in this EELS data. Several IR active vibrational modes are also expected to occur in the energy range that we observe peaks in EELS. These modes include isoindole deformation at 76 meV and out of plane C-H bending vibrations at 85, 91 and 108 meV [301]. As this peak is fairly broad and potentially covers a range of different phonon modes, the H_2Pc layer is most likely very disordered.

The energies of the two plasmon peaks observed in Bi_2Se_3 are very similar to the plasmon modes observed by Politano *et al.*, who described surface modes at around 119 and 162 meV in HREELS spectra with momentum transfer 0.09 $Å^{-1}$ [105]. Their work investigated the surface of cleaved Bi_2Se_3 samples and identified the surface modes as a 2D surface plasmon and Dirac plasmon. As the data presented in figure 6.3 encompasses a momentum range up to ± 0.37 $Å^{-1}$, both plasmon modes observed by Politano *et al.* should contribute to the

signal. In the spectra presented in figure 6.3, the top surface of Bi_2Se_3, which could host Dirac fermions, is not exposed, therefore, excitations from these states should be confined to the Bi_2Se_3 interfaces and the energies of such modes would most likely be influenced by the interfacing material. In the bulk of Bi_2Se_3, 18 nm away from the interface, no excitation from TSS should be possible, and even aloof excitation of the mode should not be observable. Surface plasmons could be excited from the top and bottom surfaces of the lamella as the beam travels through the specimen, but the thickness of the lamella, 40 nm, should result in the EELS spectrum being dominated by bulk plasmon modes, similar to what was observed in calculations of Ag nano-squares of various thicknesses in section 3.5. This suggests that, although the energies of observed modes align well with those of Politano *et al.*, the plasmons observed here are not the surface and Dirac plasmons.

A possible origin of the plasmon modes identified here is excitation of bulk carriers, as was observed by Kogar *et al.*. The bulk plasmon energy, E_P, can be calculated from the bulk carrier density, n_{3D}, by

$$E_P = \hbar\omega_p = \hbar\sqrt{\frac{n_{3D}e^2}{\varepsilon_r\varepsilon_0 m^*}}, \tag{6.1}$$

using values of effective mass $m^* \approx 0.19m_e$ and dielectric constant $\varepsilon_r = 26$ given by Jia et al. [94]. Other parameters take their standard values. A bulk plasmon of energy 120 meV would arise from a bulk carrier density of 5.15 $\times 10^{19}$ cm^{-3}, this value is high for Bi_2Se_3 films but not unrealistic. Bulk carrier densities of Bi_2Se_3 films often range from 5.0 $\times 10^{18}$ cm^{-3} to 3.2 $\times 10^{19}$ cm^{-3} depending on the growth method due to differences in the concentration of intrinsic defects present [302, 29]. Therefore for this plasmon to be from bulk carriers, a large quantity of intrinsic defects must be present.

A shift in bulk plasmon energy across the layer could be a consequence of a change in carrier density towards the interface [293]. To achieve the plasmon energy of 76 meV that was observed close to the interface, a decrease in bulk carrier density of 60% to 2.07 $\times 10^{19}$ cm^{-3} would be required. A change in carrier density of this much would be extreme and from literature, an increase in charge density at the interface due to the H_2Pc overlayer would be more likely [75]. Therefore, this energy shift cannot be fully explained by a change in carrier density with a long depletion zone. It is more likely that a surface plasmon is present at the interface. Considering the plasmon at 120 meV as a bulk plasmon from free carriers, the associated surface plasmon polariton (SPP) mode at a surface with air would have an energy of $E_{spp} = E_p/\sqrt{2} = 84.9$ meV. At low energy, the dielectric constant of H_2Pc has been measured as 3.25 [303]. Using this value as ε_d in equation 1.12, the energy of an SPP at the Bi_2Se_3/H_2Pc interface associated with a bulk plasmon at 120 meV would be 58.2 meV. In the data presented in figure 6.3, the interfacial peak was at 76 meV instead and an exponential

decay in peak energy towards the interface was observed. Typically a bulk plasmon mode does not shift energy towards an interface, it decreases in intensity and an SPP mode increases in intensity. Therefore the plasmon behaviour approaching this interface is not fully described by a regular bulk plasmon and SPP mode. There could be several contributing factors to this, which cannot be disentangled from each other. If we consider this peak as an SPP, an increase in energy is observed compared to the calculated value, taking into account ε_d of H_2Pc. This could be partially explained by an increase in carrier density at the interface due to charge transfer from the H_2Pc layer. However, the energy observed at the interface is the same as the H_2Pc phonon modes observed throughout the H_2Pc layer. The SPP mode could be quenched by the H_2Pc phonon mode, or at lower energy becoming lost in background noise, with the interfacial peak as an aloof excitation of the phonon excitation. As the energy of the molecular vibration is similar to the Bi_2Se_3 surface plasmon, resonant plasmon-phonon coupling could occur at the interface, resulting in a hybrid plasmon mode and enhanced signal at the vibrational excitation energy [96]. An EELS map of the Bi_2Se_3/H_2Pc interface at the H_2Pc vibrational energy of 73-79 meV is presented in figure 6.3e, but an increase in signal intensity is not observed at this interface. Further measurements would be required to determine is this is the case. Namely, momentum-resolved EELS analysis could aid in the interpretation of this data, since variations in plasmon dispersion are expected for the above options.

The results presented here suggest that the H_2Pc has a strong influence on the Bi_2Se_3 surface, with the energy of plasmon modes in Bi_2Se_3 changing throughout the full spectrum image away from the H_2Pc interface. This could mean that a bulk spectrum has not been recorded and that the plasmon modes identified into the Bi_2Se_3 layer have been influenced by the organic layer. Since we do not have a comparative dataset with a Bi_2Se_3/vacuum interface, interpretation of these results is difficult and the behaviour cannot be fully attributed to the presence of the H_2Pc overlayer.

6.4 CuPc sample

CuPc molecular overlayers were shown to have a similar effect on the Bi_2Se_3 surface to H_2Pc in the π plasmon energy range. At lower energies, the EELS spectra of the Bi_2Se_3/H_2Pc and Bi_2Se_3/CuPc samples differ more substantially.

EELS spectra, acquired on-axis, across the layers of a Al_2O_3/Bi_2Se_3/CuPc cross-section are presented in figure 6.4b. In the Al_2O_3 substrate, three low energy modes can be observed between 50 and 120 meV which, when fitted, have peak energies of 58, 77 and 106 meV. Al_2O_3 phonons have been investigated by surface EELS and show similarities to the modes

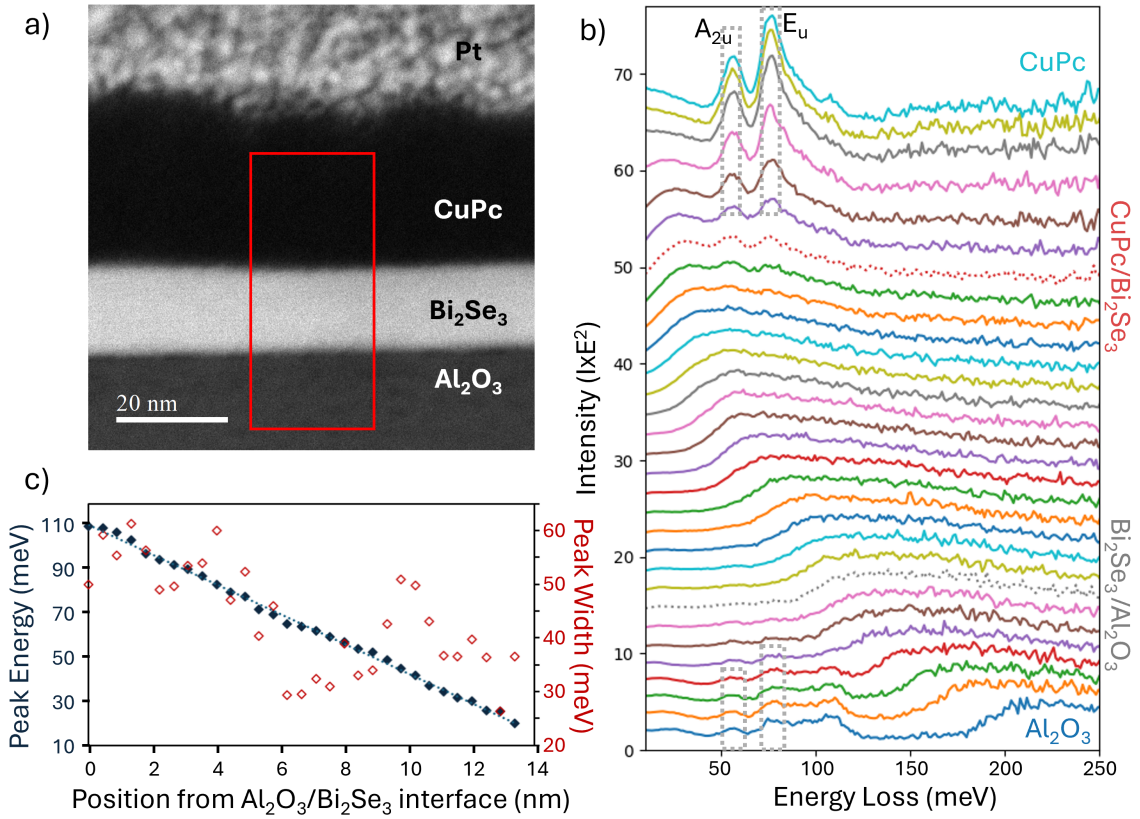

Fig. 6.4 Ultra-low-loss EELS spectra over a cross section of Al_2O_3/Bi_2Se_3/CuPc. a) HAADF STEM image of the cross section where the annotated region indicates the location of EELS spectra in b. b) EELS spectra at different regions of the sample as indicated on the HAADF image where line colours are the same as the annotations on the image. Phonon modes in bulk Al_2O_3 and CuPc are indicated and a plasmon mode in Bi_2Se_3 is observed. c) Energy and peak width of the plasmon peak in the Bi_2Se_3 layer from the Al_2O_3/Bi_2Se_3 interface to the Bi_2Se_3/CuPc interface, where peak energy is fitted with a linear trend line.

observed here [304]. Chen *et al.* observed sharp peaks at 51, 80 and 107 meV from an Al_2O_3 surface which they attributed to vibrational modes close to the surface. The first peak was said to originate from the relative movement of Al-O slabs and the second peak was attributed to vibrations of the first Al layer and surface O atoms. The third peak was said to originate from an Al-O vibration between the second layer of Al atoms and subsurface oxygen. The energy of these peaks is similar to the peak energies observed here, however, the slight differences could be due to the differences in techniques since the literature values were surface sensitive. Differences in structural defects and oxidation could also result in slight differences in energy.

In bulk CuPc, two sharp peaks are observed at 55 and 78 meV, which are close to the energy of optical phonon modes predicted from density functional theory [305]. An out of plane vibration with A_{2u} symmetry at 53.6 meV is predicted and described as a rocking/wagging vibration. At 77.9 meV, an in-plane vibrational mode is expected with E_u symmetry. These predicted values align closely with the sharp peaks observed in figure 6.4b. At the interface with Bi_2Se_3, some intensity from these phonon modes remains with both peaks fully resolvable. Since these peaks are very sharp and align well with vibrations predicted from DFT and observed by IR, molecules within the CuPc layer must be intact.

Sharp peaks are not observed in the bulk Bi_2Se_3 EELS spectrum. Instead a broader feature can be observed which decreases in energy from the substrate interface to the CuPc interface. At the centre of the Bi_2Se_3 layer, this peak has an energy of 65 meV. Alongside this peak, a smaller feature is observed only at the centre of the Bi_2Se_3 layer at 40 meV. This peak does not appear to change energy but is obscured close to the CuPc interface by the peak that shifts energy. Through the full 15 nm layer of Bi_2Se_3, from the substrate interface to CuPc interface, the main peak redshifts energy. The energy of this peak throughout the TI layer is plotted in figure 6.4c and seems to follow a linear trend, decreasing in energy from 111 meV at the interface with the substrate to 20 meV at the organic interface.

The length scale of this interaction appears much greater in this energy range than at the higher π plasmon energy range discussed in chapter 5. The results from chapter 5 suggested that a localised plasmon mode is present at the interface up to 2.5 nm into the Bi_2Se_3 layer. The results presented here, indicate that the plasmon mode continues to change in energy all the way through the TI layer and even extends into the Al_2O_3 substrate. There appears to be no recovery of a bulk Bi_2Se_3 plasmon in the 15 nm Bi_2Se_3 layer, but it seems unlikely that the CuPc layer would influence the plasmonic behaviour so deep into the layer.

In literature, plasmon peaks have been identified in this energy range at 55 and 72 meV by Jia *et al.*, who attributed these peaks to a surface and bulk plasmon mode respectively [94]. These plasmons were observed using surface sensitive HREELS on the surface of a plan view sample of Bi_2Se_3. Both plasmon modes were observed to have strong plasmon damping and minimal dispersion before disappearing at large q, therefore, if these are the same plasmon modes observed in our data, then they would not be present or have greatly reduced intensity in off-axis data. The bulk carrier density in the samples measured by Jia *et al.* was 1.9×10^{19} cm^{-3}. In our case, the bulk carrier density was not measured but using equation 6.1 with the same values as before, the bulk carrier density from a plasmon energy of 65 meV would be approximately 1.5×10^{19} cm^{-3}. Bulk carrier densities of Bi_2Se_3 can vary from 10^{17} to 10^{19} cm^{-3} depending on doping from intrinsic defects so this value is reasonable for our system [33]. Since shifts in bulk plasmon energy can be explained by

changes to carrier density [293], the carrier density throughout the layer could be varying as a result of charge depletion from the CuPc overlayer. If this was the case, the carrier density at the CuPc interface would be be up to 80% lower than at the centre of the layer. This is unrealistic, therefore other explanations are required. The associated energy of a surface plasmon polariton can be calculated using equation 1.12 with $\varepsilon_d = 2.1025$ [303]. For a bulk plasmon energy of 65 meV, the SPP energy would be 36 meV. This is similar to the plasmon energy observed close to the CuPc interface. A redshift of the surface plasmon energy could be possible due to coupling between a surface plasmon and molecular vibrational excitations [96], which could explain lower energies of around 20 meV observed at the interface.

In TEM images of this Al_2O_3/Bi_2Se_3/CuPc sample, shown in figure 5.9 in section 5.4, the top surface of Bi_2Se_3 is not flat and instead has several small step edges. As shown by Politano *et al.*, step edges at the surface of Bi_2Se_3 can change the plasmonic behaviour, especially at the surface resulting in dispersionless modes. It is therefore possible that, alongside the effect of the CuPc layer, step edges could contribute to some of the surface behaviour. Future studies could investigate this further by acquiring qEELS spectra in regions with and without step edges.

Off-axis EELS spectra across the thin films are presented in figure 6.5, alongside on-axis data. The off-axis spectra are much noisier due to the low electron counts. These spectra were acquired with the same parameters as the Bi_2Se_3/H_2Pc data with an exposure time of 15 ms for off-axis compared to a 10 ms exposure time for on axis data.

In bulk Al_2O_3, the off-axis dataset shows a broad cluster of peaks from 55 to 105 meV, which spans the energy range of peaks identified in the on-axis spectrum. This suggests that these modes have not dispersed significantly. This is expected from literature where the phonon dispersion of these modes was predicted to be small [306]. This confirms the assignment of these peaks to optical phonon modes. The off-axis spectrum acquired at the centre of the Bi_2Se_3 layer does not show any well resolved peaks and any features present blend in with the background noise. The Bi_2Se_3 plasmon peak has significantly reduced in energy and its dispersion is unknown. This is consistent with the plasmon modes identified by Jia *et al.*, which were not observed at large values of q [94].

At the Al_2O_3/Bi_2Se_3 interface, a broad feature can be observed in figure 6.5 between 75 and 105 meV. As this feature has overlap with the phonon modes identified in bulk Al_2O_3 which were also observed in off-axis data, this feature could be from bulk Al_2O_3 features. In CuPc, small differences can be observed including a broad feature around 175 meV, which was not present in on-axis data. This feature could be a phonon mode that has dispersed from a lower energy that was not observable in the on-axis data. The two sharp CuPc phonon modes can be observed in the off-axis dataset but are of lower intensity and are blue shifted

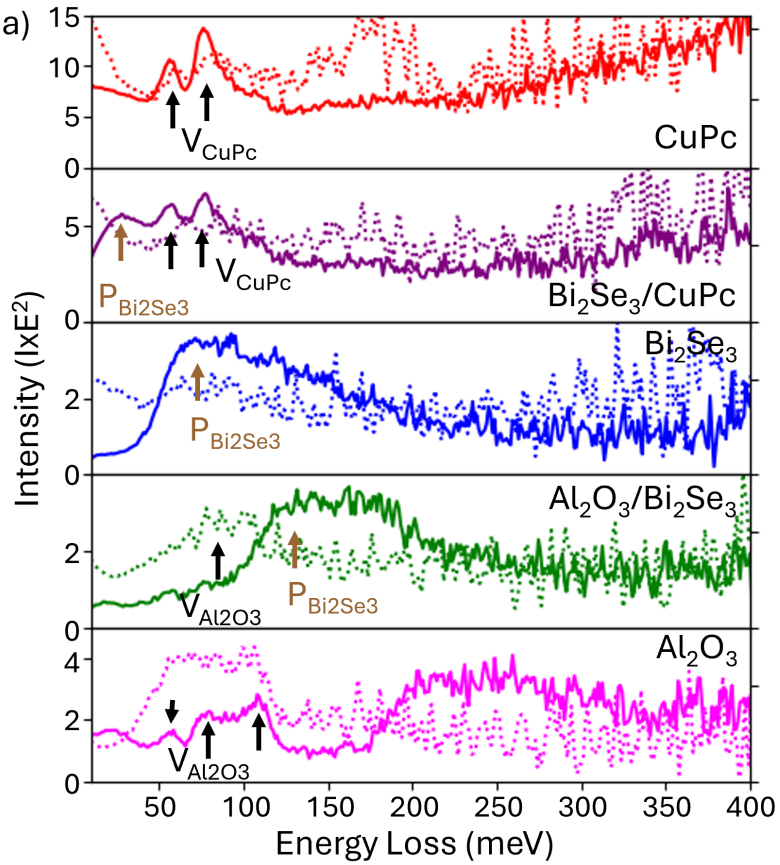

Fig. 6.5 On and off axis EELS spectra for each region of the Al_2O_3/Bi_2Se_3/CuPc sample, where on axis data is presented as solid lines and off axis data as dotted lines. Phonon modes, V_{CuPc}, are identified in CuPc and at the Bi_2Se_3/CuPc interface in on/off axis data. A plasmon mode, $P_{Bi_2Se_3}$, is identified on on axis data in Bi_2Se_3 and at the Al_2O_3/Bi_2Se_3 and Bi_2Se_3/CuPc interfaces but not in off axis data. Al_2O_3 phonon modes, $V_{Al_2O_3}$, are identified in Al_2O_3 in on axis data and in Al_2O_3 and at the Al_2O_3/Bi_2Se_3 interface in off axis data.

by around 4 meV. As these modes have been identified as specific molecular vibrations, they are not expected to disperse. At the organic interface, no clear peaks were observed in off-axis data, indicating possible dispersion of modes and a decrease in spectral intensity.

It is not possible from this data to fully determine the origins of the unusual plasmon behaviour in the Bi_2Se_3 thin film at this energy. Due to the shift in energy being observed across the full Bi_2Se_3 layer, it is possible that the CuPc overlayer has a much longer interaction depth at this energy than expected. Possible explanations of the shift in energy of plasmon modes include changes to the carrier density throughout the layer, resonant coupling between Bi_2Se_3 plasmons and CuPc vibrational excitations and the presence of surface plasmon

polaritons at the interface. Further work is required to fully understand this behaviour and distinguish the effects of charge transfer, coupling and SPPs from each other in this system.

6.5 Comparison

In comparing the two phthalocyanine samples, it must also be considered that the differing growth methods and thicknesses of Bi_2Se_3 crystals could influence the plasmonic behaviour observed. An increase in carrier density can result in a shift of plasmon energies in the ultra-low energy range discussed here [292, 94]. As Bi_2Se_3 is known to be intrinsically n-doped due to crystalline defects [236, 237], there is the possibility of differing carrier densities when comparing the two samples since differing carrier densities have been observed in differently grown samples [307]. Some ultra-low loss data was acquired for a sample of $Al_2O_3/Bi_2Se_3/C_{60}$, but due to the thickness of the sample and possible C_{60} amorphisation, it was not presented here. However, the EELS spectrum in the Bi_2Se_3 layer could be compared with spectrum from the Al_2O_3/Bi_2Se_3/CuPc sample to determine if the differences between samples observed here could be attributed to differences in carrier density between samples. It is also possible that the thickness of Bi_2Se_3 layer could influence the plasmonic behaviour. Acoustic plasmons are expected to occur in thin films of Bi_2Se_3, where coupling can occur between top and bottom surfaces. However, these are expected at lower energies than observed here and should only be observable at surfaces so are ruled out.

EELS spectra acquired in the Bi_2Se_3 layer for each sample show different plasmon energies with plasmons identified at 120 and 190 meV in the CVT grown Bi_2Se_3/H_2Pc sample and at 60 meV in the MBE grown Bi_2Se_3/CuPc sample. Since the energies of Bi_2Se_3 plasmons in this energy range are highly dependent on the bulk carrier density [292], the difference in plasmon energy between samples could suggest a greater number of bulk carriers in the CVT sample. In literature, the carrier density of CVT grown Bi_2Se_3 has been shown to vary between 3×10^{18}cm^{-3} [308] and 3.2×10^{19}cm^{-3} [29]. To confirm if this difference in energy was due to the TI crystal, data acquired for an MBE grown Bi_2Se_3/C_{60} crystal is presented, alongside the Bi_2Se_3/CuPc spectra for the centre of the Bi_2Se_3 layer, in figure 6.6.

Figure 6.6a shows EELS spectra for each sample summed over a range of over ±0.41 Å^{-1} and ±0.46 Å^{-1} in momentum around the Γ point for Bi_2Se_3/C_{60} and Bi_2Se_3/CuPc respectively. Fitting was carried out on spectra after removal of the ZLP using a power law function, using a pseudo-Voigt function for the plasmon peak, shown in figure 6.6a. For the Bi_2Se_3/C_{60} sample, shown in red, the plasmon energy was found to be 63 ± 0.4 meV and an additional feature could be fitted at 113 ± 4 meV. The plasmon peak in the Bi_2Se_3/CuPc

sample was observed to have a very similar energy of 64±0.6 meV, indicating that the Bi_2Se_3 plasmon at the centre of the layer is the same for samples with different organic overlayers but similar TI properties. The similarity of these two datasets indicate that MBE grown TI films have the similar plasmon energies regardless of the type of organic present. However, the presence of an additional feature in the Bi_2Se_3/C_{60} sample indicates that there are some differences in the plasmon behaviour and presents the possibility of modification to the Bi_2Se_3 plasmons far into the thin film due to the organic overlayer. The organic layer has likely not been the sole cause for changes in plasmon energy between the two phthalocyanine samples, differences in carrier densities, film thickness and lamella quality could also contribute. In the 2D data presented in figure 6.6b, the Bi_2Se_3 plasmon energy is indicated and in the Bi_2Se_3/C_{60} sample a horizontal line in intensity was observed at 264 meV as highlighted by a dashed grey line in the figure. This feature appears to be a sharp step edge at energy E_g, which could be the Bi_2Se_3 bandgap. Although typically observed at 300 meV, the Bi_2Se_3 bandgap has been observed at energies as low as 220±5 meV [309], so its observation at 264 meV is reasonable.

Momentum-resolved EELS spectra presented in figure 6.6c were acquired using the 'ω-q' slit method described in section 2.6. The spectrum was taken from the centre of the Bi_2Se_3 layer in both samples, around 8 nm from the organic interface. The measurements were carried out using a 2 mrad convergence angle, with the sample orientated to align the diffraction spots with the 'ω-q' slit. Due to the requirement of a small rotation of the sample to align with the slit resulting in changes to the magnification, momentum steps differ between measurements for each sample. The use of a specimen rod with the capability to rotate as well as tilt the sample would make alignment of samples to the slit orientation easier and remove differences in measurements introduced by post specimen optics. Spectra are presented as IxE^2 to make it easier to visualise the peaks.

At 0 $Å^{-1}$, qEELS spectra for both samples show a small peak at 30 meV, which was not observed in on-axis data possibly due to its low energy and the small momentum range it is present over. At 70 meV another peak can be identified which is likely the feature observed in on-axis data presented earlier. This feature is at the same energy in both samples indicating that, although this peak varies in energy across the TI layer, it is consistent between Bi_2Se_3 samples of the same thickness, grown with the same methodology. At the next pixel in the 'ω-q' dataset, 0.114 and 0.137 $Å^{-1}$, the peak at 30 meV is no longer present and the subsequent 70 meV peak has reduced slightly in energy. Additional intensity is observed at higher energies in the Bi_2Se_3/C_{60} sample, shown in red in figure 6.6c, with currently unknown origins. The small dispersion of this mode and its quick decline in intensity is similar to what Jia *et al.* observed for bulk and surface plasmons from bulk carriers [94],

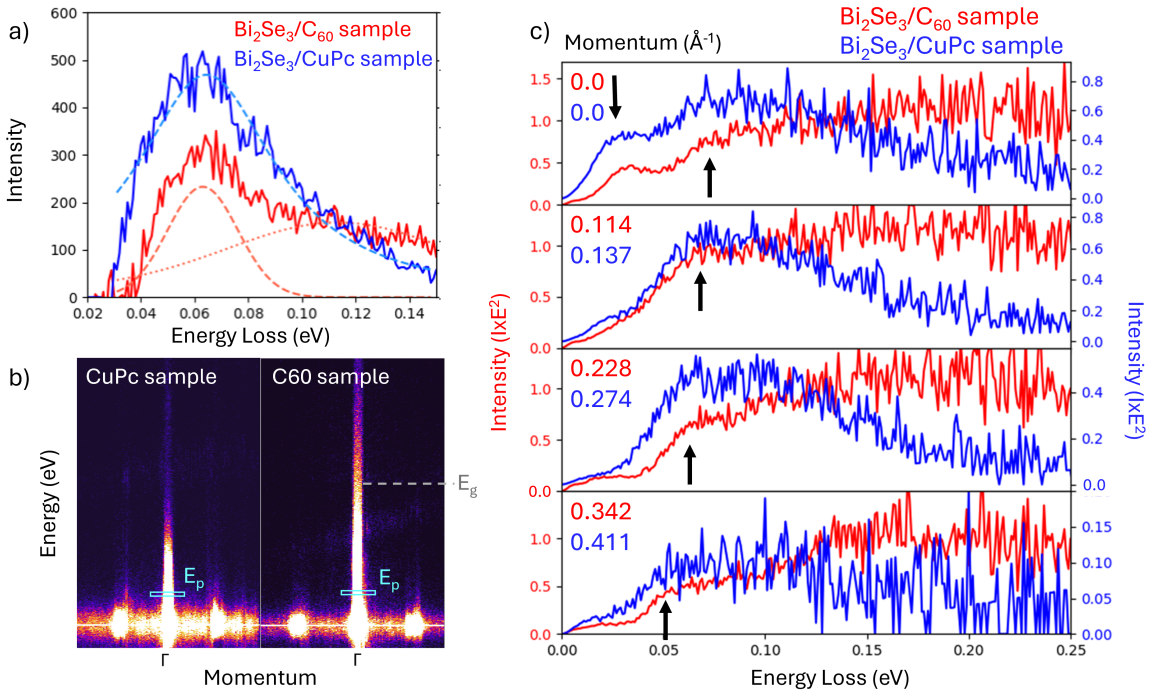

Fig. 6.6 Comparison of qEELS data from the centre of a 15 nm Bi_2Se_3 thin film for two MBE grown samples on sapphire substrates with organic overlayers. a) ZLP subtracted EELS spectra summed over ± 0.41 Å^{-1} and ± 0.46 Å^{-1} in momentum around the centre Γ position acquired in the centre of a Bi_2Se_3 film in samples of Bi_2Se_3/C_{60} (red) and Bi_2Se_3/CuPc (blue) respectively. A plasmon peak can be seen as a shoulder on the ZLP and components of a fit containing a power law function for the ZLP (dotted) and pseudo-Voigt for the plasmon (dashed) for each sample are shown. b) 2D qEELS spectra for each sample with indication of the plasmon peak, E_p at the energy fitted in a. A bandgap feature, characterised by a sharp step edge, E_g, is indicated in the Bi_2Se_3/C_{60} sample at 264 meV. c) qEELS spectra from each sample extracted at the momentum positions given close to the central Γ point. A peak at 60 meV can be observed in both (and 100 meV) with a similar small dispersion, indicating that the plasmon modes of these samples is similar.

therefore, it is proposed that the plasmon mode observed here is a bulk plasmon from bulk Bi_2Se_3 carriers.

In the two phthalocyanine samples discussed in this chapter, phonon modes identifed in bulk H_2Pc and CuPc were distinct from each other, with one broad peak in the H_2Pc spectrum and two sharp peaks in the CuPc spectrum at similar energies around 70 meV. The broad H_2Pc peak was attributed to a combination of different vibrational modes, the lack of individually resolved vibration peaks could be a result of disorder within the layer. Although the phonon modes are different between materials, the distance from the interface, at which the bulk Pc spectrum was recovered, is very similar. At just 2.5 nm into the Pc layer in

both samples, the spectrum no longer changes with distance from the interface, indicating that the effect of the Bi_2Se_3 surface does not extend far into the molecular overlayer. This contrasts with the interaction depth observed at higher energies as discussed in chapter 5, where the bulk EELS spectrum was not recovered until around 2.5 nm into the Pc layer. At higher energy, the interface mode was observed to decay symmetrically on either side of the interface and did not extend past 3 QL into the Bi_2Se_3 layer. In the data presented here, the Bi_2Se_3 spectrum changes throughout the layer towards the interface in both cases and does not seem to recover a bulk state. The trend in plasmon energies towards each phthalocyanine interface is similar between samples and persists deep into the TI layer, not appearing to be confined to the first QL. In the organic however, there is no change to the energies of phonon modes into the layer indicating that these modes are not changed by proximity to the Bi_2Se_3 layer.

The energy of plasmon modes in Bi_2Se_3 was observed to redshift to lower energies towards the phthalocyanine interface in both cases. An exponential redshift of the plasmon energy until reaching the energy of a H_2Pc phonon was observed in the H_2Pc sample and a linear redshift in energy to lower than phonon modes was observed in the CuPc sample. Differences in interfacial behaviour between Bi_2Se_3 and the two Pc molecules are expected due to their differences in electronic structure [290, 266]. ARPES and scanning tunnelling microscopy (STM) measurements suggest a larger shift of the Bi_2Se_3 Dirac point due to CuPc of 336 meV [75], compared to 100 meV due to H_2Pc [6]. There is also a possibility of differences in molecular ordering between films, which could change the collective behaviour and coupling between phonon modes along molecular stacks. There are two many differences between these two samples to be able to accurately isolate the behaviour due to the organic molecules, but the results here do hint towards longer interaction depths than previously thought, with changes to the Bi_2Se_3 plasmons possibly observed past the first couple of QLs. The differing trends in the behaviour also hints towards the possibility of differences in the interaction at the interface that should be studied in further detail on more equivalent samples. Coupling between molecular phonons and TI plasmons across the interface could be possible due to the similar energies of these excitations and could result in larger depths of surface modification than the creation of hybridised states at the interface.

The results presented here suggest that plasmonic behaviour in Bi_2Se_3 can vary substantially between samples with different bulk properties. This must be considered to accurately assess the effect of organic molecular overlayers on the surface and deposition of different organics at different regions on the same Bi_2Se_3 film would clarify this. Furthermore, since the Bi_2Se_3 plasmons were observed to shift in energy throughout the full Bi_2Se_3 layer, a control sample without an organic dopant present is required for the results to be conclusive.

Finally, these systems have lots of potential to modify the TI surface but further measurements are required to quantify the degree of modification in this energy range. Samples need to be compared to those without surface dopants to view the Dirac plasmon modes in this system using STEM EELS to be able to understand that effect of organics on these.

6.6 Conclusion

In conclusion, low energy plasmons were observed in Bi_2Se_3 and showed changes in energy on approach to organic interfaces. Samples were grown using different methodologies and varied in film thickness, both of which influence the plasmonic behaviour in the Bi_2Se_3 layer. As a result, a clear comparison on the effect of different molecular overlayers could not be made.

Phonon modes in two different phthalocyanine thin films were identified, with two sharp phonons at 58 and 78 meV identified in CuPc and a broad peak at 76 meV, potentially composed of several phonon modes, in H_2Pc. Additionally, phonon modes were identified in the insulating substrates with three modes identified in SiO_2 at 56, 97 and 145 meV and three modes in Al_2O_3 at 58, 77 and 106 meV, consistent with literature. Distinct plasmon modes were identified in the TI layer, differing between samples. In the CVT grown Bi_2Se_3/H_2Pc sample, plasmon modes were identified at 120 and 190 meV 18 nm from the H_2Pc interface and showed an exponential decrease in energy towards the organic layer. In contrast, the MBE grown Bi_2Se_3/CuPc sample displayed a linear decrease in plasmon energy decreasing from 111 meV at the Al_2O_3 interface to 20 meV at the CuPc interface. At the centre of this layer, the plasmon energy was 65 meV. To clarify these results, the spectrum at the centre of the TI layer in an MBE grown sample of Bi_2Se_3/C_{60} was investigated and was observed to have some similarities with the Bi_2Se_3/CuPc results.

In literature, plasmon modes in this energy range were identified as bulk and surface plasmon resulting from bulk carriers and their energy was strongly dependent on the bulk carrier density [292, 94, 293]. Different growth methods have been shown to produce Bi_2Se_3 thin films with varied bulk carrier densities so it is proposed that the large difference between the Bi_2Se_3 spectra between samples is at least partially due to differences in carrier density. The higher energy of plasmon modes in the CVT grown Bi_2Se_3/H_2Pc sample suggests a higher carrier density than in the MBE grown samples investigated, however, measurements of the carrier density would be required to confirm this hypothesis. The Bi_2Se_3 plasmon mode identified in the centre of the Bi_2Se_3 layer in MBE grown samples was observed to show a small dispersion to lower energy with increasing momentum in qEELS data, accompanied

by a quick drop in intensity and disappearance at large q. The drop in intensity is consistent with the behaviour of the bulk plasmon mode observed by Jia *et al.* [94].

To clarify the results presented in this chapter, measurements of the system without an organic dopant could be performed. Samples with the same growth parameters, thickness and carrier density are required to accurately compare plasmonic behaviour at Bi_2Se_3/organic interfaces at low energies and isolate the influence of molecular dopants. Analysis of samples with free top and bottom surfaces without the presence of either a substrate or organic overlayer would give insight into both bulk and surface plasmons in Bi_2Se_3. This would provide a reference dataset to compare to the results presented here to help identify features that arise due to both the organic overlayer and insulating substrate. Measurements could be carried out on samples prepared by exfoliation as described in section 2.2.5. Although the bulk carrier density of these flakes would likely differ from films grown by MBE and CVT, it would still allow for bulk features to be identified without shifts in energy towards interfaces. In addition, Bi_2Se_3 flakes prepared via exfoliation can have regions of different QL thickness, such as the sample presented in figure 2.2 in section 2.2.5, which has regions that are 10 QL and 50 QL thick. By comparing these two regions which should have little difference in the way of defect convention and carrier density, it should be possible to identify surface plasmon modes arising from the top and bottom interfaces. The thinner regions of flakes will show surface peaks but thicker regions will be dominated by bulk effects. In addition, aloof-beam EELS measurements could assist in identifying surface plasmon modes. Simulated EELS in COMSOL could aid in this analysis by illustrating the effect of thickness on surface plasmon modes. As the Dirac plasmon will not be modelled in COMSOL, comparison between simulations and experimental data could aid in identification of the Dirac plasmon mode. These experiments alongside qEELS measurements of the same system would provide a complete picture of the low energy plasmonic behaviour of Bi_2Se_3 without molecular dopants and aid in understanding the results presented in this chapter.

Simulations containing the Dirac plasmon would be useful to highlight its expected energy and the influence of interfacing materials. Future work would be required to investigate how best to model these modes. One option could be to introduce an interfacial region with the density of states of the Bi_2Se_3 surface containing the contribution from TSS. The surface properties could be obtained using surface sensitive EELS or optical techniques. Another option would be to approximate the TSS as a 2D conduction layer with Dirac carrier properties. Otherwise it could be useful to include the dynamics of the system and modelling the electron beam as discrete particles instead of a continuous beam, and then considering the path, energy and dispersion of electrons within the material including their propagation at interfaces and in the bulk.

Furthermore, a study of the Bi_2Se_3/C_{60} interface at these energies would prove useful since the behaviour at this interface at higher energies has been more completely analysed in chapter 4. This could be carried out using lamella extracted from the samples discussed in chapter 4 in further work at SuperSTEM and was attempted in the most recent experiment but not possible due to amorphisation of C_{60} layer and sample damage. Momentum-resolved EELS measurements of the plasmon modes identified in Bi_2Se_3 in each sample in bulk regions and approaching each interface would give insight into the nature of the plasmons and could indicate the presence of more exotic plasmon modes such as Dirac and acoustic plasmons being excited at interfaces.

This chapter demonstrates that the low-energy Bi_2Se_3 plasmon behaviour is more complex than that π plasmon behaviour at higher energies. The plasmon behaviour at this energy is strongly dependent on the characteristics of the Bi_2Se_3 film itself and must be considered in future work. Energy shifts observed near the organic interfaces which persist throughout the Bi_2Se_3 layers suggest that that interaction depth between Bi_2Se_3 and organic overlayers may be greater than expected. This could have implications for potential applications of these systems, as modifications of the TI surface at higher energies do not correlate with lower energy surface modifications. Small shifts in π plasmon energy due to varied organics could be accompanied with energy shifts to lower energy bulk plasmons and SPPs and could modify TI properties below the surface further than the topmost few QL. These results point to the possibility of engineering TI properties at and below the surface for enhanced functionality in applications such as photodetector and plasmonic sensing.

7 Conclusion and Future Outlook

The central theme underlying the work presented here is that organic adsorbates can be used to modify the behaviour of interfacial plasmons in the topological insulator Bi_2Se_3. The ultimate aim would be to demonstrate not just modification but also tunability of these plasmonic features through the choice of organic overlayer. Here, we show that distinct layers do, indeed, have an effect, although in some cases it is more subtle than might have been expected. Using electron energy loss spectroscopy (EELS), supporting simulated spectra and momentum-resolved EELS, it was shown that organic molecular overlayers act as surface dopants, altering the energy, localisation and dispersion of plasmon modes on the Bi_2Se_3 surface. Slight changes in interfacial plasmon energy and confinement hint towards differences in TI/organic interactions between molecules.

Simulations of EELS spectra using analytical and numerical methods, presented in Chapter 3, highlighted both the utility and limitations of modelling EELS spectra using bulk dielectric functions. While relativistic analytical calculations of Al_2O_3/Bi_2Se_3 interfaces accurately replicated bulk EELS spectra, they failed to capture plasmon modes localised to the interface, indicating that these arise from interface localised states not captured by coupling of dielectric properties. COMSOL simulations of nanoparticles illustrated the impact of size, shape and beam position on the excitement of localised plasmon modes, with hybridised states observed in nanosphere dimers. Simulated spectra of metallic thin films and Al/Mg_2Si interfaces showed strong agreement with experimental observations, with clear identification of interfacial plasmon modes. However, simulations at the Bi_2Se3/C60 interface diverged from experimental data, suggesting the presence of hybridisation effects, which are not captured by models relying solely on bulk dielectric functions. A rough Bi_2Se3/C60 interface with step edges was simulated and indicated only a small increase in decay length of an SPP at the interface. A localised interface state, modelled by a 2 nm Ag layer, was shown to have more localised excitations than an SPP mode indicating

differences in plasmon confinement expected when a 2D localised state is present at the interface compared to an SPP mode. Comparisons to simulated EELS spectra could therefore be used to highlight features arising from interface localised states such as 2D π plasmons and hybridised plasmon modes.

Experimental data from chapters 4 and 5 revealed distinctive interfacial plasmon modes at Bi_2Se_3/insulator boundaries. At the Al_2O_3/Bi_2Se_3 interface, a $\sqrt{q}$-dispersing surface plasmon was observed at 5.3 eV, localised to within 2 nm of the interface, which was not replicated by analytical EELS calculations. This feature was attributed to a 2D π plasmon, similar to that observed in graphene, originating from π electrons in the first Se layer. At an interface with SiO_2, discussed in chapter 5, a surface plasmon (SP) mode was observed to coexist with the Bi_2Se_3 π plasmon at 5.6 and 7.0 eV respectively. They were both observed within the first Bi_2Se_3 QL, indicating that the SP does not originate from the π electrons within the first Se layer and is distinct from the 2D π plasmon observed at the Al_2O_3/Bi_2Se_3 interface. These differences indicate the necessity of considering the influence of the substrate in analysing plasmonic behaviour in thin TI films and indicate possible substrate-induced modification of TI surfaces. This should be taken into consideration for future device integration.

Molecular doped surfaces were shown to have different behaviour than interfaces with insulators. Crystalline C_{60} overlayers, discussed in chapter 4, were observed to enhance EELS signal in the measured energy range in the first layer of C_{60} atoms. At the Bi_2Se_3/C_{60} interface, a mode at 6.3 eV was observed to be localised to the interface with a symmetric decay on either side. The energy of this mode was not replicated by calculated EELS spectra indicating it was not solely due to coupling of bulk dielectrics from either side of the interface. The surface plasmon at the Bi_2Se_3/C_{60} interface showed little momentum dependence and was almost dispersionless in the first BZ of Bi_2Se_3. This suggests the formation of a hybrid state at this interface and hybrid plasmon excitation. DFT simulations, carried out by collaborators, suggests a transfer of charge from the Bi_2Se_3 surface to the first layer of C_{60} molecules, which could explain why the signal was enhanced at these molecules. The localisation of surface electrons to individual C_{60} molecules could also explain the lack of plasmon dispersion observed.

The Bi_2Se_3 surface was also modified by the presence of a monolayer of graphene and amorphous carbon thin film. The energy of the plasmon mode at the interface was 6.0 eV. The energy of the plasmon mode at Bi_2Se_3/H_2Pc and Bi_2Se_3/CuPc interfaces was observed to be similar, with a localised mode observed at 6.4 eV. This mode was observed to decay away from the interface within 2.3 nm for the Bi_2Se_3/H_2Pc sample and 2.5 nm for the Bi_2Se_3/CuPc sample.

At ultra-low energies, in the meV range, explored in chapter 6, the interaction between Bi_2Se_3 and phthalocyanine overlayers revealed complex behaviour. Differences in plasmon modes between CVT and MBE grown Bi_2Se_3 thin films could not be fully explained by the effect of different organic dopants. Plasmon modes in Bi_2Se_3 were observed at 120 and 190 meV in the CVT grown Bi_2Se_3/H_2Pc sample and at 64 meV at the centre of the TI layer in MBE grown Bi_2Se_3/CuPc and Bi_2Se_3/C_{60} samples. Although Politano et al. identified surface and Dirac plasmon modes at similar energies the to modes we observe in the Bi_2Se_3/H_2Pc sample, the presence of these peaks in bulk of Bi_2Se_3 suggests that they are not surface excitations. Instead, these modes could be attributed to a bulk plasmon mode from free carriers, which varies in energy with carrier density [292]. The lower energy of the bulk plasmon mode in MBE grown samples suggests a lower carrier density and indicates a strong dependence of the low-energy plasmonic behaviour on the TI properties, such as layer thickness and carrier density. Phonon modes in the phthalocyanine layers overlapped with Bi_2Se_3 plasmon energies, suggesting potential plasmon-phonon coupling across the interface. Distinct trends in plasmon energy towards organic interfaces, exponential for H_2Pc and linear for CuPc, indicate complex interactions with larger than expected interaction depths that merit further investigation.

Overall, this work establishes that surface plasmon modes in Bi_2Se_3 are highly sensitive to organic molecular overlayers, with distinct plasmon energies, localisation and dispersion observed compared to insulating substrate interfaces. The presence of the Bi_2Se_3 π plasmon was not observed simultaneously as a surface plasmon at any of the organic interfaces. Surface localised features were observed in each case at slightly different energies of 6.3, 6.0, 6.4 and 6.4 eV for C_{60}, graphene, H_2Pc and CuPc respectively. The interface plasmon was revealed to be most confined at the Bi_2Se_3/C_{60} interface, indicating a strong interaction between the TI π plasmon and dipoles on individual molecules on the surface. Reduced confinement at other organic interfaces hints towards coupling between molecules and TI surfaces and that a well ordered organic surface could influence the interfacial behaviour. A transfer of charge from the TI surface to C_{60} was observed, which agreed with expectations since C_{60} is an electron acceptor. For phthalocyanine samples, a charge transfer to the Bi_2Se_3 surface would be expected from some literature studies [75]. The creation of a hybridised state is likely for these interfaces, however, momentum resolved EELS of each system could confirm this. The observed surface-localised modes and energy shifts highlight the potential for engineering plasmonic properties through interface design.

The limitations of this work have been primarily in sample preparation, with great difficulty found when preparing cross-sections. Improvements in the quality of data, especially for ultra-low energy experiments in chapter 6, could be made with thinner FIB prepared

specimen. Attempts were made to prepare a cross-section with a sharp Bi_2Se_3/vacuum interface as a control specimen but a useable sample was not obtained. In attempt to prepare a Bi_2Se_3 lamella with a Bi_2Se_3/vacuum interface, samples were prepared from bulk Bi_2Se_3 crystals and from MBE and CVT grown thin films. In each case, the Bi_2Se_3 surface either amorphised from the ion beam or amorphous material remained from substrate or protection layers. Future work would involve optimising this preparation to produce useable samples. The use of a protective layer which could be dissolved by a solvent to produce a Bi_2Se_3/vacuum interface could be an option, but would require analysis to ensure that the Bi_2Se_3 surface has not been compromised or doped by the protective layer or solvent.

With recent advances in instrumentation, including the ability to measure EELS spectra at ultra-low energies, and their wider availability, further measurements could be made to fully understand the low energy Bi_2Se_3 plasmonic behaviour. Investigation of the low energy Bi_2Se_3 plasmons in equivalent thin films with different organic dopants and a Bi_2Se_3/vacuum would shed light on the surface interaction and determine how much of the behaviour observed in chapter 6 was due to the organic dopants. The ω-q slit qEELS method could be utilised for each system to accurately measure the interface plasmon dispersion at both the ultra-low and π plasmon energies, to confirm the existence of hybridised plasmons at interfaces. As these techniques have been recent advances, continued use and experimentation will improve upon results.

The work presented in this thesis not only deepens our understanding of interfacial plasmon behaviour in Bi_2Se_3 but highlights the potential of modulating the surface properties through organic overlayers. Variations in energy, confinement and dispersion of Bi_2Se_3 plasmons with different organic dopant overlayers reveals rich interfacial interactions and presents opportunities for the development of tunable TI-based plasmonic devices. By doping the surface with molecules with specific electronic and dielectric properties, it is possible to adjust the interface environment and charge distribution, modifying the TI plasmons in predictable ways. This tunability is important in the development of broadband TI photodetectors, where performance can be improved by enhanced light absorption at specific energies. As the chemical potential and resonance energies of organic layers could be tuned via gating or optical switching [69], these systems show potential as active plasmonic devices, with tunable photodetection and sensing abilities. By enclosing the Bi_2Se_3 surface with an insulating substrate and organic overlayer, the surface is protected from air and the substrates used are applicable to electronic devices. This work lays the foundation for exploiting TI/organic interfaces in next-generation optoelectronic and plasmonic devices.

References

[1] Dragoman M and Dragoman D 2008 *Progress in Quantum Electronics* **32** 1–41

[2] Gramotnev D K and Bozhevolnyi S I 2010 *Nature Photonics* **4** 83–91

[3] Ortmann F, Roche S and Valenzuela S O 2015 *Topological Insulators* (Wiley)

[4] Xu Y, Miotkowski I, Liu C, Tian J, Nam H, Alidoust N, Hu J, Shih C K, Hasan M Z and Chen Y P 2014 *Nature Physics* **10** 956–963

[5] Ren Z, Taskin A A, Sasaki S, Segawa K and Ando Y 2012 *Physical Review B* **85** 155301

[6] Jakobs S, Narayan A, Stadtmüller B, Droghetti A, Rungger I, Hor Y S, Klyatskaya S, Jungkenn D, Stöckl J, Laux M, Monti O L, Aeschlimann M, Cava R J, Ruben M, Mathias S, Sanvito S and Cinchetti M 2015 *Nano Letters* **15** 6022–6029

[7] Shen S Q 2017 *Topological Insulators: Dirac Equation in Condensed Matter* 2nd ed (Springer)

[8] Qi X L and Zhang S C 2010 *Physics Today* **63** 33–38

[9] Maciejko J, Hughes T L and Zhang S C 2011 *Annual Review of Condensed Matter Physics* **2** 31–53

[10] Moore J E 2010 *Nature* **464** 194–198

[11] Turkevich R V, Demikhovskii V Y and Protogenov A P 2017 *Semiconductors* **51** 1495–1499

[12] Bianchi M, Guan D, Bao S, Mi J, Iversen B B, King P D and Hofmann P 2010 *Nature Communications* **1** 128

[13] Hasan M Z and Moore J E 2011 *Annual Review of Condensed Matter Physics* **2** 55–78

[14] Hsieh D, Qian D, Wray L, Xia Y, Hor Y S, Cava R J and Hasan M Z 2008 *Nature* **452** 970–974

[15] Xia Y, Qian D, Hsieh D, Wray L, Pal A, Lin H, Bansil A, Grauer D, Hor Y S, Cava R J and Hasan M Z 2009 *Nature Physics* **5** 398–402

[16] Gehring P, Gao B F, Burghard M and Kern K 2012 *Nano Letters* **12** 5137–5142

[17] Taskin A A, Sasaki S, Segawa K and Ando Y 2012 *Physical Review Letters* **109** 066803

[18] Di Pietro P, Ortolani M, Limaj O, Di Gaspare A, Giliberti V, Giorgianni F, Brahlek M, Bansal N, Koirala N, Oh S, Calvani P and Lupi S 2013 *Nature Nanotechnology* **8** 556–560

[19] Okada K N, Ogawa N, Yoshimi R, Tsukazaki A, Takahashi K S, Kawasaki M and Tokura Y 2016 *Physical Review B* **93** 081403

[20] Kuznetsov K A, Safronenkov D A, Kuznetsov P I and Kitaeva G K 2021 *Applied Sciences* **11** 5580

[21] Glinka Y D, Babakiray S, Johnson T A, Holcomb M B and Lederman D 2015 *Physical Review B* **91** 195307

[22] Zhang H, Yao J, Shao J, Li H, Li S, Bao D, Wang C and Yang G 2014 *Scientific Reports* **4** 5876

[23] Wang Y and Law S 2020 *Journal of Optics* **22** 125001

[24] Wang C C, Shieu F S and Shih H C 2021 *Nanomaterials* **11** 1352 ISSN 2079-4991

[25] Tian Y, Liu H, Li J, Liu B and Liu F 2025 *Nanomaterials* **15** 431

[26] Yao J, Shao J, Wang Y, Zhao Z and Yang G 2015 *Nanoscale* **7** 12535–12541

[27] Liu C, Zhang H, Sun Z, Ding K, Mao J, Shao Z and Jie J 2016 *Journal of Materials Chemistry C* **4** 5648–5655

[28] Pandey A, Yadav R, Kaur M, Singh P, Gupta A and Husale S 2021 *Scientific Reports* **11** 832

[29] Jiao W H, Jiang S, Feng C M, Xu Z A, Cao G H, Xu M, Feng D L, Yamada A, Matsubayashi K and Uwatoko Y 2012 *AIP Advances* **2** 022148

[30] Henini M (ed) 2013 *Molecular Beam Epitaxy* (Elsevier) ISBN 9780123878397

[31] Walsh L A and Hinkle C L 2017 *Applied Materials Today* **9** 504–515

[32] Bai A, Hilse M, Patil P D, Engel-Herbet R and Peiris F 2022 *Journal of Crystal Growth* **591** 126714

[33] Mazumder K and Shirage P M 2021 *Journal of Alloys and Compounds* **888** 161492

[34] Gautam S, Verma A K, Balapure A, Singh B, Ganesan R, Kumar M S, Singh V N, Gahtori B and Kushvaha S S 2022 *Journal of Electronic Materials* **51** 2500–2509

[35] Hsieh D, Xia Y, Qian D, Wray L, Meier F, Dil J H, Osterwalder J, Patthey L, Fedorov A V, Lin H, Bansil A, Grauer D, Hor Y S, Cava R J and Hasan M Z 2009 *Physical Review Letters* **103** 146401

[36] Mazumder K, Sharma A, Kumar Y, Bankar P, More M A, Devan R and Shirage P M 2018 *Physical Chemistry Chemical Physics* **20** 18429–18435

[37] Mazumder K, Sharma A, Kumar Y and Shirage P M 2018 *Physical Chemistry Chemical Physics* **20** 28257–28266

[38] Han G, Chen Z G, Ye D, Yang L, Wang L, Drennan J and Zou J 2014 *Journal of Materials Chemistry A* **2** 7109–7116

[39] Stauber T 2014 *Journal of Physics: Condensed Matter* **26** 123201

[40] Sasaki S, Segawa K and Ando Y 2014 *Physical Review B* **90** 220504

[41] Zhang J M, Ming W, Huang Z, Liu G B, Kou X, Fan Y, Wang K L and Yao Y 2013 *Physical Review B* **88** 235131

[42] Teng J, Liu N and Li Y 2019 *Journal of Semiconductors* **40** 081507

[43] Zhang H, Liu C X, Qi X L, Dai X, Fang Z and Zhang S C 2009 *Nature Physics* **5** 438–442

[44] Fei F, Zhang S, Zhang M, Shah S A, Song F, Wang X and Wang B 2020 *Advanced Materials* **32** 1904593

[45] Cha J J, Kong D, Hong S S, Analytis J G, Lai K and Cui Y 2012 *Nano Letters* **12** 1107–1111

[46] Jia S, Beidenkopf H, Drozdov I, Fuccillo M K, Seo J, Xiong J, Ong N P, Yazdani A and Cava R J 2012 *Physical Review B* **86** 165119

[47] Wang L L, Huang M, Thimmaiah S, Alam A, Bud'ko S L, Kaminski A, Lograsso T A, Canfield P and Johnson D D 2013 *Physical Review B* **87** 125303

[48] Li Z, Meng Y, Pan J, Chen T, Hong X, Li S, Wang X, Song F and Wang B 2014 *Applied Physics Express* **7** 065202

[49] Ando Y 2013 *Journal of the Physical Society of Japan* **82** 102001

[50] Hong S S, Cha J J, Kong D and Cui Y 2012 *Nature Communications* **3** 757

[51] Zhang J, Chang C Z, Zhang Z, Wen J, Feng X, Li K, Liu M, He K, Wang L, Chen X, Xue Q K, Ma X and Wang Y 2011 *Nature Communications* **2** 574

[52] Yoshimi R, Tsukazaki A, Kozuka Y, Falson J, Takahashi K, Checkelsky J, Nagaosa N, Kawasaki M and Tokura Y 2015 *Nature Communications* **6** 6627

[53] Zou W, Wang W, Kou X, Lang M, Fan Y, Choi E S, Fedorov A V, Wang K, He L, Xu Y and Wang K L 2017 *Applied Physics Letters* **110** 212401

[54] Ren Z, Taskin A A, Sasaki S, Segawa K and Ando Y 2011 *Physical Review B* **84** 165311

[55] Arakane T, Sato T, Souma S, Kosaka K, Nakayama K, Komatsu M, Takahashi T, Ren Z, Segawa K and Ando Y 2012 *Nature Communications* **3** 636

[56] Yang F, Taskin A A, Sasaki S, Segawa K, Ohno Y, Matsumoto K and Ando Y 2014 *Applied Physics Letters* **104** 161614

[57] Xu Y, Miotkowski I and Chen Y P 2016 *Nature Communications* **7** 11434

[58] Yang F, Taskin A A, Sasaki S, Segawa K, Ohno Y, Matsumoto K and Ando Y 2015 *ACS Nano* **9** 4050–4055

[59] Zhang M and Wei Z T 2018 *Electronic Materials Letters* **14** 298–304

[60] Lee J, Son J, Kim Y I, Ryu B, Cho B, Kim S, Park S D and Oh M W 2018 *Applied Sciences* **8** 735

[61] Uesugi E, Uchiyama T, Goto H, Ota H, Ueno T, Fujiwara H, Terashima K, Yokoya T, Matsui F, Akimitsu J, Kobayashi K and Kubozono Y 2019 *Scientific Reports* **9** 5376

[62] Noesges B A, Zhu T, Repicky J J, Yu S, Yang F, Gupta J A, Kawakami R K and Brillson L J 2020 *Physical Review Materials* **4** 054001

[63] Chen T, Chen Q, Schouteden K, Huang W, Wang X, Li Z, Miao F, Wang X, Li Z, Zhao B, Li S, Song F, Wang J, Wang B, Van Haesendonck C and Wang G 2014 *Nature Communications* **5** 5022

[64] Kim Y M, Lee K, Fu L, Oh M W, Yang S H, Ning S, Han G, Kim M, Kim J S, Jeong M, Jang J, Lee E, Okunishi E, Sawada H, Kim S i, Pennycook S, Lee Y and Kim S 2021 *Materials Today Physics* **17** 100347

[65] Bianchi M, Hatch R C, Li Z, Hofmann P, Song F, Mi J, Iversen B B, Abd El-Fattah Z M, Löptien P, Zhou L, Khajetoorians A A, Wiebe J, Wiesendanger R and Wells J W 2012 *ACS Nano* **6** 7009–7015

[66] Walsh L A, Smyth C M, Barton A T, Wang Q, Che Z, Yue R, Kim J, Kim M J, Wallace R M and Hinkle C L 2017 *J. Phys. Chem. C* **121** 23551–23563

[67] Lee K W and Lee C E 2020 *Scientific Reports* **10** 14504

[68] Zhang X, Liu Y, Ma X and Abulimiti B 2019 *Journal of Cluster Science* **30** 319–328

[69] Yeh W H, Petefish J W and Hillier A C 2012 *Analytical Chemistry* **84** 1139–1145

[70] Sarkar S, Yang J, Tan L Z, Rappe A M and Kronik L 2018 *Chemistry of Materials* **30** 1849–1855

[71] Kitazawa T, Yaji K, Shimozawa K, Kondo H, Yamanaka T, Yaguchi H, Ishida Y, Kuroda K, Harasawa A, Iwahashi T, Ouchi Y, Komori F, Shin S and Kanai K 2020 *Advanced Materials Interfaces* **7** 2000524

[72] Wang J, Hewitt A S, Kumar R, Boltersdorf J, Guan T, Hunte F, Maggard P A, Brom J E, Redwing J M and Dougherty D B 2014 *Journal of Physical Chemistry C* **118** 14860

[73] Pia A D, Lisi S, Luca O D, Warr D A, Lawrence J, Otrokov M M, Aliev Z S, Chulkov E V, Agostino R G, Arnau A, Papagno M and Costantini G 2018 *ChemPhysChem* **19** 2405–2410

[74] Caputo M, Panighel M, Lisi S, Khalil L, Santo G D, Papalazarou E, Hruban A, Konczykowski M, Krusin-Elbaum L, Aliev Z S, Babanly M B, Otrokov M M, Politano A, Chulkov E V, Arnau A, Marinova V, Das P K, Fujii J, Vobornik I, Perfetti L, Mugarza A, Goldoni A and Marsi M 2016 *Nano Letters* **16** 3409–3414

[75] Sk R, Mulani I and Deshpande A 2018 *The Journal of Physical Chemistry C* **122** 22996–23001

[76] Sessi P, Bathon T, Kokh K A, Tereshchenko O E and Bode M 2014 *Nano Letters* **14** 5092–5096

[77] Bathon T, Sessi P, Kokh K A, Tereshchenko O E and Bode M 2015 *Nano Letters* **15** 2442–2447

[78] Hewitt A S, Boltersdorf J, Maggard P A and Dougherty D B 2017 *Surface Science* **662** 87–92

[79] Cuxart M G, Valbuena M A, Robles R, Moreno C, Bonell F, Sauthier G, Imaz I, Xu H, Nistor C, Barla A, Gargiani P, Valvidares M, Maspoch D, Gambardella P, Valenzuela S O and Mugarza A 2020 *ACS Nano* **14** 6285–6294

[80] Williams D B D B and Carter C B 2009 *Transmission electron microscopy : a textbook for materials science* (Springer) ISBN 9780387765006

[81] Egerton R 2011 *Electron Energy-Loss Spectroscopy in the Electron Microscope* 3rd ed (Springer US)

[82] Hartel P, Rose H and Dinges C 1996 *Ultramicroscopy* **63** 93–114 ISSN 03043991

[83] Pennycook S and Jesson D 1991 *Ultramicroscopy* **37** 14–38

[84] Brydson R 2020 *Electron Energy Loss Spectroscopy* 1st ed (Garland Science) ISBN 9781003076858

[85] Atkins P and de Paula J 2014 *Atkins' Physical chemistry* 10th ed (Oxford: Oxford University Press) ISBN 9780199697403

[86] Egerton R 2014 *Microscopy and Microanalysis* **20** 658–663

[87] Lagos M J, Bicket I C, Mousavi M S S and Botton G A 2022 *Microscopy* **71** i174–i199

[88] Czycholl G 2023 *Solid State Theory, Volume 1* (Berlin, Heidelberg: Springer Berlin Heidelberg) ISBN 978-3-662-66134-5

[89] Maier S A 2007 *Plasmonics: Fundamentals and Applications* (New York, NY: Springer US) ISBN 978-0-387-33150-8

[90] Pennycook S J and Nellist P D (eds) 2011 *Scanning Transmission Electron Microscopy* (New York, NY: Springer New York) ISBN 978-1-4419-7199-9

[91] Shu G J, Zhou Y, Kao M Y, Klingshirn C J, Huang M R S, Huang Y L, Liang Y, Kuo W C H and Liou S C 2019 *Applied Physics Letters* **114** 202103

[92] Autore M, Di Pietro P, Di Gaspare A, D'Apuzzo F, Giorgianni F, Brahlek M, Koirala N, Oh S and Lupi S 2017 *Journal of Physics: Condensed Matter* **29** 183002

[93] Campos A, Troc N, Cottancin E, Pellarin M, Weissker H C, Lermé J, Kociak M and Hillenkamp M 2019 *Nature Physics* **15** 275–280

[94] Jia X, Zhang S, Sankar R, Chou F C, Wang W, Kempa K, Plummer E W, Zhang J, Zhu X and Guo J 2017 *Physical Review Letters* **119** 136805

[95] Stauber T, Gómez-Santos G and Brey L 2017 *ACS Photonics* **4** 2978–2988

[96] Konečná A, Neuman T, Aizpurua J and Hillenbrand R 2018 *ACS Nano* **12** 4775–4786

[97] Liou S C, Chu M W, Sankar R, Huang F T, Shu G J, Chou F C and Chen C H 2013 *Physical Review B* **87** 085126

[98] Greffet J J 2012 Introduction to Surface Plasmon Theory *Plasmonics. Springer Series in Optical Sciences* ed Enoch S and Bonod N (Springer, Berlin, Heidelberg) pp 105–148

[99] Saito H and Kurata H 2014 *Microscopy* **63** 155–159

[100] Kramberger C, Hambach R, Giorgetti C, Rümmeli M H, Knupfer M, Fink J, Büchner B, Reining L, Einarsson E, Maruyama S, Sottile F, Hannewald K, Olevano V, Marinopoulos A G and Pichler T 2008 *Physical Review Letters* **100** 196803

[101] Kinyanjui M K, Kramberger C, Pichler T, Meyer J C, Wachsmuth P, Benner G and Kaiser U 2012 *EPL (Europhysics Letters)* **97** 57005

[102] Tizei L H, Mkhitaryan V, Lourenço-Martins H, Scarabelli L, Watanabe K, Taniguchi T, Tencé M, Blazit J D, Li X, Gloter A, Zobelli A, Schmidt F P, Liz-Marzán L M, García De Abajo F J, Stéphan O and Kociak M 2020 *Nano Letters* **20** 2973–2979

[103] Ginley T, Wang Y, Wang Z and Law S 2018 *MRS Communications* **8** 782–794

[104] Grigorenko A N, Polini M and Novoselov K S 2012 *Nature Photonics* **6** 749–758

[105] Politano A, Silkin V, Nechaev I, Vitiello M, Viti L, Aliev Z, Babanly M, Chiarello G, Echenique P and Chulkov E 2015 *Physical Review Letters* **115** 216802

[106] Deshko Y, Krusin-Elbaum L, Menon V, Khanikaev A and Trevino J 2016 *Optics Express* **24** 7398

[107] Hale L L, Wang Z, Harris C T, Brener I, Law S and Mitrofanov O 2023 *APL Photonics* **8** 051304

[108] Ginley T P and Law S 2018 *Advanced Optical Materials* **6** 1800113

[109] Glinka Y D, Babakiray S, Johnson T A, Holcomb M B and Lederman D 2016 *Nature Communications* **7** 13054

[110] Van Duyne R P 2004 *Science* **306** 985–986

[111] Chen H, Ming T, Zhao L, Wang F, Sun L D, Wang J and Yan C H 2010 *Nano Today* **5** 494–505

[112] Stefancu A, Halas N J, Nordlander P and Cortes E 2024 *Nature Physics* **20** 1065–1077

[113] Zheng Y B, Kiraly B, Cheunkar S, Huang T J and Weiss P S 2011 *Nano Letters* **11** 2061–2065

[114] Morawitz H and Philpott M R 1974 *Physical Review B* **10** 4863–4868

[115] Jiang N, Zhuo X and Wang J 2017 *Chemical Reviews* **118** 3054–3099

[116] Knox C, Rogers M and Moorsom T 2020 Van der Waals epitaxy of C60 on the topological insulator Bi2Se3 Tech. rep. University of Leeds

[117] Knox C S, Vaughan M T, Burnett A D, Ali M, Sasaki S, Linfield E H, Davies A G and Freeman J R 2022 *Physical Review B* **106** 245203

[118] Ichimiya A and Cohen P I 2004 *Reflection High-Energy Electron Diffraction* (Cambridge University Press) ISBN 9780521453738

[119] Moorsom T, McCauley M, Nizamuddin Bin Muhammad Mustafa A, Ramadan S, Burton J, Sasaki S, MacLaren D A and Petrov P K 2024 *Scientific Reports* **14** 30927

[120] Giannuzzi L and Stevie F 1999 *Micron* **30** 197–204

[121] Giannuzzi L A and Stevie F A 2005 *Introduction to Focused Ion Beams: Instrumentation, Theory, Techniques and Practice* (Springer)

[122] Schaffer M, Schaffer B and Ramasse Q 2012 *Ultramicroscopy* **114** 62–71

[123] Yao N (ed) 2007 *Focused Ion Beam Systems* (Cambridge University Press) ISBN 9780521831994

[124] Park Y, Nagai T, Takai M, Lehrer C, Frey L and Ryssel H 1999 *Nuclear Instruments and Methods in Physics Research Section B: Beam Interactions with Materials and Atoms* **148** 25–31

[125] Telari K A, Rogers B R, Fang H, Shen L, Weller R A and Braski D N 2002 *Journal of Vacuum Science & Technology B: Microelectronics and Nanometer Structures Processing, Measurement, and Phenomena* **20** 590–595

[126] Mayer J, Giannuzzi L A, Kamino T and Michael J 2007 *MRS Bulletin* **32** 400–407

[127] Vitale S M and Sugar J D 2022 *Microscopy and Microanalysis* **28** 646–658

[128] Zhong X, Wade C A, Withers P J, Zhou X, Cai C, Haigh S J and Burke M G 2021 *Journal of Microscopy* **282** 101–112

[129] Lotnyk A, Poppitz D, Ross U, Gerlach J W, Frost F, Bernütz S, Thelander E and Rauschenbach B 2015 *Microelectronics Reliability* **55** 2119–2125

[130] Lee J Z, Wynn T A, Schroeder M A, Alvarado J, Wang X, Xu K and Meng Y S 2019 *ACS Energy Letters* **4** 489–493

[131] Zhou J, Wei N, Zhang D, Wang Y, Li J, Zheng X, Wang J, Alsalloum A Y, Liu L, Bakr O M and Han Y 2022 *Journal of the American Chemical Society* **144** 3182–3191

[132] Lv J, Zhang H, Zhang D, Liu L and Han Y 2022 *Accounts of Materials Research* **3** 552–564

[133] Long D M, Singh M K, Small K A and Watt J 2022 *Nanotechnology* **33** 503001

[134] Zhang X, Li Y, Mu W, Bai W, Sun X, Zhao M, Zhang Z, Shan F and Yang Z 2021 *2D Materials* **8** 032002

[135] Green A J, Dey S, An Y Q, O'Brien B, O'Mullane S, Thiel B and Diebold A C 2016 *Journal of Vacuum Science & Technology A: Vacuum, Surfaces, and Films* **34** 061403

[136] Reimer L and Kohl H 2008 *Transmission Electron Microscopy* (*Springer Series in Optical Sciences* vol 36) (New York, NY: Springer New York) ISBN 978-0-387-40093-8

[137] Brydson R (ed) 2011 *Aberration-Corrected Analytical Transmission Electron Microscopy* (Wiley) ISBN 9780470518519

[138] Krivanek O L, Dellby N, Hachtel J A, Idrobo J C, Hotz M T, Plotkin-Swing B, Bacon N J, Bleloch A L, Corbin G J, Hoffman M V, Meyer C E and Lovejoy T C 2019 *Ultramicroscopy* **203** 60–67

[139] Krivanek O L, Lovejoy T C, Dellby N and Carpenter R W 2013 *Journal of Electron Microscopy* **62** 3–21

[140] Browning N, Wallis D, Nellist P and Pennycook S 1997 *Micron* **28** 333–348

[141] Scott J, Thomas P J, MacKenzie M, McFadzean S, Wilbrink J, Craven A J and Nicholson W A 2008 *Ultramicroscopy* **108** 1586–1594

[142] Egerton R F and Takeuchi M 1999 *Applied Physics Letters* **75** 1884–1886

[143] Koh A L, Bao K, Khan I, Smith W E, Kothleitner G, Nordlander P, Maier S A and Mccomb D W 2009 *ACS Nano* **3** 3015–3022

[144] Egerton R 2012 *Microscopy Research and Technique* **75** 1550–1556 ISSN 1059-910X

[145] Meyer J C, Eder F, Kurasch S, Skakalova V, Kotakoski J, Park H J, Roth S, Chuvilin A, Eyhusen S, Benner G, Krasheninnikov A V and Kaiser U 2012 *Physical Review Letters* **108** 196102

[146] Leapman R D, Rez P and Mayers D F 1980 *The Journal of Chemical Physics* **72** 1232–1243

[147] Wang Z, Yin J and Jiang Y 2000 *Micron* **31** 571–580 ISSN 09684328

[148] Berger S D, McKenzie D R and Martin P J 1988 *Philosophical Magazine Letters* **57** 285–290

[149] Seraphin S, Jiao J and Zhou D 1993 *Journal of Materials Research* **8** 1895–1899

[150] Hage F S, Ramasse Q M, Kepaptsoglou D M, Prytz O , Gunnaes A E, Helgesen G and Brydson R 2013 *Physical Review B* **88** 155408

[151] Yamaguchi A, Haruta M, Nemoto T and Kurata H 2018 *Applied Physics Letters* **113** 053101

[152] Do H T B, Zhao M, Li P, Soh Y W, Rangaraj J, Liu B, Jiang T, Zhang X, Lu J, Song P, Teng J and Bosman M 2025 *Preprint* URL https://arxiv.org/abs/2411.07572v2

[153] Shekhar P, Malac M, Gaind V, Dalili N, Meldrum A and Jacob Z 2017 *ACS Photonics* **4** 1009–1014

[154] Dwyer C, Aoki T, Rez P, Chang S, Lovejoy T and Krivanek O 2016 *Physical Review Letters* **117** 256101

[155] Kinyanjui M K, Benner G, Pavia G, Boucher F, Habermeier H U, Keimer B and Kaiser U 2015 *Applied Physics Letters* **106** 203102

[156] Hage F S, Hardcastle T P, Scott A J, Brydson R and Ramasse Q M 2017 *Physical Review B* **95** 195411

[157] Liou S C, Shie C S, Chen C H, Breitwieser R, Pai W W, Guo G Y and Chu M W 2015 *Physical Review B* **91** 045418

[158] Lucas G, Burdet P, Cantoni M and Hébert C 2013 *Micron* **52-53** 49–56

[159] de la Peña F 2024 hyperspy/hyperspy: v2.2.0 URL https://hyperspy.org

[160] Stöger-Pollach M 2008 *Micron* **39** 1092–1110 ISSN 0968-4328

[161] Meier R J 2005 *Vibrational Spectroscopy* **39** 266–269

[162] Browning N D, Arslan I, Erni R and Reed B W 2011 Low-Loss EELS in the STEM *Scanning Transmission Electron Microscopy* (Springer New York) pp 659–688

[163] García De Abajo F J 2010 *Reviews of Modern Physics* **82** 209–275

[164] García de Abajo F J and Howie A 2002 *Physical Review B* **65** 115418

[165] Bolton J and Chen M 1995 *Ultramicroscopy* **60** 247–263

[166] Maclean E D W, Craven A J and McComb D W 2001 *Inst. Phys. Conf. Ser* **168** 259–262

[167] Konečná A, Venkatraman K, March K, Crozier P A, Hillenbrand R, Rez P and Aizpurua J 2018 *Physical Review B* **98** 205409

[168] Cherqui C, Thakkar N, Li G, Camden J P and Masiello D J 2016 *Annual Review of Physical Chemistry* **67** 331–357

[169] Colliex C, Kociak M and Stéphan O 2016 *Ultramicroscopy* **162** A1–A24

[170] Wu Y, Li G and Camden J P 2018 *Chemical Reviews* **118** 2994–3031

[171] Hohenester U and Trügler A 2012 *Computer Physics Communications* **183** 370–381

[172] Lagos M J, Trügler A, Hohenester U and Batson P E 2017 *Nature* **543** 529–532

[173] Zhang K J, Da B and Ding Z J 2018 *Ultramicroscopy* **185** 55–64

[174] Hohenester U 2014 *Computer Physics Communications* **185** 1177–1187

[175] Horák M and Šikola T 2020 *Ultramicroscopy* **216** 113044

[176] Koh A L, Fernández-Domínguez A I, McComb D W, Maier S A and Yang J K 2011 *Nano Letters* **11** 1323–1330

[177] Wiener A, Duan H, Bosman M, Horsfield A P, Pendry J B, Yang J K, Maier S A and Fernández-Domínguez A I 2013 *ACS Nano* **7** 6287–6296

[178] Křápek V, Konečná A, Horák M, Ligmajer F, Stöger-Pollach M, Hrtoň M, Babocký J and Šikola T 2020 *Nanophotonics* **9** 623–632

[179] El-Khoury P Z, Abellan P, Gong Y, Hage F S, Cottom J, Joly A G, Brydson R, Ramasse Q M and Hess W P 2016 *Analyst* **141** 3562–3572

[180] Fan Z, Bosman M, Huang Z, Chen Y, Ling C, Wu L, Akimov Y A, Laskowski R, Chen B, Ercius P, Zhang J, Qi X, Goh M H, Ge Y, Zhang Z, Niu W, Wang J, Zheng H and Zhang H 2020 *Nature Communications* **11** 3293

[181] Horák M, Křápek V, Hrtoň M, Konečná A, Ligmajer F, Stöger-Pollach M, Šamořil T, Paták A, Édes Z, Metelka O, Babocký J and Šikola T 2019 *Scientific Reports* **9** 4004

[182] Yang Y, Hobbs R G, Keathley P D and Berggren K K 2020 *Optics Express* **28** 27405

[183] Raza S, Stenger N, Pors A, Holmgaard T, Kadkhodazadeh S, Wagner J B, Pedersen K, Wubs M, Bozhevolnyi S I and Mortensen N A 2014 *Nature Communications* **5** 4125

[184] Raza S, Esfandyarpour M, Koh A L, Mortensen N A, Brongersma M L and Bozhevolnyi S I 2016 *Nature Communications* **7** 13790

[185] Isoniemi T, Maccaferri N, Ramasse Q M, Strangi G and De Angelis F 2020 *Advanced Optical Materials* **8** 2000277

[186] Assadillayev A, Hinamoto T, Fujii M, Sugimoto H, Brongersma M L and Raza S 2021 *ACS Photonics* **8** 1582–1591

[187] Wu Y, Konečná A, Cho S H, Milliron D J, Hachtel J A and García de Abajo F J 2024 *ACS Nano* **18** 15130–15138

[188] Wang Y, Yang S and Crozier P A 2023 *Microscopy and Microanalysis* **29** 1307–1314

[189] Gallina P, Konečná A, Liška J, Idrobo J C and Šikola T 2023 *Physical Review Applied* **19** 024042

[190] Maciel-Escudero C, Yankovich A B, Munkhbat B, Baranov D G, Hillenbrand R, Olsson E, Aizpurua J and Shegai T O 2023 *Nature Communications* **14** 8478

[191] Yang H, Konečná A, Xu X, Cheong S W, Batson P E, García De Abajo F J and Garfunkel E 2022 *ACS Nano* **16** 18795–18805

[192] Egerton R, Wang Y and Crozier P A 2023 *Microscopy and microanalysis : the official journal of Microscopy Society of America, Microbeam Analysis Society, Microscopical Society of Canada* **29** 362–364

[193] Egerton R F, Venkatraman K, March K and Crozier P A 2020 *Microscopy and Microanalysis* **26** 1117–1123

[194] Govyadinov A A, Konečná A, Chuvilin A, Vélez S, Dolado I, Nikitin A Y, Lopatin S, Casanova F, Hueso L E, Aizpurua J and Hillenbrand R 2017 *Nature Communications* **8** 95

[195] Konečná A, Li J, Edgar J H, García de Abajo F J and Hachtel J A 2021 *Small* **17** 2103404

[196] Johnson D W and Spence J C H 1974 *Journal of Physics D: Applied Physics* **7** 304

[197] Arakawa E and Williams M 1968 *Journal of Physics and Chemistry of Solids* **29** 735–744

[198] Johnson P B and Christy R W 1972 *Physical Review B* **6** 4370

[199] Eljarrat A and Koch C T 2019 *Ultramicroscopy* **206** 112825

[200] Garcia-Molina R, Gras-Marti A, Howie A and Ritchie R H 1985 *Journal of Physics C: Solid State Physics* **18** 5335–5345

[201] Schmidt F P, Ditlbacher H, Hofer F, Krenn J R and Hohenester U 2014 *Nano Letters* **14** 4810–4815

[202] Chen Y and Ming H 2012 *Photonic Sensors* **2** 37–49

[203] Unser S, Bruzas I, He J and Sagle L 2015 *Sensors* **15** 15684–15716

[204] Li G, Cherqui C, Wu Y, Bigelow N W, Simmons P D, Rack P D, Masiello D J and Camden J P 2015 *Journal of Physical Chemistry Letters* **6** 2569–2576

[205] Brennan J 2021 *Fabrication, characterisation, and analysis of plasmonic noble metal nanostructures* Ph.D. thesis University of Glasgow

[206] Hohenester U and Krenn J 2005 *Physical Review B* **72** 195429

[207] Xue H j, Yang H h, Wu R l, Zhang L, Jin F c and Liu X 2023 *Plasmonics* **18** 1233–1240

[208] Dahiya A, Jalendra G, Tamta S and Senthil Kumar P 2023 *Materials Today: Proceedings* **78** 858–863

[209] Halas N J, Lal S, Chang W S, Link S and Nordlander P 2011 *Chemical Reviews* **111** 3913–3961

[210] Kadkhodazadeh S, De Lasson J R, Beleggia M, Kneipp H, Wagner J B and Kneipp K 2014 *Journal of Physical Chemistry C* **118** 5478–5485

[211] Schmidt F P, Ditlbacher H, Hohenester U, Hohenau A, Hofer F and Krenn J R 2012 *Nano Letters* **12** 5780–5783

[212] Kawasaki N, Meuret S, Weil R, Lourenço-Martins H, Stéphan O and Kociak M 2016 *ACS Photonics* **3** 1654–1661

[213] Keast V J, Walhout C J, Pedersen T, Shahcheraghi N, Cortie M B and Mitchell D R 2016 *Plasmonics* **11** 1081–1086

[214] Rosenblatt G, Simkhovich B, Bartal G and Orenstein M 2020 *Physical Review X* **10** 011071

[215] Rocca M 1995 *Surface Science reports* **22** 1–71

[216] Schaffer B, Riegler K, Kothleitner G, Grogger W and Hofer F 2009 *Micron* **40** 269–273

[217] Sevgili O, Orak I and Tiras K S 2022 *Physica E: Low-dimensional Systems and Nanostructures* **144** 115380

[218] Maclean E 2002 *Valence losses at interfaces in aluminium alloys* Ph.D. thesis University of Glasgow

[219] Matetskiy A V, Kibirev I A, Zotov A V and Saranin A A 2016 *Applied Physics Letters* **109** 021606

[220] Cinchetti M, Dediu V A and Hueso L E 2017 *Nature Materials* **16** 507–515

[221] Yang H H, Chu Y H, Lu C I, Butler C J, Sankar R, Chou F C and Lin M T 2015 *Nano Letters* **15** 6896–6900

[222] Wu L, Ireland R M, Salehi M, Cheng B, Koirala N, Oh S, Katz H E and Armitage N P 2016 *Applied Physics Letters* **108** 221603

[223] Wei T, Liu Y, Cui P, Li X and Zhang Z 2022 *Physical Review B* **105** 205408

[224] Whitcher T J, Silly M G, Yang M, Das P K, Peyrot D, Chi X, Eddrief M, Moon J, Oh S, Castro-Neto A H, Breese M B, Wee A T, Silly F and Rusydi A 2020 *NPG Asia Materials* **12** 37

[225] Chen Q, Dwyer C, Sheng G, Zhu C, Li X, Zheng C and Zhu Y 2020 *Advanced Materials* **32** 1907619

[226] Dodabalapur A, Katz H and Haddon R 1995 *Science* **269** 1560–1562

[227] Latzke D W, Ojeda-Aristizabal C, Griffin S M, Denlinger J D, Neaton J B, Zettl A and Lanzara A 2019 *Physical Review B* **99** 045425

[228] Wang Y, Holden J M, Rao A M, Lee W T, Bi X X, Ren S L, Lehman G W, Hager G T and Eklund P C 1992 *Physical Review B* **45** 14396

[229] Romberg H, Sohmen E, Merkel M, Knupfer M, Alexander M, Golden M S, Adelmann P, Pietrus T, Fink J, Seemann R and Johnson R L 1993 *Synthetic Metals* **56** 3038–3043

[230] Mendil N, Daoudi M, Berkai Z and Belghachi A 2018 *Journal of Physics and Energetics* **02** 6–10

[231] Zhang C and Ding T 2024 *Responsive Materials* **2** e20240024

[232] Politano A and Chiarello G 2014 *Nanoscale* **6** 10927–10940

[233] Despoja V, Novko D, Dekanić K, Šunjić M and Marušić L 2013 *Physical Review B* **87** 075447

[234] Bansal N, Kim Y S, Edrey E, Brahlek M, Horibe Y, Iida K, Tanimura M, Li G H, Feng T, Lee H D, Gustafsson T, Andrei E and Oh S 2011 *Thin Solid Films* **520** 224–229

[235] Lutterotti L and Scardi P 1990 *J. Appl. Cryst* **23** 246–252

[236] Xue L, Zhou P, Zhang C X, He C Y, Hao G L, Sun L Z and Zhong J X 2013 *AIP Advances* **3** 052105

[237] Callaert C, Bercx M, Lamoen D and Hadermann J 2019 *Acta Crystallographica Section B: Structural Science, Crystal Engineering and Materials* **75** 717–732

[238] Mortelmans W, De Smet K, Meng R, Houssa M, De Gendt S, Heyns M and Merckling C 2021 *Advanced Materials Interfaces* **8** 2100438

[239] Kriegner D, Harcuba P, Veselý J, Lesnik A, Bauer G, Springholz G and Holý V 2017 *Journal of Applied Crystallography* **50** 369–377

[240] Medlin D L, Ramasse Q M, Spataru C D and Yang N Y 2010 *Journal of Applied Physics* **108** 043517

[241] David W I F, Lbberson R M, Matthewman J C, Prassides K, John T, Dennis S, Hare J P, Kroto H W, Taylor R and Walton D R M 1991 *Nature* **353** 147–149

[242] Li J Q, Zhao Z X, Li Y L, Zhu D B, Gan Z Z and Yin D L 1992 *Physica C: Superconductivity* **196** 135–140

[243] Hytch M J H, Snoeck E and Kilaas R 1998 *Ultramicroscopy* **74** 131–146

[244] Hÿtch M J 1997 *Scanning Microscopy* **11** 53–66

[245] Chung J and Rabenberg L 2007 *Applied Physics Letters* **91** 231902

[246] Muto S, Van Tendeloo G and Amelinckx S 1993 *Philosophical Magazine B: Physics of Condensed Matter; Statistical Mechanics, Electronic, Optical and Magnetic Properties* **67** 443–463

[247] Zhao W B, Zhang X D, Ye Z Y, Zhang J L, Li C Y, Yin D L, Gu Z N, Zhou X H and Jin Z X 1994 *Thin Solid Films* **240** 14–21

[248] Cai W and Nix W D 2016 *Imperfections in Crystalline Solids* (Cambridge University Press) ISBN 9781107123137

[249] Rafferty B and Brown L M 1998 *Physical Review B* **58** 10326

[250] Gillet E and Ealet B 1992 *Surface Science* **273** 427–436

[251] Balzarotti A, Antonangeli F, Girlanda R and Martino G 1984 *Physical Review B* **29** 5903

[252] Gignac W J, Williams R S and Kowalczyk S P 1985 *Physical Review B* **32** 1237–1247

[253] Nascimento V B, De Carvalho V E, Paniago R, Soares E A, Ladeira L O and Pfannes H D 1999 *Journal of Electron Spectroscopy and Related Phenomena* **104** 99–107

[254] Hansen P L, Fallon P J and Krätschmer W 1991 *Chemical Physics Letters* **181** 367–372

[255] Ren S L, Wang Y, Rao A M, McRae E, Holden J M, Hager T, Wang K A, Lee W T, Ni H F, Selegue J and Eklund P C 1991 *Applied Physics Letters* **59** 2678–2680

[256] Terauchi M, Nishimura S and Iwasa Y 2005 *Journal of Electron Spectroscopy and Related Phenomena* **143** 167–172

[257] Larsson S, Volosov A and Rosén A 1987 *Chemical Physics Letters* **137** 501–504

[258] Dravid V P, Liu S and Kappes M M 1991 *Chemical Physics Letters* **185** 75–81

[259] Gordeev Y, Mikoushkin V M and Shnitov V 2000 *Molecular Materials* **13** 1–12

[260] Sakaguchi N, Tanda L and Kunisada Y 2016 *Ultramicroscopy* **169** 37–43

[261] Korneychuk S, Partoens B, Guzzinati G, Ramaneti R, Derluyn J, Haenen K and Verbeeck J 2018 *Ultramicroscopy* **189** 76–84

[262] Nagashima A, Nuka K, Itoh H, Ichinokawa T, Oshima C, Otani S and Ishizawa Y 1992 *Solid State Communications* **83** 581–585

[263] Stern F 1967 *Physical Review Letters* **18** 546–548

[264] Shu G J, Liou S C, Karna S K, Sankar R, Hayashi M and Chou F C 2018 *Physical Review Materials* **2** 044201

[265] Scrocco M, Ercolani C and Paoletti A 1993 *Journal of Electron Spectroscopy and Related Phenomena* **63** 155–166

[266] Zhou Q, Liu Z F, Marks T J and Darancet P 2021 *Journal of Physical Chemistry A* **125** 4055–4061

[267] Yoshida H 2014 *Analytical and Bioanalytical Chemistry* **406** 2231–2237

[268] Stock T J Z, Ogundimu T, Baribeau J, Lu Z and Nogami J 2015 *physica status solidi (b)* **252** 545–552

[269] Roth F, Herzig M, Lupulescu C, Darlatt E, Gottwald A, Knupfer M and Eberhardt W 2015 *Journal of Applied Physics* **118** 185310

[270] Willey T M, Bagge-Hansen M, Lee J R I, Call R, Landt L, van Buuren T, Colesniuc C, Monton C, Valmianski I and Schuller I K 2013 *The Journal of Chemical Physics* **139** 034701

[271] Naumann M and Knupfer M 2018 *The Journal of Chemical Physics* **149** 084704

[272] Politano A, Marino A R, Formoso V, Farías D, Miranda R and Chiarello G 2012 *Plasmonics* **7** 369–376

[273] Cupolillo A, Politano A, Ligato N, Cid Perez D, Chiarello G and Caputi L 2015 *Surface Science* **634** 76–80

[274] Liu Y and Willis R F 2010 *Physical Review B* **81** 081406

[275] Hanson G W 2008 *IEEE Transactions on Antennas and Propagation* **56** 747–757

[276] Kim J, Park S, Jang H, Koirala N, Lee J B, Kim U J, Lee H S, Roh Y G, Lee H, Sim S, Cha S, In C, Park J, Lee J, Noh M, Moon J, Salehi M, Sung J, Chee S S, Ham M H, Jo M H, Oh S, Ahn J H, Hwang S W, Kim D and Choi H 2017 *ACS Photonics* **4** 482–488

[277] Shin S Y, Kim N D, Kim J G, Kim K S, Noh D Y, Kim K S and Chung J W 2011 *Applied Physics Letters* **99** 082110

[278] Dzujah D U, Pradipto A M, Hidayat R and Nakamura K 2023 *RSC Advances* **13** 1446–1454

[279] Jovanović V B, Radović I, Borka D and Mišković Z L 2011 *Physical Review B* **84** 155416

[280] Chae J, Hong S B, Kim D, Kim D K, Kim J, Jeong K, Park S H and Cho M H 2021 *Applied Surface Science* **554** 149623

[281] Voigtländer B 2019 *Atomic Force Microscopy* (Cham: Springer International Publishing) ISBN 978-3-030-13653-6

[282] Yang L H, Gong J M, Sulyok A, Menyhárd M, Sáfrán G, Tőkési K, Da B and Ding Z J 2021 *Physical Chemistry Chemical Physics* **23** 25335–25346

[283] Eberlein T, Bangert U, Nair R R, Jones R, Gass M, Bleloch A L, Novoselov K S, Geim A and Briddon P R 2008 *Physical Review B* **77** 233406

[284] Gass M H, Bangert U, Bleloch A L, Wang P, Nair R R and Geim A K 2008 *Nature Nanotechnology* **3** 676–681

[285] Garvie L, Rez P, Alvarez J and Buseck P 1998 *Solid State Communications* **106** 303–307

[286] Cruickshank A C, Dotzler C J, Din S, Heutz S, Toney M F and Ryan M P 2012 *Journal of the American Chemical Society* **134** 14302–14305

[287] Tao R, Todorovic R, Liu J, Meyer R J, Arnold A, Walkosz W, Zapol P, Romanenko A, Cooley L D and Klie R F 2011 *Journal of Applied Physics* **110** 124313

[288] Orti E and Bredas J L 1992 *Journal of the American Chemical Society* **114** 8669–8675

[289] Dahms U, Burkert M, Starke M, Höhne H J, Link R and Hamann C 1988 *physica status solidi (b)* **149** K85–K88

[290] Grobosch M, Schmidt C, Kraus R and Knupfer M 2010 *Organic Electronics* **11** 1483–1488

[291] Alexander J A, Scheltens F J, Drummy L F, Durstock M F, Hage F S, Ramasse Q M and McComb D W 2017 *Ultramicroscopy* **180** 125–132

[292] Kogar A, Vig S, Thaler A, Wong M H, Xiao Y, Reig-I-Plessis D, Cho G Y, Valla T, Pan Z, Schneeloch J, Zhong R, Gu G D, Hughes T L, Macdougall G J, Chiang T C and Abbamonte P 2015 *Physical Review Letters* **115** 257402

[293] Liu L, Miotkowski I, Zemlyanov D and Chen Y P 2024 *The Journal of Chemical Physics* **160** 141101

[294] Politano A 2021 *Physical Chemistry Chemical Physics* **23** 26061–26069

[295] Politano A, Lamuta C and Chiarello G 2017 *Appl. Phys. Lett* **110** 211601

[296] Richter W and Becker C R 1977 *physica status solidi (b)* **84** 619–628

[297] Haas B, Koch C T and Rez P 2024 *Applied Physics Letters* **125** 150502

[298] Mao R, He P, Liu F, Shi R, Du J and Gao P 2025 *ACS Nano*

[299] Venkatraman K, Rez P, March K and Crozier P A 2018 *Microscopy* **67** i14–i23

[300] Aroca R, Dilella D P and Loutfy R O 1982 *Journal of Physics and Chemistry of Solids* **43** 707–711

[301] El-Saady A A, Roushdy N, Farag A A M, El-Nahass M M and Abdel Basset D M 2023 *Optical and Quantum Electronics* **55** 662

[302] Pistore V, Viti L, Schiattarella C, Riccardi E, Knox C S, Yagmur A, Burton J J, Sasaki S, Davies A G, Linfield E H, Freeman J R and Vitiello M S 2024 *Advanced Optical Materials* **12** 2301673 ISSN 2195-1071

[303] El-Saady A, Farag A, Abdel Basset D M, Roushdy N and El-Nahass M 2023 *Physica B: Condensed Matter* **669** 415339

[304] Chen J, Crowell J and Yates J 1987 *Surface Science* **187** 243–264

[305] Li D, Peng Z, Deng L, Shen Y and Zhou Y 2005 *Vibrational Spectroscopy* **39** 191–199

[306] Heid R, Strauch D and Bohnen K P 2000 *Physical Review B* **61** 8625–8627 ISSN 0163-1829

[307] Kim Y S, Brahlek M, Bansal N, Edrey E, Kapilevich G A, Iida K, Tanimura M, Horibe Y, Cheong S W and Oh S 2011 *Physical Review B* **84** 073109

[308] Li H D, Wang Z Y, Kan X, Guo X, He H T, Wang Z, Wang J N, Wong T L, Wang N and Xie M H 2010 *New Journal of Physics* **12** 103038

[309] Martinez G, Piot B A, Hakl M, Potemski M, Hor Y S, Materna A, Strzelecka S G, Hruban A, Caha O, Novák J, Dubroka A, Drašar v and Orlita M 2017 *Scientific Reports* **7** 6891

A

COMSOL Simulations

The simulation was set up in COMSOL with the following settings using the 'electromagnetic waves, frequency domain' package.

The geometry was set up as discussed in the main text, section 3.4, for each scenario with the beam path defined as a line through the simulation region. The nanoparticle or thin film was surrounded by a region of vacuum and the full simulation region surrounded by an additional vacuum layer defined as a 'perfectly matched layer' artificial domain to prevent unphysical reflections. Materials were defined using refractive indices calculated from Kramers Kronig analysis of experimental EELS data or from reference.

The 'Electromagnetic Waves, Frequency Domain' package was used to set up the simulation. The 'wave equation' was added to all components with the electric field displacement model set to refractive index. Initial values were added to the simulation region and sample to set the initial electric field to zero. An edge current was applied to the line of the beam path with a current defined by $I_0 exp(i\omega z/v_e)$ to represent the electron beam.

A free tetrahedral mesh was applied to the model with a larger node density in the sample region. The maximum distance between nodes was restricted to 40 nm to remain smaller than the wavelength of light in the desired energy range. The perfectly matched layer was meshed using a swept mesh with boundary layers. A finer mesh was used along the beam path.

Simulations were performed as parametric sweeps over the energy loss, where the electric field was calculated at each energy. Along the beam path an 'edge probe' was used to calculate the single scattering spectrum at each energy. The single scattering spectrum was obtained from integration of $\Re[E_z exp(-i\omega z/v_e)]$ along the beam path z.

A direct solver was selected for the calculations to prevent long computation times found at higher energies when using the suggested iterative solver. The solver selected was

'PARDISO' as it had the most consistent computation times. The computation time at each energy was between 1 minute and 1 minute 30 seconds.

Simulation results of the electric field distribution were presented as a slice through the 3D model after subtraction of a background simulation with no materials ($E_{induced} - E_0$). EELS spectra presented were calculated from subtracting a simulation with only vacuum from a spectrum containing the sample.